

# **The Effects of Irradiation on Inconel X-750**

By

Colin D. Judge

A Thesis

Submitted to the School of Graduate Studies

In Partial Fulfillment of the Requirements

For the Degree of

Doctor of Philosophy

McMaster University

@ Copyright by Colin D. Judge, September 2015

Doctor of Philosophy (2015)

McMaster University (Department of Materials Science and Engineering) Hamilton, Ontario

TITLE: The Effects of Irradiation on Inconel X-750

AUTHOR: Colin D. Judge

SUPERVISORS: Professor Gianluigi A. Botton

Dr. Malcolm Griffiths

NUMBER OF PAGES: xxx, 226

## Abstract

Inconel X-750 is a Ni-rich super-alloy with high strength and creep resistance. In CANDU reactors, it is used as tight fitting fuel channel annulus spacers (in the form of a spring). Unlike other reactor designs, the CANDU reactor has a high thermal neutron flux spectra, which, combined with the higher thermal neutron cross section of  $^{58}\text{Ni}$  results in an enhancement of the radiation damage and the internal production of helium and hydrogen. In recent years, it has been observed these spacers are losing ductility and strength following irradiation. The mechanical property evolution of these components is dependent on the irradiation temperature and dose. The primary degradation mechanism remains unclear, and thus provides the focus of this investigation. Inconel X-750 irradiated to these extreme conditions have never been examined prior to this research. The microstructural characterization included in this dissertation include: fractography, microstructural evolution and mechanical property evolution. The discussion of the microstructural evolution is focused on the characterization of helium bubbles. The bubbles form homogeneously in the matrix and aligned along sinks such as dislocations, grain boundaries and precipitates. Electron energy loss spectroscopy (EELS) has been used to probe individual nano-sized bubbles to provide insights into the helium density, helium-to-vacancy ratio, and pressures through the use of a hard sphere equation of state (HSEOS). In addition to understanding the influence of irradiation on helium bubbles, the evolution of secondary strengthening precipitates, gamma prime, are of interest as these precipitates play an important role on the strength and creep resistance of the unirradiated material. The stability of these precipitates with irradiation is thus an important factor to consider with respect to the microstructural degradation. The microstructure is linked to the mechanical properties via microhardness testing on adjacent material. A major contribution to this field is an approach to utilize a focused ion beam (FIB) and transmission electron microscopy (TEM) to perform high

resolution failure analysis of an intergranular fracture surface. Although this technique is not altogether revolutionary, the application of this approach towards post irradiation examination of heavily irradiated Inconel X-750 is unique. This approach provides direct evidence of likely degradation mechanisms, and provides insights for future post irradiation failure analysis for other applicable nuclear components. Working with ex-service material creates some complications with respect to known and unknown variables making it difficult to assess all factors responsible for material degradation. To compliment the program, a controlled proton irradiation program has been performed to gain additional insights into in the effects of irradiation on the microstructure and mechanical property evolution of Inconel X-750, due to the inability to perform controlled experiments with in-service reactor components. In addition to providing a detailed analysis of a CANDU component's degradation, this study provides comprehensive information on irradiation damage processes applicable to other reactor core components.

## **Acknowledgements**

When I started this Ph.D. program, my life was relatively easy and straight forward. I was a relatively junior scientist at Chalk River, had recently married, and the decision to begin working on a Ph.D. was among the easiest of my carrier. Shortly thereafter, my wife and I welcomed our first child, Desmond James Judge. Not to say that Desmond made things difficult, but my life was no longer as easy or straight forward as it once was. Two years later, we welcomed our second child, Simon Colin Judge. Without the support of my wife, Andrea, this thesis would not be possible. She was patient and understanding, especially during extended research trips to Hamilton and/or Idaho.

I started my career studying Nuclear Materials in 2005, when Professor Rick Holt offered me a summer position working with him in his Nuclear Materials research group at Queen's University. This position smoothly transitioned into a M.Sc. thesis program upon undergraduate graduation in 2006. Special thanks go to Rick for introducing me to the nuclear industry, and guiding me to the researcher I am today.

I would like to express my appreciation to Dr. Malcolm Griffiths at CNL who truly made this research program possible. Malcolm is my supervisor and branch Manager at the Canadian Nuclear Laboratory. His insistence that the microstructure of Inconel X-750 be characterized with the TEM has been critical to the industry, and without his persistence, the work within this dissertation would not have been possible. His work has lead to the first look at grain boundary helium bubbles in Inconel X-750 CANDU spacers in 2010, which quickly transitioned into this Ph.D. program.

Professor Gianluigi Botton at McMaster University has acted in a supervisory capacity for this thesis program. I did not know Gianluigi very well upon starting this program, but over the past few years I have gained a great deal of respect and admiration for Gianluigi. His patients, encouragement and helpful suggestions have been invaluable, and I look forward to continue working with him in a collaborative sense for many years to come.

I would like to thank all of my Chalk River colleagues. This work is a small part of a larger initiative, and without their help, this work would have been much harder to accomplish (if at all). Specifically: Michael Stewart, Gregory Morin, Dr. On-Ting Woo, Lori Walters, Dr. Grant Bickel, Dr. Michael Wright, Andrew Buyers, Kris Dunn, Rob Beiers, Craig Lemoine, Craig Buchanan, Erin Sullivan, and Clinton Mayhew.

Part of this work was performed at Idaho National Laboratory, and I would like to thank the following for their help in TEM sample preparation and microhardness measurements: Jim Madden, Dr. Jim Cole, Dr. Brandon Miller, Jatu Burns and Dr. John Jackson. The greatest limitation to obtaining good microscopy is good sample preparation; I only hope the quality of the microscopy contained within this dissertation stands up to the quality of the TEM lamella prepared at INL.

The microscopy performed at McMaster University was done with the assistance of Dr. Glynis De Sylveira, Dr. Nicola Gauquelin, Dr. Andreas Korinek, and Professor Gianluigi Botton.

The proton irradiation was performed in collaboration with Dr. George Jiao and Professor Gary Was at the University of Michigan. Nanohardness testing was performed in collaboration with Dr. Vineet Bhakhri and Professor Robert Klassen at Western University.

I would like to acknowledge the financial support for this program from the CANDU Owners Group, Joint Project 4363 working group 3, Joint Project 4452 working group 3, and CNL (formally AECL) Science and Technology programs, and permission to use the data within this dissertation. A cooperative research and development agreement (CRADA) No. 11-CR-16 between Battelle Energy Alliance (through the National Scientific User Facility) and the Canadian Nuclear Laboratories was used to gain access to INL FIB and TEM facilities as part of this research program. Partial funding for technical support at McMaster was obtained from the ORF-RE “Nuclear Ontario” project. The Canadian Centre of Electron Microscopy (CCEM) at McMaster University was used to perform the majority of the microstructural analysis. The CCEM is a national facility supported by NSERC and McMaster University.

Finally, I finish where I began, and thank my family one more time. My father always instructed me to prepare as much as possible, however, always understand what you know and more importantly, what you don’t know. The following is a quote was used by my father, David Gordon Judge, in his M.Sc. Thesis at Queen’s University, and I feel honoured to include it here so this message can be passed on to future generations in my family.

To my sons, Desmond and Simon...

*“Examinations are formidable even to the best prepared, for the greatest fool may ask more than the wisest man can answer”*

- Charles Caleb Colton 1780-1832

## **Publications**

The work performed in this dissertation have been used in the following published journals and upcoming publications:

**C.D. Judge**, M. Griffiths, L. Walters, M. Wright, G.A. Bickel, O.T. Woo, M. Stewart, S.R. Douglas, F. Garner, “Embrittlement of Nickel Alloys in a CANDU Reactor Environment”, in: T. Yamamoto (Ed.), *Effects of Radiation on Nuclear Materials*, vol. 25, ASTM International, Anaheim, CA, 2012, pp. 161–175.

**C.D. Judge**, N. Gauquelin, L. Walters, M. Wright, J.I. Cole, J. Madden, G.A. Botton, and M. Griffiths, “Intergranular fracture in irradiated Inconel X-750 containing very high concentrations of helium and hydrogen”, *Journal of Nuclear Materials* 2015, 457 (0), 165-172.

O.T. Woo, **C.D. Judge**, H. Nordin, D. Finlayson, C. Andrei, “The microstructure of unirradiated and neutron irradiated Inconel X-750”, in: *Microscopy and Microanalysis*, Nashville, Tennessee, 2011, p. 011.

M. Griffiths, G.A. Bickel, S.A. Donohue, P. Feenstra, **C.D. Judge**, L. Walters, M.D. Wright, “In-Reactor Degradation of Ni-Alloy Components in CANDU Reactor Cores”, 16th Int. Conference on Environmental Degradation of Materials in Nuclear Power Systems – Water Reactors, Asheville, North Carolina, USA, August 11-15, 2013; Asheville, North Carolina, USA, 2013.

**C.D. Judge**, C. Mayhew, M.D. Wright, “Fractography Examination of Ex-Service Inconel X-750 CANDU Spacers”, to be submitted to *Journal of Nuclear Materials*, 2015. Presented at NuMat 2014.

**C.D. Judge**, V. Bhakhri, Z. Jiao, R.J. Klassen, G. Was, M. Griffiths, G.A. Botton, “The effects of proton irradiation on the microstructural and mechanical property evolution of Inconel X-750 with high concentrations of helium”, to be submitted to *Journal of Nuclear Materials*, 2015.

**C.D. Judge**, A. Korinek, G.A. Bickel, J.I. Cole, J. Madden, G.A. Botton, M. Griffiths, “Electron energy loss spectroscopy analysis of helium bubbles in ex-service Inconel X-750 CANDU spacer material”, to be submitted to *Journal of Nuclear Materials*, 2015/2016.

# Table of Contents

Section	Description	Page No.
Abstract.....		i
Acknowledgements.....		iii
Publications.....		vi
Table of Contents.....		vii
List of Tables .....		xiii
List of Figures .....		xiv
1. CHAPTER ONE GENERAL INTRODUCTION.....		1
2. CHAPTER TWO BACKGROUND AND THEORY.....		5
2.1 Inconel X-750 .....		5
2.2 Inconel X-750 in CANDU Reactors.....		8
2.3 Radiation Damage in a CANDU Reactor.....		13
2.3.1 Fast Neutron Damage.....		15
2.3.2 Thermal Neutron Damage.....		17
2.3.3 Rate Theory Calculations.....		18
2.3.4 Production of Helium and Hydrogen in Inconel.....		20
2.4 The Impact of Irradiation Damage on the Microstructure and Mechanical Property Evolution.....		23
2.4.1 Hardening Mechanisms.....		23

2.4.2	Irradiation Induced $\gamma'$ Disordering and Dissolution .....	25
2.4.3	Irradiation-Induced Defects in FCC Microstructures.....	30
2.4.3.1	Irradiation Induced Defects .....	30
2.4.3.2	Cavity Formation.....	33
2.4.4	Density and Pressure of Helium in Bubbles.....	38
2.4.4.1	Equations of State for High Pressure Helium.....	39
2.4.4.2	Experimental Estimates of Helium Density in Bubbles .....	41
2.4.4.3	Pressure Limitations for Helium Bubbles .....	43
2.5	Review of Applicability of the Proton Irradiation to Emulate In-Reactor Neutron Irradiation.....	45
2.5.1	Accelerated Irradiations; Electrons, Protons or Heavy Ions .....	45
2.6	Mechanisms for Grain Boundary Embrittlement in Irradiated Materials.....	48
2.6.1	Cavity/Bubble Embrittlement .....	49
2.6.2	Hydrogen Embrittlement.....	51
2.6.3	Grain Boundary $\gamma'$ Embrittlement.....	52
2.7	Experimental Methods .....	53
2.7.1	Transmission Electron Microscopy.....	53
2.7.1.1	Sample Preparation.....	53
2.7.1.2	TEM Imaging .....	55
2.7.1.3	Electron Energy Loss Spectroscopy .....	57

2.7.2	Micro-Mechanical Testing .....	60
2.7.2.1	Relationship between Hardness and Yield Strength.....	60
3.	CHAPTER THREE EXPERIMENTAL PROCEEDURE .....	62
3.1	Material Selection and Preparation.....	62
3.1.1	Ex-Service Neutron Irradiated Material.....	62
3.1.2	Proton Irradiated Material .....	64
3.1.2.1	Helium Implantation.....	68
3.1.2.2	Proton Irradiation.....	70
3.2	Fractography (Scanning Electron Microscopy).....	72
3.3	X-750 Sectioning .....	73
3.4	TEM.....	74
3.4.1	Imaging Cavities and Helium Bubbles.....	75
3.4.2	Tomography of He Bubbles .....	78
3.4.3	Helium Density Measurements .....	78
3.4.3.1	EELS Acquisition.....	78
3.4.3.2	Quantification of He Density.....	79
3.4.3.3	Determination of the Energy Shift of the 1s→2p Transition .....	79
3.4.3.4	List of Assumptions for Helium Density Measurements .....	80
3.4.4	Gamma Prime Characterization .....	80
3.5	Micro-Mechanical Testing.....	83

3.5.1	Micro-hardness.....	83
3.5.2	Nanohardness .....	84
4.	CHAPTER FOUR EXPERIMENTAL RESULTS .....	85
4.1	Examination of Inconel X-750 CANDU Spacers.....	85
4.1.1	Fractography of Ex-Service Inconel X-750 CANDU Spacers.....	86
4.1.2	Microstructure Evolution of Ex-Service Inconel X-750 CANDU Spacers .....	90
4.1.2.1	Characterization of Homogenous Helium Bubbles.....	91
4.1.2.1.1	Helium Density Approximation Using Electron Energy Loss Spectroscopy.....	97
4.1.2.1.2	Estimating the Bubble Pressure Using A Hard Sphere Equation of State (HSEOS)	105
4.1.2.1.3	Linking Quantitative Bubble Size and Density Distribution with Helium Density Approximations.....	109
4.1.2.2	Characterization of Grain Boundary Helium Bubbles .....	112
4.1.2.3	Characterization of Helium Bubbles in Grain Boundary Precipitates.....	130
4.1.2.4	Characterization of Helium Bubble Alignment on Dislocation and Subgrain Features 135	
4.1.2.5	Characterization of Gamma Prime Precipitate Stability.....	137
4.1.2.6	FIB and TEM Characterization of Intergranular Fracture Surfaces .....	144
4.1.3	Micro-Hardness of Ex-Service Inconel X-750 CANDU Spacers.....	153
4.1.4	Discussion: Ex-Service Inconel X-750 CANDU Spacers.....	155
4.1.4.1	Intergranular Fracture and Likely Fracture Mechanisms .....	155
4.1.4.2	Microstructural and Mechanical Property Evolution of the Matrix .....	159

4.1.4.2.1	Irradiation Induced Defects .....	160
4.1.4.2.2	Helium Bubbles .....	161
4.1.4.2.3	Gamma Prime Precipitates .....	163
4.1.4.3	Hardening Mechanisms .....	164
4.1.4.4	Microstructural Features Which May Influence Grain Boundary Strength .....	166
4.1.4.5	Estimating the Helium-Vacancy Ratio .....	169
4.1.4.6	Estimating the Bubble Pressure with a Hard Sphere Equation of State and Measured Helium Density .....	170
4.1.4.7	Effect of Local Microstructural Inhomogeneities on Bubble Size and Density .....	170
4.2	Proton Irradiated Material .....	172
4.2.1	Effect of Proton Irradiation on the Microstructural Evolution of Inconel X-750 .....	172
4.2.1.1	Helium Bubbles .....	175
4.2.1.2	Voids .....	176
4.2.1.3	Stability of Gamma Prime .....	181
4.2.1.3.1	STEM Diffraction of Gamma Prime .....	191
4.2.2	Effect of Proton Irradiation on the Mechanical Property Evolution of Inconel X-750	195
4.2.2.1	Micro-Hardness .....	195
4.2.2.2	Nanohardness .....	196
4.2.3	Discussion: Proton Irradiated Materials .....	202
4.2.3.1	Suppression of Void Formation with Helium .....	202

4.2.3.2	Characterization of Gamma Prime .....	203
4.2.3.3	Irradiation Hardening .....	204
5.	CHAPTER FIVE GENERAL DISCUSSION.....	207
5.1	How Well did Protons Emulate Neutron Irradiation .....	207
5.2	Considerations in Characterizing Grain Boundary Helium Bubbles.....	208
5.3	Considerations in Characterization of Gamma Prime .....	210
6.	CHAPTER SIX CONCLUSIONS.....	213
6.1	Thesis Overview and Conclusions.....	213
6.2	Ex-Service Inconel X-750 CANDU Spacers.....	214
6.3	Proton Irradiated Inconel X-750.....	216
7.	Recommendations for future work.....	218
8.	Acknowledgements and collaborations.....	220
9.	REFERENCES .....	221

## List of Tables

<b>Table Number</b>	<b>Description</b>	<b>Page No.</b>
TABLE 1	Chemical composition and heat treatment of X-750 used as garter spring material in CANDU reactors.....	10
Table 2	Hard sphere coefficients obtained from fitting HSEOS to MD results. ....	40
Table 3	Ex-Service Test Material .....	63
Table 4	Chemical composition and heat treatment specifications for spacer material compared to bar stock “representative” material for the proton irradiation. ....	65
Table 5	Summary of results for high pressure bubbles. ....	108
Table 6	Quantitative bubble statistics for material irradiated at 300-330°C to 51.2-55.0 dpa and 16830 appm helium (as measured in the bulk material). ....	110
Table 7	Summary of individual components to unirradiated material strength, and relative barrier strengths for main microstructural defects with irradiation. ....	160
Table 8	Summary of contributors to strength following irradiation. ....	166
Table 9	Summary Table of grain boundary characterization for 51.2-55.0 dpa and 17300-18600 appm helium material irradiated at 120-280°C and 300-330°C. ....	168

## List of Figures

Figure Number	Page No.
Figure 1: Crystal structure of a) $\gamma$ (matrix) and b) $\gamma'$ (secondary precipitate). .....	7
Figure 2: Time-Temperature-Transformation Diagram for Inconel X-750 [8]. The red dot indicates the specific heat treatment used for Inconel X-750 CANDU spacers as noted in TABLE 1.....	8
Figure 3: Cross section schematic of a fuel channel in a CANDU reactor.....	9
Figure 4: Optimized and non-optimized X-750 CANDU spacers fit around a Zr-2.5Nb Pressure Tube. ....	10
Figure 5: Flux and temperature profile for a CANDU fuel channel.....	12
Figure 6: Temperature estimates for an individual spacer (optimized) showing the circumferential temperature gradient. Material pinched between the “hot” pressure tube and the “cool” calandria tube at the 6 o’clock position is irradiated at lower temperatures compared to non-pinched material. ....	12
Figure 7: Temperature estimates for an optimized spacer at the pinched location showing the expected gradient at any given time during irradiation. ....	13
Figure 8: Relative neutron spectra experienced by the CANDU Inconel X-750 spacer for an average CANDU channel power [6].....	14
Figure 9: DPA calculations for Inconel X-750 using an average bundle power CANDU channel flux. ....	18
Figure 10: Theoretical swelling rate in Ni-alloys after 10 EFPY CANDU equivalent irradiation. ....	20

Figure 11: Neutron cross sections for the (n,  $\alpha$ ) and (n, p) reactions of  $^{59}\text{Ni}$ . ..... 22

Figure 12: Production of Helium and Hydrogen in Inconel X-750 using an average power CANDU channel flux. .... 23

Figure 13: Temperature relationship on the disordering of  $\gamma'$  in X-750 spacers (no He addition) irradiated in-situ with 1 MeV  $\text{Kr}^{2+}$  ions (Dose Rate of  $10^{-3} \text{ dpa}\cdot\text{s}^{-1}$ ) at the IVEM-tandem facility in Argonne National Laboratories [47, 49]..... 28

Figure 14: Temperature relationship on the disordering of  $\gamma'$  in X-750 spacers (with 200 appm pre-implanted He) irradiated in-situ with 1 MeV  $\text{Kr}^{2+}$  ions (Dose Rate of  $10^{-3} \text{ dpa}\cdot\text{s}^{-1}$ ) at the IVEM-tandem facility in Argonne National Laboratories [48, 49]. .... 28

Figure 15: Temperature relationship on the disordering of  $\gamma'$  in X-750 spacers (with 400 and 5000 appm pre-implanted He) irradiated in-situ with 1 MeV  $\text{Kr}^{2+}$  ions (Dose Rate of  $10^{-3} \text{ dpa}\cdot\text{s}^{-1}$ ) at the IVEM-tandem facility in Argonne National Laboratories [48, 49]. .... 29

Figure 16: Microhardness HV0.2 of irradiated Inconel 718 as a function of irradiation dose. Reproduced from [43]..... 29

Figure 17: Hardness of Alloy 718 as a function of test temperature and dose. Reproduced from [44]. 30

Figure 18: Irradiation induced defect structures from neutron irradiated Inconel X-750 with approximately 55 dpa and 18000 appm helium from 6 and 12 o'clock respectively (i.e.  $\sim 200$  and  $300^\circ\text{C}$  respectively). Extracted from [11]..... 33

Figure 19: Change in Yield Strength in Ni as a function of He bubble density. Reproduced from Knapp et al [68]. .... 37

Figure 20: Equilibrium pressure as a function of cavity radius using Equation 6. .... 39

Figure 21: Pressure estimates for an equilibrium bubble (Figure 19), loop punching, and SIA emission for a pure Ni metal..... 44

Figure 22: Difference in damage morphology, displacement efficiency and average recoil energy for 1MeV particles of different types in Ni. Reproduced from [98]..... 48

Figure 23: Cavities in cold worked 316SS Thimble tube attributed to embrittlement and intergranular fracture [33]..... 50

Figure 24: Schematic outlining interbubble fracture [30]..... 51

Figure 25: Schematic outlining hypothetical fracture mechanism associated with grain boundary decoration of brittle secondary precipitate,  $\gamma'$  [110]..... 52

Figure 26: A through-focal series of small voids in stainless steel irradiated with Ni ions. Extracted from [118]..... 56

Figure 27: Classic particle view of electron scattering by a single atom. (a) Elastic scattering caused by Coulomb interactions with the nucleus, and Inelastic scattering caused by Coulomb repulsion from the (b) inner-shell electrons and (c) outer-shell electrons [121]. ..... 59

Figure 28: An Electron Energy-Loss Spectrum for Inconel X-750 including the base elements, Ti, Cr, Ni, and Fe, in addition to noting the inconvenient location of He-k edge. .... 60

Figure 29: DPA and He calculations and ex-service material used for microstructural characterization. .... 63

Figure 30: PT temperature profile and flux profiles ( $E > 1\text{MeV}$ ) for a) Material A, b) Material B, c) Material C and d) Material D..... 64

Figure 31: Comparison of hypothetical swelling calculations for neutron irradiation in CANDU ( $\sim 10^{-7}$  dpa/s) and proton irradiation at the UofM Tandatron accelerator ( $\sim 10^{-5}$  dpa/s). Dots

indicate irradiation temperatures for the pinched and non-pinched spacers in CANDU (blue) and simulated temperatures in proton irradiation experiments..... 67

Figure 32: He concentration profiles as a result of four tailored implantations designed to create a 1  $\mu\text{m}$  wide region with approximately 6000 appm He. .... 69

Figure 33: Irradiation damage as a function of depth using a proton energy of 1.2 MeV in Inconel X-750 at the Tandetron accelerator at the Michigan Ion Beam Laboratory. The dpa is calculated from SRIM full-cascade and SRIM K-P..... 71

Figure 34: Post crush test images of (A) 12 o'clock showing brittle fracture (limited to no ductility prior to fracture), top, and (B) 6 o'clock showing no fracture and plastic deformation, bottom [10, 13, 14]..... 73

Figure 35: Schematic outlining process of experimental determination of the inelastic mean free path..... 77

Figure 36: TEM micrographs of gamma prime in a) bright-field, b) dark-field and c) [0, 0, 1] zone axis diffraction (left=gamma matrix, right=gamma prime/gamma overlay). Note the bright-field image and dark-field image are not of the same area. .... 83

Figure 37: Fracture surfaces of (A) unirradiated material, (B) 6.4-6.7 dpa and 1700-1800 appm helium material irradiated at 120-280°C, (C) 6.4-6.7 dpa and 1700-1800 appm helium material irradiated at 300-330°C, (D) 16.9-23.6 dpa and 5400-7700 appm helium material irradiated at 120-280°C, (E) 16.9-23.6 dpa and 5400-7700 appm helium material irradiated at 300-330°C, (F) 51.2-55.0 dpa and 17300-18600 appm helium material irradiated at 120-280°C, and (G) 51.2-55.0 dpa and 17300-18600 appm helium material irradiated at 300-330°C..... 88

Figure 38: Secondary intergranular cracks from material irradiated to 51.2-55.0 dpa/17300-18600 appm helium (A)&(C) 120-280°C and (B)&(D) 300-330°C..... 89

Figure 39: Bright-field TEM (imaged in overfocus +500 nm) analysis of non-optimized spacer material irradiated to 6.4-6.7 dpa and 1700-1800 appm helium at (A) 120-280°C, (B) 300-330°C, and (C) quantitative analysis of bubble size distribution..... 93

Figure 40: Bright-field TEM (imaged in overfocus +500 nm) analysis of non-optimized spacer material irradiated to 16.9-23.6 dpa and 5400-7700 appm helium at (A) 120-280°C, (B) 300-330°C, and (C) quantitative analysis of bubble size distribution. .... 94

Figure 41: Bright-field TEM (imaged in overfocus +500 nm) analysis of optimized spacer material irradiated to 42.8-46.4 dpa and 14500-15700 appm helium at (A) 300-330°C, and (B) quantitative analysis of bubble size distribution..... 95

Figure 42: Bright-field TEM (imaged in underfocus -500 nm) analysis of optimized spacer material irradiated to 51.2-55.0 dpa and 17300-18600 appm helium at (A) 120-280°C, (B) 300-330°C, and (C) quantitative analysis of bubble size distribution. .... 97

Figure 43: Helium bubble imaged in (a) HAADF, and (b) Helium EELS map following a 2<sup>nd</sup> order log-polynomial background subtraction..... 99

Figure 44: Helium bubble imaged in (a) HAADF, and (b) Helium EELS map following a 2<sup>nd</sup> order log-polynomial background subtraction..... 99

Figure 45: EELS spectra from the example shown in Figure 43. The signal from the pre-burst bubble, burst bubble are shown in blue and orange respectively. The red line is the Helium signal following subtraction of the two spectra respectively..... 100

Figure 46: Helium density as a function of the inverse of bubble radius (1/r)..... 100

Figure 47: (a) Extracted He 1s→2p transition as a function of bubble diameter, and (b) 1s→2p transition shift as a function of bubble diameter. Red data points are for bubbles which popped during STEM EELS acquisition. .... 101

Figure 48: Variance of helium density comparing the cross section measurement with equation (1) giving additional confidence for the use of equation (1) for more detailed analysis. Open data points were used for determination of  $C_p$ . ..... 102

Figure 49: Helium density as a function of inverse bubble radius. (A) Using integrated intensity and helium cross section (no error), (B) using Equation 10 (no error), and (C) using Equation 10 with propagation of error. .... 104

Figure 50: (A) Helium density as a function of bubble diameter and (B) He/V as a function of bubble diameter..... 105

Figure 51: Bubble pressure as calculated using the Carnahan-Starling approximation outlined in Equation 7-Equation 9 for (A) pressure at room temperature (20°C), and (B) pressure at 588 K (315°C). Equilibrium pressure shown for reference following Equation 6. .... 106

Figure 52: EELS signal from (A) 1.6 nm diameter bubble with a calculated pressure of 3.8 GPa, (B) 1.3 nm diameter bubble with a calculated pressure of 4.2 GPa, and (C) 1 nm diameter bubble with a calculated pressure of 6.2 GPa. .... 108

Figure 53: EELS spectra at the energy window of the He K-edge from a popped bubble (no helium) and the matrix with no visible bubble. .... 112

Figure 54: Grain boundary helium bubbles imaged in the overfocus (+500 nm) condition for material irradiated to 6.4-6.7 dpa and 1700-1800 appm helium at (A) 120-280°C, (B) 300-330°C ..... 113

Figure 55: Grain boundary helium bubbles imaged in the overfocus (+500 nm) condition for material irradiated to 16.9-23.6 dpa and 5400-7770 appm helium at (A) 120-280°C, (B) 300-330°C ..... 114

Figure 56: Grain boundary helium bubbles imaged in the overfocus (+500 nm) condition for material irradiated to 42.8-46.4 dpa and 14500-15700 appm helium 300-330°C. .... 115

Figure 57: Grain boundary helium bubbles imaged in the overfocus (+500 nm) condition for material irradiated to 51.2-55.0 dpa and 17300-18600 appm helium at (A) 120-280°C and (B) 300-330°C..... 116

Figure 58: Helium bubble characterization of 51.2-55.0 dpa and 17300-18600 appm helium material irradiated at 120-280°C (A) imaged edge-on in overfocus (+500 nm) condition, (B) helium bubble analysis of the matrix (red) and grain boundary (blue) with a measured boundary area coverage measured at approximately 6%..... 118

Figure 59: Matrix helium bubble distribution from the grain boundary shown in Figure 57..... 118

Figure 60: Helium bubble characterization of 51.2-55.0 dpa and 17300-18600 appm helium material irradiated at 120-280°C (same area as edge-on analysis shown in Figure 57 but tilted 15° off edge) (A) imaged in overfocus (+500 nm) condition, and (B) grain boundary helium bubble analysis. Boundary area coverage measured at approximately 8% with an average bubble spacing measured at approximately 3.1 nm..... 119

Figure 61: Edge-on grain boundary helium bubble analysis for 51.2-55.0 dpa and 17300-18600 appm helium material irradiated at 300-330°C. (A) TEM micrograph imaged in the overfocus (+500 nm) condition, (B) helium bubble analysis of matrix (red) and boundary (blue) with a grain boundary area coverage loss of approximately 14%. .... 120

Figure 62: Matrix helium bubble distribution from the grain boundary shown in Figure 60. 121

Figure 63: A second edge-on grain boundary helium bubble analysis for 51.2-55.0 dpa and 17300-18600 appm helium material irradiated at 300-330°C. (A) TEM micrograph imaged in

the overfocus (+500 nm) condition, (B) helium bubble analysis of matrix (red) and boundary (blue) reporting a grain boundary area coverage loss of approximately 14%. ..... 121

Figure 64: Matrix helium bubble distribution from the grain boundary shown in Figure 62. 122

Figure 65: Frame images from 3-D tomography reconstruction of a grain boundary in 51.2-55.0 dpa and 17300-18600 appm helium material irradiated at 300-330°C..... 124

Figure 66: Frame images from 3-D tomography reconstruction of a second grain boundary for 51.2-55.0 dpa and 17300-18600 appm helium material irradiated at 300-330°C. .... 124

Figure 67: Schematic representation of the 3-D tomography analysis of a grain boundary edge-on and tilted 90° to show the boundary plane giving a better representation of the bubble distribution and spacing on the boundary. .... 125

Figure 68: In-plane grain boundary analysis boundary for 51.2-55.0 dpa and 17300-18600 appm helium material irradiated at 300-330°C. (A) TEM micrograph underfocus (-500 nm) condition (B) helium bubble analysis assuming only larger bubbles on boundary (i.e., neglecting smaller bubbles which may be in matrix either above or below boundary through thickness), and (C) helium bubble distribution on in-plane grain boundary. Grain boundary area coverage loss estimated at ~12% and average spacing of 3.5 nm. .... 128

Figure 69: Analysis of grain boundary analysis from Figure 66. (A) Helium bubble size distribution comparison between in-plane boundary presented in Figure 66 and matrix presented in Figure 41(c), and (B) the bubble spacing distribution on the grain boundary presented in Figure 66. 129

Figure 70: Helium bubble size distribution within a grain boundary chromium carbide in material irradiated to approximately 51.2-55.0 dpa with 17300-18600 appm helium at 300-

330°C. (A) TEM micrograph imaged in the overfocus condition (+ 500 nm), (B) bubble size distribution, and (C) EELS mapping. .... 132

Figure 71: Helium bubble size distribution within a second grain boundary chromium carbide in material irradiated to approximately 51.2-55.0 dpa with 17300-18600 appm helium at 300-330°C. (A) TEM micrograph imaged in the overfocus condition (+ 500 nm), (B) bubble size distribution, and (C) EELS mapping. .... 133

Figure 72: Helium bubble size distribution within a grain boundary eta precipitate in material irradiated to approximately 51.2-55.0 dpa with 17300-18600 appm helium at 120-280°C. (A) TEM micrograph imaged in the overfocus condition (+ 500 nm), (B) bubble size distribution, and (C) EELS mapping..... 134

Figure 73: HAADF image of sub-grain features with helium bubble alignment (a) low magnification, and (b) higher magnification. .... 136

Figure 74: Bright-field TEM image of sub-grain features with helium bubble alignment imaged in the overfocus condition (+500 nm) (a) low magnification, and (b) higher magnification. .... 136

Figure 75: Gamma prime characterization of non-optimized Inconel X-750 spacers (A) bright-field TEM image showing strain field around gamma prime, (B) TEM diffraction showing gamma prime superlattice points, (C)&(D) intensity profiles of electron diffraction pattern showing gamma prime superlattice reflection. .... 139

Figure 76: Gamma prime characterization of TEM lamella #1 from unirradiated optimized Inconel X-750 spacer. (A) EELS maps of Cr, Ti and Ni, (B) electron diffraction pattern showing gamma prime superlattice reflections, and (C)&(D) intensity profiles of electron diffraction pattern showing gamma prime superlattice reflections. .... 140

Figure 77: Gamma prime characterization of TEM lamella #2 from unirradiated optimized Inconel X-750 spacer. (A) EELS maps of Cr, Ti and Ni, (B) electron diffraction pattern showing gamma prime superlattice reflections, and (C)&(D) intensity profiles of electron diffraction pattern showing gamma prime superlattice reflections. .... 141

Figure 78: 51.2-55.0 dpa and 17300-18600 appm He, 120-280°C gamma prime characterization. .... 142

Figure 79: 51.2-55.0 dpa and 17300-18600 appm He, 300-330°C gamma prime characterization. .... 143

Figure 80: FIB lamella preparation from the intergranular fracture surface of ex-service neutron irradiated Inconel X-750 irradiated to approximately 51.2-55.0 dpa and 17300-18600 appm helium at 300-330°C. Images showing a) rough milling, b) higher magnification of rough milling showing secondary intergranular crack, and c) final TEM specimen with secondary intergranular crack for detailed analytical TEM characterization. .... 145

Figure 81: EELS maps of intergranular fracture surface from ex-service neutron irradiated material with approximately 51.2-55.0 dpa and 17300-18600 appm helium at 300-330°C..... 147

Figure 82: EELS maps of a secondary crack tip from ex-service neutron irradiated material with approximately 51.2-55.0 dpa and 17300-18600 appm helium at 300-330°C..... 149

Figure 83: Higher magnification and resolution EELS maps of secondary crack shown in Figure 80 (near bottom of crack)..... 150

Figure 84: Higher magnification EELS map of secondary crack tip shown in Figure 80 (near bottom of crack)..... 151

Figure 85: HAADF image of grain boundary ahead of secondary crack shown in Figure 79 and Figure 80. .... 152

Figure 86: Micro-hardness of ex-service material as a function of dpa. Measurements were performed on same material presented in Section 4.1.2. Red data points are representative of material irradiated at approximately 120-280°C and black data points are representative of material irradiated at approximately 300-330°C. .... 154

Figure 87: Schematic of potential interaction of grain boundary helium bubbles on material degradation [10]...... 158

Figure 88: Yield strength increase for helium bubbles as a function of applied barrier strength. .... 161

Figure 89: TEM cross section lamella from material irradiated to target damage and helium level at 5 μm depths of (a) 20 dpa, 6000 appm helium irradiated at 250°C, (b) 20 dpa, 6000 appm helium irradiated at 380°C, (c) 40 dpa, 12000 appm helium irradiated at 380°C, and (d) 60 dpa, 18000 appm helium irradiated at 380°C. The profiles show the dpa depth profile (red) and helium density profile (blue) for all samples. Note that all irradiation conditions can be examined in detail within each TEM lamella, including unirradiated material for reference. ... 174

Figure 90: He bubbles in the underfocussed condition (-500 nm) for (a) 20 dpa 6000 appm He 250°C, (b) 20 dpa 6000 appm He 380°C, (c) 40 dpa 12000 appm He 380°C, and (d) 60 dpa 18000 appm He 380°C..... 177

Figure 91: Grain boundary helium bubbles for 20 dpa 6000 appm He 380°C conditions. All conditions show similar bubble alignment on grain boundaries..... 178

Figure 92: Voids in irradiated material without He implantation for material irradiated at 380°C up to 40 dpa and 60 dpa and 40-450 dpa and 60-675 dpa respectively. Red arrows indicate locations of voids (but not limited to)..... 179

Figure 93: Voids in regions with no helium implantation for 60 dpa, 60-150 dpa, 150-675 dpa and 675 dpa respectively. Red arrow indicating location of 1-3 nm He bubbles in region pre-implanted with 18000 appm He. .... 180

Figure 94: STEM HAADF image of large voids at 225 dpa 0 He irradiated at 250°C. The voids align along precipitate boundaries (gamma prime and eta phases highlighted) indicating different vacancy mobility in secondary precipitates compared to the matrix. .... 181

Figure 95: Bright-field and dark-field images of  $\gamma'$  in unirradiated material imaged in (A) Bright-field, (B) electron diffraction showing gamma prime superlattice reflection (green circle), (C) dark-field, and (D) EELS spectrum imaging of  $L_{2,3}$  edges of Cr, Ti, and Ni. Red circles highlight location of  $\gamma'$ . Green circle highlights selection for dark-field on (110) superlattice reflection. .... 184

Figure 96: Bright-field and dark-field images of  $\gamma'$  in irradiated material (20 dpa-6000 appm He) irradiated at 250°C. EELS spectrum imaging of the same region was performed to show the chemical signatures of the precipitate have not changed significantly. Red circles highlight location of  $\gamma'$ . Green circle highlights selection for dark-field on (110) superlattice reflection. .... 185

Figure 97: Bright-field and dark-field images of  $\gamma'$  in irradiated material (20 dpa – 6000 appm He) irradiated at 380°C. EELS spectrum imaging of the same region was performed to show the chemical signatures of the precipitate have not changed significantly. Red circles highlight location of  $\gamma'$ . Green circle highlights selection for dark-field on (110) superlattice reflection. .... 186

Figure 98: Gamma prime characterization in specimen irradiated to target 20 dpa, 6000 appm He irradiated at 250°C. .... 187

Figure 99: Gamma prime characterization in specimen irradiated to target 20 dpa, 6000 appm He irradiated at 380°C.....	188
Figure 100: Gamma prime characterization in specimen irradiated to target 40 dpa, 12000 appm He irradiated at 380°C. ....	189
Figure 101: Gamma prime characterization in specimen irradiated to target 60 dpa, 18000 appm He irradiated at 380°C. ....	190
Figure 102: STEM diffraction on the (001) zone axis for unirradiated material. (A) HAADF image of gamma prime, (B) diffraction pattern from large gamma prime precipitate showing a strong superlattice reflection, (C) diffraction pattern from small gamma prime precipitate showing a weak superlattice reflection, and (D) diffraction pattern from gamma matrix with no superlattice reflection.....	193
Figure 103: STEM diffraction on the (001) zone axis for material irradiated to 20 dpa with 6000 appm helium. (A) HAADF image of gamma prime, (B) diffraction pattern from large gamma prime showing a faint superlattice reflection, and (C) diffraction pattern from gamma matrix (small gamma prime) with no superlattice reflection. ....	194
Figure 104: Change in Micro-hardness for samples implanted with helium (0 dpa), and with and without helium irradiated to 20 dpa, 40 dpa and 60 dpa respectively (dpa values representative of full-cascade SRIM). ....	196
Figure 105: Nanohardness profile for material irradiated to a target dpa and helium concentration of 20 dpa and 6000 appm helium at 250°C.....	198
Figure 106: Nanohardness profile for material irradiated to a target dpa and helium concentration of 20 dpa and 6000 appm helium at 380°C.....	199

Figure 107: Nanohardness profile for material irradiated to a target dpa and helium concentration of 40 dpa and 12000 appm helium at 380°C..... 200

Figure 108: Nanohardness profile for material irradiated to a target dpa and helium concentration of 60 dpa and 18000 appm helium at 380°C..... 201

Figure 109: Effect of thickness on characterizing  $\gamma'$  with TEM. As thickness increases, it becomes increasingly more difficult to differentiate individual  $\gamma'$  or comment on elemental distribution if characterized with spectroscopy techniques in STEM. Image created courtesy of Allan Lockley [135]..... 212

## List of Acronyms and Symbols

$a_1, a_2, a_3, a_4$	coefficients used in calculating hard sphere diameter of helium (Equation 9)
$\alpha$	recombination rate parameter (Equation 1-Equation 2)
$\alpha$	obstacle strength (barrier specific) (Equation 5)
AECL	Atomic Energy of Canada Limited
appm	atomic parts per million
$\mathbf{b}$	burgers vector (Equation 5)
$C(i,v)$	point defect concentration (Equation 1-Equation 2)
CANDU	CANadian Deuterium Uranium
CAES	Center of Advanced Energy Studies
CCEM	Canadian Centre of Electron Microscopy
CNL	Canadian Nuclear Laboratories
$C_p$	Proportional constant Equation 10
CRL	Chalk River Laboratories
CRSS	Critical Resolved Shear Stress
$D$	diffusion coefficient (Equation 1-Equation 2)
$d(t)$	mean diameter (Equation 5)
dpa	displacements per atom
$d_g$	effective hard sphere diameter of helium atoms (Equation 8-Equation 9)
EELS	Electron Energy Loss Spectroscopy
$\Delta E_{1s \rightarrow 2p}$	blue shift of the $1s \rightarrow 2p$ transition
FCC	Face Centre Cubic
FE	Finite Element
FMC	Fuel and Materials Cells

G	damage rate (Equation 1-Equation 2)
G	shear modulus (Equation 5)
$\gamma$	gamma ray
$\gamma$	surface tension (Equation 6)
$\gamma'$	gamma prime secondary precipitate
$\gamma''$	gamma double prime precipitate
HVEMS	Hot Vacuum Extraction Mass Spectroscopy
i	interstitials (Equation 1-Equation 2)
INL	Idaho National Laboratory
k	Boltzmann's constant
$k(i,v)^2$	sink strength (Equation 1-Equation 2)
$\lambda$ , IMFP	Inelastic Mean Free Path
MD	Molecular Dynamic
$\mu$	Shear Modulus
$N(t)$	mean density (Equation 5)
$N_{He}$	Density of Helium (Equation 7)
NSUF	National Scientific User Facility
P	Pressure (Equation 7)
$P_{eq}$	Equilibrium pressure (Equation 6)
$P_{SIA}$	Pressure for SIA emission from a bubble
$P_{loop}$	Pressure for loop punching from a bubble
PKA	Primary Knock on Atom
$\phi$	total flux
r	bubble radius (Equation 6)
SEM	Scanning Electron Microscope (Microscopy)

SCC	Stress Corrosion Cracking
$\sigma_\alpha$	spectral-average $^{59}\text{Ni}$ (n, $\alpha$ ) cross section
$\sigma_p$	spectral-average $^{59}\text{Ni}$ (n,p) cross section
$\sigma_T$	spectral-average total absorption cross section of $^{59}\text{Ni}$
$\sigma_\gamma$	spectral-average $^{59}\text{Ni}$ (n, $\gamma$ ) cross section
$\sigma_y$	Yield Strength
$\sigma_{LR}$	Long Range Hardening
$\sigma_{SR}$	Short Range Hardening
$\sigma_{SA}$	Solution Anneal Hardening Component
SFT	Stacking Fault Tetrahedral
SIA	Self Interstitial Atom
SIRT	Simultaneous Iterative Reconstruction Technique
SRIM	Stopping Range in Metals
STEM	Scanning Transmission Electron Microscope (Microscopy)
t	irradiation time
$t_{\text{abs}}$	Absolute Thickness
$t_{\text{rel}}$	Relative Thickness
T	Taylor factor (Equation 5)
T	Temperature (Equation 7)
TEM	Transmission Electron Microscopy (Microscopy)
TTT	Time temperature transformation
v	vacancies (Equation 1-Equation 2)
VHN	Vickers Hardness Number
y	packing fraction of helium (Equation 7-Equation 8)

## **CHAPTER ONE**

### **GENERAL INTRODUCTION**

Nickel forms the basis for a large class of materials called super-alloys that have good mechanical strength and good creep resistance at elevated temperatures. These alloys are not used extensively in thermal power reactors because they absorb the slow thermal neutrons needed to maintain the nuclear fission chain reactions. When power reactors were first designed and built the long term effect of neutron irradiation on the core materials was largely unknown. Accelerated tests were therefore conducted in liquid metal fast research reactors having radiation damage rates that were an order of magnitude higher than conventional power reactors. This approach has been shown to give good correlations for many alloys, but for nickel alloys in particular the adverse effect of neutron irradiation in a power reactor environment with a high thermal neutron flux compared with a fast reactor environment with low thermal neutron flux needs to be considered. Thermal neutrons create damage by neutron absorption causing transmutation of a nucleus and particle emission leading to increased damage in addition to that of just fast neutrons. Therefore in a high thermal neutron flux the contribution to radiation damage from the  $(n, \gamma)$  reaction needs to be taken into account for elements with a high thermal neutron capture cross section, such as Ni rich super-alloys.

Inconel X-750<sup>®</sup> is a common super-alloy used in the nuclear industry. The high strength and creep resistance of this material make it an ideal candidate for structural components within reactor cores. The material contains approximately 70 wt% Ni, and of this; approximately 68% is the isotope <sup>58</sup>Ni, which has a high thermal neutron capture cross section.

In light water reactors (LWR) Inconel X-750 has been utilized as fuel assembly hold down springs, control rod guide tube support pins, jet pump beams, and core internal bolts [1-5]. All these components operate within a coolant environment, and with the exception of core internal bolts were reported to have minimal radiation damage. Note that these components were not irradiated within a high thermal neutron flux. Premature failures of some of these components were determined to be a result of intergranular stress corrosion cracking (SCC). Recent experiences have shown that heavily irradiated Inconel X-750 may fracture completely intergranularly in the absence of a corrosive environment [6]. This invokes questions regarding how irradiation is affecting the microstructure, and hence influencing the mechanical properties of the material.

Modern heavy water CANDU<sup>®</sup> reactors use Inconel X-750 as internal spacers (a.k.a. garter spring) to maintain a gap between the hot Zr-2.5wt%Nb pressure tube and the cool Zircaloy-2 calandria tube. The spacers operate in a dry CO<sub>2</sub> (up to 5% O<sub>2</sub>) atmosphere (i.e. they are not susceptible to SCC). The CANDU reactor has an extremely high thermal neutron flux spectra compared to other reactor designs (LWR), which, combined

---

\* Inconel is a registered trademark of Special Metals Corporation.

\* CANDU is a registered trademark of Atomic Energy of Canada Ltd. (AECL).

with the high thermal neutron cross section of  $^{58}\text{Ni}$  results in enhanced radiation damage, and internal production of helium and hydrogen. Post irradiated examination on ex-service Inconel X-750 CANDU spacers indicated a reduced strength and ductility compared to unirradiated material. The mechanical property evolution of these components is dependent on the irradiation temperature and dose of the material. Material has been removed for study in this dissertation with up to approximately 55 displacements per atom (dpa), approximately 18000 appm helium, and irradiated at two nominal temperatures: 120-280°C and 300-330°C.

The microstructure and mechanical properties from material irradiated in a power reactor to these combined levels of dpa and helium have never been examined before. As the reduced ductility and strength cannot be explained in terms of corrosion, the effect of irradiation on the microstructure of Inconel X-750 will provide valuable insights into potential material degradation mechanisms. With ex-service material it is difficult to assess all the factors responsible for material degradation. The cost associated with working with heavily irradiated materials from power reactors also limits the scope of the investigation. Therefore, in addition to characterizing neutron irradiated material, a controlled proton irradiation program has been performed to determine the effects of irradiation on Inconel X-750.

In summary, the objectives of this research project are:

To investigate the effects of neutron irradiation on the microstructure and mechanical property evolution of Inconel X-750.

To utilize advanced microscopy techniques to perform failure analysis on an Inconel X-750 reactor component to elucidate potential degradation mechanisms responsible for reduced strength and ductility.

To investigate the effects of proton irradiation on the microstructure and mechanical property evolution of Inconel X-750.

To compare the effects of irradiation from CANDU reactors with proton irradiations with respect to microstructure and mechanical properties.

## CHAPTER TWO

### BACKGROUND AND THEORY

The experimental work presented within this dissertation involves the characterization of neutron and proton irradiated Inconel X-750. This chapter reviews Inconel X-750 and its use within CANDU reactors and the fundamental theories associated with irradiation damage in metals and the impact on mechanical degradation. Studies associated with accelerated irradiations with protons to emulate neutron irradiation are discussed in terms of phase changes, lattice defects and cavity production in FCC metals. Experimental techniques utilized for this research are reviewed and discussed in terms of applicability for characterizing radiation damage.

#### 2.1 Inconel X-750

Inconel X-750 is a precipitation hardened super-alloy with high strength, resistance to creep at elevated temperatures, and excellent corrosion resistance [7]. The most significant contribution to strengthening in Ni super-alloys is from precipitation strengthening obtained from a fine array of gamma prime,  $\gamma'$ , within the  $\gamma$  matrix. The  $\gamma'$  precipitates are coherent precipitates with an  $L1_2$  ordered phase with chemical form  $Ni_3(Ti, Al)$ .  $\gamma'$  has a slight lattice mismatch (0.5%) from the face centre cubic (FCC)  $\gamma$  matrix due to the solute aggregates, Al and Ti (as shown in Figure 1). This local concentration of solute aggregates may contribute to the matrix hardening in the form of

solid-solution strengthening, however the ordered structure of the  $\gamma'$  is reported as a major contributor to the high strength [7]. The ordered structure decreases  $111\langle 110 \rangle$  slip and thus increases the strength of the material. Moreover, the passage of  $\langle 110 \rangle$  dislocations through the  $\gamma'$  precipitates is impeded more at elevated temperatures. Dislocations in an fcc lattice ( $\gamma$  and  $\gamma'$ ) have a burgers vector of  $(1/2)[110]$ , however, in the  $\gamma'$  precipitate, shear on the  $111$  by this vector will substitute a Ni atom onto the Al or Ti lattice site (and vice versa) resulting in the formation of an antiphase boundary (i.e. a layer of misplaced atoms). The easiest (and therefore most common) burgers vector for  $\gamma'$  is  $[100]$ , which is energetically expensive, requiring approximately four times the amount of energy compared to a normal dislocation within the  $\gamma$  matrix. The resulting high strength and creep resistance of these alloys at elevated temperatures is one reason for its use in the aerospace and nuclear industries. The formation of  $\gamma'$  precipitates follows the time-temperature-transformation (TTT) diagram shown in Figure 2 [8].

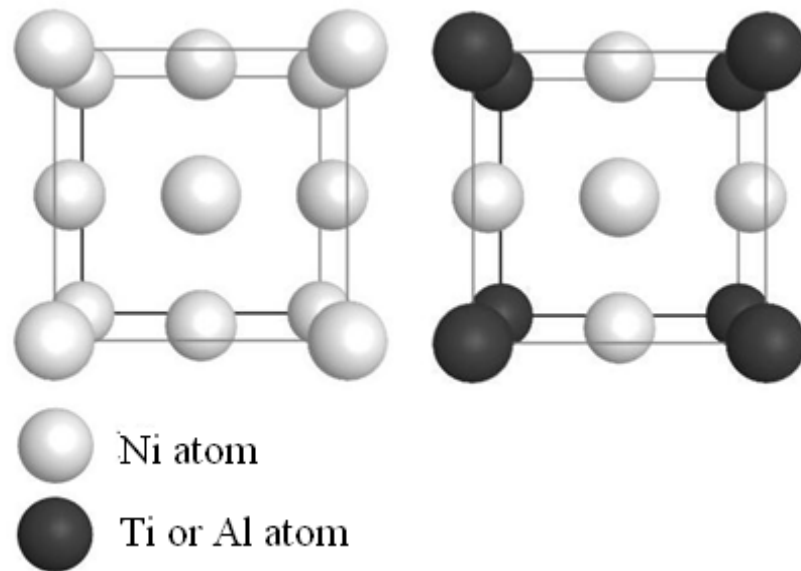


**Figure 1: Crystal structure of a)  $\gamma$  (matrix) and b)  $\gamma'$  (secondary precipitate).**

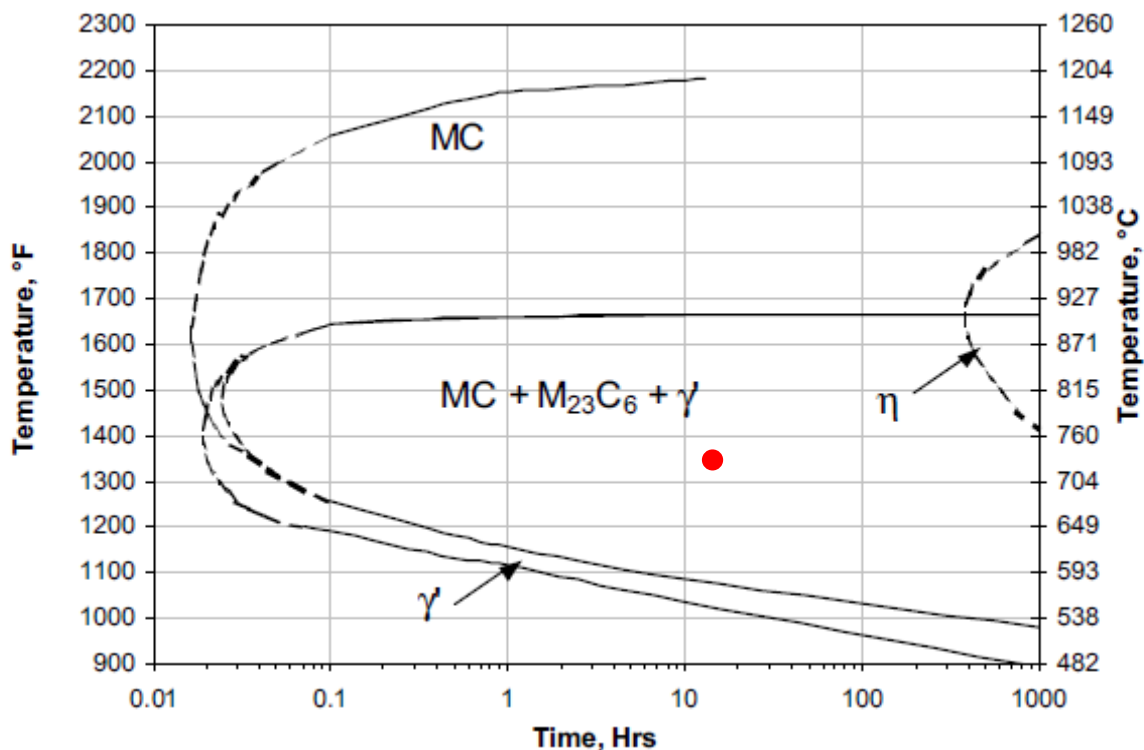


**Figure 2: Time-Temperature-Transformation Diagram for Inconel X-750 [8]. The red dot indicates the specific heat treatment used for Inconel X-750 CANDU spacers as noted in TABLE 1.**

## 2.2 Inconel X-750 in CANDU Reactors

In modern CANDU reactors, Inconel X-750 is used in the form of a fuel channel annulus spacer. The primary function of these spacers is to maintain an insulating gap between the hot Zr-2.5Nb pressure tube and the cool Zircaloy-2 calandria tube. Figure 3 shows a simplified cross section schematic of a CANDU fuel channel. There are approximately 380 horizontal fuel channels in each CANDU reactor, and four spacers per channel to support the pressure tube. In other words, there are approximately 1520 Inconel X-750 spacers per reactor. There are two current spacer designs used in CANDU reactors; the

non-optimized X-750 spacers and the optimized spacers, Figure 4. Both designs incorporate Inconel X-750 of the same chemical composition and heat treatment, TABLE 1, but the non-optimized spacer has a tighter pitch (i.e. the individual coils are closer together), and is made of a heavier gage wire, Figure 4. The non-optimized wire has a cross section of approximately 1 mm x 1 mm, while the optimized wire has a cross section of approximately 0.7 mm x 0.7 mm. Both spacers have a hooked end that is designed to sit at the top of the pressure tube (i.e. 12 o'clock using the conventional clock nomenclature), and a Zr girdle wire that runs through the centre of the coil.

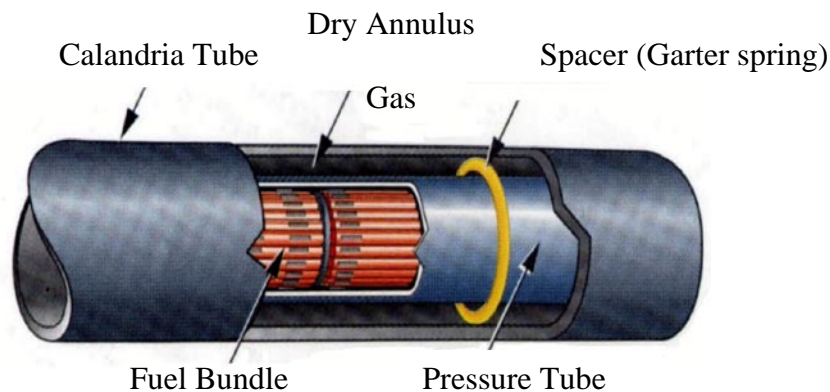


**Figure 3: Cross section schematic of a fuel channel in a CANDU reactor.**

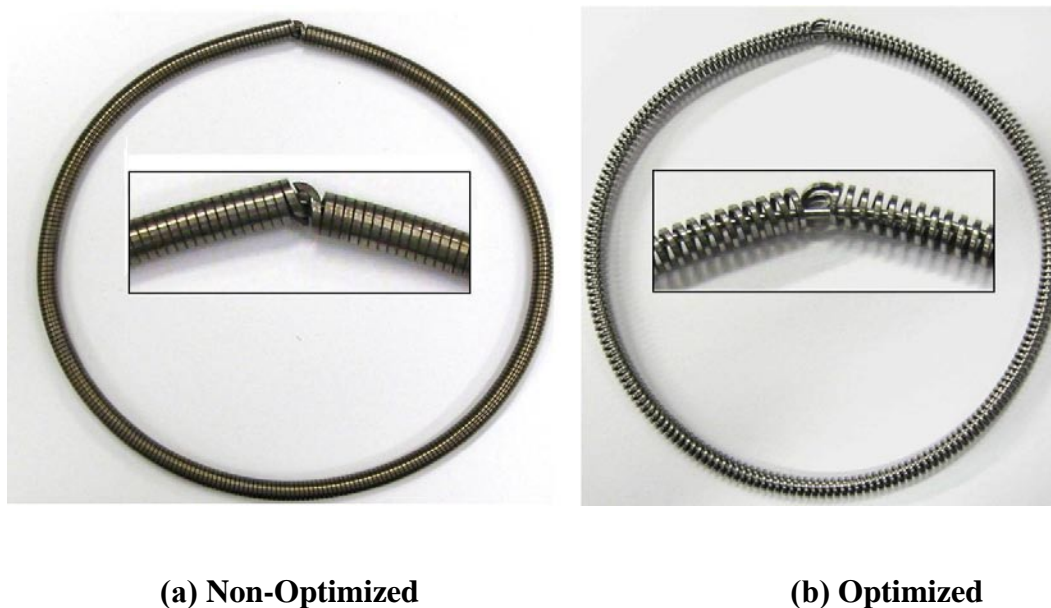


**Figure 4: Optimized and non-optimized X-750 CANDU spacers fit around a Zr-2.5Nb Pressure Tube.**

**TABLE 1 - Chemical composition and heat treatment of X-750 used as garter spring material in CANDU reactors**

Base Element	Ni (Nickel)	
Aluminum	0.40 to 1.00%	% by wt
Carbon	0.08% maximum	% by wt
Cobalt	1.00% maximum	% by wt
Chromium	14.00 to 17.00%	% by wt
Copper	0.50% maximum	% by wt
Iron	5.00 to 9.00%	% by wt
Manganese	1.0% maximum	% by wt
Niobium	1.20% maximum	% by wt
Nickel	70.00% minimum	% by wt
Sulfur	0.01% maximum	% by wt
Silicon	0.50% maximum	% by wt
Tantalum	1.20% maximum	% by wt
Titanium	2.25 to 2.75	% by wt
Balance	[none specified]	
Other elements	Nb+Ta 0.70-1.20	
Solution Treatment	2000-2200°F (1093-1204°C), no hold time specified	
Precipitation Hardening	1350±25°F (732±14°C), hold for 16 ± ½ hr, air cool	

The spacers operate in a dry CO<sub>2</sub> environment. The operating conditions for the spacers are dependent on many factors. Figure 5 shows an example of a typical flux and temperature profile for an individual fuel channel. These profiles differ for different fuel channels within the reactor; therefore, it is important to recognize that different spacers experience different irradiation and temperature environments pending on the specific fuel channel and axial position. During irradiation and under the added weight of the nuclear fuel and heavy water, the pressure tube creeps and sags with respect to the calandria tube, resulting in “pinching” of the spacer between the hot pressure tube and the cool calandria tube [6, 9-16]. As a result, the temperature of the spacer varies as a function of circumferential location, Figure 6. Material that becomes pinched between the two tubes operates at approximately 120-280°C, while material not pinched between the two tubes operates between approximately 300-330°C. The high variability in the low temperature regime arises as a result of local contact points at the pinched location. Locations in direct contact with the pressure tube are at higher temperatures compared to locations in direct contact with the calandria tube, as shown in Figure 7. Additional variability exists due to pressure tube movement during operation. During reactor heat up and cool down, and during normal operation, the pressure tube elongates in the axial direction. The spacers are designed to accommodate this movement by rolling, and therefore, the pinched section of spacer has a non-uniform temperature during service.

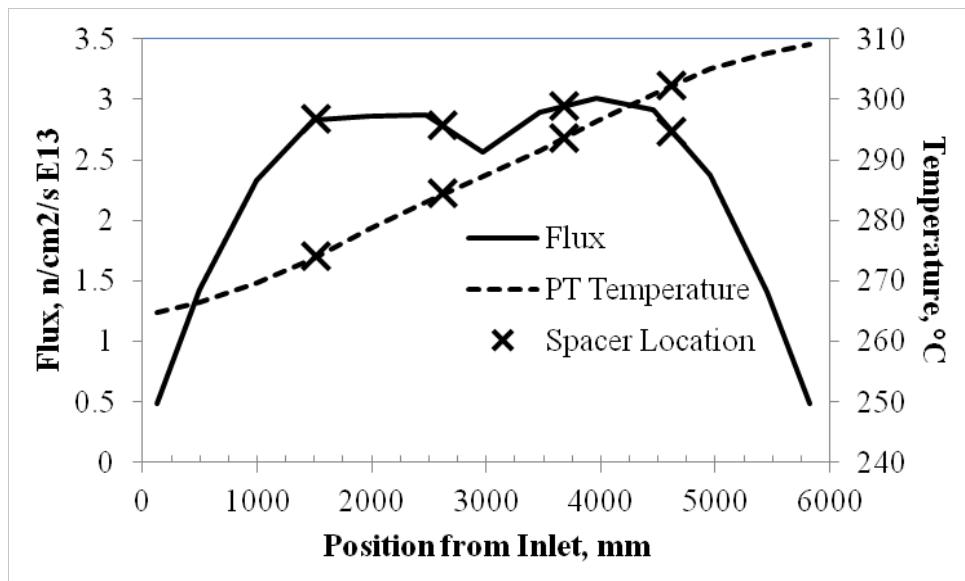


Figure 5: Flux and temperature profile for a CANDU fuel channel.

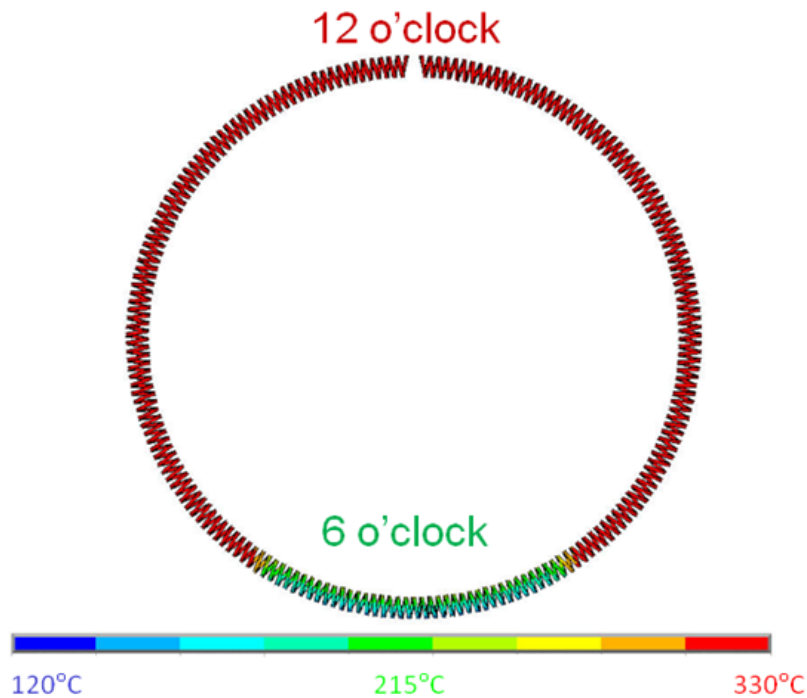
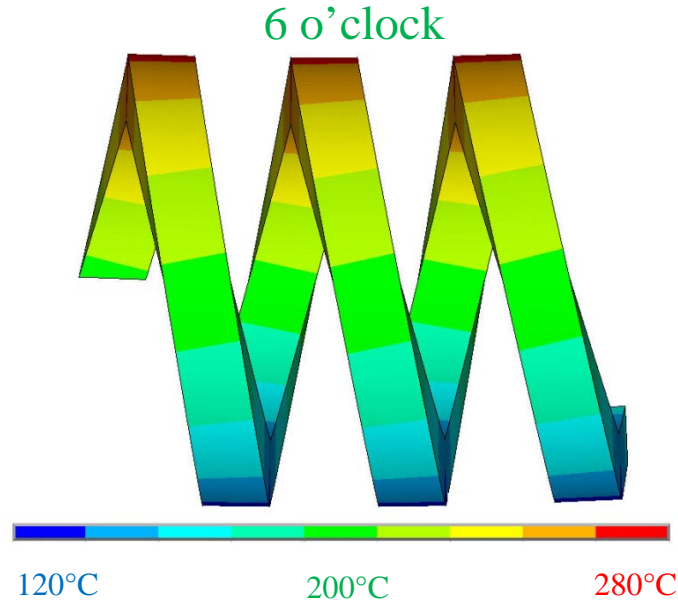


Figure 6: Temperature estimates for an individual spacer (optimized) showing the circumferential temperature gradient. Material pinched between the “hot” pressure tube and the “cool” calandria tube at the 6 o’clock position is irradiated at lower temperatures compared to non-pinched material.



**Figure 7: Temperature estimates for an optimized spacer at the pinched location showing the expected gradient at any given time during irradiation.**

### **2.3 Radiation Damage in a CANDU Reactor**

The maximum flux of fast neutrons in CANDU fuel is about  $4 \times 10^{13}$  n/cm<sup>2</sup>/s,  $E > 1$  MeV. Since each fuel channel in a CANDU reactor is surrounded by its own pressure barrier, the fast neutrons emitted by fission within a cluster of fuel elements have an opportunity to collide first with nuclei in the fuel cladding, second in the heavy water coolant, then in the pressure tube which holds the flowing coolant, then in the spacer which separates the pressure tube from the calandria tube and finally with the calandria tube which excludes the colder moderator from the fuel channel.

It is rare for a given neutron to collide more than once with the structures in a fuel channel before it undergoes repeated collisions and slowing down in the heavy water

moderator. Consequently, fast neutrons produced by fission in the fuel have energies in the MeV or keV range when they interact with the structural materials. By the time a neutron returns to a fuel channel from the moderator and impinges on a spacer, its energy has been reduced to thermal energy levels ( $E < 0.5\text{eV}$ ). Figure 8 shows a typical neutron spectrum experienced by the CANDU Inconel X-750 spacer material in an average power channel [6]. The total thermal neutron flux experienced by a spacer averaged over all locations within the CANDU core is about  $1.4 \times 10^{14} \text{ n/cm}^2/\text{s}$ .

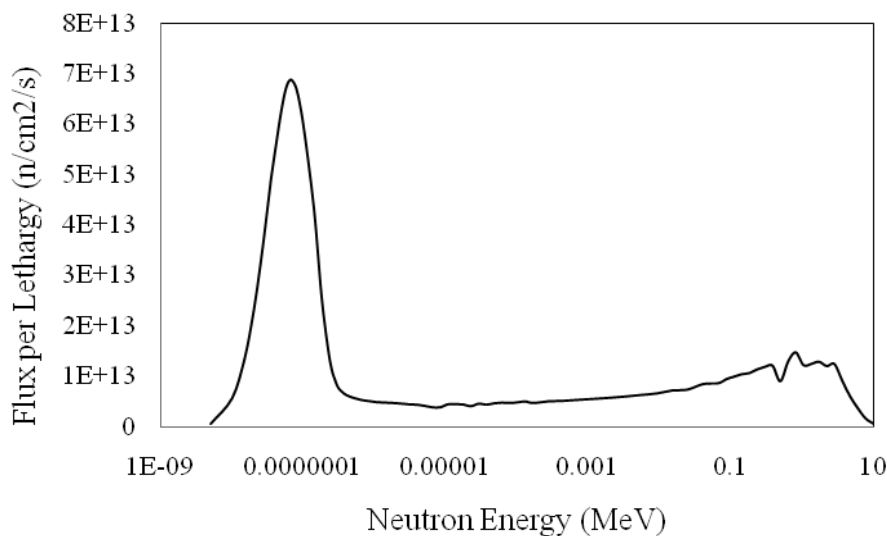


**Figure 8: Relative neutron spectra experienced by the CANDU Inconel X-750 spacer for an average CANDU channel power [6].**

In the reactor core, radiation damage occurs primarily due to the direct displacements caused by fast neutrons resulting in collision cascades. Displacement damage to Inconel X-750 however can also occur from the interaction of thermal neutrons. Thermal neutrons create damage primarily by neutron absorption causing transmutation of a

nucleus and particle emission. The recoil of the nucleus and to a lesser extent the emitted particles themselves then lead to displacement damage.

### **2.3.1 Fast Neutron Damage**

In the core of a nuclear reactor, most of the atomic displacement damage is caused primarily by direct collisions of neutrons with atoms in the components. The damage process follows several stages.

In a perfect Ni lattice (no vacancies or grain boundaries) the energy to displace an atom from the crystal lattice needs to exceed a threshold energy to cause damage. The minimum neutron energy needed to displace a Ni atom from its lattice site is approximately 600 eV. If this minimum neutron energy is reached, the displaced Ni atom will then have a recoil energy of approximately 40 eV (enough energy to create a primary knock-on-atom (PKA)). With a glancing collision, the incoming neutron energy needs to be higher. Neutron energies below 600 eV cannot displace Ni nuclei from lattice positions to create interstitial and vacancy point defects (i.e. Frenkel Pairs).

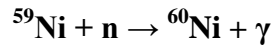
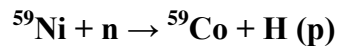
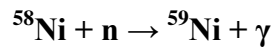
If the neutron energy is above the threshold displacement energy, the recoil energy of the PKA is transferred to nearby nuclei. The PKA is charged and thus partially slowed by electrical repulsion leading to heat. However, much of its energy is transferred by direct collision to nearby nuclei which, in turn, recoil and are displaced from their lattice positions. Each is able to participate in secondary collisions. A collision cascade develops that can involve hundreds of displaced atoms, the number depending on the

initial PKA recoil energy. This cascade happens in a very short time. Once the cascade develops, the internal electrical forces amongst defects and the temperature dependence of interstitial diffusion may cause the mobile interstitials to recombine at a nearby lattice vacancy – the instantaneous yield is known as the cascade efficiency. After the cascade is created, further recombination of displaced atoms with vacancies can occur. Total recombination can be achieved at low reactor operating temperatures or with very high point defect sink densities – this is often referred to as the “recombination-dominated” regime. For most engineering alloys at typical reactor operating temperatures the interstitial and vacancy point defects can migrate to separate sinks – in these circumstances the microstructure can evolve and the material is in the so-called “sink-dominated” regime.

The accumulated radiation damage depends strongly on the incident energies of the neutrons. In a thermal power reactor the neutron energies span ten orders of magnitude: from 10 MeV to 0.0001 eV. Each location in the reactor has a different fraction of neutrons in each energy range (called an energy group). For an average CANDU fuel channel power profile, each Ni atom will be displaced approximately once per year by fast neutrons (i.e. a total contribution of approximately 25 displacements per atom (dpa) in a CANDU spacer by end of life conditions). As previously indicated, this fast damage is supplemented by thermal neutron spectrum due to the interactions that can occur between the neutrons and the material.

### 2.3.2 Thermal Neutron Damage

For components containing natural nickel such as the Inconel X-750 garter springs (which contain ~70% wt.% Ni, 68% of which is  $^{58}\text{Ni}$ ), neutron absorption at thermal energies will cause the following transmutations:



With the abundance of thermal energy neutrons in the CANDU reactor,  $^{59}\text{Ni}$  (which does not exist in natural nickel) will be generated by thermal neutron capture by  $^{58}\text{Ni}$ . Transmutation of  $^{58}\text{Ni}$  to  $^{59}\text{Ni}$  occur with subsequent (n,  $\gamma$ ), (n, p) and (n,  $\alpha$ ) reactions as shown above. Therefore Inconel X-750 garter springs will experience both direct damage displacement and recoil displacement from thermal neutron capture. The  $^{59}\text{Ni}$  (n,  $\gamma$ ), (n, p) and (n,  $\alpha$ ) reactions are very exothermic, producing both charged particles and heavy atomic recoils which lead to radiation damage. For the (n,  $\alpha$ ) reaction with  $^{59}\text{Ni}$  the total damage energy is 176.2 keV per neutron capture and therefore the subsequent total number of displacements per neutron capture in  $^{59}\text{Ni}$  is 1762 [17]; whereas the hydrogen and gamma reactions produce 222 and 4.9 displacements respectively [18].

Figure 9 shows the dpa from an average CANDU bundle power channel at the spacer position. The  $^{59}\text{Ni}$  isotope produced by the  $^{58}\text{Ni}$  (n,  $\gamma$ ) reaction and the subsequent (n,  $\alpha$ ), (n, p) and (n,  $\gamma$ ) reactions make up the majority of the total dpa. Figure 9 shows that the

(n,  $\alpha$ ) reaction has the largest contribution to the total irradiation damage (~35 dpa by spacer end of life). The damage caused by direct collisions with epithermal and fast neutrons (>600 eV) contributes approximately 25 dpa at spacer end of life (i.e. a total of ~60 dpa spacer end of life in an average bundle power CANDU channel<sup>1</sup>).

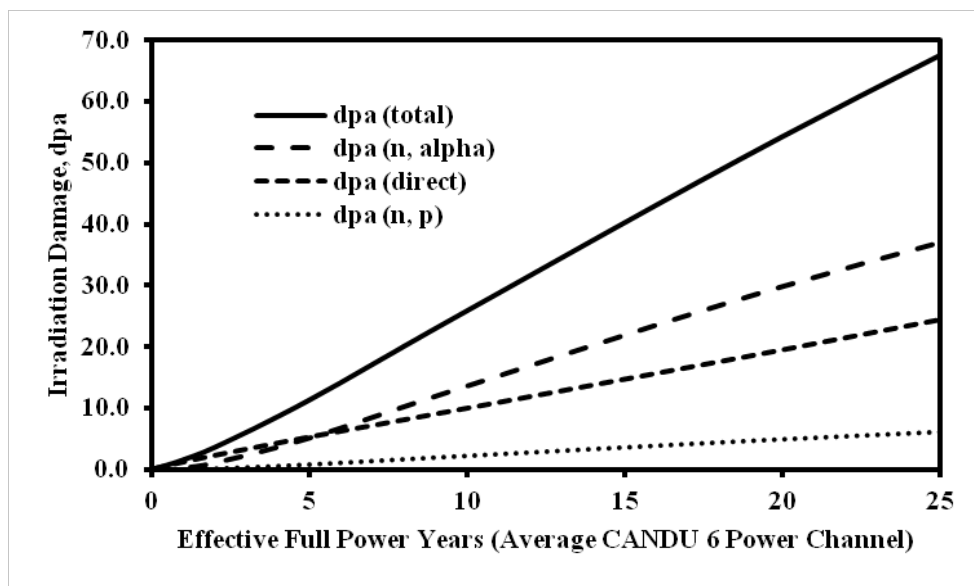


**Figure 9: DPA calculations for Inconel X-750 using an average bundle power CANDU channel flux.**

### 2.3.3 Rate Theory Calculations

Radiation damage rate-theory allows us to explore the interplay of dose, dose rate and temperature on the evolution of microstructure in these materials. As it was shown in Figure 6, the material in an individual spacer ranges from as low as 120-280°C to 300-330°C depending on the circumferential location. Based on the equations described by Heald and Speight [19], and shown below, the theoretical swelling for CANDU spacers

<sup>1</sup> dpa at end of life will exceed 60 dpa for higher power channels.

can be developed as a function of irradiation temperature Figure 10. The key parameters used for these calculations are: 30% interstitial bias for dislocations, a dose rate of  $10^{-7}$  dpa/sec, 3 % damage efficiency, vacancy migration energy = 1.38 eV, dislocation density =  $4 \times 10^{14} \text{ m}^{-2}$ , neutron sink density =  $2 \times 10^{14} \text{ m}^{-2}$ . These calculations assume that bias-driven swelling is occurring and are only intended to illustrate that the temperature range found in a CANDU spacer is close to the transition one might expect between a recombination dominated regime and a sink dominated regime. This transition region and the magnitude of the net vacancy flux to neutral sinks will vary as the microstructure evolves (i.e. as irradiation modifies the microstructure, the swelling curves change).

**Equation 1**  $G - \Sigma[k(v)^2].D(v).C(v) - \alpha .C(v).C(i) = 0$

**Equation 2**  $G - \Sigma [k(i)^2].D(i).C(i) - \alpha .C(v).C(i) = 0$

Where:

i	-	interstitials
v	-	vacancies
G	-	damage rate, dpa.s <sup>-1</sup>
k(i,v) <sup>2</sup>	-	sink strength, m <sup>-2</sup>
D	-	diffusion coefficient, m <sup>2</sup> .sec <sup>-1</sup>
C(i,v)	-	point defect concentrations
α	-	recombination rate parameter

The competition between sinks and recombination determines the location of the curves as a function of dpa rate. Because of the interplay between various sinks that evolve as a function of both dpa and dpa rate the curves will also shift as the microstructure evolves

and the curve shown in Figure 10 shows the expectation following 10 effective full power years (EFPY) of CANDU equivalent irradiation.

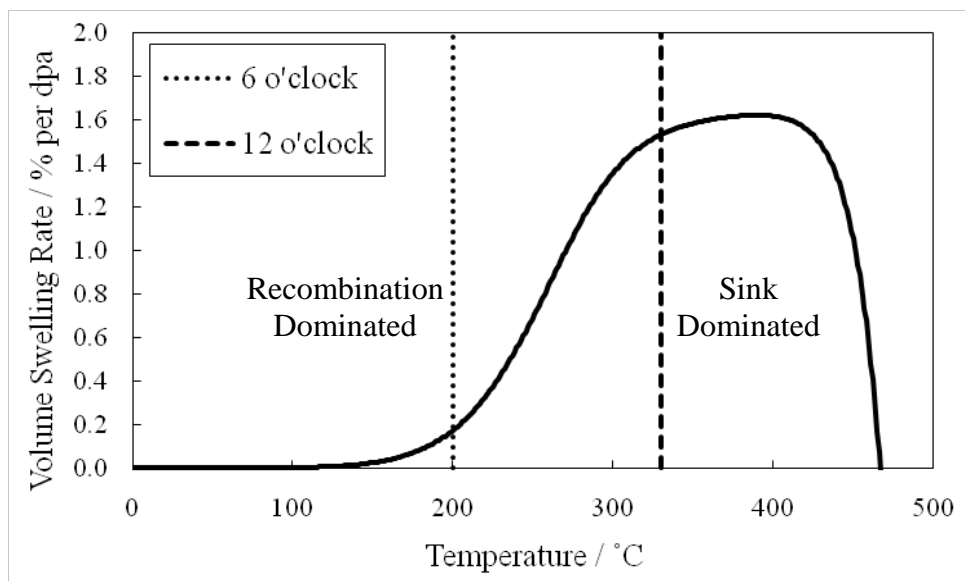


**Figure 10: Theoretical swelling rate in Ni-alloys after 10 EFPY CANDU equivalent irradiation.**

### 2.3.4 Production of Helium and Hydrogen in Inconel

Total dpa is not the only factor to consider when attempting to understand the effects of irradiation on the mechanical properties and microstructure in the Inconel spacer material. As previously shown, the  $(n, \alpha)$  and  $(n, p)$  reactions generate helium and hydrogen. Although hydrogen is relatively soluble and mobile as an interstitial; helium is not. Helium will act to stabilize small vacancy clusters to form bubbles and/or cavities,

thereby accelerating the onset of void swelling which could contribute to a form of grain boundary embrittlement [9, 20-33].

The energy dependent (n, p) and (n, α) reaction cross sections for <sup>59</sup>Ni are shown in Figure 11. Note that the <sup>59</sup>Ni cross sections reverse such that at higher neutron energies there is a higher probability to produce hydrogen compared to helium production. Energies and displacements will increase somewhat for fast neutron reactions with <sup>59</sup>Ni. The formula for calculating the hydrogen and helium production from the two step <sup>58</sup>Ni(n,γ)→<sup>59</sup>Ni(n,p)+<sup>59</sup>Co [34] and <sup>58</sup>Ni(n,γ)→<sup>59</sup>Ni(n,α)+<sup>56</sup>Fe [35] reactions were developed by Greenwood et al. [17, 34] and are listed below:

$$\text{Equation 3} \quad \frac{N(H)}{N_o(^{58}Ni)} = \frac{\sigma_p}{\sigma_T} + \frac{\sigma_p e^{-\sigma_\gamma \phi t}}{(\sigma_\gamma - \sigma_T)} - \frac{\sigma_\gamma \sigma_p e^{-\sigma_\gamma \phi t}}{(\sigma_\gamma - \sigma_T) \sigma_T}$$

$$\text{Equation 4} \quad \frac{N(He)}{N_o(^{58}Ni)} = \frac{\sigma_\alpha}{\sigma_T} + \frac{\sigma_\alpha e^{-\sigma_\gamma \phi t}}{(\sigma_\gamma - \sigma_T)} - \frac{\sigma_\gamma \sigma_\alpha e^{-\sigma_\gamma \phi t}}{(\sigma_\gamma - \sigma_T) \sigma_T}$$

Where:

$N(H)$	= hydrogen atoms produced
$N(He)$	= helium atoms produced
$N_o(^{58}Ni)$	= initial number of <sup>58</sup> Ni atoms
$\sigma_\alpha$	= spectral-averaged <sup>59</sup> Ni(n,α) cross section
$\sigma_p$	= spectral-averaged <sup>59</sup> Ni(n,p) cross section
$\sigma_T$	= spectral-averaged total absorption cross section of <sup>59</sup> Ni
$\sigma_\gamma$	= spectral-averaged <sup>58</sup> Ni(n,γ) cross section
$\phi$	= total flux
$t$	= irradiation time

The above equations show that if the neutron spectrum contains a significant thermal component, then  $^{58}\text{Ni}$  will be rapidly converted to  $^{59}\text{Ni}$  and the hydrogen and helium will be subsequently produced in a non-linear fashion due to the time required for the growth of  $^{59}\text{Ni}$  upon which time the production of hydrogen and helium will be near linear, as shown in Figure 12. Depending on the neutron spectrum the  $^{59}\text{Ni}$  contribution to helium generation can be very large or very small. The largest contributions will be in mixed spectra reactors such as the CANDU.

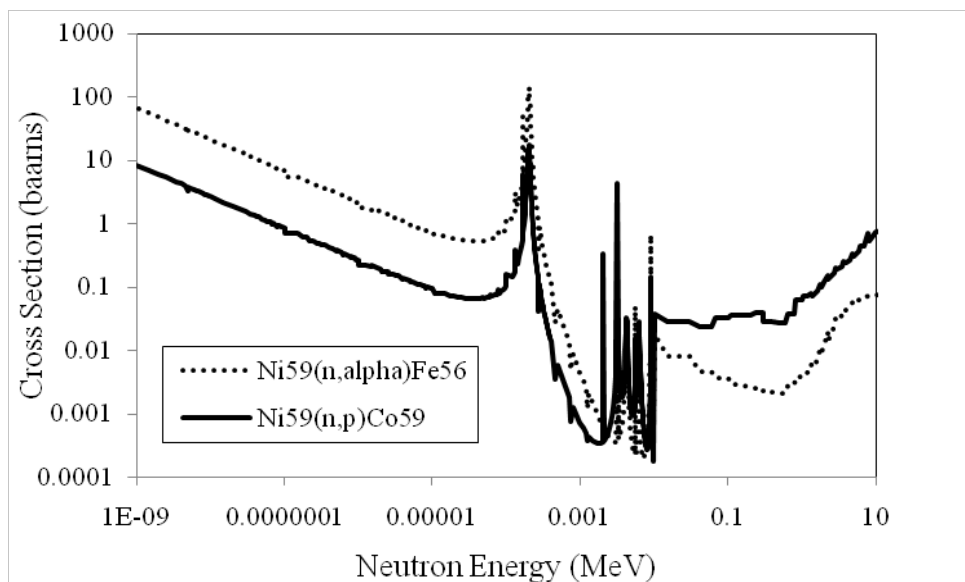


**Figure 11: Neutron cross sections for the (n,  $\alpha$ ) and (n, p) reactions of  $^{59}\text{Ni}$ .**

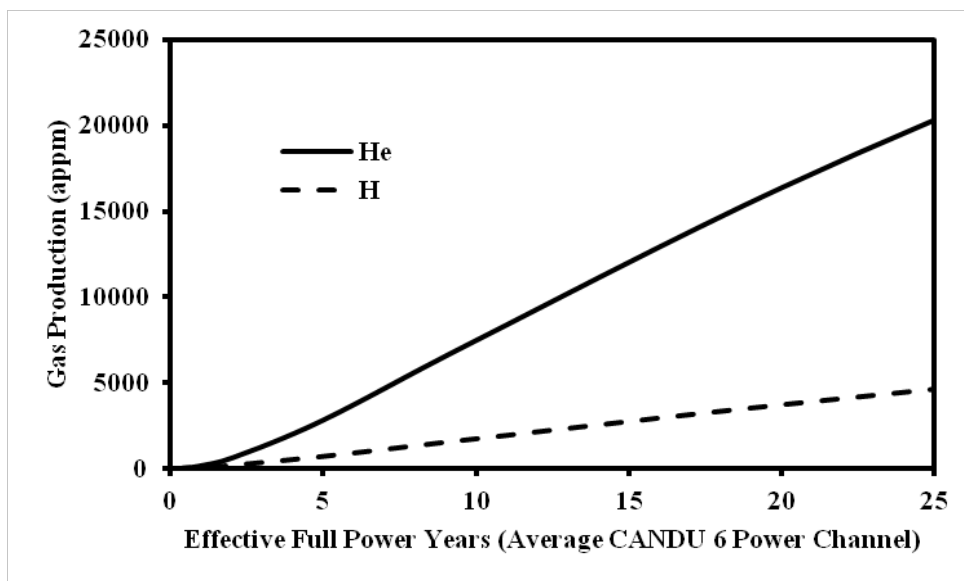


**Figure 12: Production of Helium and Hydrogen in Inconel X-750 using an average power CANDU channel flux.**

## **2.4 The Impact of Irradiation Damage on the Microstructure and Mechanical Property Evolution**

Radiation damage can significantly alter the microstructure of materials and thus lead to drastic changes in the mechanical properties. This section will review the impact of irradiation on the microstructure and mechanical properties of FCC metals, with emphasis on Ni rich alloys. The influence of irradiation dose and temperature will be discussed in terms of phase stability of  $\gamma'$  secondary precipitates and irradiation defects (loops, stacking faults and cavities). The reviewed microstructural evolution will be discussed in terms of impact on mechanical properties.

### **2.4.1 Hardening Mechanisms**

Irradiation hardening in a metal are caused by source hardening and friction hardening [36]. Source hardening is the increase in stress required to start a dislocation moving, whereas friction hardening is the resistance to dislocation motion which obstacles

introduce. In terms of understanding how irradiation defects harden the material, this will be discussed in terms of friction hardening. The sources of friction hardening can be classified as either long-range or short-range hardening mechanisms. Long-range forces occur as a result of repulsive interactions between moving dislocations and the dislocation network of the component. Short-range forces however, are due to the interaction of moving dislocations and obstacles which lie on the respective slip plane. Following irradiation, these obstacles can be loops, SFT's, cavities (loops and/or bubbles), or precipitates. Dislocations can overcome these barriers by bowing around the obstacle or climbing as a result of mass transport. Climb is typically a phenomena associated with creep, and for the purposes of this section, we will limit the discussion to bowing around the obstacle. The degree of hardening for different obstacles can be derived using a standard dispersive barrier model [37-41], originally proposed by Orowan [37] as shown in Equation 5.

**Equation 5:** 
$$\sigma(t) = T\alpha Gb\sqrt{\langle d(t) \rangle \langle N(t) \rangle}$$

Where: T = Taylor factor.

$\alpha$  = dispersive barrier strength.

G = shear modulus (~72.0 GPa (120-280°C) and 68.3 GPa (300-330°C [42])

b = burgers vector for X-750 (0.35607 nm)

d(t) = mean diameter of defect (nm)

N(t) = mean density of defect (#/nm<sup>3</sup>)

Stoller and Zinkle [38] show for fcc and bcc alloys that  $T$  has a value of 3.06. The individual contribution to hardening for different obstacles can be defined by the dispersive barrier strength,  $\alpha$ . Different irradiation induced defects will have different barrier strengths, and the nature of the defects will also change the relative barrier strength of that obstacle. A perfect barrier in terms of the Orowan model will have a value of  $\alpha=1$ .

Dislocation bowing is one form of obstacle strengthening, however, obstacle cutting may also contribute to hardening. Shearing of particles or voids by the burgers vector increases the surface area requiring additional work to shear the particle; ordered structures being sheared general anti-phase boundaries, increasing the energy required to bypass the structure; differences in the elastic moduli of the particle and matrix affects the line tension requiring additional stresses to cut the particle [36].

#### **2.4.2 Irradiation Induced $\gamma'$ Disordering and Dissolution**

Coherent secondary precipitates such as  $\gamma'$  make super-alloys such as Inconel X-750 very strong and resistant to creep at elevated temperatures [7]. The same mechanisms that lead to irradiation hardening in some alloys can also affect the stability of the  $\gamma'$  precipitates, leading to loss of strength following irradiation [43, 44]. During irradiation, the thermodynamic state of precipitates are modified by ballistic effects. The precipitate phase will become dissolved via irradiation-induced mixing, while thermodynamically driven back to a more stable state. The irradiation-induced mixing will also interrupt the order inside of the phase. In the case of  $\gamma'$  ( $\text{Ni}_3(\text{Ti, Al})$ ), the Ti and Al solute atoms will move from their preferred lattice site, and either take temporary residence at a free

vacancy site or as an interstitial. Thermodynamics will act to drive these atoms back to their stable lattice positions. There is limited experimental studies performed on Inconel X-750, however, in other Ni-Al alloys, many studies and models have predicted the effects of irradiation on the stability of  $\gamma'$  precipitates [45, 46]. Nelson et al. [46] reported that the  $\gamma'$  precipitate stability depended on a new equilibrium between the radiation dissolution and radiation enhanced diffusion. For temperatures below approximately 300-325°C and a dose rate of  $10^{-2}$  dpa/sec, Nelson reported that the  $\gamma'$  precipitates will be disordered; above this critical temperature, the  $\gamma'$  precipitates remain an ordered phase. Camus et al. [45] showed that at a dose rate of  $10^{-3}$  dpa/s and at temperatures below approximately 270°C, that the  $\gamma'$  precipitates will disorder first and dissolve later. At temperatures between 270°C and 350°C, the dissolution process is slowed down and the reordering is increased leading to the  $\gamma'$  precipitates being disordered and dissolved simultaneously. These observations are of course heavily dependent on the dose rate of the experimental irradiation as noted by both Camus and Nelson. A higher rate of ballistic mixing will not give adequate time necessary for the time dependent thermal diffusion, leading to potential shifts in the critical temperature.

Recent work by Zhang et al. [11, 47-49] at Queen's University studied the disordering of  $\gamma'$  in Inconel X-750 using heavy ion ( $\text{Kr}^{2+}$ ) and a dose rate of  $10^{-3}$  dpa/sec. These results are consistent with the observations by both Camus [45] and Nelson [46] in which below a critical temperature of approximately 400°C, disordering will occur at relatively low dose ( $<0.06$  dpa) and at temperatures above this critical temperature, the precipitates remain ordered, Figure 13. Further to these observations, the influence of helium

concentration on the disordering of  $\gamma'$  was studied. It was determined that although material with pre-implanted helium had the same critical disordering temperature, the disordering required higher damage to fully disorder the  $\gamma'$ , Figure 14 and Figure 15 (i.e. helium affected the disordering rate of  $\gamma'$ ) [47-49].

The impact of disordering and dissolution of secondary precipitates has been studied extensively in Alloy 718, which is precipitation hardened with both  $\gamma'$  and  $\gamma''$  [43, 44]. Following irradiation, the material softened, indicating the contribution of secondary precipitates to hardening was larger than the contribution of irradiation hardening via void and loop formation. Carsughi et al investigated this effect on proton irradiated Alloy 718 [43]. The results, Figure 16, show a slight increase in hardness with low dose followed by a gradual decrease below that of the starting material.

Complementary work by Thomas et al investigated the impact of hardness in Alloy 718 from reactor components as a function of both irradiation damage and test temperature [44]. These results, Figure 17, show that a drop in hardness of 100 VHN was not observed upon  $\gamma'$  disordering (3.5 dpa), but following dissolution (20 dpa) indicating that softening in the material is linked with both disordering and dissolution of secondary phases. This observation was linked with solute strengthening associated with local Al and Ti concentrations. In other words, the disordering of  $\gamma'$  removes the potential anti-phase boundary contribution to hardening, but the solution hardening from local Al and Ti concentrations were shown to delay the decrease in hardening until dissolution occurred. This result suggests that the ordering effect of  $\gamma'$  is very small.

		Temperature, °C					
		60	200	300	400	500	600
Dose, dpa	0	●	●	●	●	●	●
	0.014	●	●	●	●	●	●
	0.058	○	○	○	○	●	●
	0.271	○	○	○	○	●	●
	0.678	○	○	○	○	●	●
	2.711	○	○	○	○	●	●
	5.422	○	○	○	○	●	●

○: no  $\gamma'$  superlattice diffraction observed

●:  $\gamma'$  superlattice diffraction observed

**Figure 13: Temperature relationship on the disordering of  $\gamma'$  in X-750 spacers (no He addition) irradiated in-situ with 1 MeV  $\text{Kr}^{2+}$  ions (Dose Rate of  $10^{-3} \text{ dpa}\cdot\text{s}^{-1}$ ) at the IVEM-tandem facility in Argonne National Laboratories [47, 49].**

		Temperature, °C					
		60	200	300	400	500	600
Dose, dpa	0	●	●	●	●	●	●
	0.014	●	●	●	●	●	●
	0.058	●	●	●	●	●	●
	0.271	●	●	●	●	●	●
	0.678	●	●	●	●	●	●
	2.711	○	○	○	○	●	●
	5.422	○	○	○	○	●	●

○: no  $\gamma'$  superlattice diffraction observed

●:  $\gamma'$  superlattice diffraction observed

**Figure 14: Temperature relationship on the disordering of  $\gamma'$  in X-750 spacers (with 200 appm pre-implanted He) irradiated in-situ with 1 MeV  $\text{Kr}^{2+}$  ions (Dose Rate of  $10^{-3} \text{ dpa}\cdot\text{s}^{-1}$ ) at the IVEM-tandem facility in Argonne National Laboratories [48, 49].**

		Temperature, °C					
		60	200	300	400	500	600
Dose, dpa	0	●	●	●	●	●	●
	0.014	●	●	●	●	●	●
	0.058	●	●	●	●	●	●
	0.271	●	●	●	●	●	●
	0.678	●	●	●	●	●	●
	2.711	●	●	●	●	●	●
	5.422	○	○	○	○	●	●

○: no  $\gamma'$  superlattice diffraction observed

●:  $\gamma'$  superlattice diffraction observed

**Figure 15: Temperature relationship on the disordering of  $\gamma'$  in X-750 spacers (with 400 and 5000 appm pre-implanted He) irradiated in-situ with 1 MeV  $\text{Kr}^{2+}$  ions (Dose Rate of  $10^{-3} \text{ dpa}\cdot\text{s}^{-1}$ ) at the IVEM-tandem facility in Argonne National Laboratories [48, 49].**

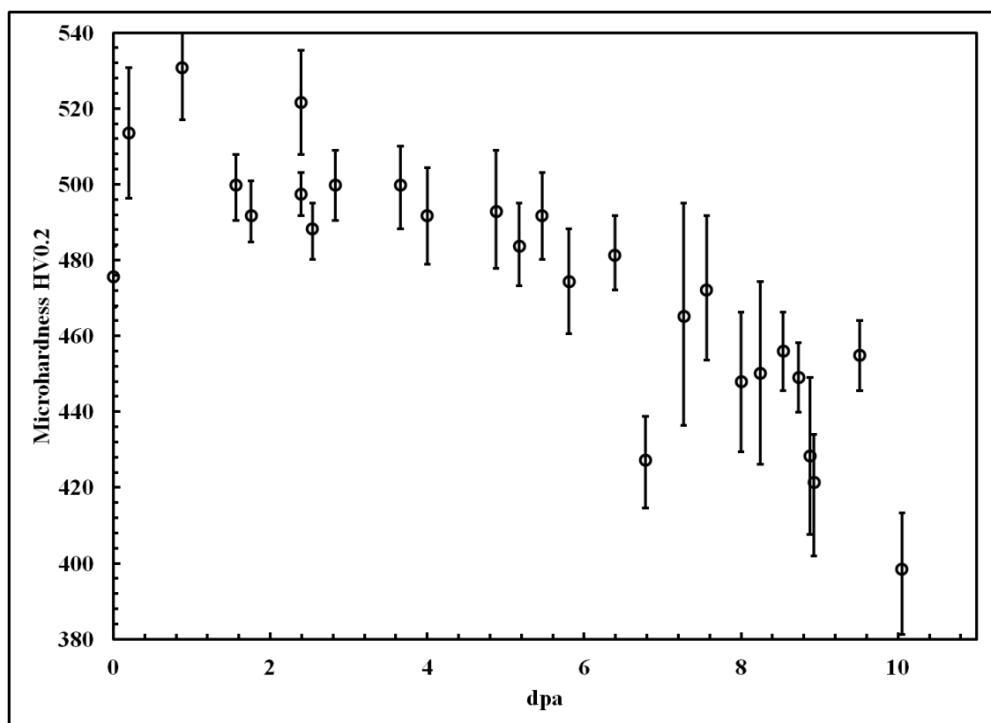


**Figure 16: Microhardness HV0.2 of irradiated Inconel 718 as a function of irradiation dose. Reproduced from [43].**

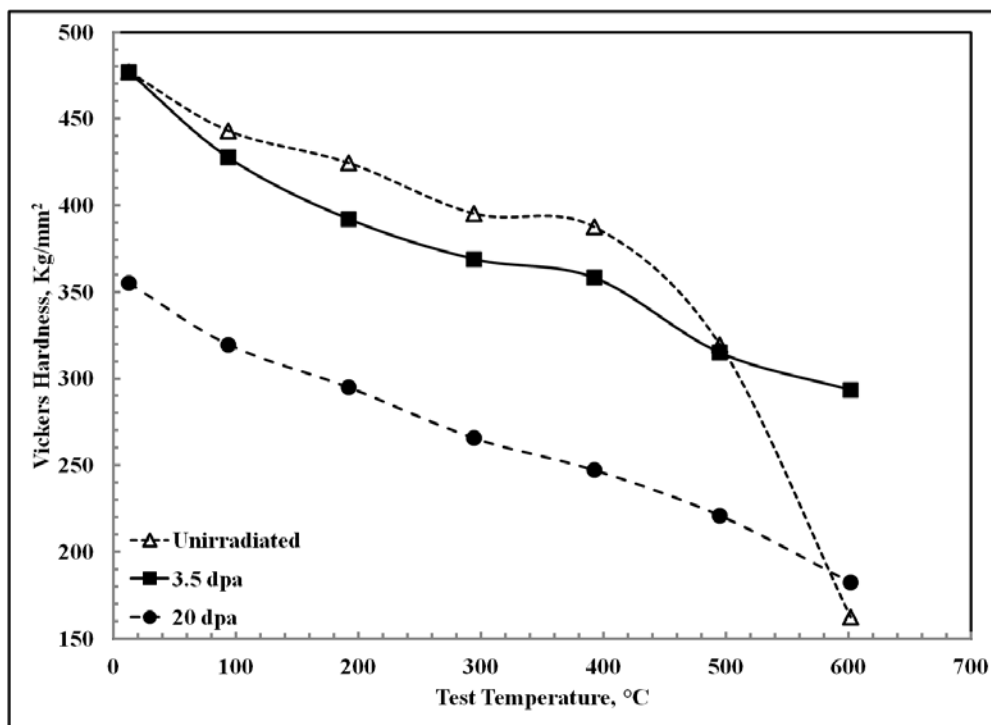


**Figure 17: Hardness of Alloy 718 as a function of test temperature and dose. Reproduced from [44].**

### 2.4.3 Irradiation-Induced Defects in FCC Microstructures

Irradiation induced defects in fcc materials have been well studied, specifically in Ni rich alloys [11, 21, 47-57]. These defects primarily consist of stacking fault tetrahedral (SFT's), dislocation loops (interstitial and vacancy) and cavities.

#### 2.4.3.1 Irradiation Induced Defects

At temperatures where self interstitial atoms and vacancies are both mobile, defect cluster formation and geometries can be quite complex. Visible defects in fcc metals at temperatures regimes specific to Inconel X-750 spacers (i.e. 120-330°C) are faulted loops (a.k.a. Frank loop), perfect loops, SFT's and voids. Faulted or perfect loops can be in the form of an added or removed plane of atoms causing either an extrinsic or intrinsic

stacking fault. Faulted loops form on the closed packed planes of the materials and are entirely sessile. The stacking order of the loop can be restored by an atomic shear of one layer of atoms in the form of  $a/6\langle 112 \rangle$  Shockley partial dislocation that sweeps across the faulted loop. This is the nature of how a perfect loop is formed. The resultant burgers vector shifts to  $a/2\langle 110 \rangle$  on the 111 habit plane. Upon unfauling, rotation of the glide cylinder gradually changes the habit plane from 111 to 110 creating a pure edge loop geometry, changing the loop from being sessile to being glissile. With continued irradiation, these perfect loops may evolve to a clustered dislocation network. It is reported that for medium-high atomic number fcc metals (such as Ni), many of the vacancies can be tied up in sessile vacancy clusters (like SFT's, loops or cavities) that form during the displacement cascades. As a result, the majority of the observed dislocation loops in fcc metals are interstitial in type [21].

SFT's are only observed in closed packed systems such as fcc metals. The general formation of SFT's come from small faulted loops. The  $1/3\langle 111 \rangle$  faulted loop dissociates to  $a/6\langle 110 \rangle$  stair rod dislocation and a  $a/6\langle 112 \rangle$  Shockley partial [49]. Six stair rods dislocations would bind a 3-dimensional SFT [54].

The interaction of dislocations and irradiation induced defects has been well studied in the open literature. Hardening is largely due to the creation of high densities of sessile defect clusters, which act as strong barriers to dislocation motion in the matrix. The defect structure evolves with irradiation, eventually reaching equilibrium (i.e., recombination and nucleation become even and defect density remains unchanged with continued irradiation). Thus, irradiation hardening from loop formation is finite and

saturates upon saturation of the defect structures. Using the dispersive barrier strength approach to estimate the impact of defect structures has shown loops to have a barrier strength of approximately 0.1 (well below that of a perfect obstacle).

A large amount of work on defect structures in Inconel X-750 was performed by Zhang et al [11, 47] was performed for both neutron irradiated material and accelerated ion irradiated material. For neutron irradiated material (same material from this investigation with approximately 55 dpa and 18000 appm helium), the defect size distribution from two temperature regimes is shown in Figure 18 [11]. Defect densities were not given because of different (unknown) sample thickness limiting reliable quantification. The high density of small defects (SFTs and dislocation loops) in both the low and high temperature material were concluded to have formed during collapse of the cascade, consistent with [54, 58]. The low concentration of large defects in the lower irradiation temperature material is indicative that the majority of freely migrating point defects were recombined during the collision cascade, whereas the higher irradiation temperature material, point defect migration enabled the formation of larger interstitial loops.

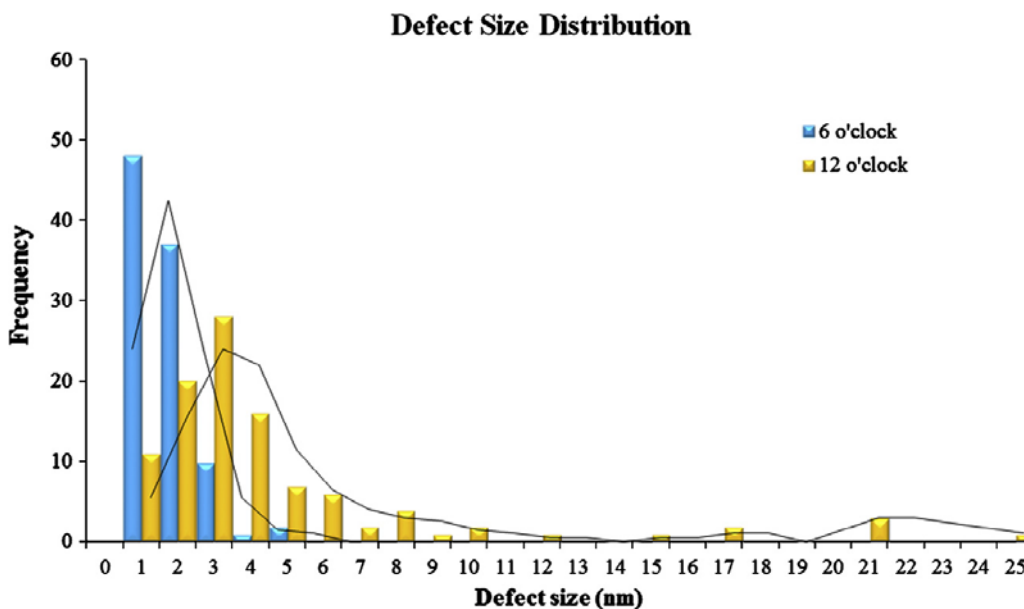


**Figure 18: Irradiation induced defect structures from neutron irradiated Inconel X-750 with approximately 55 dpa and 18000 appm helium from 6 and 12 o'clock respectively (i.e. ~200 and 300°C respectively). Extracted from [11].**

#### 2.4.3.2 Cavity Formation

A cavity defines both a void (without gas) and a bubble (with gas). The requirement to nucleate a cavity usually requires higher temperatures to allow for the vacancy clusters to stabilize prior to their collapse forming 2-dimensional vacancy loops (lower energy state). Vacancy clusters forming in the presence of gas however (helium for example) can become stabilized in their 3-dimensional form [21, 25, 59-64]. In many materials with helium generation from transmutation processes, the cavity size distribution is typically bimodal; a high density of pressurized helium bubbles and a low density of large underpressurized voids [57, 62, 65-67]. The visible cavity density is noted to increase rapidly at relatively low dose and saturate for damage levels up to ~1-50 dpa [21, 56, 57]. For cavities above a critical radius, a transition to voids occur which is determined by a

balance between dislocation bias-induced vacancy flux and thermal emission of vacancies from the high pressurized bubbles. The balance between vacancy and SIA flux can be demonstrated using the rate theory calculations shown in Section 2.3.3. As the defect concentration rapidly increases (i.e. formation of cavities) at relatively low dose, the overall swelling will drop significantly. The temperature transition from sink to recombination dominated regimes will not be greatly affected, but the overall impact on swelling will be significantly reduced. Transition from bubbles to voids is reportedly highly dependent on pressure state of the helium bubbles. Experimental procedures for how gas pressures are determined in sub-microscopic cavities will be discussed in more detail in subsequent chapters.

The formation of cavities and helium bubbles in irradiated Ni alloys is generally well established, but many questions remain regarding the impact of these cavities/bubbles on hardening and mechanical properties. The hardening associated with cavities/bubbles greatly depends on how they interact with dislocations (i.e. their relative barrier strengths). It has been much debated in the open literature how helium filled bubbles harden the matrix. Cavity size, density and internal pressure influence the surrounding strain fields in the matrix, and therefore influence how dislocations interact with the cavities.

It has been suggested that matrix hardening associated with bubbles can be estimated using a standard dispersed barrier model [37-41], originally proposed by Orowan [37] (i.e. the bubbles will impede dislocation motion much like precipitates) using Equation 5. Barrier strengths ( $\alpha$  in Equation 5) have been reported for vacancies to be 1 (i.e. perfectly

hard barriers). Supporting work for this hypothesis has been primarily influenced with helium implanted Ni alloys [68]. Ni alloys were implanted with helium up to 10 at. % and it was shown that hardening occurred that was approximately seven times greater than the standard Orowan mechanism would predict, which would indicate that bubbles pin dislocations more effectively than precipitates. Figure 19 shows the change in yield strength (as determined by nano hardness and FE modeling) as a function of helium bubble density [68].

With the aid of in-situ TEM and molecular dynamic (MD) simulations, comparisons between different bubbles (i.e. under-pressurized bubbles and over-pressurized bubbles) have been made [69]. It was suggested that depending on the characteristics of the bubble, different dislocation-bubble interactions will occur. In an under-pressurized bubble (i.e. an equilibrium bubble with no dislocation “punching”) a bypass mechanism involving the shearing of a bubble by a dislocation occurs. In other terms, a segment of dislocation annihilates at the matrix-bubble interface and re-nucleates at the trailing bubble surface as the dislocation travels past the bubble. The energy required to bypass the bubble is simply given by the stress required to create a dislocation line segment (i.e. the critical resolved shear stress (CRSS) of the matrix<sup>2</sup>), and the length of the segment. Using the dispersive barrier approach to calculate the strength, a representative barrier strength for this approach as been reported as 0.16 [36]. An over-pressurized bubble with “punching” has a degree of lattice mismatch at the bubble-matrix boundaries, which act

---

<sup>2</sup> The CRSS of the matrix would be related to the annealed material, and not the precipitation hardened material.

as strong barriers to dislocation motion leading to a stronger dispersive barrier strength as previously discussed. Recent MD simulations for pure Ni [70] suggest a bubble size dependence on the obstacle strength of voids. It has been suggested that there is a transition in obstacle strength at a void size of approximately 2 nm (materials with cavities  $>2$  nm will have higher hardening compared to materials with cavities  $<2$  nm). This transition is associated with the energy of a leading partial dislocation and a trailing partial dislocation. As the leading partial dislocation is initially pinned by the cavity, the trailing partial is temporarily repelled. The energy required for the trailing partial to bypass the cavity increases substantially at a transitional bubble size of approximately 2 nm, however this critical size is approximate and may vary pending on the specific material (in other words, the critical cavity size may be on the order of 1-3 nm for Inconel X-750). This transition is specific to the use of a dislocation bypass mechanism, however estimates for relative barrier strengths as a function of cavity size were not provided in the literature.

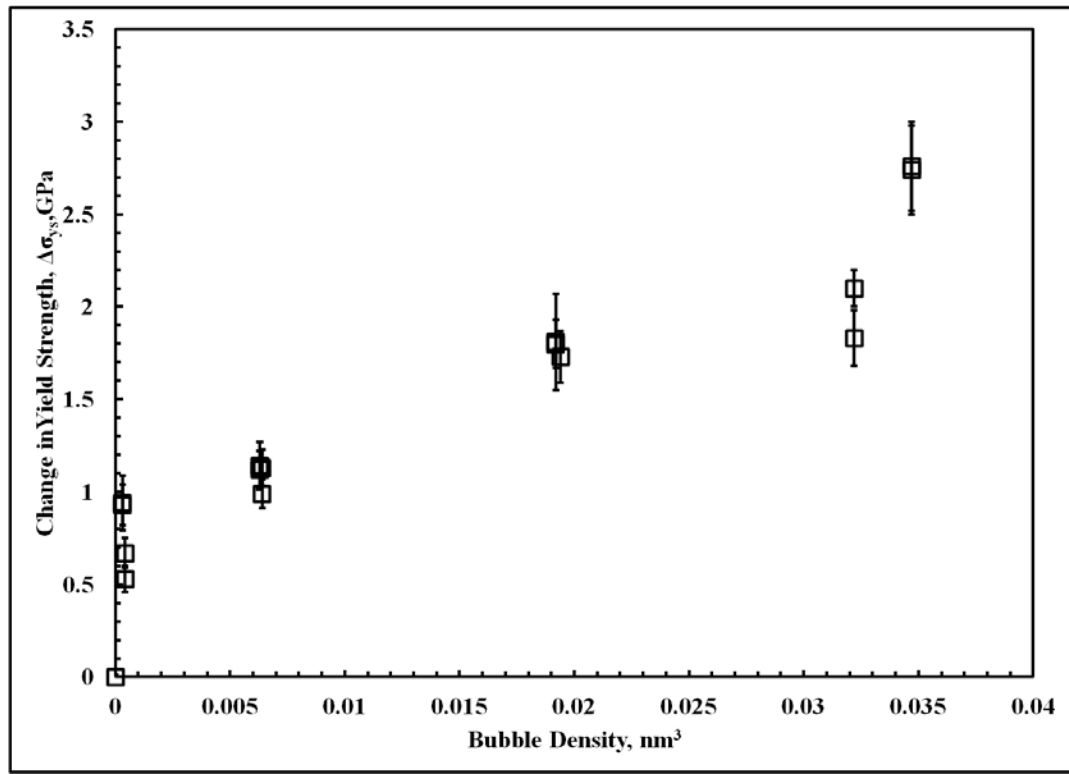


**Figure 19: Change in Yield Strength in Ni as a function of He bubble density. Reproduced from Knapp et al [68].**

#### 2.4.4 Density and Pressure of Helium in Bubbles

The pressure not only affects the hardening mechanisms described in Section 2.4.3.2, but also determines the swelling for a given helium content (He/V ratio). The state of helium within cavities has also been postulated to control bubble growth through overpressure, loop formation and/or SIA emission [30, 71, 72]. The equilibrium pressure,  $P_{eq}$ , required to balance the surface tension of a cavity is governed by [73]:

$$\text{Equation 6: } P_{eq} = \frac{2\gamma}{r}$$

Where:

- $\gamma$  is the surface tension of Ni, equal to be 1.89 N/m [72].
- $r$  is the cavity radius.

It is recognized that the validity of using Equation 6 can be brought into question, as the small nature of bubbles may not be governed by the surface tension of the material and the radius of the cavity. However, for the purposes of the work presented in this dissertation, it is assumed that this balance exists, and validity discussed in terms of the experimental results. For Ni, the equilibrium pressure as a function of cavity diameter is shown in Figure 20. For these high pressures, the concept of an ideal gas is not appropriate for helium, as the gas is incompressible [60]. As a result of the incompressibility, the pressure is higher than that of an ideal gas. As such, equations of state for high pressure helium are used.

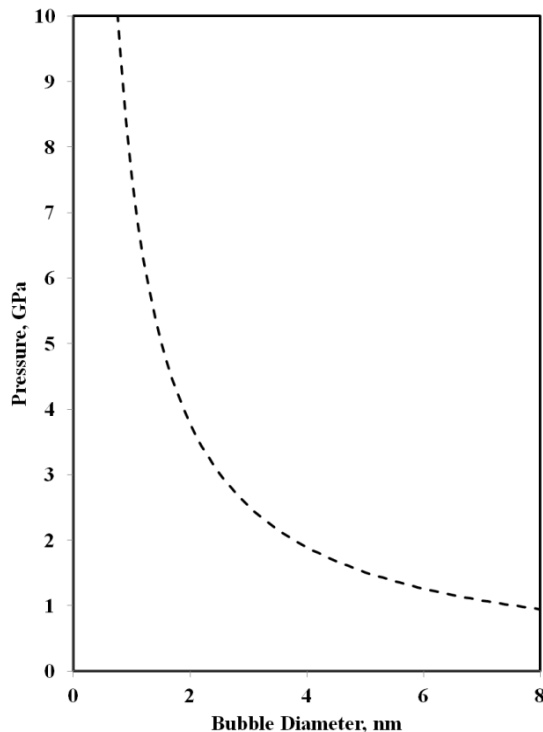


**Figure 20: Equilibrium pressure as a function of cavity radius using Equation 6.**

#### 2.4.4.1 Equations of State for High Pressure Helium

Because helium does not conform perfectly to that of an ideal gas at the pressures of interest, a common approach to calculate the compressibility of helium ( $Z$ ) and thus pressure, is to use a virial expansion in terms of the helium density and volume in the form of a hard sphere equation of state (HSEOS). The Carnahan and Starling HSEOS is of the form [74]:

$$\text{Equation 7: } Z = \frac{P}{N_{He}kT} = \frac{1+y+y^2-y^3}{(1-y)^3}$$

Where: - P is pressure (Pa)

- $k$  is the Boltzmann's constant ( $1.3806488 \times 10^{-23}$  J/K)
- $T$  is temperature (Kelvin, K)
- $N_{He}$  is the helium density (atoms/m<sup>3</sup>).
- $y$  is the packing fraction of helium and is proportional to the helium density, such that:

$$\text{Equation 8: } y = \left( \frac{\pi d_g^3}{6} \right) N_{He}$$

- $d_g$  is the effective hard sphere diameter of the helium atoms in the form:

$$\text{Equation 9: } d_g = a_1 \left[ a_2 - a_3 \ln \left( \frac{T}{a_4} \right) \right]$$

- $a_1$ ,  $a_2$ ,  $a_3$ , and  $a_4$  are coefficients (typically obtained from MD simulation).

Stoller and Osetsky [75] recently updated the coefficients used in calculating the hard sphere diameter of helium with MD simulations (Table 2).

**Table 2: Hard sphere coefficients obtained from fitting HSEOS to MD results.**

Fitting Parameter	HSEOS (Stoller and Osetsky [75])
$a_1$	0.319332
$a_2$	0.865456
$a_3$	0.041802
$a_4$	9.228038

Therefore with experimental measurements of helium density, and bubble diameter, the pressures within individual bubbles can be calculated using Equation 7 through Equation 9.

#### **2.4.4.2 Experimental Estimates of Helium Density in Bubbles**

Two experimental techniques used to measure the helium density in bubbles will be discussed in detail. The first involves a direct measure of the total bubble volume (through means of transmission electron microscopy), and total helium concentration (either through experimental measures, or calculated helium concentrations as discussed in Section 2.3.4). The result is an average helium density, and an average bubble size. This technique, although relatively simple, does not give a distribution of helium-vacancy ratios or density as a function of bubble size. It has also been suggested that assuming that all helium resides in detectable bubbles is incorrect and leads to higher estimates of helium density, helium-vacancy ratios, and pressures which are unrealistic [72]. It is also assumed that regions characterized by TEM are representative of the bulk (i.e. helium bubbles are uniformly distributed throughout the matrix). This too, may also be false. Two sets of notable experiments reporting these inconsistencies were performed on helium pre implanted material by Fenske et al. [76-83] and Van Swygenhoven et al. [84-87]. In both experiments, the measured helium density was such that the calculated pressures were beyond the bounds to emit SIA, and therefore yielded an unphysical result. It was concluded that helium (up to 60% in some cases) must have been residing in sub-microscopic defects not detectable by the TEM analysis. Extending this discussion, it is possible that the detection limits of the TEM used in the investigation were not

sufficient to quantify the bubble density leading to higher calculated pressures. The second method in estimating the helium density in bubbles involves diffraction experiments to study the state of helium within the bubbles. It has been shown that the so-called blue energy shift of the  $1s \rightarrow 2p$  transition is directly proportional to the helium density. The energy shift is associated with Pauli repulsion between electrons and neighbouring helium atoms [88]. The energy shift can be measured by electron energy loss spectroscopy (EELS) in a TEM or by vacuum ultraviolet reflectance. The energy transition for atomic helium is 21.218 eV. For this dissertation, only the EELS experimental work will be discussed in detail. It has been shown that as the helium density ( $N_{\text{He}}$ ) increases, the energy shift of the  $1s \rightarrow 2p$  transition ( $\Delta E_{1s \rightarrow 2p}$ ) increases linearly by a proportional constant ( $C_p$ ) [88, 89] as follows:

$$\text{Equation 10: } \Delta E_{1s \rightarrow 2p} = N_{\text{He}} \cdot C_p$$

Values of the proportional constant have been experimentally determined for different materials (Al, Ni, and Ni alloys) between 0.019-0.044 eV/nm<sup>3</sup> [88-93]. This type of analysis is usually performed on large regions with pre-implanted helium, but recent advances in electron microscopy and spectroscopy have enabled EELS analysis from individual helium bubbles as illustrated by the recent works of Taverna et al. [89], Frécharde et al. [93], and Wu et al. [94]. These works followed the procedure as described by Walsh [92] to use the electron cross section of helium, and the EELS spectra to quantify the total helium density within individual bubbles. Further details on this technique can be found in reference [92].

#### 2.4.4.3 Pressure Limitations for Helium Bubbles

Pressures above the equilibrium pressures shown in Figure 20 can be denoted as overpressurized bubbles. There are factors which limit the maximum pressure a bubble may reach, which may govern bubble growth mechanics [30, 71, 72]. These factors are mechanisms of stress relief in the form of ejection of a helium or metal atom (SIA emission), or the punching out of a dislocation loop. Trinkhaus [73] calculated the limiting pressure for SIA emission as a relation of the equilibrium pressure (Equation 6) and the shear modulus of the metal ( $\mu$ ) as follows:

$$\text{Equation 11: } P_{SIA} \cong \frac{2\gamma}{r} + \frac{\mu}{2}$$

Trinkhaus also showed that the approximation for the pressures for loop punching are accurate following the simple expression linking the shear modulus of the material and the burgers vector ( $b$ ) for the dislocation being punched around the bubble as follows:

$$\text{Equation 12 } P_{loop} \cong \frac{2\gamma}{r} + \frac{\mu b}{r}$$

Using the shear modulus for pure Ni (77 GPa) [72], and the burgers vector of 0.35607 nm, Figure 21 shows the pressures for an equilibrium bubble, and pressures necessary for loop punching and SIA emission governing the maximum possible pressures in bubbles without forcing bubble growth. It is shown that it is more favourable to punch out a cluster of interstitials in the form of a loop than it is to emit a helium atom or metal atom in the form of a SIA.

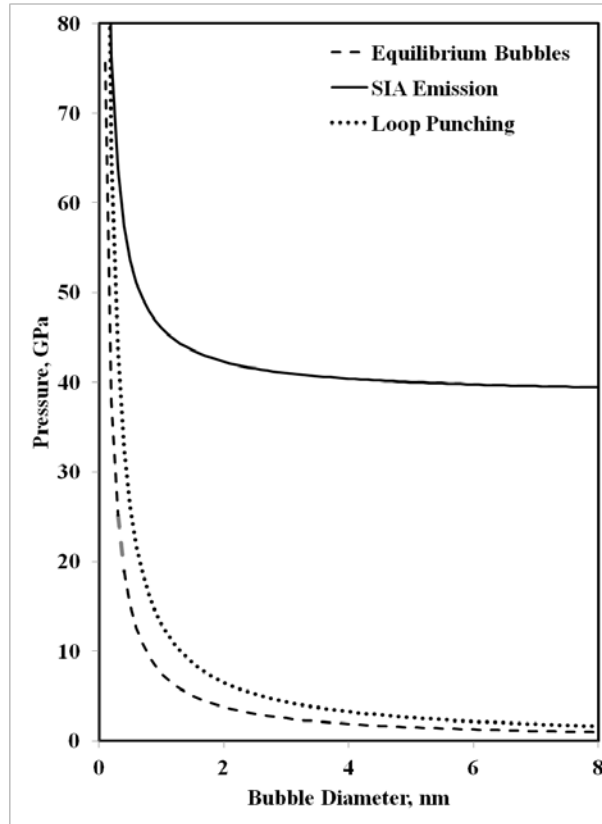


**Figure 21: Pressure estimates for an equilibrium bubble (Figure 20), loop punching, and SIA emission for a pure Ni metal.**

## **2.5 Review of Applicability of the Proton Irradiation to Emulate In-Reactor Neutron Irradiation**

There are plenty of incentives for using charged particles to bombard materials to study the effects of irradiation on materials; savings on cost and time being at the top. Typical in-reactor irradiations can take from a few years to decades before fruition, cost upwards of multiple millions of dollars, and yield only a limited range of test conditions. Therefore, in an attempt to gain a better understanding of irradiation effects (faster and cheaper) a process of using heavy ions to investigate irradiation in materials was developed [95-98]. These experiments could carefully control test parameters such as dose, dose rate, and temperature, however, the ability to adequately emulate in-reactor neutron irradiation continues to be the source of scientific debate within the research community [97]. The ability to rapidly reach end-of-life conditions however continues to draw vast industrial interest in accelerated irradiations via charged particles. This section will review aspects of accelerated irradiations, and notable experiments with relevance to Ni irradiation.

### **2.5.1 Accelerated Irradiations; Electrons, Protons or Heavy Ions**

When deciding to perform an accelerated irradiation to emulate neutron irradiation conditions, there are multiple options available: electrons, protons, or heavy ions. Each options has their own set of advantages and disadvantages, and careful consideration is required to adequately emulate the specific conditions of interest for the experiment. Figure 22 outlines the difference in damage morphology, displacement efficiency and average recoil for 1MeV particles in Ni [98].

Although electron irradiation is suitable to produce a Frenkel pair, it is not sufficient to produce any form of collision cascades. The main advantage of electron irradiation, is the relative cost. Electron irradiation can be performed in a transmission electron microscope, and as this tool can be used to characterize radiation damage, this approach lends itself to a relatively cheap and available technique to perform experiments aimed at understanding some of the fundamental mechanisms of irradiation induced defect structures [99-101]. This approach has the advantage and disadvantage (pending view point) of having a very high dose rate, enabling relatively short irradiation times to reach the target dose, however this high dose rate requires a large temperature shift to be deemed “representative” to in-reactor conditions. In addition, electron irradiation have a strong Gaussian dose profile in the sample thickness, producing a non-uniform distribution for analysis [96, 97]. It is also important to understand that the irradiation is performed on a thin foil, and surface effects can be difficult to account for. Electron irradiation is a very useful tool, but is relatively limited in its applicability to emulate neutron irradiation. In terms of assessing the impact of irradiation on mechanical properties, electron irradiation is not a suitable experimental approach.

Heavy ion irradiation is advantageous as high dose rates are achievable in relatively short irradiation times. Unlike electron irradiation, heavy ions produce collision cascades, enabling study of cascade recombination effects during irradiation [97]. There are no transmutation elements generated with heavy ions, or sample activation lending this approach advantageous to laboratory testing without concern of added radiation hazards. Unlike electron irradiation testing, heavy ion irradiations are not performed directly with

the electron beam in a TEM, however some facilities have been developed with in-situ heavy ion accelerators linked with electron microscopes to investigate the development of irradiation damage as it happens within the material [102, 103]. Zhang et al. [11, 47, 48] studied the effects of ion irradiation on Inconel X-750 spacer material as a function of dose and temperature. Although heavy ions do not produce any transmutations, pre-implanting the material with helium was shown to be suitable to emulate neutron irradiation. The disordering of gamma prime, bubble growth, and irradiation defect structures were characterized with great success, however, this form of irradiation is limited to very small sample volumes unsuitable to assess the impact of irradiation on mechanical properties. The accelerated condition of the testing requires a large temperature shift to emulate swelling and irradiation induced segregation, leading to questions regarding the applicability of studying disordering and dissolution processes relevant to reactor operating conditions. Because of the elevated irradiation temperatures and dose rates, the phase equilibrium may not be adequately representative of in-reactor conditions.

Proton irradiation has a smaller cascade compared to heavy ions, as shown in Figure 22, however produces relatively uniform damage depths of up to 40  $\mu\text{m}$  with only a few MeV. These damage depths are sufficient to perform post irradiation mechanical testing to assess crack initiation, or microhardness measurements [96, 98, 104-107]. The dose rates are modest in comparison to electron and heavy ions; however, still require a temperature shift compared to neutron irradiation for the results to be comparable, and in

many cases, the success of the temperature shift can only be concluded following the experiment.

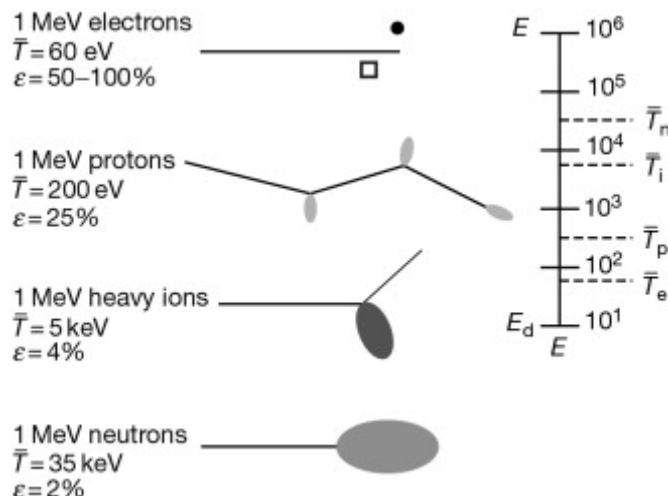


**Figure 22: Difference in damage morphology, displacement efficiency and average recoil energy for 1MeV particles of different types in Ni. Reproduced from [98].**

## 2.6 Mechanisms for Grain Boundary Embrittlement in Irradiated Materials

Grain boundary embrittlement in irradiated materials is something which is very difficult to manage in irradiated structural components. This form of embrittlement is typically difficult to manage and predict with respect to degradation rates. Because of these issues, many mechanisms of grain boundary embrittlement are of great scientific and industrial interest. In terms of irradiated fcc structures and Ni-rich super-alloys, the primary mechanisms for discussion are: cavity/bubble embrittlement, hydrogen embrittlement, and grain boundary  $\gamma'$  embrittlement.

### **2.6.1 Cavity/Bubble Embrittlement**

Cavities on grain boundaries have been hypothesized as causing embrittlement and intergranular fracture in cold worked 316SS thimble tubes used in light water reactors [33]. Figure 23 shows a series of cavities formed in the matrix and aligned along grain boundaries as a function of dose and temperature, which has been attributed to loss of ductility.

Grain boundary helium bubbles in Nimonic PE16 (another Ni super-alloy hardened with  $\gamma'$ ) irradiated in a fast neutron environment to 20 dpa and approximately 20 appm helium was attributed to reduced ductility and intergranular fracture in post-irradiation mechanical testing [108]. It was concluded that:

“Irradiation embrittlement of Nimonic PE16 resulted from the presence of grain boundary helium bubbles which acted as cavity nuclei during subsequent straining.”

Both of these examples are from materials with relatively low concentrations of helium.

The nature of embrittlement associated with cavities or helium bubbles will also be influenced by the state helium within the bubbles (i.e., under pressurized or over pressurized). Evans [30] describes an interbubble fracture mechanism associated with a plane of over pressurized helium bubbles. This phenomena was used to explain the delamination of surfaces following helium ion irradiation. A plane of high pressurized bubbles creates a tensile stress perpendicular to the bubble containing plane, leading to parting the material at this plane. This mechanism only applies in the event that both loop punching and SIA emission is significantly impeded by interaction of a high density of

other defects within the material such that pressures in excess of the shear modulus may exist. Figure 24 shows a schematic representation of the interbubble fracture mechanism. This is similar to that which would be expected from hydrogen blister formation in steels. Although this mechanism has not been used to explain intergranular fracture, it could be hypothesized that a plane of high pressurized bubbles on a grain boundary may lead to a similar phenomena, and thus it is included for discussion purposes.

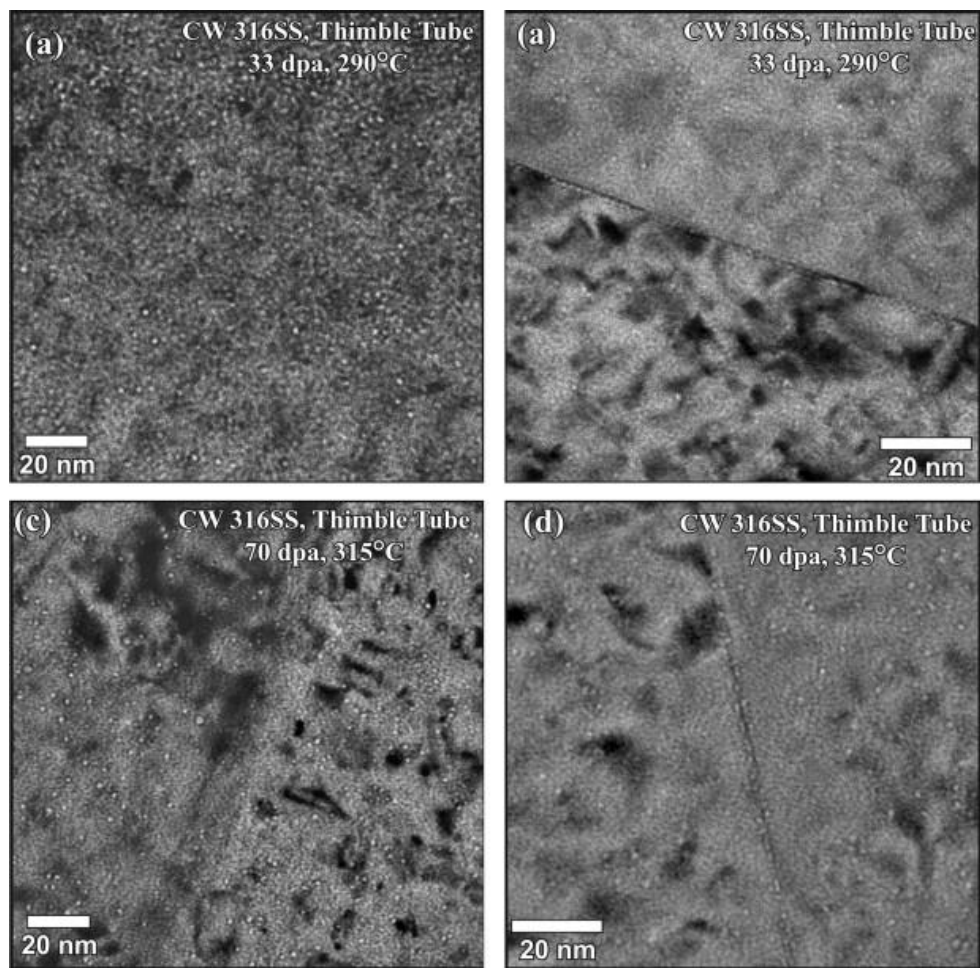


**Figure 23: Cavities in cold worked 316SS Thimble tube attributed to embrittlement and intergranular fracture [33].**

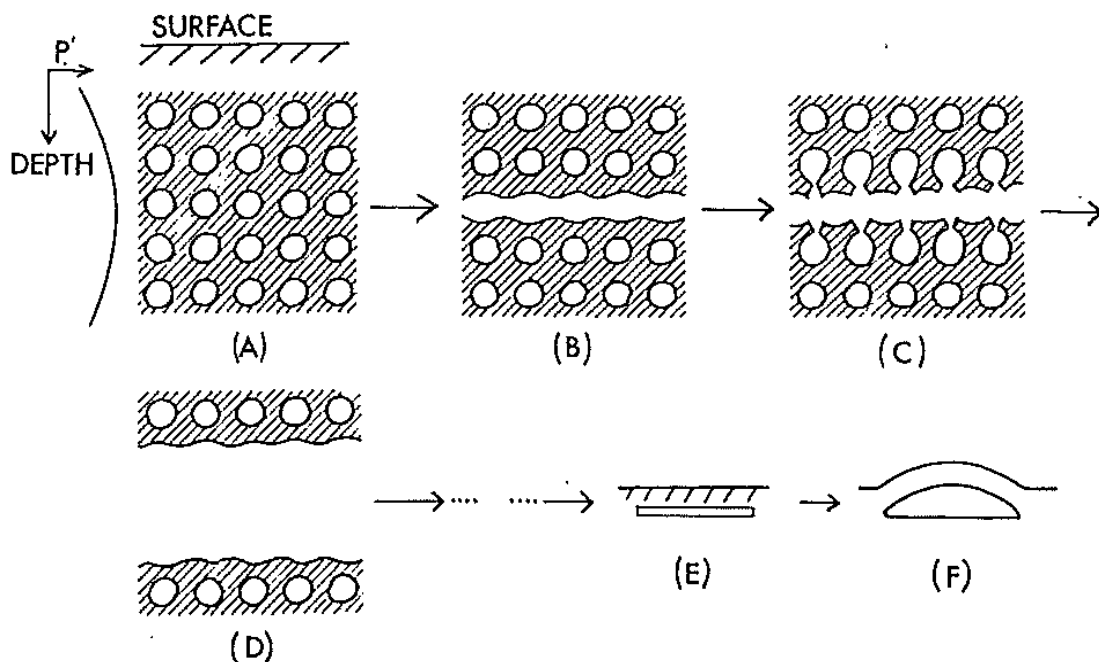


**Figure 24: Schematic outlining interbubble fracture [30].**

## 2.6.2 Hydrogen Embrittlement

Nickel base materials that have been heat treated to produce carbides on grain boundaries are susceptible to hydrogen embrittlement [1, 109]. Carbides are intentionally formed on the grain boundaries to decrease the relative susceptibility of stress corrosion cracking<sup>3</sup> in reactor coolant water [5]; however the incoherent carbides are strong trap sites and promote hydrogen segregation to grain boundaries. Increased hydrogen concentrations at grain boundaries are reported to promote intergranular fracture in X-750 [1]. As shown in Figure 12, approximately 5000 appm of hydrogen is produced by end-of-life condition in an average CANDU channel spacer by <sup>59</sup>Ni transmutation. Although hydrogen is relatively mobile as an interstitial in Ni alloys, strong trap sites such as grain boundary

<sup>3</sup> This form of SCC is often referred to as “Primary Water SCC” (PWSCC)

carbides may locally retain trace hydrogen concentrations. Even very low, but local concentrations of hydrogen can have deleterious effects on grain boundary embrittlement [1, 109], thus this effect cannot be ruled out.

### 2.6.3 Grain Boundary $\gamma'$ Embrittlement

It has been observed in some irradiated Ni-Fe alloys that secondary precipitates which have undergone disordering and dissolution may re-precipitate on, or along, grain boundaries following irradiation resulting in reduced ductility and intergranular fracture [110, 111]. This has been found with grain boundary decoration of both  $\gamma'$  and  $\eta$  phase in different materials. Figure 25 shows a schematic of a hypothetical fracture mechanism associated with grain boundary decoration of  $\gamma'$  precipitates.

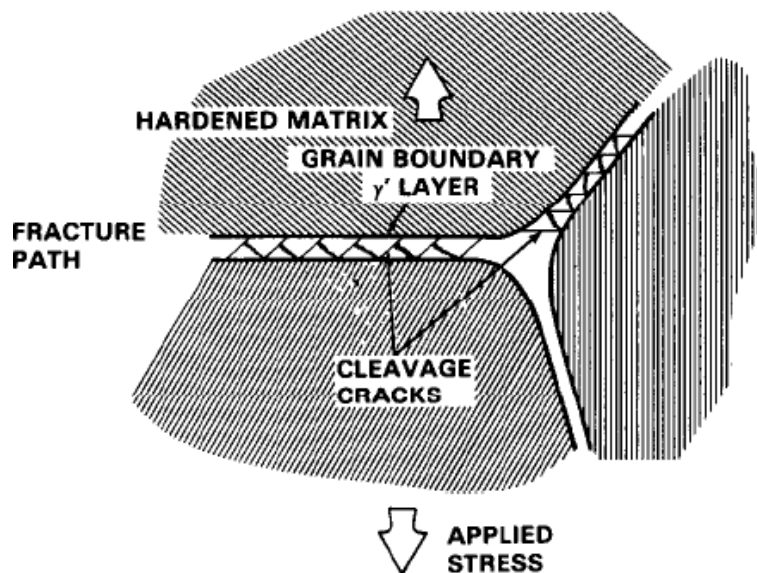


**Figure 25:** Schematic outlining hypothetical fracture mechanism associated with grain boundary decoration of brittle secondary precipitate,  $\gamma'$  [110].

## **2.7 Experimental Methods**

This section will discuss applicable experimental methods in studying the effects of irradiation on microstructural and mechanical property evolution in material.

### **2.7.1 Transmission Electron Microscopy**

TEM is used extensively in the nuclear industry to investigate the effects of irradiation on microstructural changes in materials [11, 21, 22, 24, 32, 48, 51, 56, 99, 100, 107, 112-115]. The experimental methods used in obtaining quality TEM results are discussed in this section.

#### **2.7.1.1 Sample Preparation**

As with any microstructural investigations, sample preparation is the major hurdle in obtaining quality results. There are many methods which can be used in preparing TEM samples, each with advantages and limitations. Two specific techniques will be introduced and discussed in detail with respect to applications to radiation damage investigations; electropolishing, and ion milling with a focused ion beam (FIB).

Electropolishing is typically performed on a 3 mm disk, which is cut from the bulk material, mechanically thinned, and electro-chemically polished to electron transparency. This may introduce artifacts such as mechanical damage, so special care must be taken using this approach. This approach does however, prepare a surface which is relatively clean of preparation induced irradiation damage; something unavoidable with the use of a FIB. Working with very highly radioactive materials however, requires significant<sup>4</sup> time

---

<sup>4</sup> In this case, “significant” refers to anything beyond reason. At CNL, we follow the ALARA principle, meaning exposures should be As Low As Reasonably Achievable.

to handle the material at relatively close proximity. In addition to a higher potential radiation exposure to workers, there are limitations to the relative size of the samples which can be utilized for electropolishing. In the current study for example, the samples are 0.7 mm x 0.7 mm cross section wire, and are not sufficient to prepare a 3 mm disk. Techniques have been developed to electropolish such a small cross section [112] by sandwiching a small section of material between two copper disks prior to electropolishing. This technique has proven successful, however, not consistently, requiring multiple samples to be prepared to increase the probability of achieving a high quality sample. Therefore, this increases the potential radiation exposure to the worker.

Working with a FIB does not entirely remove the radiation hazard, but does reduce the time required for workers and scientists to be in close proximity to the samples. The FIB is an attractive approach for investigating the radiation damage of components because very small volumes of material can provide many TEM lamellae. In addition, the final TEM lamellae are incredibly small, with very low residual radioactive fields, thereby allowing the samples to be investigated at facilities otherwise not open to receive highly radioactive components. The FIB does however come with some drawbacks. There is some damage induced to the sample in the form of irradiation induced loops and defects which may affect the microstructural observations, pending the primary focus of the investigation. Aitkaliyeva et al [116] have investigated the limitations of different preparation technique (electropolishing and FIB) for studying the effects of irradiation, and have outlined techniques following preparation with a FIB which can reduce the damage. These include decreasing ion energy for final thinning of the TEM lamella, and

lamella cleaning with the use of a TEM nano-mill to remove potential damaged layers from the FIB.

### **2.7.1.2 TEM Imaging**

In the TEM, there are multiple imaging techniques which can be used to highlight certain microstructural features, such as phase contrast, structure-factor contrast, and diffraction contrast [117, 118].

Phase contrast imaging is typically associated with high resolution TEM, however, not exclusively. Phase contrast occurs when local changes in the phase of the electron wave occur during interacting with the specimen [117]. For example, phase contrast imaging is utilized in this research primarily using Fresnel contrast imaging of cavities/bubbles. The difference in the inner potentials of the bubble compared to the matrix leads to fringe formation in the image when out of focus [118]. These fringes are formed by the phase shift between electrons passing through the void and those passing through the adjacent material. This effect is greatly influenced by the degree of under or overfocus of the objective lens. Figure 26 shows an example of through-focal series of small voids in irradiated stainless steel. Voids will appear as bright dots with a dark Fresnel fringe in the overfocus condition and dark dots with a bright Fresnel fringe in the underfocus condition.

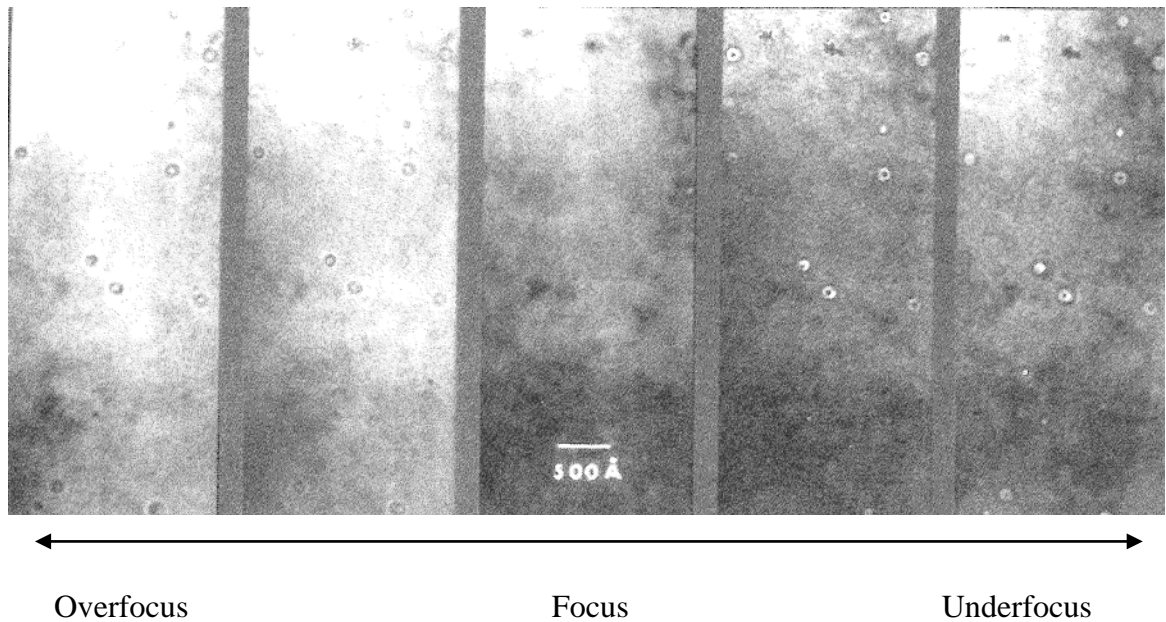


**Figure 26: A through-focal series of small voids in stainless steel irradiated with Ni ions. Extracted from [118].**

Another form of imaging, complementary to phase contrast, is Z-contrast imaging. Modern microscopes using an annular dark-field or high angle annular dark-field (HAADF) detector to generate images from very high angle, incoherently scattered electrons (as opposed to Bragg scattered electrons) and is very sensitive to variations in the atomic number of the atoms. This technique is performed in scanning transmission electron microscopy, and can be utilized in parallel with spectroscopy techniques such as EDS and EELS.

Structure factor contrast is another term of mass-thickness imaging [117]. Regions with different structure factors (defects, bubbles, amorphous layers) compared to the matrix have different extinction distances and lead to contrast in the TEM image. This technique

can be used to image cavities and amorphous zones much like phase contrast imaging, but in focus rather than being in an out of focus condition.

Diffraction contrast is a heavily utilized technique in characterizing irradiated materials [11, 13, 36, 47-49, 96-99, 105, 107, 117, 119, 120]. Defects in the material will lead to local variations in the Bragg diffraction conditions, leading to certain contrast based on the diffraction condition and aperture arrangement. This can be performed in bright-field when the objective aperture is placed on the transmitted electron beam, or in dark-field with the objective aperture placed on a specific diffraction vector of interest.

### **2.7.1.3 Electron Energy Loss Spectroscopy**

Electron energy loss spectroscopy (EELS) measures the energy that monoenergetic electrons lose as they interact with a bulk material (i.e., the sample). The electron interactions can take place in the form of elastic scattering, or inelastic scattering as shown with the classic particle view of electron scattering shown in Figure 27 [121]. Elastic scattering occurs as a result of Coulomb interactions with the atomic nucleus shown in Figure 27(a). These interactions generally produce scattering which are responsible for electron diffraction discussed in the previous section. Generally speaking, the elastic scattering results in relatively negligible exchange of energy, making up the zero loss peak in an EELS spectra shown in Figure 28 for Inconel X-750.

Inelastic scattering occurs as a result of Coulomb interactions between the incident electrons and the atomic electrons of the sample. Energy is transferred from the incident electrons to the atomic electrons resulting in an orbital jump to a higher energetic state.

Inner-shell electrons, Figure 27(b) and outer-shell electrons Figure 27(c) both contribute to inelastic scattering, and the energy loss associated with each orbital is indicative of the specific atom. Another form of inelastic scattering noteworthy is associated with Plasmons. Plasmon signals are produced from the harmonic interaction of outer-shell electrons within the sample whose energy is proportional to the square root of the valence electron density within the sample [121]. For the majority of materials, this energy is within the 5-30 eV range. For Inconel X-750 the Plasmon energies are at approximately 10-30 eV, as shown in Figure 28. The intensity of the Plasmon signal is directly proportional to the sample thickness, and limits the amount of information that can be obtained from thick samples in the low energy loss regime. In addition to bulk Plasmon excited within the sample, electrons can also create surface Plasmons at free surfaces. This is increasingly important for thin samples, but also for characterization of voids or bubbles where multiple free surfaces exist within the sample interior [89].

Figure 28 shows a typical EELS spectra from Inconel X-750 showing the specific edges produced from the inelastic interactions. Following the jump to higher energies, the electrons quickly lose their energy in a de-excitation process to a lower orbital, and as a result emit the excess energy in the form of an x-ray, Auger, or cathodoluminescence. Each of these signals can be utilized to learn additional information from the material; the most notable and commonly used in transmission electron microscopy is energy-dispersive X-ray spectroscopy (or EDS).

A major advantage of utilizing EELS in irradiated materials with hydrogen and helium is with respect to the detection limits for low atomic numbers such as hydrogen and helium.

Previous discussions have illustrated how EELS can be used in measuring the helium density within nano sized bubbles to ascertain helium-vacancy ratios, helium densities, and pressures through a hard sphere equation of state.

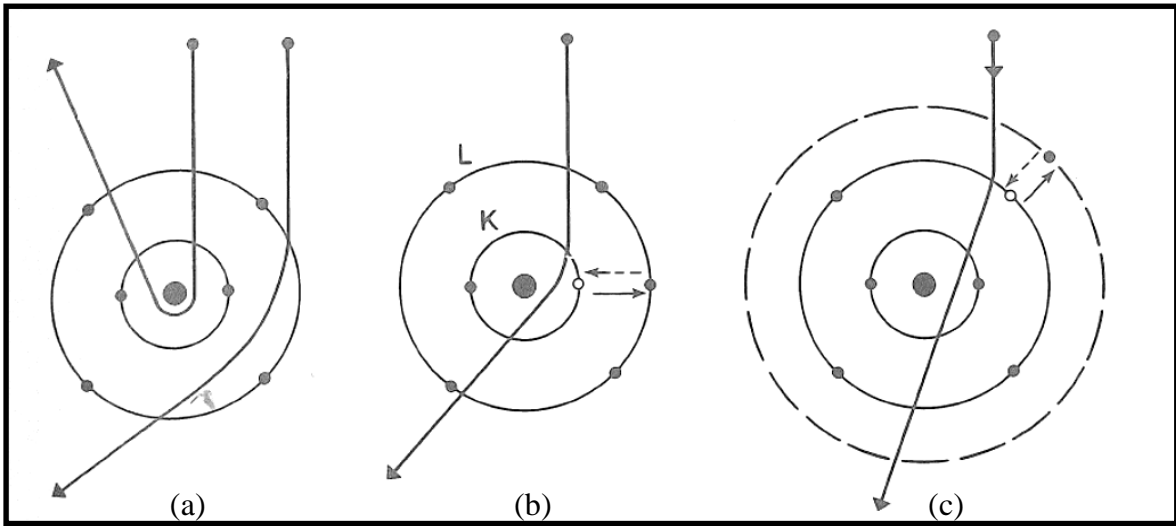


**Figure 27: Classic particle view of electron scattering by a single atom. (a) Elastic scattering caused by Coulomb interactions with the nucleus, and Inelastic scattering caused by Coulomb repulsion from the (b) inner-shell electrons and (c) outer-shell electrons [121].**

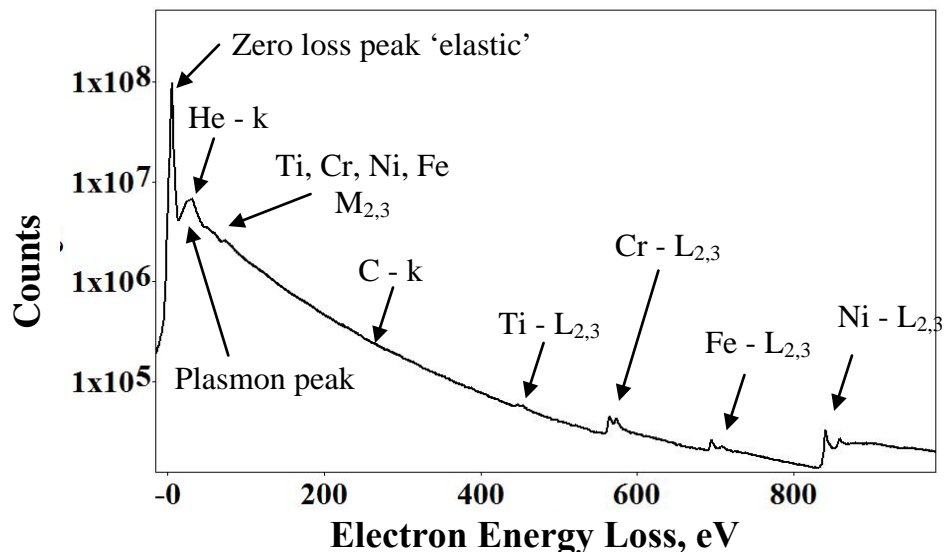


**Figure 28: An Electron Energy-Loss Spectrum for Inconel X-750 including the base elements, Ti, Cr, Ni, and Fe, in addition to noting the inconvenient location of He-k edge.**

## 2.7.2 Micro-Mechanical Testing

### 2.7.2.1 Relationship between Hardness and Yield Strength

Measurement and predictions of material properties in nuclear components as they change during service is important to demonstrate continuing fitness-for-service. The most desirable method of measuring these properties is by performing standardized American Society for Testing and Materials (ASTM) mechanical tests on ex-service material removed from reactor. This is not always a viable testing option for nuclear components due to the size limitations of available material and the high residual radioactivity that put additional limits on sample sizes. As an alternative, correlations have been developed between less intrusive test methods (i.e. micro-hardness) and standardized mechanical testing (tensile tests) to predict changes in yield strength. This

method has proven effective in predicting and demonstrating yield strength of light water reactor (LWR) core components [106].

Originally described in detail by Tabor [122], indentations produced by hardness testing create permanent impressions in the material. These impressions were shown to be related to the plastic properties (i.e. yield strength) of the material. This was further verified for a series of unirradiated and irradiated materials [106]. As summarized in [106], correlations are strong for irradiated austenitic and ferritic steels producing the following relationships:

$$\Delta\sigma_y = 3.03 \cdot \Delta H_V \quad \text{For austenitic steel}$$

$$\Delta\sigma_y = 3.06 \cdot \Delta H_V \quad \text{For ferritic steel}$$

Where  $\Delta\sigma_y$  is expressed in MPa and  $\Delta H_V$  is expressed in  $\text{Kg/mm}^2$ .

Although no correlations have been produced for irradiated Ni alloys, it is assumed that a correlation of  $\sim 3$  will give an adequate approximation to predict changes in yield strength with irradiation.

## **CHAPTER THREE**

### **EXPERIMENTAL PROCEEDURE**

#### **3.1 Material Selection and Preparation**

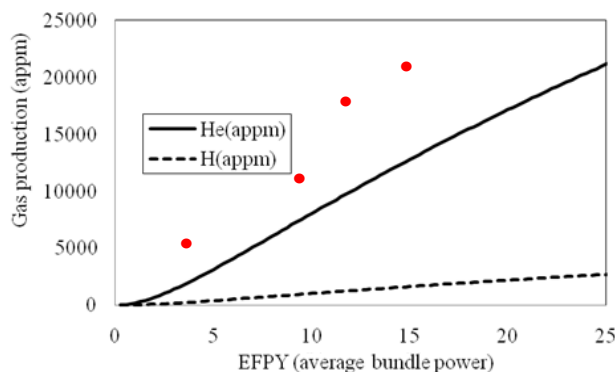
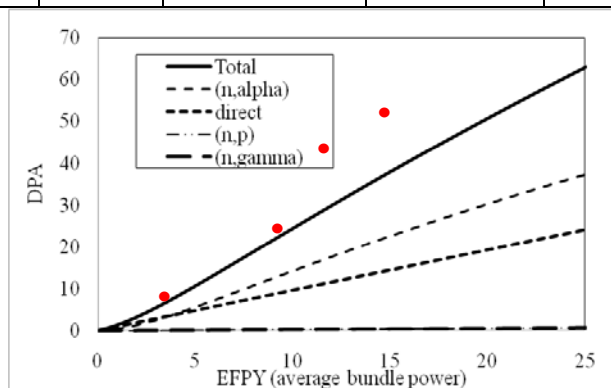
Ideally the material used for the proton irradiation would be unirradiated Inconel X-750 spacers, however, there are size requirements for the proton irradiation samples and the spacer geometry does not conform to these requirements. Material was required to be fabricated to be representative of the unirradiated microstructure. Therefore, this section is broken into two main categories: ex-service neutron irradiated material and proton irradiated material.

##### **3.1.1 Ex-Service Neutron Irradiated Material**

The ex-service material was sectioned directly from spacers removed from CANDU reactors. A section of spacer was obtained from nominal pinched material (120-280°C) and nominal un-pinched material (300-330°C). Table 3 and Figure 29 show the general operating conditions associated with the ex-service material in terms of total accumulated dpa and He concentrations. Figure 30 reports the respective fuel channel pressure tube temperature profiles and flux profiles (>1MeV) for each removed spacer. Note that the two non-optimized spacers operated at a lower total flux compared to the two optimized spacers, and also that the two optimized spacers had very similar in reactor operating conditions (flux and temperature profiles).

**Table 3: Ex-Service Test Material**

Material ID	Type	EFPY	Estimated DPA	Calculated He (appm)	Flux Spectrum and PT Temperature Distribution
A	Non-Optimized	3	6.4-6.7	1700-1800	Figure 30-A
B	Non-Optimized	9.4	16.9-23.6	5400-7700	Figure 30-B
C	Optimized	11.15	42.8-46.4	14500-15700	Figure 30-C
D	Optimized	14.26	51.2-55.0	17300-18600	Figure 30-D



• - Ex-Service Material for examination

**Figure 29: DPA and He calculations and ex-service material used for microstructural characterization.**

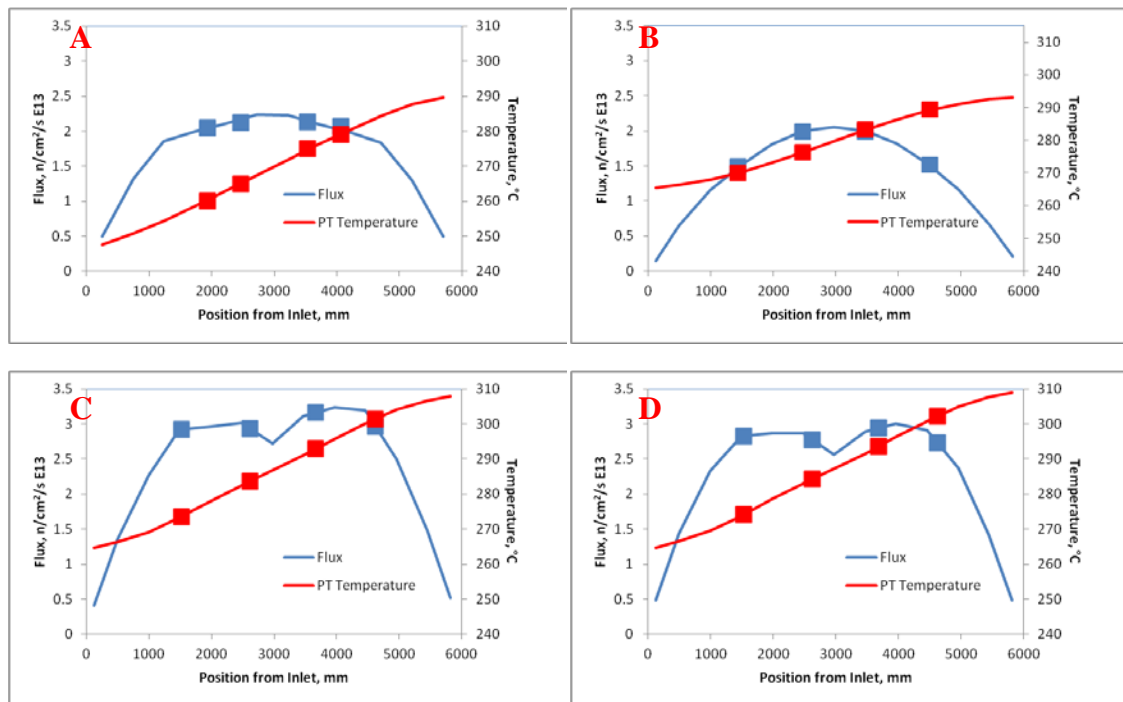


**Figure 30: PT temperature profile and flux profiles ( $E > 1\text{MeV}$ ) for a) Material A, b) Material B, c) Material C and d) Material D.**

### 3.1.2 Proton Irradiated Material

The proton irradiation program was conducted in collaboration with Professor Gary Was and Dr. Z. (George) Jiao at the University of Michigan. Dr. Jiao and Professor Was had significant contributions to the design and experimental execution of the proton irradiation.

Ideally in any accelerated irradiation program it is desired to use the same material as used in reactor; however, the proton irradiation test program requires material with dimensions of 2 mm x 2 mm x 20 mm which is outside of the specifications for spacer geometries. The material selected to be used for the irradiation program is from a bar

stock of X-750 heat treated under conditions determined appropriate to be “representative” of X-750 spacer material. Table 4 shows the chemical composition and heat treatment specifications for spacer material compared to the “representative” X-750 material for the proton irradiation program.

**Table 4: Chemical composition and heat treatment specifications for spacer material compared to bar stock “representative” material for the proton irradiation.**

Garter Spring (SPEC)			X-750 Bar Stock (ACTUAL)	
<b>Base Element</b>	Ni (Nickel)		Ni (Nickel)	
<b>Aluminum</b>	0.40 to 1.00%	% by wt	0.68	% by wt
<b>Carbon</b>	0.08% maximum	% by wt	0.03	% by wt
<b>Cobalt</b>	1.00% maximum	% by wt	0.11	% by wt
<b>Chromium</b>	14.00 to 17.00%	% by wt	15.81	% by wt
<b>Copper</b>	0.50% maximum	% by wt	0.033	% by wt
<b>Iron</b>	5.00 to 9.00%	% by wt	8.68	% by wt
<b>Manganese</b>	1.0% maximum	% by wt	0.20	% by wt
<b>Niobium</b>	1.20% maximum	% by wt	0.93	% by wt
<b>Nickel</b>	70.00% minimum	% by wt	70.19	% by wt
<b>Sulphur</b>	0.01% maximum	% by wt	0.001	% by wt
<b>Silicon</b>	0.50% maximum	% by wt	0.16	% by wt
<b>Tantalum</b>	1.20% maximum	% by wt	0.02	% by wt
<b>Titanium</b>	2.25 to 2.75	% by wt	2.55	% by wt
<b>Other elements</b>	Nb+Ta 0.70-1.20	% by wt	0.95	% by wt
<b>Solution Treatment</b>	2000-2200°F (1093-1204°C), no hold time specified		1625±25°F (885±14°C) for 24hrs	
<b>Precipitation Hardening</b>	1350±25°F (732±14°C), hold for 16 ± ½ hr, air cool		1350±25°F (732±14°C), hold for 16 ± ½ hr, air cool	

The goal of the proton irradiation program is to have material irradiated to different doses with and without He to assist in the interpretation of ex-service neutron irradiated experimental data and gain a more complete understanding of the fundamental mechanisms of radiation damage. Because the dpa rates are accelerated in the proton irradiation program compared to neutron irradiation, the irradiation temperature needs compensation to attempt equivalency with respect to He bubble nucleation and growth (i.e. swelling) compared to ex-service neutron irradiated material. The appropriate temperature shifts can be calculated two different ways: keeping the number of defects lost to sinks per unit volume as invariant (Equation 8.158 in [36]), and keeping the swelling rate invariant (Equation 8.162 in [36]). The first temperature shift equation is noted as more relevant for radiation induced segregation (RIS) studies, and the later for swelling. These calculations are based on freely migrating point defects, and at best only give an estimation regarding the temperature shift; there is no adjustment for the affect of displacement damage rate on helium bubble and point defect cluster nucleation density. In the present investigation, the temperature shifts were calculated using both equations, and based on the experimental experience of Professor Gary Was biased to be closer to the swelling value; 250°C to simulate 200°C from neutron irradiation and 380°C to simulate 330°C from neutron irradiation at the recommendation of Professor Gary Was [123]. The adequacy of the temperature shift can only be determined after the experiment is complete with information on the microstructure evolution.

Using rate theory and the concepts outlined in Section 2.3.3, the temperature shifts recommended for this program can be compared. Using an unirradiated material as a

baseline and shifting the dose rate from  $10^{-7}$  dpa/sec (neutron) to  $10^{-5}$  dpa/sec (proton), as shown in Figure 31, the temperature shifts in this study place the low temperature securely in the recombination dominated regime, and the high temperature in the transition from recombination to sink dominated.

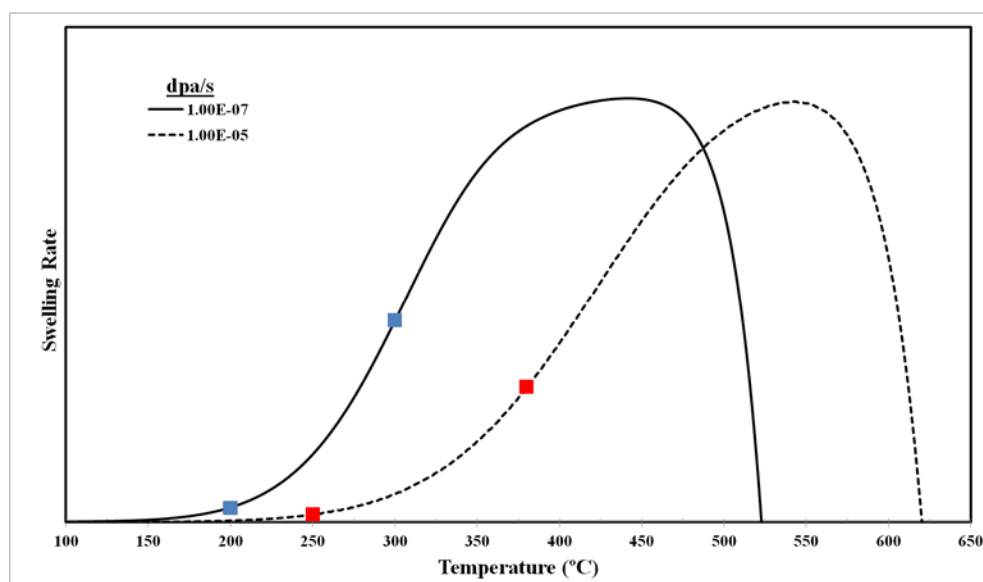


**Figure 31: Comparison of hypothetical swelling calculations for neutron irradiation in CANDU ( $\sim 10^{-7}$  dpa/s) and proton irradiation at the UofM Tandatron accelerator ( $\sim 10^{-5}$  dpa/s). Dots indicate irradiation temperatures for the pinched and non-pinched spacers in CANDU (blue) and simulated temperatures in proton irradiation experiments.**

In the first phase of the irradiation, material was irradiated at both temperatures up to 20 dpa with 6000 appm helium. Irradiations up to 40 and 60 dpa with and without 12000 and 18000 appm He respectively were performed only at 380°C. The proton irradiation program was designed to give material irradiated to 20, 40 and 60 dpa with

and without 6000, 12000 and 18000 appm He respectively. These conditions match closely the irradiation conditions of ex-service material B, C, and D respectively.

### **3.1.2.1 Helium Implantation**

Helium implantations in Inconel X-750 samples have been performed at the University of Western Ontario (UWO) at room temperature aimed to achieve 6000 appm helium at a depth of approximately  $5 \pm 0.5$   $\mu\text{m}$  from the surface, as shown in Figure 32. For target materials with higher helium concentrations, additional implantations will be performed between irradiation steps to 12000 appm and 18000 appm helium respectively. SRIM calculations have been performed with these helium energies indicate that the implantation process may generate approximately 0.35-0.5 dpa at the helium plateau per implantation [124]. Therefore, approximately 1-1.5 dpa is generated for the material with 18000 appm helium. This low dpa is small with respect to the target doses, and should be considered as an experimental uncertainty.

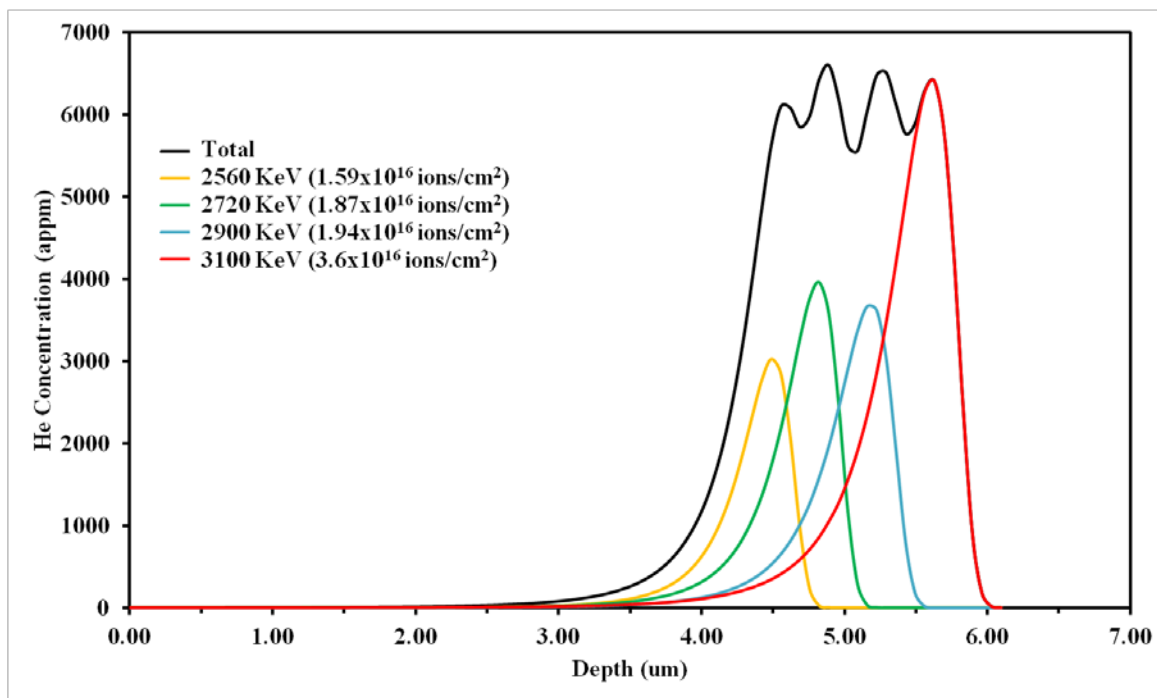


**Figure 32: He concentration profiles as a result of four tailored implantations designed to create a 1  $\mu\text{m}$  wide region with approximately 6000 appm He.**

The stage to hold the Inconel X-750 for helium implantation is a nickel block with a cooling channel integrated into the design to allow temperature control. A thermocouple built into the centre of the block (1 mm below the surface) allows for close temperature monitoring during the implantation to ensure that the temperature does not exceed the experimental target. The temperature never exceeded 28°C during the implantation. Carbon/copper tape is used to fix the samples to the stage and the implantation surface is normal to the beam. The stage is then loaded into the chamber and pumped down to less than  $10^{-7}$  torr prior to implantation.

Beam alignment was performed via a two step process; step one was to ensure all apertures are aligned with the samples. To ensure even implantation, a 13 mm x 17 mm

aperture was used. Step two uses laser alignment to ensure the entire surface of the samples will be evenly implanted.

Fluence control is achieved via a charge integration of the helium current on the stage. The stage itself was isolated from the beam line and the current fed into a digital current integrator. The pulse output is inputted into a computer to ensure that the proper fluence is used. Four different implantations were performed, 2560 keV, 2720 keV, 2900 keV and 3100 keV. The total current on the stage ranged from 750 nA to 1.3  $\mu$ A.

### **3.1.2.2 Proton Irradiation**

Proton irradiations were performed using a specially designed stage connected to the Tandetron accelerator at the Michigan Ion Beam Laboratory. A proton energy of 1.2 MeV was used, resulting a nearly uniform damage rate through the first 6  $\mu$ m of the proton range of 9  $\mu$ m as shown in Figure 33. The experiment was designed using the damage depth profiles as calculated with SRIM full-cascade, however, a recent study has shown that the Kinchin-Pease approximation may better represent proton irradiation for a comparison to neutron exposure [125]. As a result, the expected damages obtained in this study may be off by a factor of 2 (i.e. rather than obtaining 20, 40 and 60 dpa target doses, it may be 10, 20 and 30 dpa respectively). For the purposes of this dissertation, the SRIM full-cascade calculations will be used, however both depth profiles are presented in Figure 33 for reference.

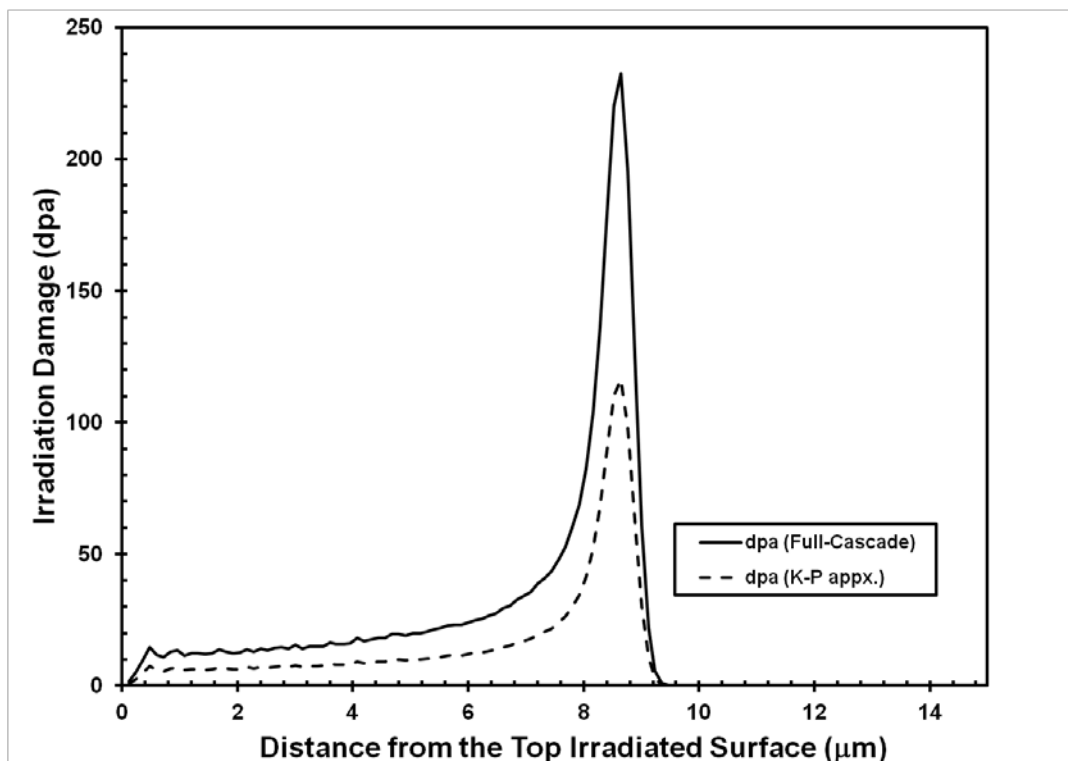


**Figure 33: Irradiation damage as a function of depth using a proton energy of 1.2 MeV in Inconel X-750 at the Tandetron accelerator at the Michigan Ion Beam Laboratory. The dpa is calculated from SRIM full-cascade and SRIM K-P.**

The irradiation stage was designed to control the sample temperature by controlling the stage temperature. The stage was heated using a resistive cartridge heater and cooled using room temperature air flowing through cooling lines that penetrate the back of the stage. The stage surface is constructed with copper to provide appropriate heat conduction away from the samples. A thin layer of indium was placed between the X-750 samples and the stage surface. Indium is molten at the irradiation temperatures used in this experiment, maximizing the thermal contact between sample and stage and ensuring appropriate thermal contact throughout the experiment.

During the irradiation, the temperature was monitored at three locations on each sample; the top, centre and bottom. The temperature was measured continuously using a high resolution two dimensional, thermal imaging system (pyrometer). During irradiation, the sample temperature was controlled to within  $\pm 10^{\circ}\text{C}$  of the irradiation set point via controlling the stage temperature with room temperature air.

The irradiation stage is electrically isolated from the beam line, and four rectangular apertures are used to define the area on the sample bars to be irradiated. An area of approximately 10 mm by 12 mm is used to ensure all samples are irradiated evenly. The beam-line was set to raster scan across all regions within the aperture to ensure all regions on the samples received the same dose. The irradiations were performed on the order of  $1-4 \times 10^{-5}$  dpa/s.

### **3.2 Fractography (Scanning Electron Microscopy)**

Material was provided to this research program following destructive testing in the form of “crush” testing in room temperature air between two flat platens on lengths of spacers with 15 to 24 coils loaded (in parallel) in displacement control. Figure 34 shows an example of post crush test specimens from 12 o’clock (300-330°C) and 6 o’clock (120-280°C) positions from material irradiated to 51.2-55.0 dpa and 17300-18600 appm helium [10, 13, 14]. For the purposes of fractography examination, those sections of spacers which did not fully fracture during testing were fractured within the hot cells with hot cell manipulators in the Fuel and Materials Cells (FMC) at the Canadian Nuclear Laboratories (CNL).

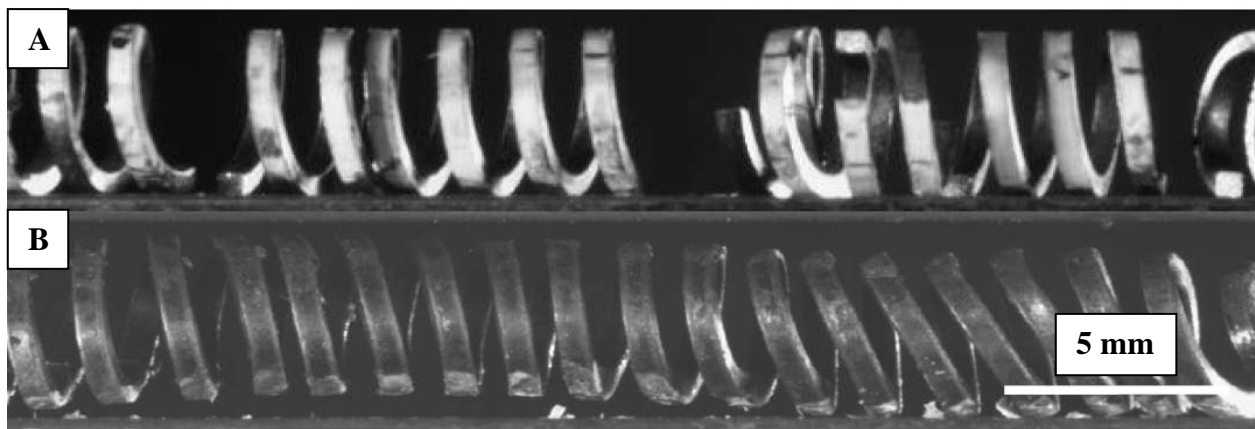


**Figure 34: Post crush test images of (A) 12 o'clock showing brittle fracture (limited to no ductility prior to fracture), top, and (B) 6 o'clock showing no fracture and plastic deformation, bottom [10, 13, 14].**

The fractography was performed on an active (i.e., shielded) JEOL JXA 840A SEM with the assistance of Clinton Mayhew (SEM operator at CNL). A 50  $\mu\text{m}$  objective aperture was used to optimize the resolution of the microscope with an acceleration potential of 7 kV and a beam current of 200 pA (as measured with a faraday cup inserted into the beam line below the aperture).

### **3.3 X-750 Sectioning**

Ex-service spacers were sectioned to less than 1 mm in length along the length of the wire. This was performed by mounting a small section in epoxy and performing multiple slices with a diamond saw in the FMC facility at CNL. Samples were either packaged and shipped to Idaho National Laboratory for TEM preparation via focussed ion beam or sent for electropolishing in an active laboratory located at Chalk River. The specimens sent to INL were also used for micro hardness measurements.

### **3.4 TEM**

TEM specimens from ex-service material were prepared via two methods: electropolishing performed at CNL and using a Quanta 3-D Dual-beam focussed ion beam (FIB) at INL. Michael Stewart and Gregory Morin (Technologists at CNL) performed the electropolishing following a similar method as documented in [112]. Because the ex-service material is of odd geometry for standard 3 mm disk preparation, the samples were thinned and sandwiched between two copper grids with a nominal 0.5mm hole in the middle. The sample was then jet electropolished to electron transparency. This technique did not have high success rate at producing suitable samples, and were still relatively thick (>100 nm). Therefore, the FIB approach was adopted for further investigation. The FIB preparation was performed at INL under a Cooperative Research and Development Agreement (CRADA) between Battelle Energy Alliance and Atomic Energy of Canada Limited (AECL now CNL) as part of the National Scientific User Facility (NSUF) at INL. Jim Madden (Microscopy specialist at INL) performed the FIB preparation of the TEM lamella for the ex-service material.

TEM specimens from the proton irradiated material were prepared exclusively using a focussed ion beam (FIB) at INL and the Centre of Advanced Energy Studies (CAES) in Idaho Falls. Jatu Burns (FIB and SEM operator at CAES) performed the FIB preparation from the proton irradiated samples.

The TEM characterization has been performed at four separate laboratories with five different microscopes; CNL using a Phillips CM-30, INL using a JEOL 2010F, CAES using a F30 G2 Tecnai, and the Canadian Centre of Electron Microscopy (CCEM) using

both Titan 80-300 high base and low base microscopes. The microscopes at CAES and the CCEM are equipped with post column image filters that allow electron energy loss spectroscopy to be performed in STEM mode.

### **3.4.1 Imaging Cavities and Helium Bubbles**

Characterization of irradiation induced cavities is performed using Fresnel contrast imaging in bright-field with an objective aperture. Fresnel contrast imaging is summarized as follows [117]:

- When the image is in perfect focus, cavities do not produce any contrast (i.e. no contrast difference between matrix and cavity).
- The contrast depends on the difference between the inner potential of the matrix and the cavity.
- When the image is underfocussed, cavities appear as bright dots, surrounded by a dark fringe.
- When the image is overfocussed, cavities appear as dark dots, surrounded by a bright fringe.

If the samples are too thick with respect to the bubble size and density, then it is difficult to obtain clean, crisp images of individual bubbles. This is primarily related to bubble overlap. Overlapping bubbles will still produce Fresnel contrast, but interpretation of individual bubbles in the resulting micrographs becomes increasingly more complex with thicker specimens. To circumvent this complication and to enable quantitative analysis of the bubble sizes, densities and spacing, it is crucial to work with specimens that have

been prepared to less than approximately 50 nm. This value will greatly depend on the specific bubble size and density of each sample, and it is impossible to predict prior to examination. Using the FIB approach to prepare specimens may lead to undesirable curtaining during the final stages of milling. This is a result of high residual strain in the materials leading to bending of the samples. During bending, non-uniform milling will take place, resulting in local holes being introduced to the specimen. Although, not entirely desirable, this does provide local regions in the samples with a range in thicknesses down to a few nm's. For any quantitative analysis on bubble density and size, the thickness of the material is required. This has been performed in multiple ways in this investigation. Low loss electron energy loss was used to provide local estimates of the relative thickness,  $t_{rel}$ , with respect to the inelastic mean free path of the material,  $\lambda$ , following [117]:

$$\text{Equation 13} \quad t_{rel} = \lambda \ln \left( \frac{I_1}{I_0} \right)$$

Where,  $I_1$  is the integrated intensity of the low loss region of the curve (<100 eV), and  $I_0$  is the integrated intensity of the zero-loss peak. This approach is quick and enables the thickness to be measured easily at the specific region of interest for quantitative analysis. This technique however only gives the relative thickness with respect to the inelastic mean free path. For irradiated materials with a high density of bubbles, this value is not known, but can be experimentally verified with another more rigorous method of determining thickness. For these experiments, a series of grain boundary tilts were performed as shown in the schematic example in Figure 35. The absolute thickness,  $t_{abs}$ ,

can then be calculated with basic algebra, and related to the  $t_{rel}$ , to determine the inelastic mean free path for this material. For all further analysis, this inelastic mean free path is used and thereby validates the quick EELS approach of measuring TEM thickness at the specific region of interest throughout the microstructural examination.

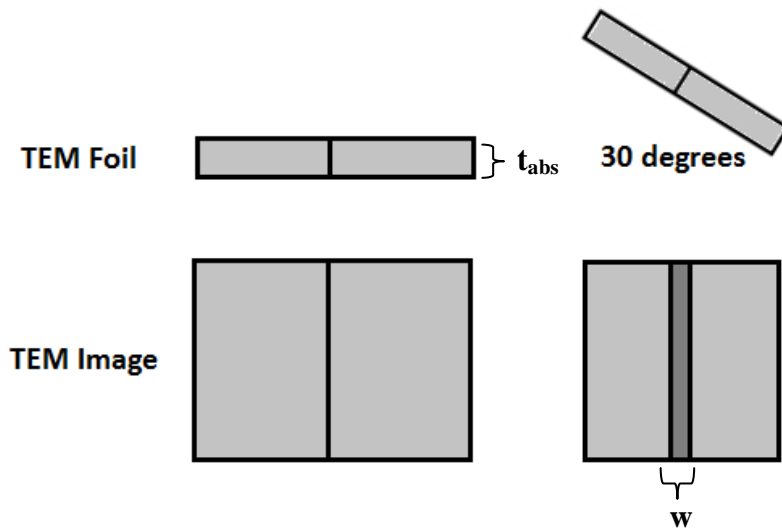


**Figure 35: Schematic outlining process of experimental determination of the inelastic mean free path.**

Quantitative analysis of helium bubbles is performed by physically drawing over the bubbles, which enables a colour threshold and analysis using ImageJ software [126]. The outside of the bubble was taken as the mid-wall of the dark (or light) fringe. The overlay images were then analyzed with an image threshold to measure the bubble diameter, and relative (x, y) locations of their centre of mass. It is assumed that the bubbles are perfect spheres. In cases where the bubbles are slightly elongated, the long axis is taken as the

diameter, and the volume/area are calculated as perfect spheres for calculation simplicity. To assist in identification of bubbles, each region was analyzed in underfocus, overfocus and focus conditions, and compared during the analysis to give higher confidence results.

### **3.4.2 Tomography of He Bubbles**

The tomography acquisition and reconstruction was performed with assistance from Dr. Andreas Korinek at the CCEM, McMaster. HAADF STEM images were collected every 2 degrees from relatively thin regions of the sample containing a grain boundary. The image reconstruction was performed using tomoj following the simultaneous iterative reconstruction technique (SIRT) [127]. The analysis and 3-dimensional rendering was performed using Chimera software [128].

### **3.4.3 Helium Density Measurements**

The quantification of the helium density is performed in two ways in the present study: using the integrated intensity of the helium signal and the use of Equation 10 and the energy shift of the  $1s \rightarrow 2p$  transition in the helium K-edge.

#### **3.4.3.1 EELS Acquisition**

EELS acquisition of helium bubbles was performed using a FEI Titan 80-300 cubed TEM at 200 kV with a 2.5 mm aperture, dispersion of 0.05 eV/ch and an exposure of 0.001 s. A step size of approximately 0.1 nm was used to probe the helium bubbles. In some cases, the bubbles burst part way through the analysis, and the implications of this are discussed in more details in the analysis.

### **3.4.3.2 Quantification of He Density**

The helium K-edge occurs within the Plasmon signal in Inconel X-750 making the background subtraction more complicated. Using a 2<sup>nd</sup> order log-polynomial background fit for the Plasmon appears to match the shape of the Plasmon quite well and enables the helium signal to be subtracted from the spectra for quantification. There are no cross sections for helium under the Hatree-Slater model in Digital Micrograph software package to be used for helium analysis, and in this absence, the hydrogenic white line cross section was used. This helps identify the number density of helium atoms that lead to the generation of the helium K-edge in the spectra. This provides a pixel map for helium atoms per nm<sup>2</sup>. To quantify the helium density (in units of atoms/nm<sup>3</sup>), a binned (x5) line profile across the EELS helium maps is performed. The local maximum is taken as the signal from the centre of the bubble, and divided by the bubble diameter. This provides a helium density estimate using the integrated intensity for helium. This technique however is not believed to be highly accurate for smaller bubbles as the relative thickness of the material will increase the Plasmon signal and thereby increase the background in the spectra.

### **3.4.3.3 Determination of the Energy Shift of the 1s→2p Transition**

The energy shift of the 1s→2p transition is obtained by similarly extracting the helium signal from the EELS spectra with a 2<sup>nd</sup> order log polynomial. The data is smoothed using three 25 point Savitsky-Golay filters to remove signal noise. The eV at the local maxima is taken as the 1s→2p transition, and the energy the shift related to the free helium of 21.218 eV.

#### **3.4.3.4 List of Assumptions for Helium Density Measurements**

This analysis includes some assumptions, listed below for reference. Standard propagation of error procedures were followed for this analysis to give higher confidence to the results.

- Error on bubble diameter measurements is estimated at approximately 0.1 nm.
- Error on  $1s \rightarrow 2p$  transition energy shift is 1.5 eV for bubbles smaller than 2 nm, 1 eV for 2-3 nm bubbles, 0.5 eV for 3-5 nm bubbles and 0.25 eV for bubbles larger than 5 nm. The difference in error changes because the general shape of the helium K-edge broadens for smaller bubbles.
- Error on  $C_p$  is obtained through regression analysis of helium density vs energy shift for bubbles greater than 3 nm. It is assumed that this error incorporates experimental error.
- It is assumed that regression analysis includes the error associated with the EELS measurements, and a linear relationship can be used to relate the helium density and He/V distributions from EELS with bubble size and density distributions

#### **3.4.4 Gamma Prime Characterization**

Characterization of  $\gamma'$  in unirradiated materials is traditionally performed in bright-field or in dark-field imaging with a selected area diffraction aperture on the  $\gamma'$  superlattice reflection as shown in Figure 36. Because of the tendency for  $\gamma'$  to become disordered relatively quickly following irradiation as discussed in Section 2.4.2, it is difficult to image the precipitates in bright-field (i.e. the strain field surrounding the  $\gamma'$  disappears),

and the precipitate becomes partially or fully disordered making imaging in dark-field difficult/impossible (i.e. the superlattice reflection is weak or non-existent pending the degree of disorder). To understand the nature of disordering and dissolution of the gamma prime following irradiation, the elemental distribution of the  $\gamma'$  can be characterized using electron energy loss spectroscopy (EELS) to locate the precipitates.  $\gamma'$  is enriched in both Ti, Al and Ni. The Al is generally difficult to characterize with EELS due to the high energy loss for the K edge and the stronger background at the L edge energy; therefore Ti and Ni enriched zones and Cr depleted zones are used to characterize the elemental distributions of  $\gamma'$ . Figure 28 shows a representative EELS spectrum from Inconel X-750. In the case of characterizing  $\gamma'$ , the core loss region of 200-1200 eV is used with a dispersion energy of 0.5 eV capturing the  $L_{2,3}$  edges of Ti, Cr, and Ni. After EELS characterization of the  $\gamma'$ , electron diffraction can be performed at approximately the same location. It is necessary to perform electron diffraction at either the [1,1,1] or [0,0,1] zone axes in order to capture the (0,1,1) or (001) superlattice reflection of  $\gamma'$ .

There are complications with this approach of characterizing  $\gamma'$ . If the specimen is too thick, a few complications arise. Individual EELS edges become drowned out by the background signal of the specimen, and mapping of the elements not possible. Also, a difficulty much like that observed with bubbles is also observed with  $\gamma'$ . If the density of gamma prime is high, and the relative size of the precipitates small, then in a TEM foil may include many precipitates through thickness. This will lead to overlap when imaging in the TEM. Overlapping precipitates will complicate the signals generated in bright-

field because we will no longer be imaging the strain field surrounding one clean  $\gamma'$ , but many leading to a convoluted tangle of diffraction contrast. EELS mapping will be unable to distinguish a difference between the  $\gamma'$  and the matrix in transmission because of the degree of overlap. Hence, it is important to recognize that in some cases, although no  $\gamma'$  is apparent from EELS mapping, it is possible that the specimen is too thick with respect to the size and spacing of the gamma prime. As with the complication with bubbles, this complication can be mitigated by working with very thin specimens.

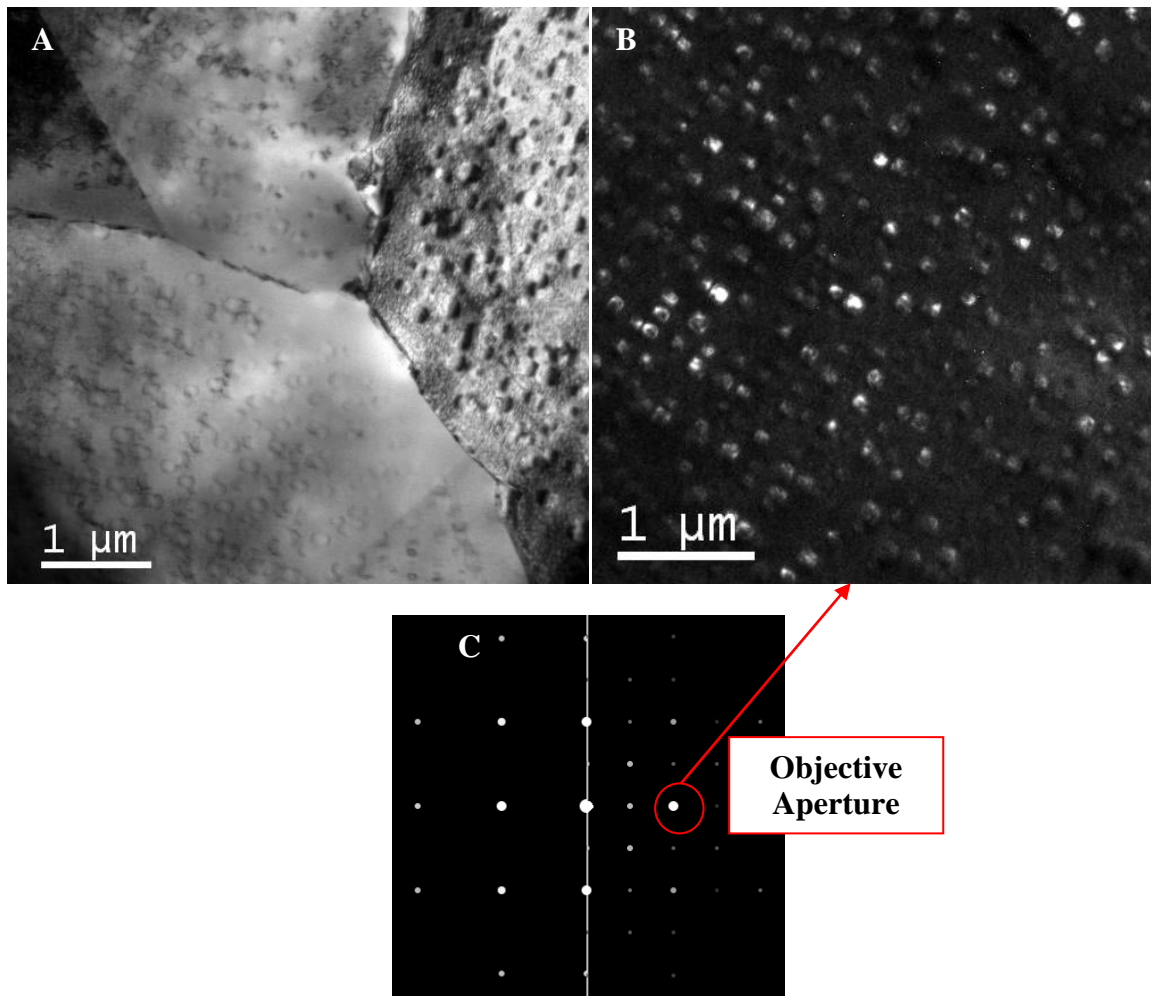


**Figure 36: TEM micrographs of gamma prime in a) bright-field, b) dark-field and c) [0, 0, 1] zone axis diffraction (left=gamma matrix, right=gamma prime/gamma overlay). Note the bright-field image and dark-field image are not of the same area.**

### **3.5 Micro-Mechanical Testing**

#### **3.5.1 Micro-hardness**

Micro-hardness testing was performed at CNL and INL. Hardness testing is performed using a Buhler micro-hardness indenter with a load of 500 g and normalized with respect to a standard block. At least five measurements are made for each specimen for statistical

and consistency purposes. The micro-hardness measurements can then be related to changes in material yield strength through the relationships outlined in Section 2.4.

### **3.5.2 Nanohardness**

Nanohardness testing was performed in collaboration with Dr. Vineet Bhakhri and Professor Robert Klassen at Western University. Nanohardness testing is performed using a Nano Test platform (Micro Materials Limited, Wrexham, UK) to conduct 200 nm deep cross-sectional nano-indentation experiments with a pyramidal, Berkovich indenter. The cross-section surfaces were prepared by sectioning proton irradiated specimens, followed by metallographic polishing to 0.05  $\mu\text{m}$  surface roughness finish. In a typical test, a row consisting of multiple indentations is made starting from the irradiated surface edge and progressively probing in to the unirradiated virgin material. In a row, the indents are placed 4.5 $\mu\text{m}$  apart such that the axis of the row is at an angle of  $\sim 11.3^\circ$  with respect to the irradiated surface edge. These diagonal indentations resulted in a net displacement of 0.7 $\mu\text{m}$  between the successive indents and rendered the ability to access precise variation in local mechanical properties arising from proton and helium irradiation dose profiles in X-750 specimens. In total, 3-4 tests are performed on each proton irradiation condition.

## **CHAPTER FOUR**

### **EXPERIMENTAL RESULTS**

In this chapter, the experimental results are reported. The results are separated into two separate sections; the ex-service neutron irradiated material investigation, and the proton irradiated material investigation. Each section will include an immediate general discussion. An overall discussion will be performed following presentation of all experimental results in a subsequent chapter.

#### **4.1 Examination of Inconel X-750 CANDU Spacers**

It is important to recognize that material irradiated to these conditions have never been characterized prior to this research. Material was provided to this project following post irradiation testing at Chalk River laboratories. Specimens were tested to failure. The characterization work included as part of this research program include: fractography, microstructural evolution, and mechanical property evolution. Specific contributions to this field include the novel approach to utilize a FIB and TEM to perform high resolution failure analysis of an intergranular fracture from heavily irradiated Inconel X-750; and a novel approach to characterize nano sized helium bubbles on grain boundaries to quantify area coverage, density and size distribution in heavily irradiated Inconel X-750.

#### **4.1.1 Fractography of Ex-Service Inconel X-750 CANDU Spacers**

An unirradiated sample was fractured to generate a baseline for the irradiated fractography characterization. Figure 37 details the fractography as a function of irradiation dose and temperature. The low dose (6.4-6.7 dpa), low temperature (120-280°C) did not fracture during crush testing. The sample was thus taken to fracture using cell manipulators. This was done for the sole purpose of comparison, and it is recognized that the difference in deformation process may influence the fracture mechanism, and this should be recognized as a potential source of uncertainty.

The unirradiated fracture surface is typical of a traditional ductile fracture (i.e., cup-and-cone), Figure 37, (A). By 6.4-6.7 dpa/1700-1800 appm helium, there is a transition in fracture mechanism to intergranular fracture at an irradiation temperature of 300-330°C, Figure 37 (C). This transition does not occur for lower temperature irradiation until somewhere between 6.4 dpa to 16.9-23.6 dpa/5400-770 appm helium, Figure 37 (B) and (D). For all material characterized with damage and helium beyond these transitions, the fracture surfaces are 100% intergranular, Figure 37 (E-G). There are no general distinctions between fracture surfaces as a function of in-reactor temperature beyond 16.9-23.6 dpa/5400-770 appm helium, Figure 37 (D-G). With continued irradiation damage and helium concentration, the degree of secondary intergranular cracking tends to increase. Higher magnification images of these secondary cracking images are shown in Figure 38 for material irradiated with 51.2-55.0 dpa/17300-18600 appm helium. Figure 38 shows features on the intergranular fracture surface consistent with the fracture propagating around grain boundary precipitates (i.e., remaining or removed precipitates

on the planar fracture surface). Based on the high radioactivity of the samples, and the small size of the remaining precipitates, it was not possible to gather any chemical information from spectroscopy techniques in the SEM (i.e. EDS). Figure 38 (B) shows features on a secondary intergranular fracture consistent with high plasticity directly adjacent to the grain boundary, which may support a local region of very high plasticity directly adjacent to the grain boundary.

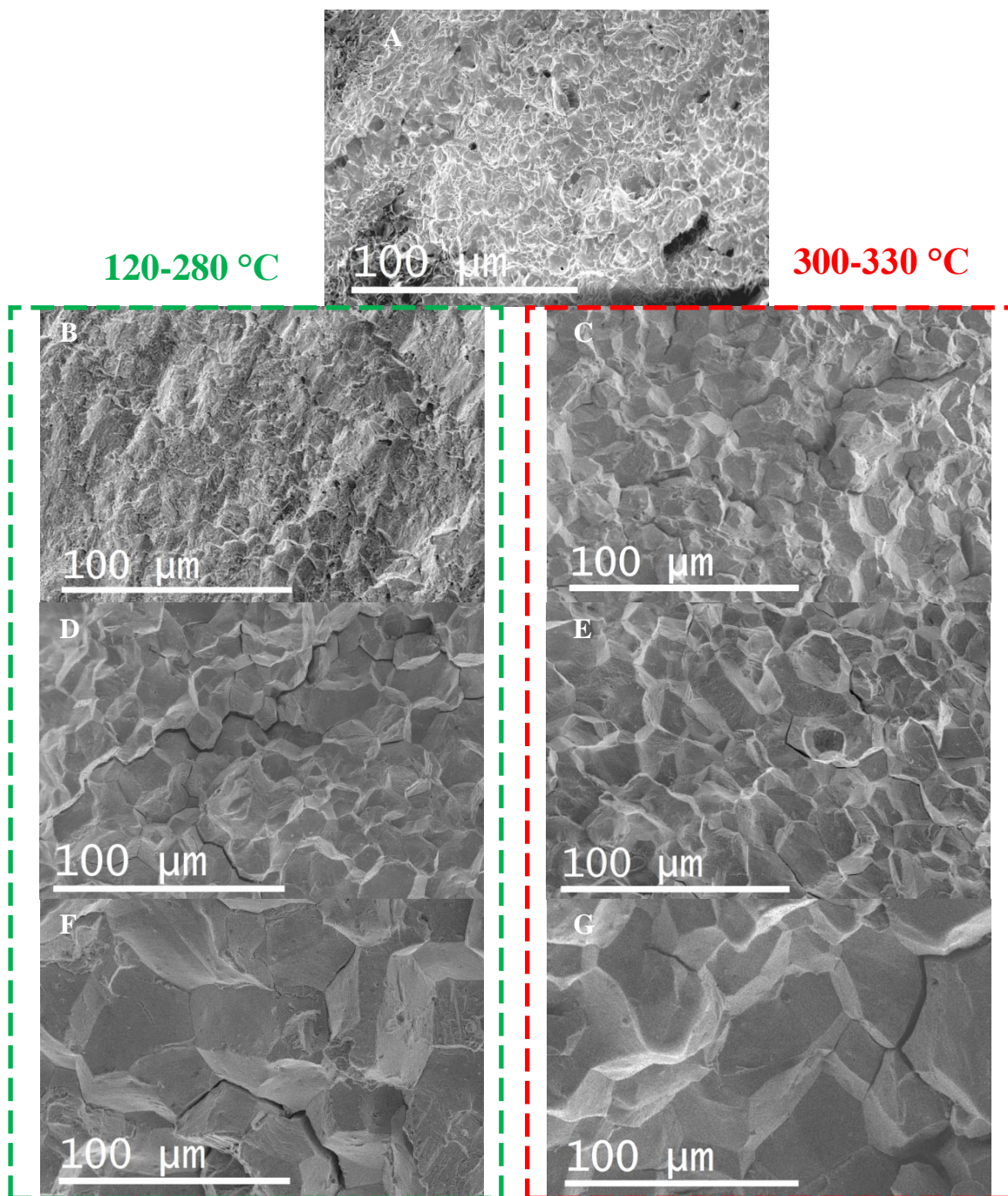


**Figure 37: Fracture surfaces of (A) unirradiated material, (B) 6.4-6.7 dpa and 1700-1800 appm helium material irradiated at 120-280°C, (C) 6.4-6.7 dpa and 1700-1800 appm helium material irradiated at 300-330°C, (D) 16.9-23.6 dpa and 5400-7700 appm helium material irradiated at 120-280°C, (E) 16.9-23.6 dpa and 5400-7700 appm helium material irradiated at 300-330°C, (F) 51.2-55.0 dpa and 17300-18600 appm helium material irradiated at 120-280°C, and (G) 51.2-55.0 dpa and 17300-18600 appm helium material irradiated at 300-330°C**

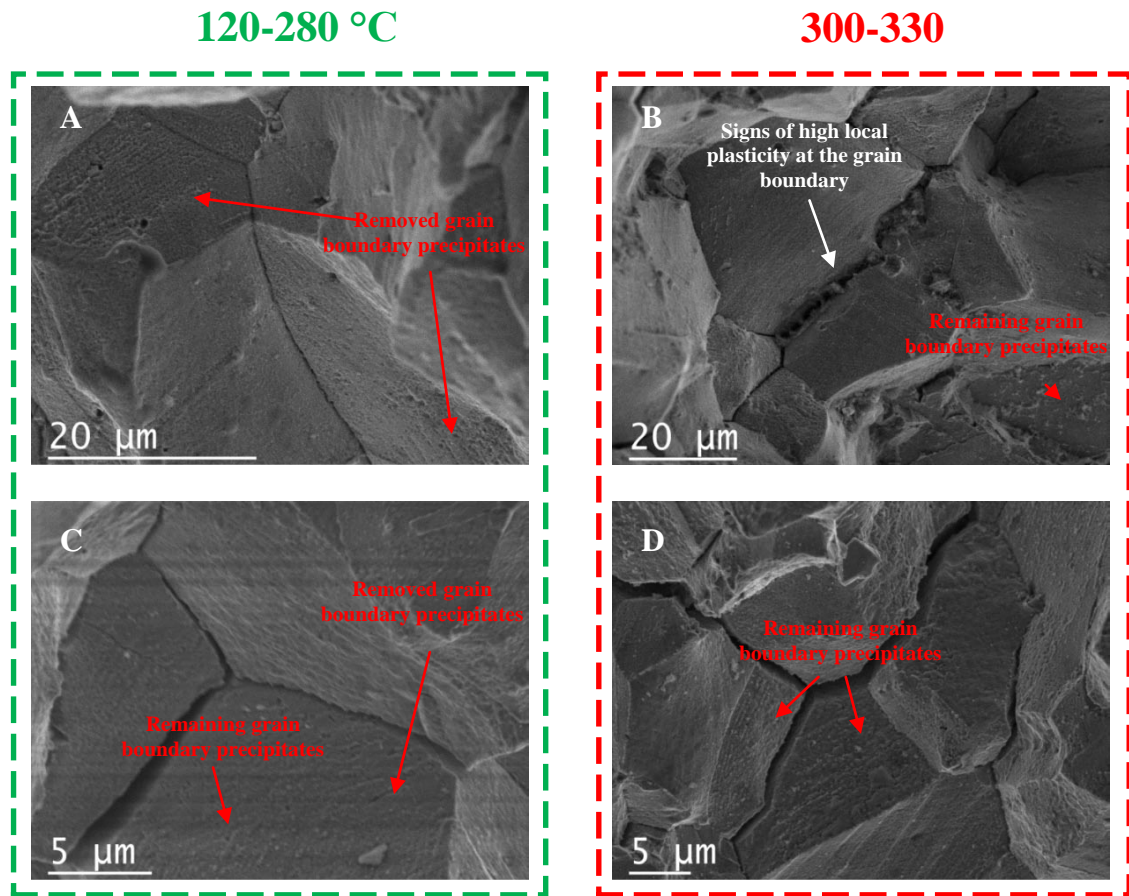


**Figure 38: Secondary intergranular cracks from material irradiated to 51.2-55.0 dpa/17300-18600 appm helium (A)&(C) 120-280°C and (B)&(D) 300-330°C.**

#### **4.1.2 Microstructure Evolution of Ex-Service Inconel X-750 CANDU Spacers**

The microstructural evolution of ex-service Inconel X-750 CANDU spacers is primarily focused on the characterization of helium bubbles forming as a function of irradiation dose and temperature. These bubbles can form homogeneously within the matrix of the material, but also at sinks such as dislocations, interphase boundaries, and grain boundaries. The characterization of helium bubbles is broken into four sub categories: homogeneous helium bubbles, grain boundary helium bubbles, helium bubbles within precipitates, and helium bubbles on sub-grain features. Measurements of the helium density within individual helium bubbles were performed with EELS to give insights into the state of helium within the bubbles and approximate He/V ratios.

In addition to understanding the influence of irradiation on helium bubble formation and growth, we are also interested in the evolution of secondary strengthening precipitates,  $\gamma'$ , as these precipitates play such an important role on the strength and creep resistance of the unirradiated material. The stability of these precipitates with irradiation is thus an important factor to consider with respect to the microstructural degradation for us to better understand the impact of irradiation on mechanical integrity. Finally, a novel approach is described which utilizes a focused ion beam to prepare site specific TEM lamella directly from an intergranular fracture surface. Although the technique of preparing the samples from a fracture surface with a FIB is not altogether revolutionary; the application of this approach towards post irradiation examination of heavily irradiated Inconel X-750 is unique. This work provides direct evidence of likely degradation

mechanisms, and provides insights for future post irradiation failure analysis for other applicable nuclear components.

#### **4.1.2.1 Characterization of Homogenous Helium Bubbles**

Homogenous helium bubbles are bubbles that form within the bulk matrix of the material. The characterization of these bubbles provides insights into the general impact of the irradiation on the bubble evolution. The sampling of material we have available from ex-service components include material irradiated to 6.4—6.7 dpa (1700-1800 appm helium) and 16.9-23.6 dpa (5400-7700 appm helium) from non-optimized spacers, and 42.8-46.4 dpa (14500-15700 appm helium) and 51.2-55.0 dpa (17300-18600 appm helium) from optimized spacers. During sectioning (outlined in Section 3.3), attempts were made to select material from a pinched region of spacer and non pinched region of spacer to obtain material irradiated at temperatures estimated to be between 120-280°C and 300-330°C respectively (temperature profile shown in Figure 6). This is believed to have been achieved for all material with the exception of the 42.8-46.4 dpa condition, where only material irradiated at 300-330°C could be verified. In all cases, it is important to note that it cannot be 100% confirmed that the material examined was located at a pinched region of the spacer, and may represent either non-pinched material or a transition between the pinched and non-pinched regimes. It should also be noted that the temperature estimates have not been experimentally validated. The temperature calculations shown in Figure 6 and Figure 7 show the expected temperature variability. As previously noted, the spacers roll during service, and the temperature at the pinched

location is expected to vary during irradiation. For the purposes of this examination, we can treat the material as hot (non-pinched) and cold (pinched). Looking at subtle differences between samples would be futile with the amount of experimental uncertainty surrounding working with limited ex-service material. In addition, because the specific location at the pinched region is unknown, the temperature range is large at 120-280°C.

Figure 39(a&b) shows material irradiated to 6.4-6.7 dpa (1700-1800 appm helium) imaged in the overfocus (+500 nm) condition. Although the TEM foils are too thick to enable quantitative analysis of bubble density, a bubble size distribution has been measured and is shown in Figure 39(c), as per the procedure outlined in Section 3.4.1. Even at relatively low<sup>5</sup> doses and helium concentrations, bubbles between 1-3 nm are apparent in both the 120-280°C material and 300-330°C material.

---

<sup>5</sup> Relatively low for CANDU conditions, but extremely high for other reactor design materials in PWR X-750.

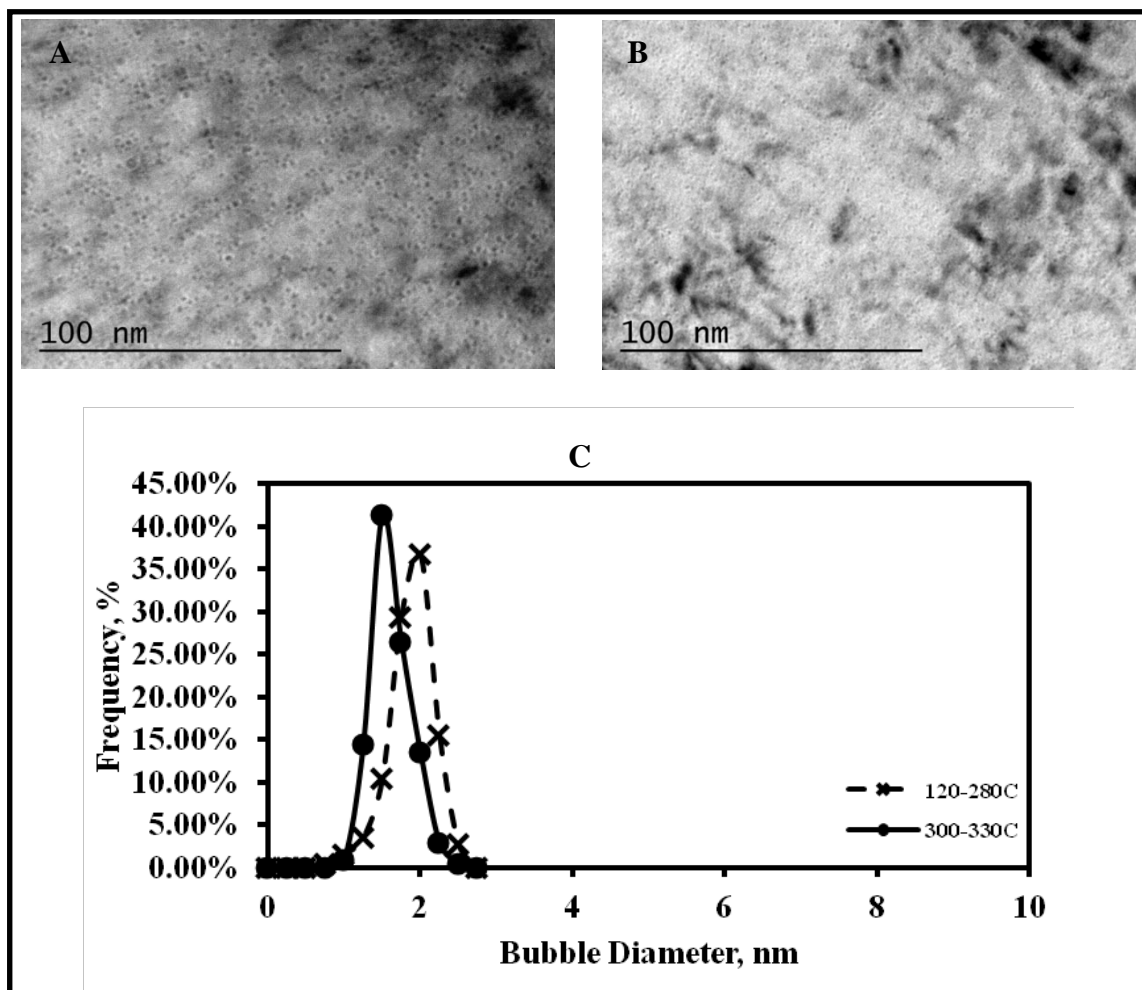


**Figure 39: Bright-field TEM (imaged in overfocus +500 nm) analysis of non-optimized spacer material irradiated to 6.4-6.7 dpa and 1700-1800 appm helium at (A) 120-280°C, (B) 300-330°C, and (C) quantitative analysis of bubble size distribution.**

Figure 40(a&b) shows material irradiated to 16.9-23.6 dpa (5400-7700 appm helium) imaged in the overfocus (+500 nm) condition. At this dose and helium concentration, a temperature dependence on the bubble growth is qualitatively apparent. The higher temperature material has larger bubbles compared to the lower temperature material. This is further verified quantitatively as shown in Figure 40(c).

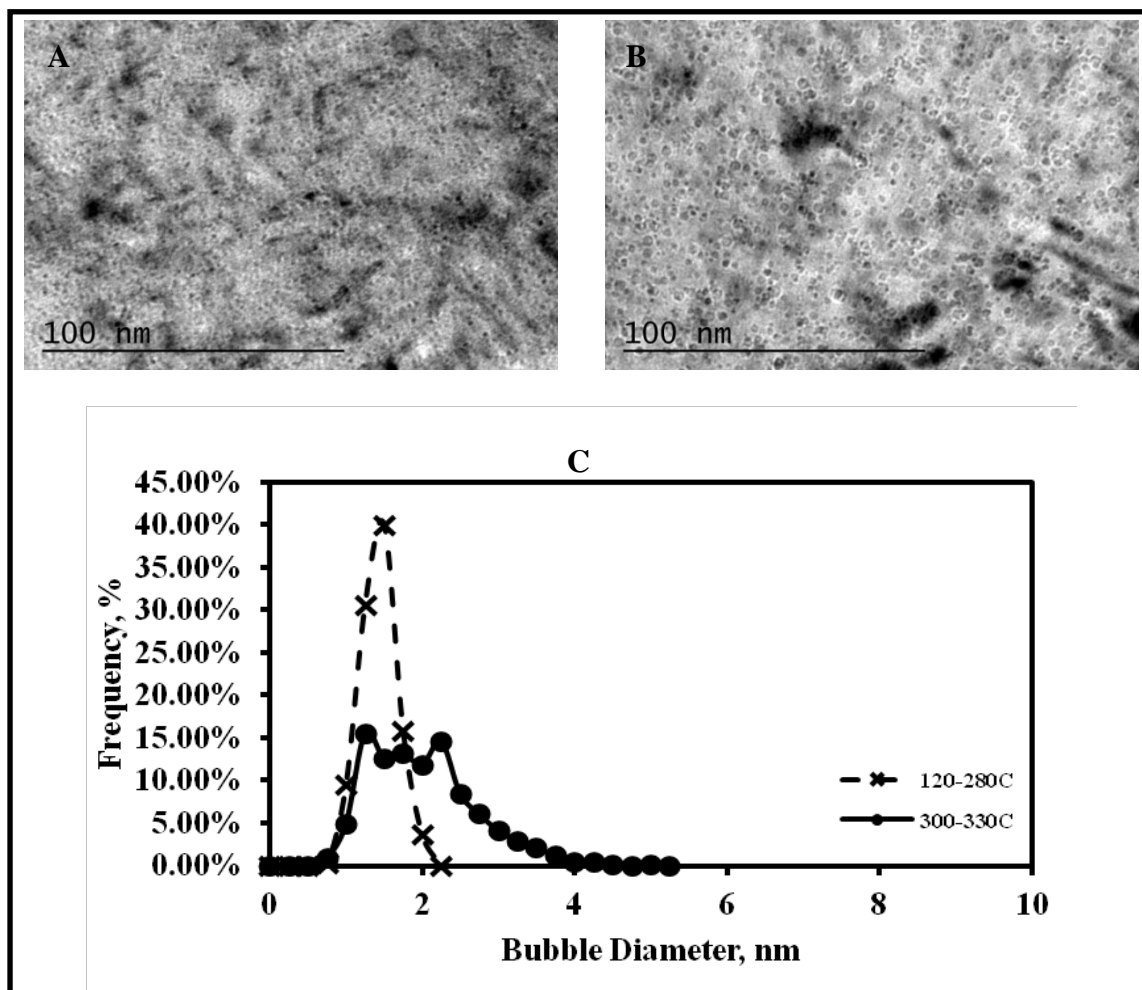


**Figure 40: Bright-field TEM (imaged in overfocus +500 nm) analysis of non-optimized spacer material irradiated to 16.9-23.6 dpa and 5400-7700 appm helium at (A) 120-280°C, (B) 300-330°C, and (C) quantitative analysis of bubble size distribution.**

Figure 41(a) shows material irradiated to 42.8-46.4 dpa (14500-15700 appm helium) imaged in the overfocus (+500 nm) condition. Only material irradiated at 300-330°C was available at this dose for characterization so no bubble size dependence could be observed for this condition, however, the operating conditions for this material are similar to higher dose material but was removed earlier in life. Please refer to Figure 30 and section 3.1.1

for details on the operating conditions for each set of material. The quantitative analysis for this material is shown in Figure 41(c).

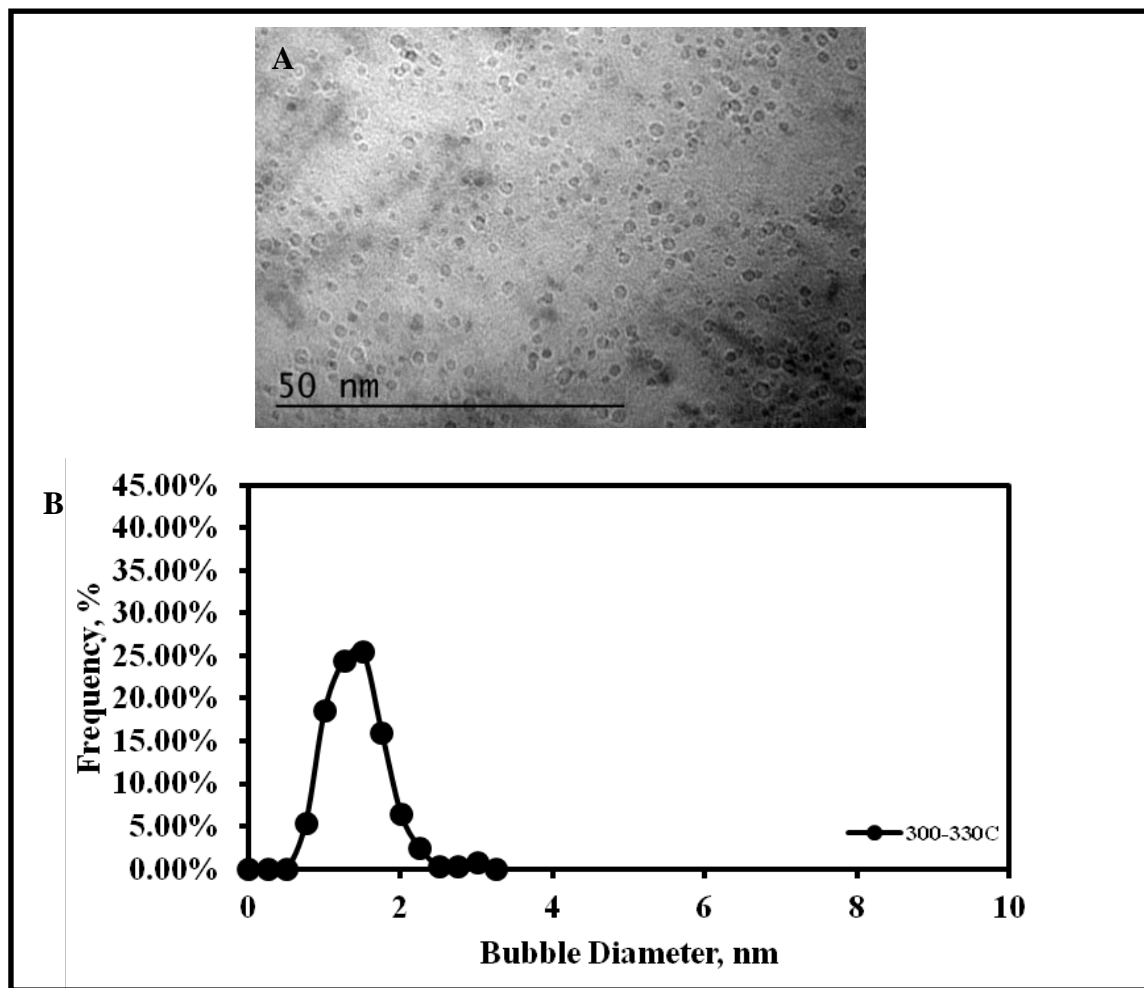


**Figure 41: Bright-field TEM (imaged in overfocus +500 nm) analysis of optimized spacer material irradiated to 42.8-46.4 dpa and 14500-15700 appm helium at (A) 300-330°C, and (B) quantitative analysis of bubble size distribution.**

Figure 42(a&b) shows material irradiated to 51.2-55.0 dpa (17300-18600 appm helium) imaged in the underfocus (-500 nm) condition. TEM specimens from each irradiation temperature were prepared thin enough to enable quantitative analysis for bubble volume and density to be determined. Similar to lower dose materials, a temperature dependence was observed at this dose level as shown quantitatively in Figure 42(c). In addition, it was determined that material irradiated at 120-280°C has a bubble density of approximately  $3.9 \times 10^{24}$  bubbles/m<sup>3</sup> and a volume of 0.9 %. Material irradiated at 300-330°C has a bubble density of approximately  $0.9 \times 10^{24}$  bubbles/m<sup>3</sup> and a volume of 1.1 %. These approximations assume that the bubbles are perfectly spherical. These numbers should be taken as lower bound approximations as they do not account for any bubble overlap which can occur, or for bubbles below the detectable limits of the TEM. It should be noted that in many cases, higher magnification images show background noise which could be interpreted as cavities, however reliable detection of these features is problematic, and thus only resolvable bubbles were included in the analysis.

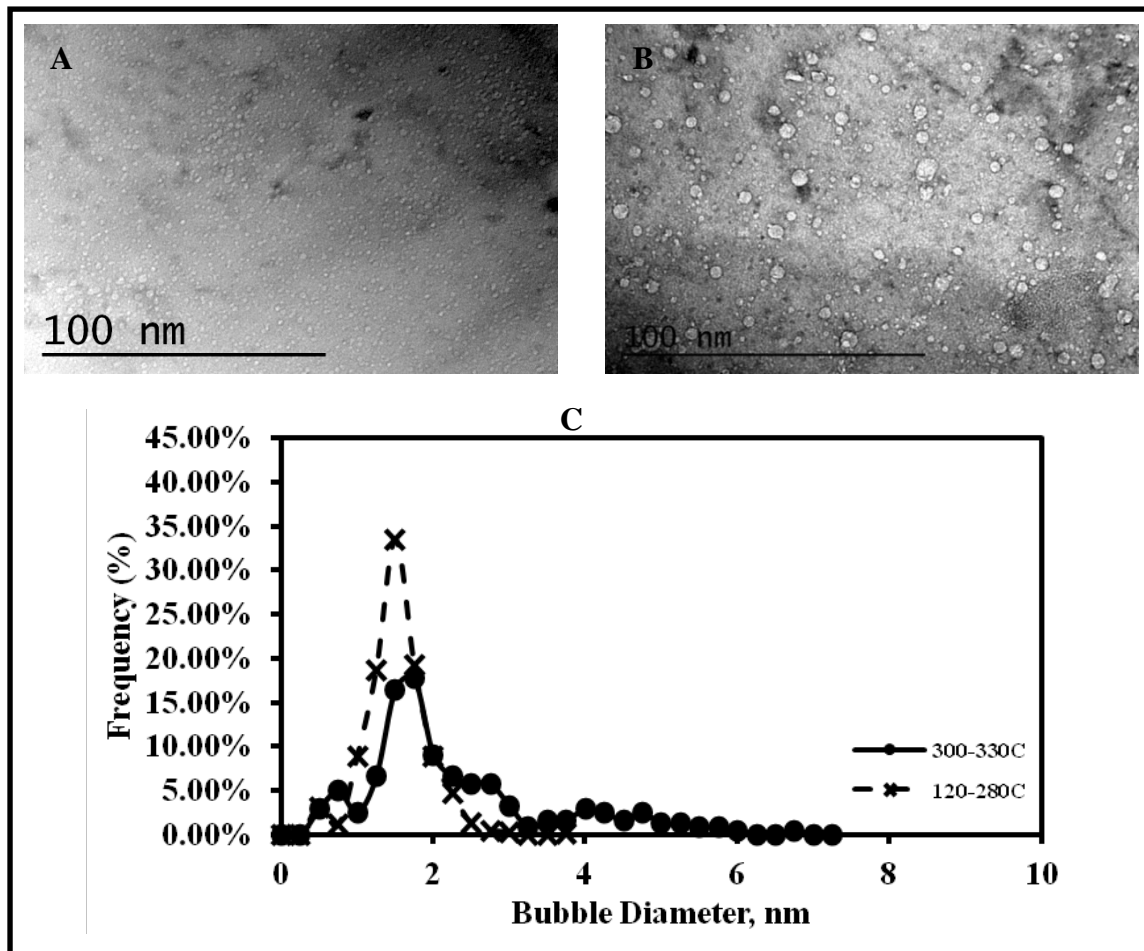


**Figure 42: Bright-field TEM (imaged in underfocus -500 nm) analysis of optimized spacer material irradiated to 51.2-55.0 dpa and 17300-18600 appm helium at (A) 120-280°C, (B) 300-330°C, and (C) quantitative analysis of bubble size distribution.**

#### 4.1.2.1.1 Helium Density Approximation Using Electron Energy Loss Spectroscopy

As outlined in Section 2.7.1.3, EELS is used to probe individual nanometer sized helium bubbles in an effort to experimentally measure the helium density from bubbles. Bubbles ranging from approximately 1-6 nm from 51.2-55.0 dpa and 17300-18600 appm helium material irradiated at 300-330°C were analyzed. Two technique approaches are used in the present study: quantification using the integrated intensity of the helium edge (and He

cross section), and the energy shift associated with the helium  $1s \rightarrow 2p$  transition. Figure 43 and Figure 44 show two examples of helium bubbles analyzed with EELS mapping. In both cases, the bubble size can be obtained directly from the HAADF images shown in Figure 43 (A) and Figure 44 (A). The EELS map shown in Figure 43 (B) and Figure 44 (B) are visual representations with the intensity in the grey scale indicative of helium density (in units of atoms/nm<sup>2</sup>). Note that during analysis of Figure 44, the bubble burst. This likely occurs in cases where the bubble exists near the surface of the lamella, or the energy of the beam causes damage to the sample sufficient to release the helium gas. In cases such as this, the pre-burst bubble is still utilized for analysis, but it cannot be 100% confirmed if the density of the bubble is representative or if it had slowly been leaking (this will impact the total density approximations). For continuity purposes, cases such as this will be highlighted throughout as red data points in following plots. The post-burst bubble gives the advantage of comparing the EELS signal generated from the helium only (i.e., relative sample thickness of pre and post-burst bubble remains the same). Figure 45 shows the EELS spectra from Figure 44 (pre-burst, burst and subtracted spectra). To quantify the helium density (in units of atoms/nm<sup>3</sup>), a binned (x5) line profile across the EELS helium maps shown in Figure 43 (B) and Figure 44 (B) gives the respective maximum He/nm<sup>2</sup>, which can then be divided by the bubble diameter giving the density in units of He/nm<sup>3</sup> (assuming all helium signal comes from within the visible bubble). A total of 42 bubbles were characterized in this study. The helium density as measured with the integrated intensity and helium cross section is shown in Figure 46. The application of this technique for smaller bubbles however leads to high error and uncertainty. For

example, a 1 nm bubble in a 20 nm thick medium does not give a comparable signal to a 5 nm bubble in a 20 nm medium. The intensity of bulk and surface Plasmons decreases the reliability of the density approximations from small bubbles using the integrated intensity and helium cross section approach [129]. For this reason, the energy shift of the  $1s \rightarrow 2p$  transition is also measured in an attempt to improve the quality of the data.

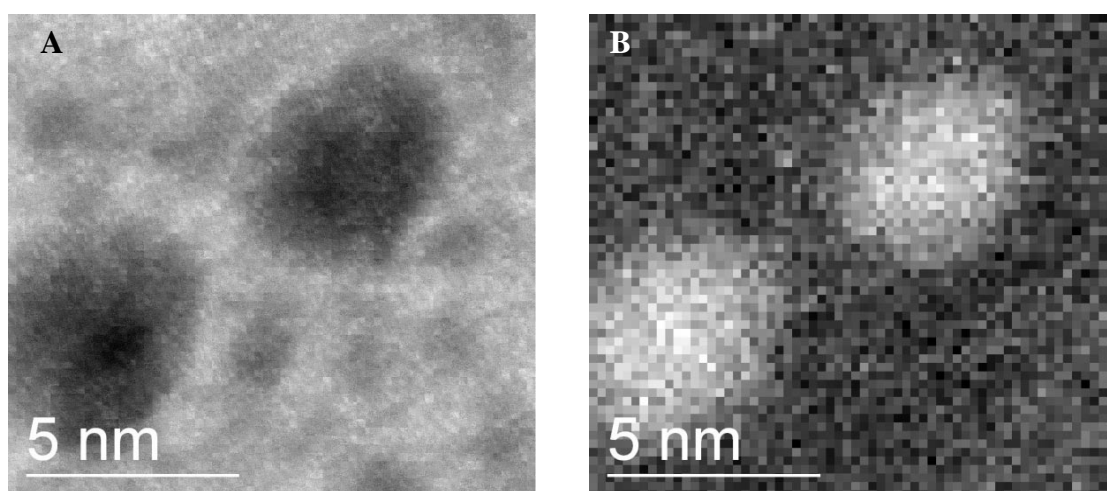


**Figure 43: Helium bubble imaged in (a) HAADF, and (b) Helium EELS map following a 2<sup>nd</sup> order log-polynomial background subtraction.**

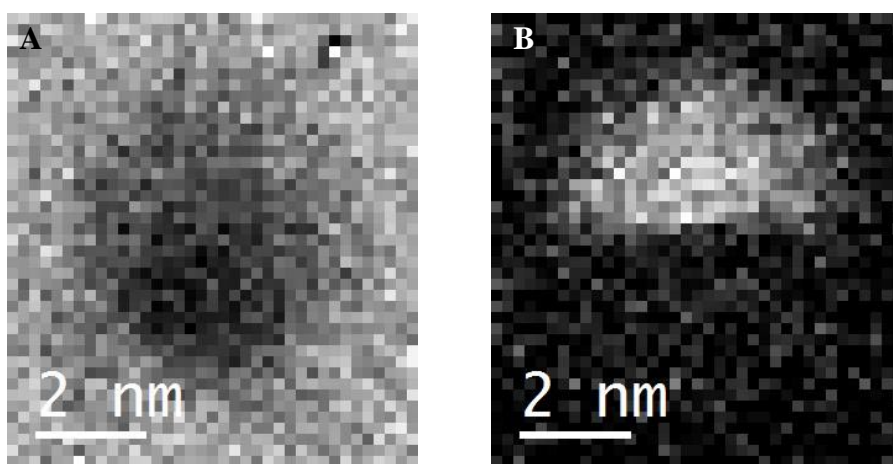


**Figure 44: Helium bubble imaged in (a) HAADF, and (b) Helium EELS map following a 2<sup>nd</sup> order log-polynomial background subtraction.**

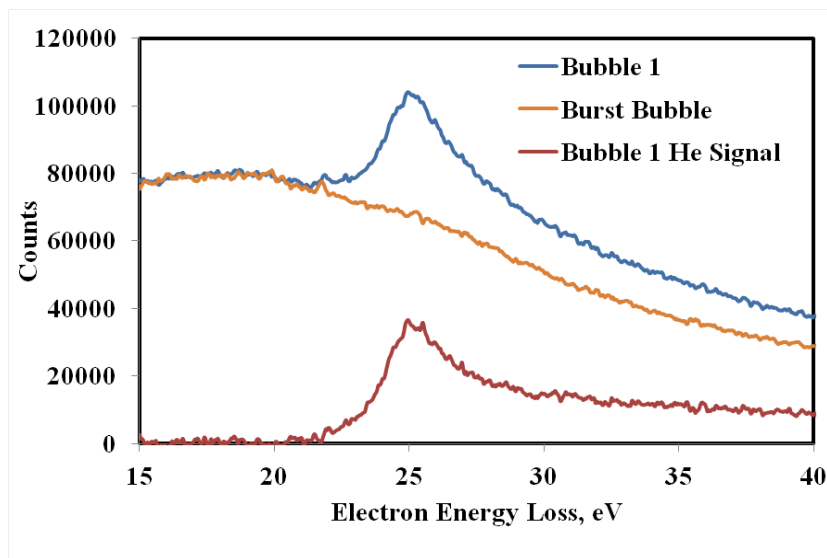


**Figure 45:** EELS spectra from the example shown in Figure 44. The signal from the pre-burst bubble, burst bubble are shown in blue and orange respectively. The red line is the Helium signal following subtraction of the two spectra respectively.

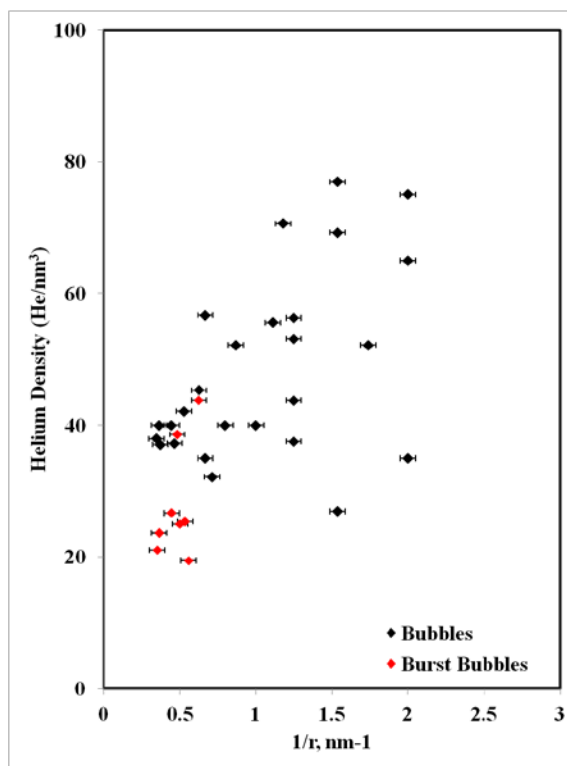


**Figure 46:** Helium density as a function of the inverse of bubble radius ( $1/r$ ).

The energy shift of the  $1s \rightarrow 2p$  transition for helium as a function of bubble size is shown in Figure 47. Each data point is smoothed with three 25 point Savitsky-Golay filters to remove signal noise in the approximation of the energy shift. The eV at the local maxima is taken as the  $1s \rightarrow 2p$  transition, and the energy the shift related to the free helium of 21.218 eV. The energy shift seems linearly related with bubble size as shown in Figure 47 (B).

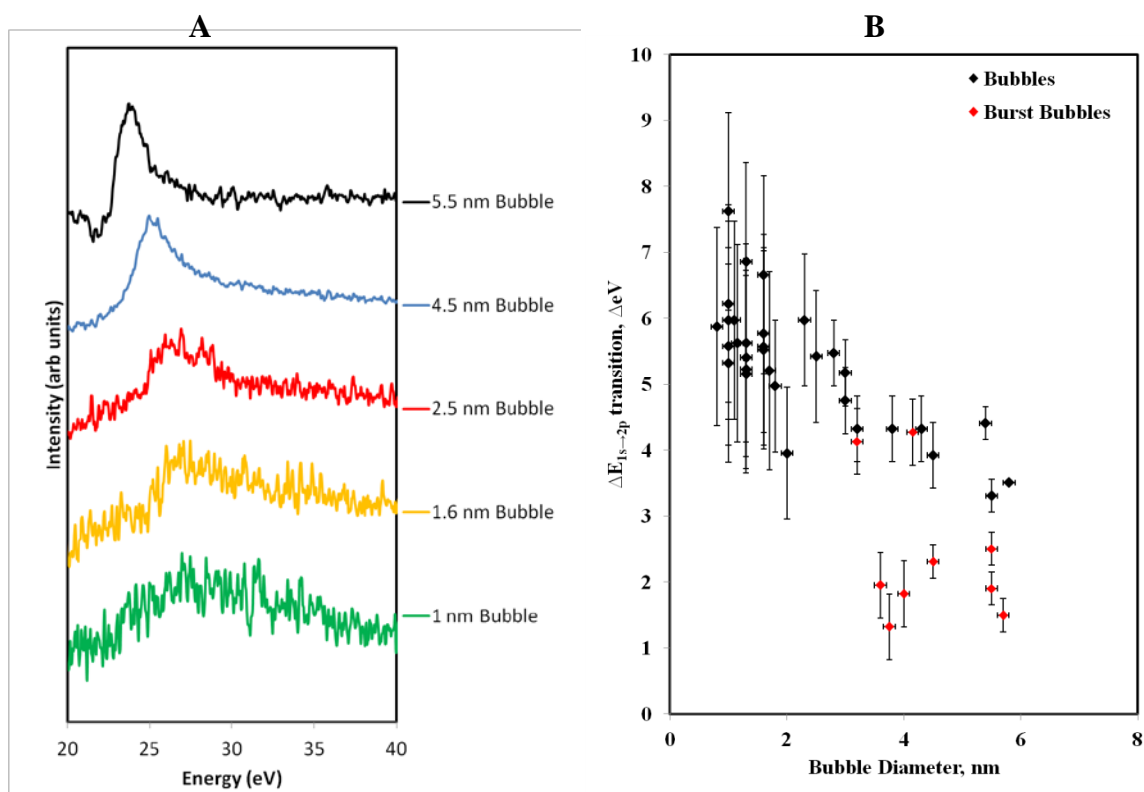


**Figure 47: (a) Extracted He  $1s \rightarrow 2p$  transition as a function of bubble diameter, and (b)  $1s \rightarrow 2p$  transition shift as a function of bubble diameter. Red data points are for bubbles which popped during STEM EELS acquisition.**

To relate the energy shift to helium density (Equation 10), the proportional constant,  $C_p$ , must be determined. This is calculated using the previous acquired data shown in Figure

46. To improve the analysis, only reliable data from bubbles greater than 3 nm are used in a regression analysis, yielding an estimate for  $C_p$  of  $0.095 \pm 0.004 \text{ eV/nm}^3$ . Equation 10 is then used with the data shown in Figure 47 (B) to calculate the helium density for all of the data. The variance of helium density as calculated using the two techniques is shown in Figure 48. The open data points highlight the data used in the regression analysis determining  $C_p$ .

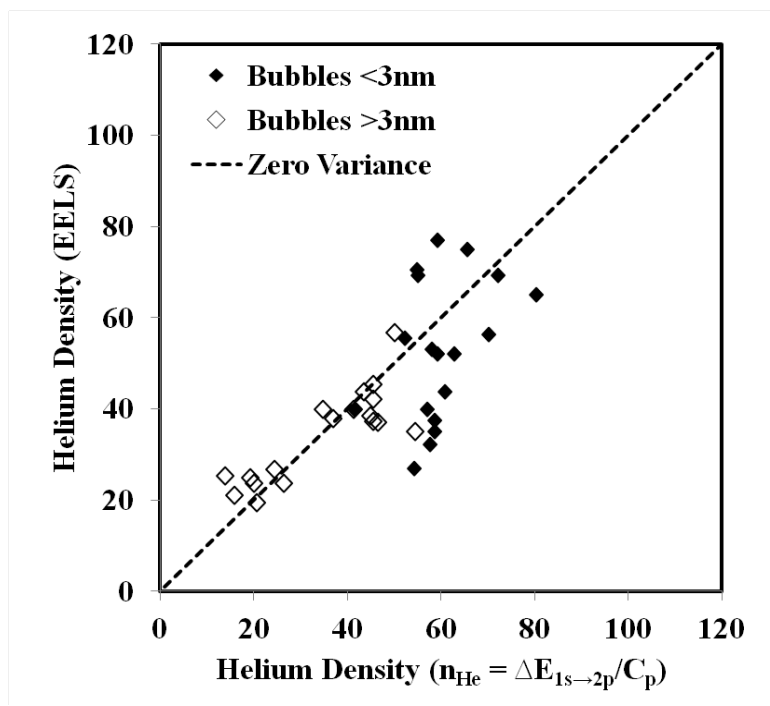


**Figure 48: Variance of helium density comparing the cross section measurement with equation (1) giving additional confidence for the use of equation (1) for more detailed analysis. Open data points were used for determination of  $C_p$ .**

The helium density as a function of inverse bubble radius is then modified, as shown in Figure 49. The data is compared between the integrated intensity method and Equation

10 in Figure 49 (A) and (B) respectively. Figure 49 (C) shows the helium density from Equation 10 with error bars (propagation of errors) included to give a more reliable representation of these approximations. As shown, using a combined approach of the integrated intensity to determine the proportional constant, and then the energy shift to calculate the helium density improves the confidence for helium density approximations from smaller bubbles and yields a better understanding of the helium density distribution for bubbles ranging from 1-6 nm. It is not the intent to present the data as a function of inverse bubble radius to lead the reader into drawing conclusions regarding a relationship with equilibrium bubble pressure (Equation 6). The data is presented like this at the direction of Dr. Roger Stoller who shared some unpublished data from Fe alloys which show similar and complementary results [42].

The helium density and helium-vacancy ratio (He/V) as a function of bubble diameter is shown in Figure 50. Regression analysis from this data is performed (assuming a linear relationship) to enable a link between the helium density approximations and the bubble size and density distributions previously reported to gain additional insight into the state of helium within the material.

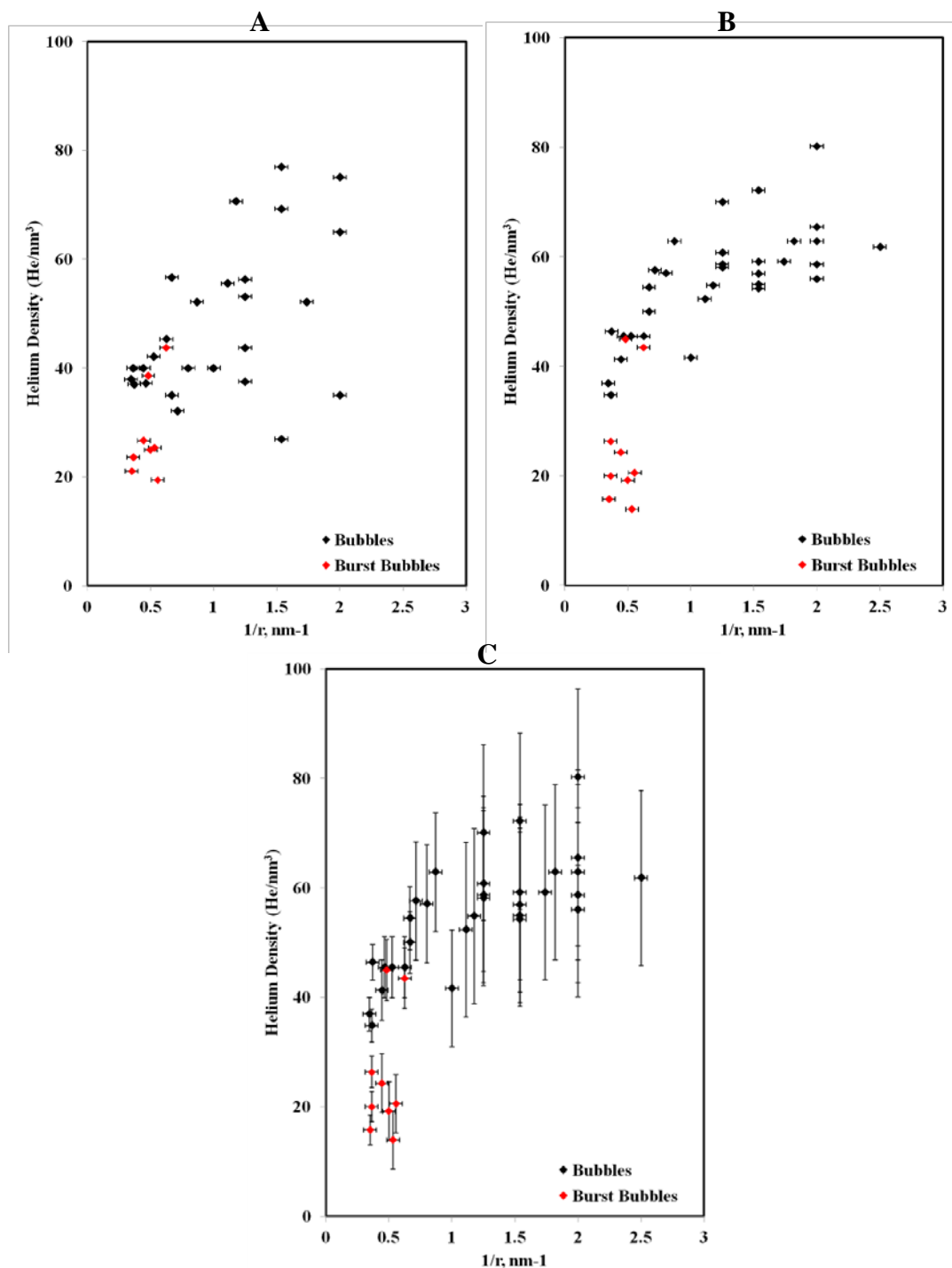


**Figure 49: Helium density as a function of inverse bubble radius. (A) Using integrated intensity and helium cross section (no error), (B) using Equation 10 (no error), and (C) using Equation 10 with propagation of error.**

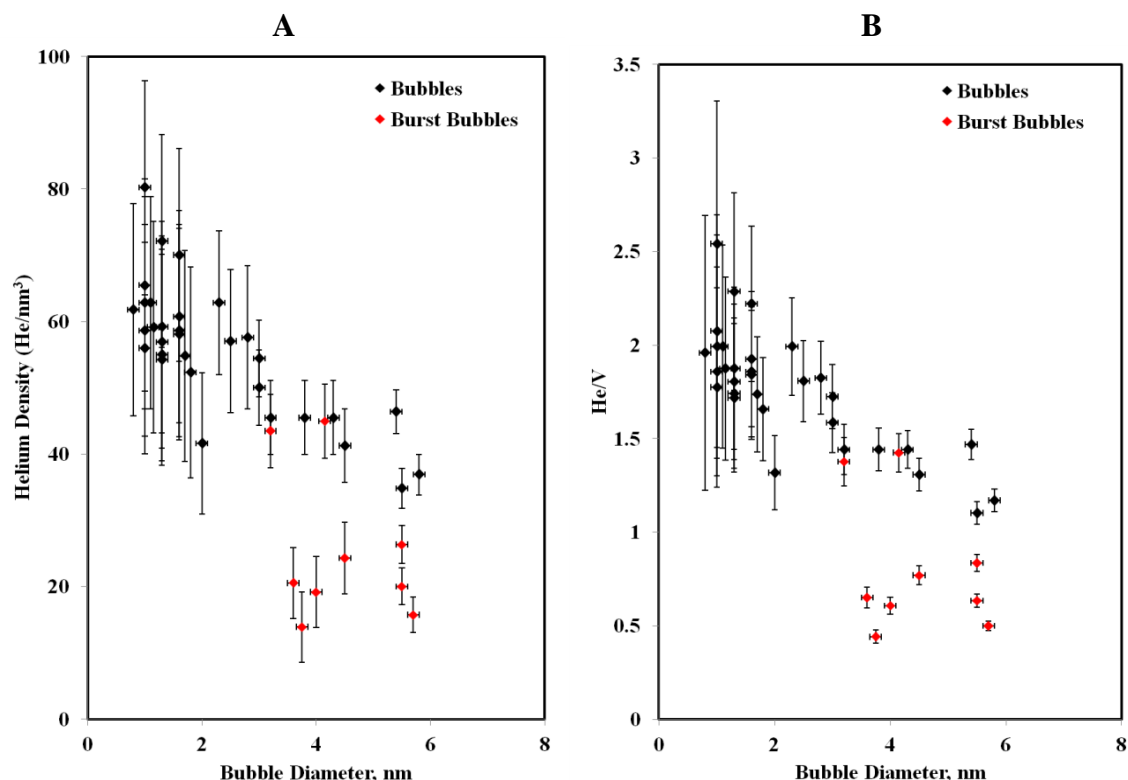


**Figure 50: (A) Helium density as a function of bubble diameter and (B) He/V as a function of bubble diameter.**

#### 4.1.2.1.2 Estimating the Bubble Pressure Using A Hard Sphere Equation of State (HSEOS)

Using the helium density shown in Figure 49 (C), the bubble pressures were calculated using the Carnahan-Starling hard sphere equation of state (HSEOS) outlined in Equation 7-Equation 9. Figure 51 shows the bubble pressures for room temperature (20°C) and estimated in-reactor temperature (~315°C) pressures. The equilibrium pressure is shown as reference following the assumption that Equation 6 is valid. As shown, all bubbles are below the equilibrium bubble pressure, and below the threshold pressure required to punch out a loop or emit a SIA according to the approximations by Trinkaus [73].

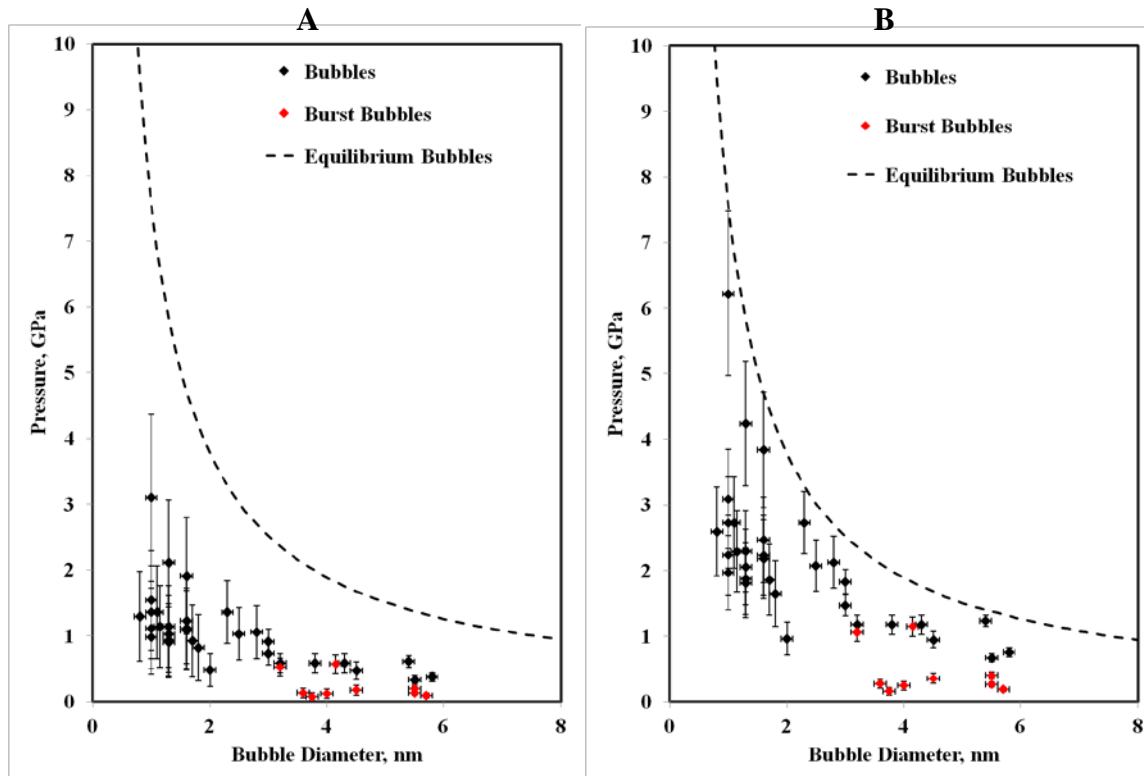


**Figure 51: Bubble pressure as calculated using the Carnahan-Starling approximation outlined in Equation 7-Equation 9 for (A) pressure at room temperature (20°C), and (B) pressure at 588 K (315°C). Equilibrium pressure shown for reference following Equation 6.**

There are three smaller bubbles which approach the equilibrium pressures. These bubbles, below 2 nm in diameter, have pressures of approximately 3.8 GPa, 4.2 GPa and 6.2 GPa respectively. The EELS signals from these bubbles are shown in Figure 52. The relative signals from the 1.6 nm and 1.3 nm bubbles are both relatively strong, but as a result of their size, their energy shift would give a more representative measure of helium density in comparison to the integrated intensity. Table 5 shows the helium density measurements from the integrated intensity approach and the energy shift for these three

high pressure bubbles. The results from the 1.3 nm bubble are consistent regardless of the experimental approach (Equation 10 or integrated intensity), and the 1.6 nm and 1 nm bubble are both underestimated with the integrated intensity approach. This is consistent with the variance analysis reported in Figure 45 where the relative relationship between the two approaches is in good agreement, but with more scatter and deviance at higher helium densities (i.e. smaller bubbles). The larger spread in the experimental data for smaller bubbles can be explained two ways: 1) there is larger experimental error in measuring the helium density in smaller bubbles compared to larger bubbles leading to greater uncertainty, and 2) assuming the variability in helium content in the small and large bubbles is constant, the impact of this variability on smaller bubbles is amplified because of the smaller net volume (i.e., a small addition of helium has a greater potential impact on the He/V ratio, and thus pressure).

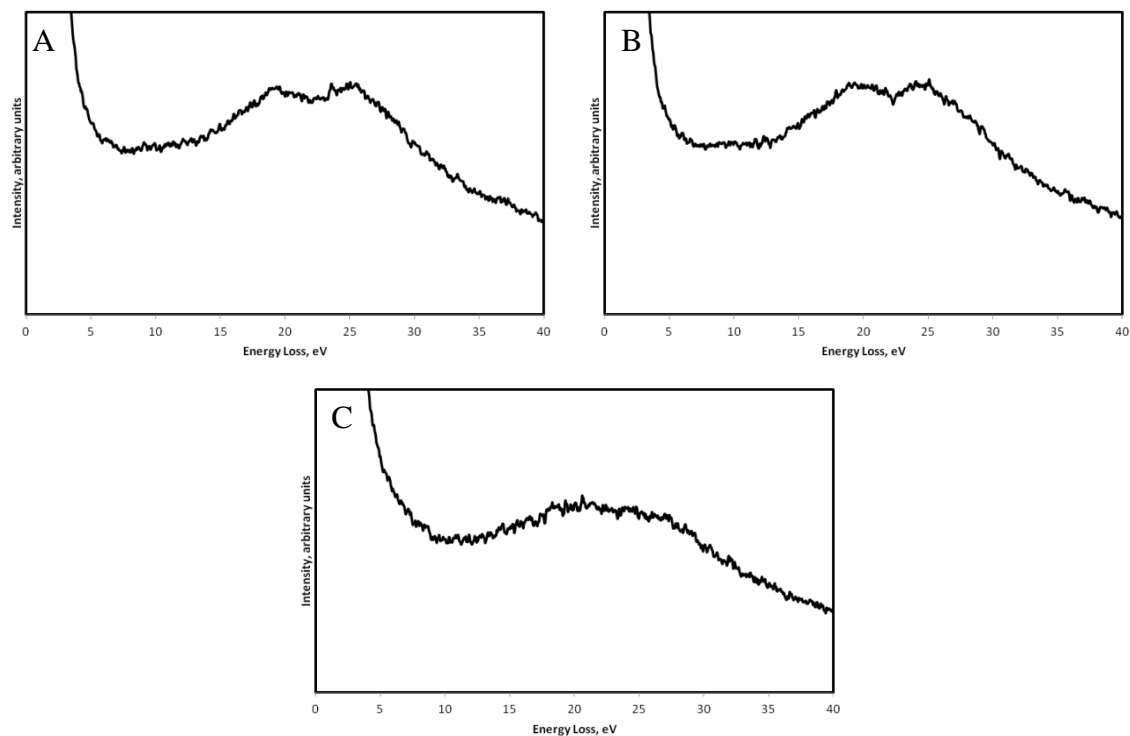


**Figure 52: EELS signal from (A) 1.6 nm diameter bubble with a calculated pressure of 3.8 GPa, (B) 1.3 nm diameter bubble with a calculated pressure of 4.2 GPa, and (C) 1 nm diameter bubble with a calculated pressure of 6.2 GPa.**

**Table 5: Summary of results for high pressure bubbles.**

Bubble Size	Calculated Pressure	Energy Shift, $\Delta E$	He Density (Equation 10)	He Density (Integrated Intensity)
1.6 nm	3.8 GPa	7.6 eV	70 He/nm <sup>3</sup>	56 He/nm <sup>3</sup>
1.3 nm	4.2 GPa	6.9 eV	72 He/nm <sup>3</sup>	69 He/nm <sup>3</sup>
1.0 nm	6.2 GPa	6.7 eV	80 He/nm <sup>3</sup>	65 He/nm <sup>3</sup>

#### **4.1.2.1.3 Linking Quantitative Bubble Size and Density Distribution with Helium Density Approximations**

Using the helium bubble size and density distribution shown in Figure 42 (C), and the linear regression analysis for helium density and He/V ratios from Figure 50, the two analysis can be used together to extract meaningful information regarding the state of helium in the bulk material. The calculated helium concentration for the bulk material as shown in Figure 29 and Table 3 can be used, however, helium density measurements were performed directly on bulk material performed by Pacific Northwest Laboratories (unpublished reports to CNL) following the methodology described in [130]. These results indicated that the helium concentration for material directly adjacent to the TEM lamella is  $16830 \pm 100$  appm Helium. This is close to the calculated helium concentration (validating the models used for calculating Helium), but measured values are more representative for detailed analysis.

There are two approaches to compare for calculating the He/V ratio, average helium density and average bubble pressure: a direct link with total helium concentration and bubble size distribution, and weighted average values using the measured helium density (EELS) and bubble size distribution.

The first approach requires the following assumptions:

- All helium in the bulk material resides within the visible bubbles.
- Helium bubbles in the matrix (i.e. homogeneous helium bubbles) are representative bubble density distributions for the bulk material.

The average He/V ratio and average helium density is calculated as 1.53 and 48.1 helium atoms/nm<sup>3</sup>. Following Equation 7-Equation 9, and using a mean bubble size of 2.3 nm, an average pressure in the bubbles is calculated at 1340 MPa.

Using the EELS data, the above assumptions are not required. Linking the EELS data and the helium bubble size and density distributions it can be shown that only 12700 ± 2100 appm helium (approximately 75 ± 12% of the bulk measurement) resides within visible matrix bubbles. The remaining helium may reside in sub-microscopic defects as others have suggested [72, 76-87], or the helium distribution is not uniform throughout the material. This is something worth further investigated. The updated He/V ratio and helium density (weighted on bubble volume) is calculated at 1.15 and 36.4 helium atoms/nm<sup>3</sup>. The average bubble pressure is calculated at 730 MPa. This provides a more representative view for the state of helium bubbles residing within the matrix of the material compared to the average approach.

A comparative table outlining the state of helium in bubbles following the two approaches is shown in Table 6.

**Table 6: Quantitative bubble statistics for material irradiated at 300-330°C to 51.2-55.0 dpa and 16830 appm helium (as measured in the bulk material).**

	Average Approach	EELS-Direct
Bubble Density (bubbles/m <sup>3</sup> )	0.87 ± 0.04 x 10 <sup>24</sup>	0.87 ± 0.04 x 10 <sup>24</sup>
Bubble Volume (%)	1.1 ± 0.2	1.1 ± 0.2
Mean Bubble Size (nm)	2.3	2.3
He/V ratio	1.53	1.15
He Density, N <sub>He</sub> (atoms/nm <sup>3</sup> )	48.1	36.4
Pressure (MPa)	1340	730
Helium Concentration (appm)	16830 ± 100	12700 ± 2100
Helium Concentration (%)	100%	75 ± 12%

To further investigate where helium may reside in the absence of visible bubbles, further analysis is justified. The advantage of mapping large regions with EELS is that the data we seek is already available for further analysis. EELS spectra from a post burst bubble is compared to the matrix material where no visible bubble resides, Figure 53. There is a visible edge at the approximate location of the helium  $1s \rightarrow 2p$  transition in the matrix, where no visible edge is present in the post burst bubble. This suggests that the conclusions by Fenske et al. [76-83] and Van Swygenhoven et al. [84-87] were correct in that some helium may reside in sub-microscopic defects below the detection limits of the technique. It can also be postulated that the helium density is not uniform within the material; more helium residing at strong sinks such as grain boundaries, precipitate interfaces, and sub-grain features like dislocations and slip bands. This has been observed in other irradiated material with helium [24, 25, 32, 33, 90, 131]. The following Sections will investigate grain boundary helium bubbles and helium bubble distribution within local microstructural inhomogeneities in the form of precipitates and sub-grain features.

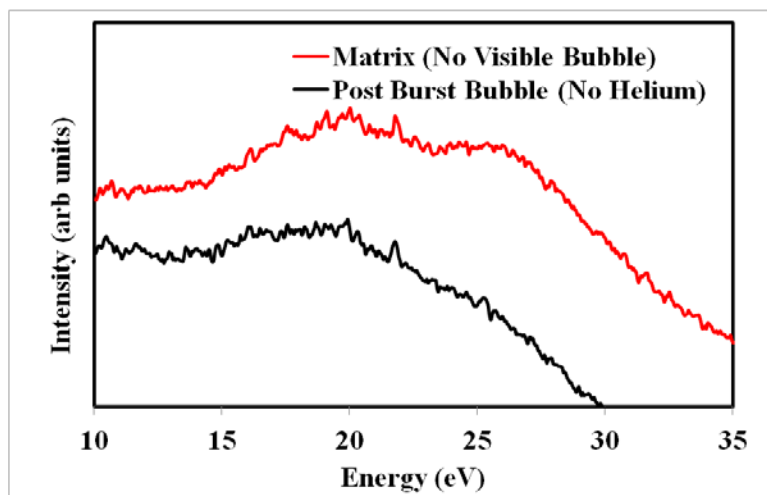


**Figure 53: EELS spectra at the energy window of the He K-edge from a popped bubble (no helium) and the matrix with no visible bubble.**

#### 4.1.2.2 Characterization of Grain Boundary Helium Bubbles

In characterizing the grain boundaries within the irradiated material, the amount of information that can be obtained is intrinsically related to the number of grain boundaries within each of the TEM lamella. In many samples, the thickness of the lamella dictates the ability to obtain quantitative data in much the same way as it did for the homogenous helium bubble characterization. Many of the TEM lamellae were too thick to enable any form of quantitative analysis. Therefore the analysis was limited to qualitative observations for many of the irradiation conditions, with the exception of the most heavily irradiated, 51.2-55.0 dpa and 17300-18600 appm helium material in which multiple characterization approaches were utilized. Imaging the grain boundaries edge-on was performed for all irradiation conditions and temperatures regardless of lamella thickness. This gives a qualitative view of the grain boundary decoration; however the

degree of bubble overlap on the grain boundary limits the overall resolution of the bubbles when imaged using Fresnel contrast in bright-field. In addition to the on-edge characterization, grain boundaries from the high dose condition were imaged in plane and with 3-D tomography which gives a more detailed view of the grain boundary helium bubbles.

Figure 54(a&b) shows material with 6.4-6.7 dpa with 1700-1800 appm helium imaged in the overfocus (+500 nm) condition for material irradiated at 120-280°C and 300-330°C respectively. Both material show a high decoration of helium bubbles on the grain boundary, however the thickness of the TEM lamella limits any quantitative analysis. Qualitatively, the bubbles on the grain boundary appear similar in size with bubbles within the matrix.

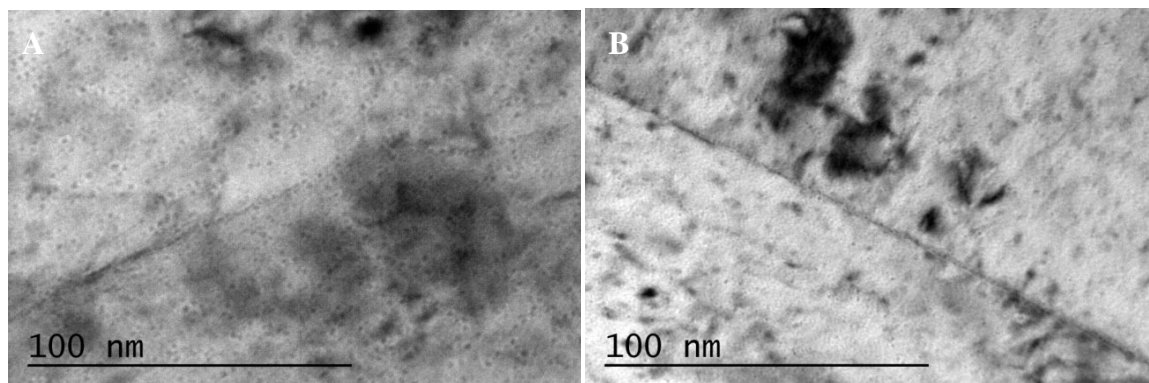


**Figure 54: Grain boundary helium bubbles imaged in the overfocus (+500 nm) condition for material irradiated to 6.4-6.7 dpa and 1700-1800 appm helium at (A) 120-280°C, (B) 300-330°C**

Figure 55(a&b) shows edge-on grain boundaries for material with 16.9-23.6 dpa and 5400-7770 appm helium imaged in the overfocus (+500 nm) condition for material

irradiated at 120-280°C and 300-330°C respectively. Both boundaries were slightly twisted, and only part of these micrographs show the grain boundary in the perfect edge-on condition. There is a slight grain boundary bubble depletion zone for the material irradiated at 300-330°C which is not observed for the lower temperature irradiated material. The depletion zone can be defined as a region adjacent to the grain boundary which has fewer bubbles compared to the matrix (note that this region is not completely free of helium bubbles and thus is not referred to it as a bubble denuded zone).

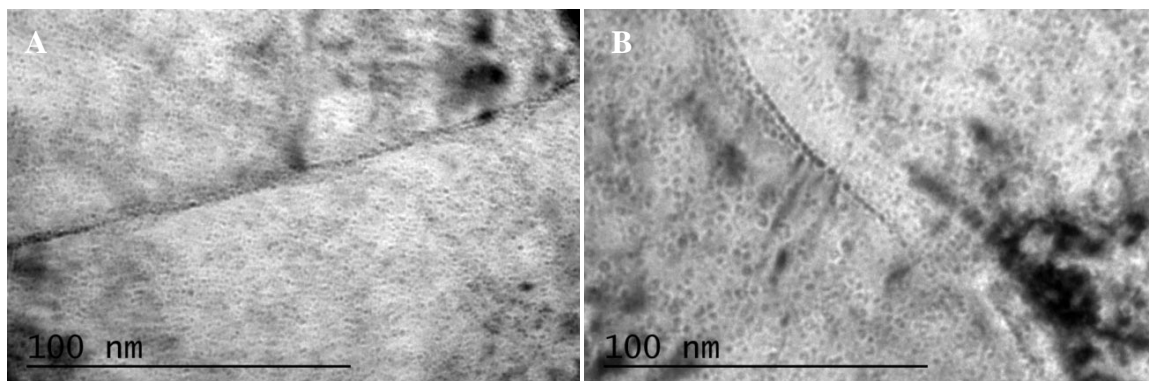


**Figure 55: Grain boundary helium bubbles imaged in the overfocus (+500 nm) condition for material irradiated to 16.9-23.6 dpa and 5400-7770 appm helium at (A) 120-280°C, (B) 300-330°C**

Material with 42.8-46.4 dpa and 14500-15700 appm helium was only available following irradiation at 300-330°C. A respective edge-on grain boundary imaged in the overfocus (+500 nm) condition is shown in Figure 56. The bubble size appears to be similar to the homogenous helium bubbles and no obvious helium bubble depletion zone is observed.

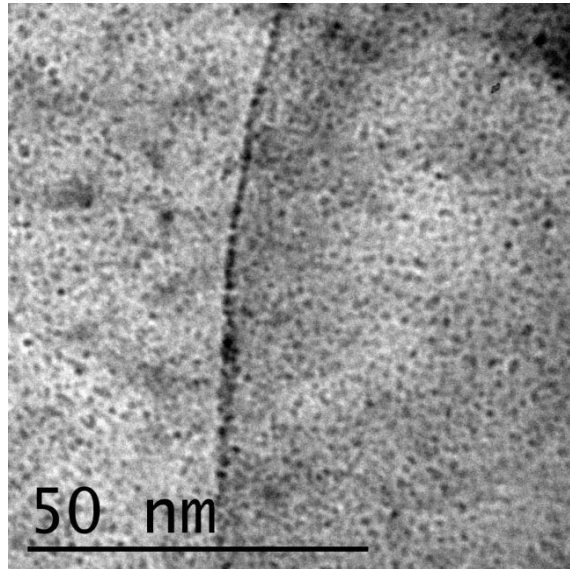


**Figure 56: Grain boundary helium bubbles imaged in the overfocus (+500 nm) condition for material irradiated to 42.8-46.4 dpa and 14500-15700 appm helium 300-330°C.**

Figure 57(a&b) shows edge-on grain boundaries for material with 51.2-55.0 dpa and 17300-18600 appm helium imaged in the overfocus (+500 nm) condition for material irradiated at 120-280°C and 300-330°C respectively. Qualitatively, it can be shown that lower irradiation temperature material shows little to no grain boundary depletion zone, whereas the elevated irradiated material shows a noticeable depletion zone, similar to the 16.9-23.6 dpa material shown in Figure 55.

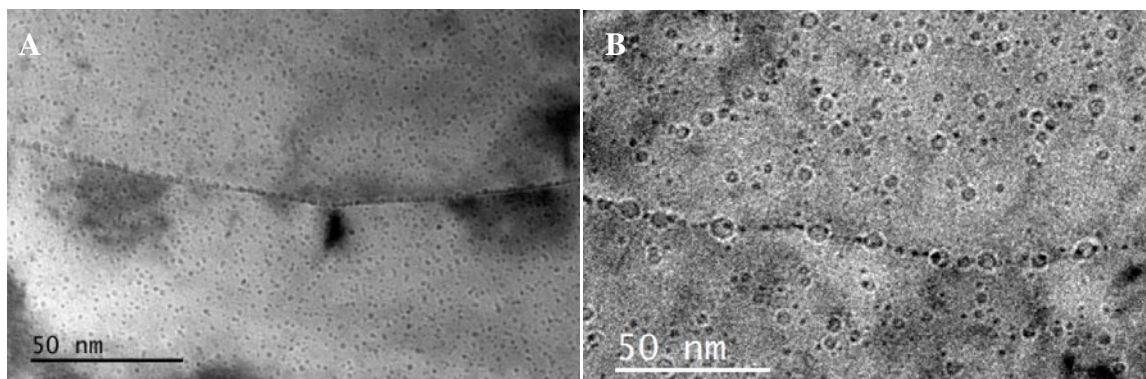


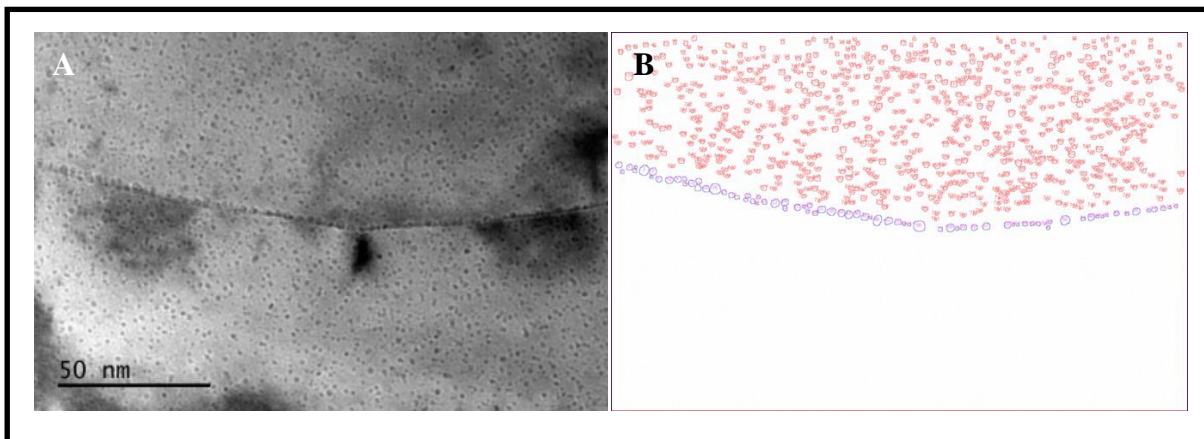
**Figure 57: Grain boundary helium bubbles imaged in the overfocus (+500 nm) condition for material irradiated to 51.2-55.0 dpa and 17300-18600 appm helium at (A) 120-280°C and (B) 300-330°C.**

The 51.2-55.00 dpa lamella included regions very thin (<20 nm thick) which enabled a more quantitative approach in characterizing the grain boundaries. Figure 58 shows the same grain boundary as Figure 57(a). The matrix bubbles and grain boundary bubbles were individually analyzed. The analysis gives bubble diameter and (x, y) coordinates of each bubble for more detailed analysis. As the boundary is imaged edge-on, and (x, y) coordinates are known for both matrix and grain boundary bubbles, we can calculate the minimum distance between matrix bubble centres and the respective nearest grain boundary centre. This gives us a helium bubble distribution plot as shown in Figure 59 (2 nm binning). This shows the population of bubbles as a function of distance from the boundary plane. This analysis does not bias the data based on bubble size, and it should be noted that bubble closer to the boundary are noticeably smaller compared to the bulk matrix bubbles and/or grain boundary bubbles. This gives an estimate of the grain boundary bubble depletion zone of approximately 4 nm.

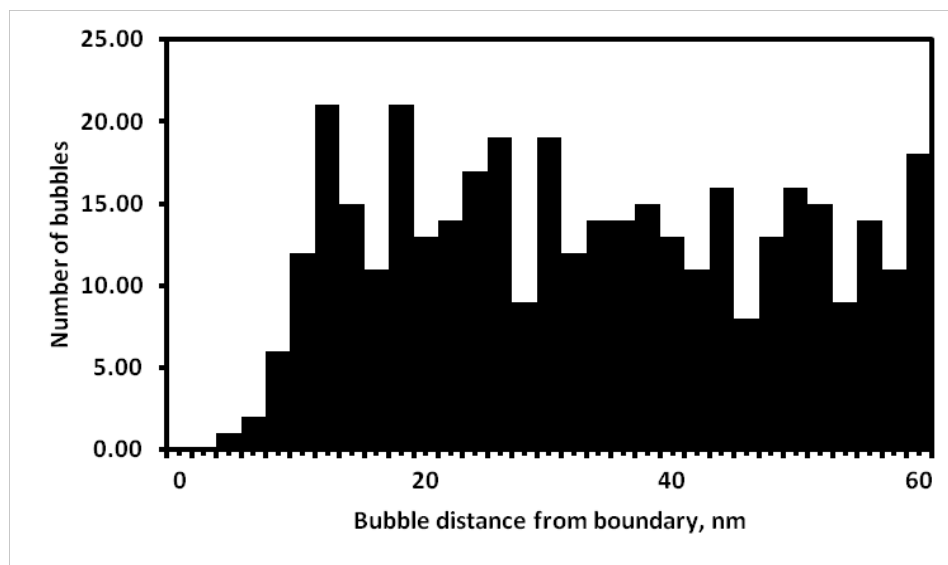
In addition to obtaining quantitative information regarding a depletion zone, we can quantify the grain boundary area loss. For the perfectly edge-on boundary we estimate the bubble coverage to be approximately 6%. It should be recognized that even though the sample was very thin (<20 nm) there may still be sufficient bubble overlap which may deflate the area coverage results. To mitigate this concern, the boundary was tilted 15° off-edge (more in-plane) as shown in Figure 60(a&b) and the grain boundary helium bubbles measured again. Special care was taken by tilting the specimen at small incremental steps and images recorded to track individual bubbles and ensure only grain boundary bubbles were included in the analysis. The grain boundary bubble size distribution is compared with the homogenous helium bubble size distributions, Figure 60(c) and it can be seen that no noticeable difference is observed. The in-plane grain boundary characterization allows for individual bubbles on the boundary to be more apparent and enables a more accurate representation of bubble coverage. The boundary coverage for the 15° tilted boundary was measured at approximately 8%. The increase in coverage is confirmation that on-edge analysis was slightly deflated by bubble overlap. The (x, y) coordinates obtained for the bubbles in this projected image also gave an average bubble spacing. The y coordinate in this case were corrected for the tilt of 15° from the projected space to true space. The bubble spacing is defined as the spacing between adjacent bubble edges, not bubble centres. An approximate bubble spacing of 3.1 nm (distribution shown in Figure 60(d)) was measured<sup>6</sup>.

---

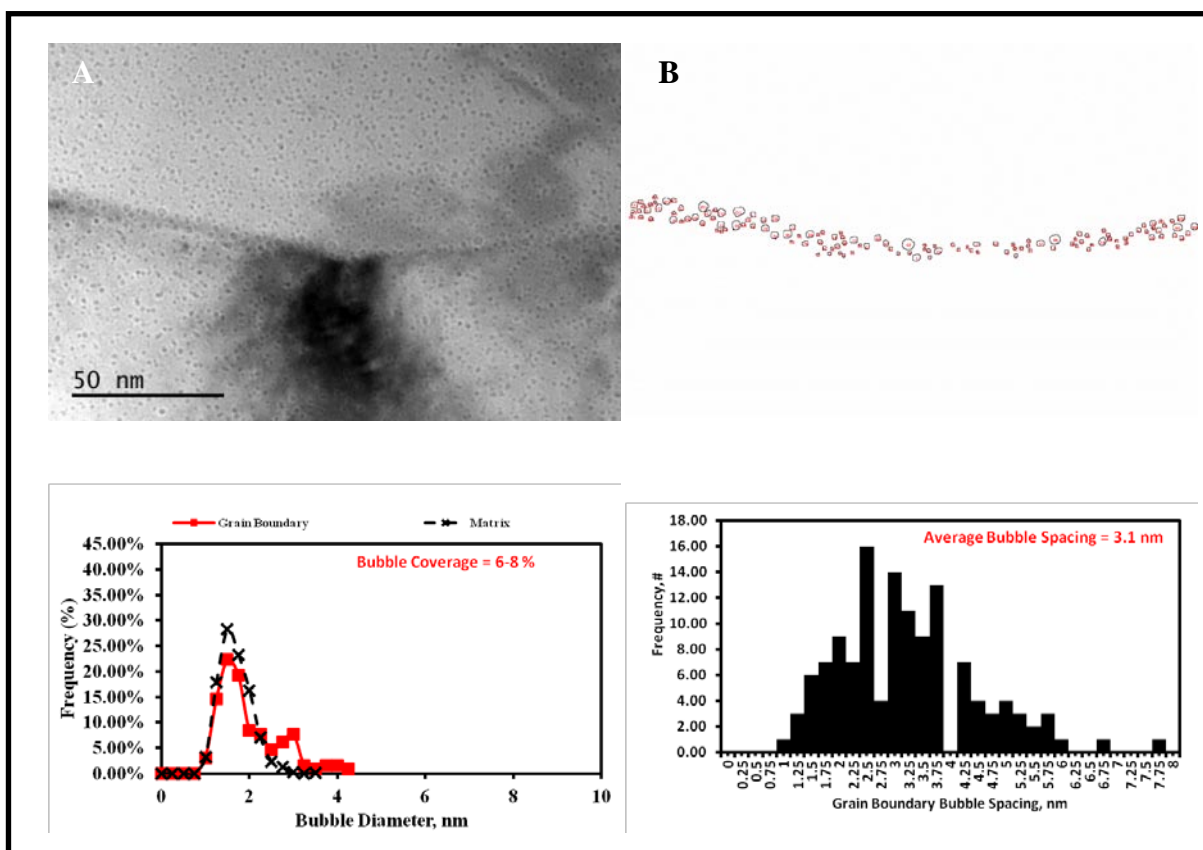
<sup>6</sup> This analysis does not include bubbles smaller than the detection limits of the TEM, and thus this spacing should be interpreted as an upper bound.



**Figure 58:** Helium bubble characterization of 51.2-55.0 dpa and 17300-18600 appm helium material irradiated at 120-280°C (A) imaged edge-on in overfocus (+500 nm) condition, (B) helium bubble analysis of the matrix (red) and grain boundary (blue) with a measured boundary area coverage measured at approximately 6%.



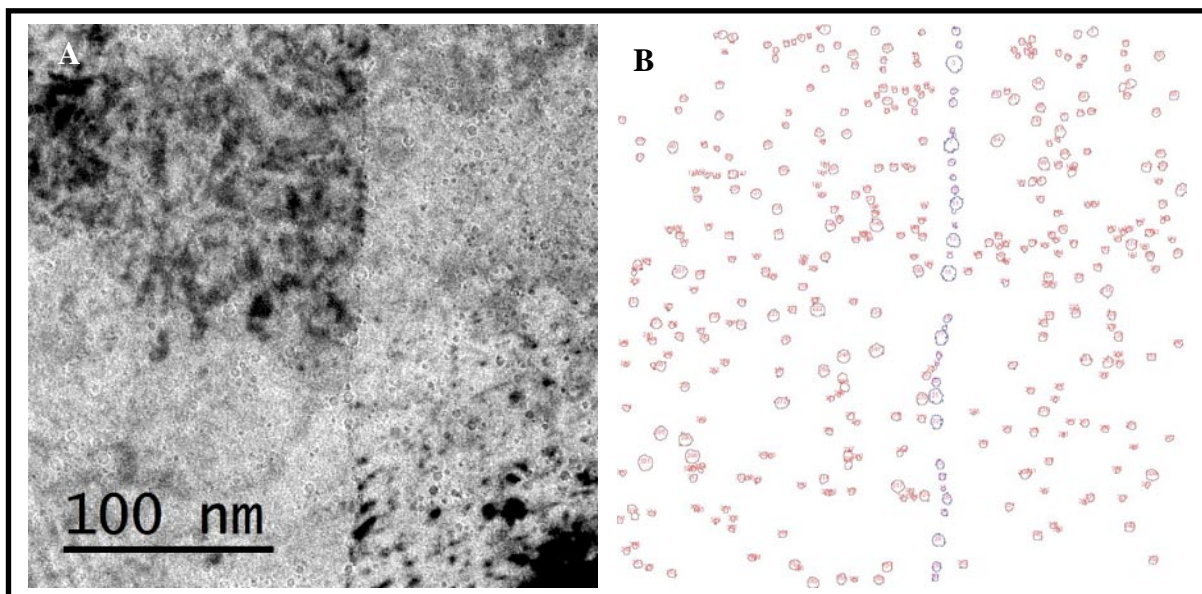
**Figure 59:** Matrix helium bubble distribution from the grain boundary shown in Figure 58.



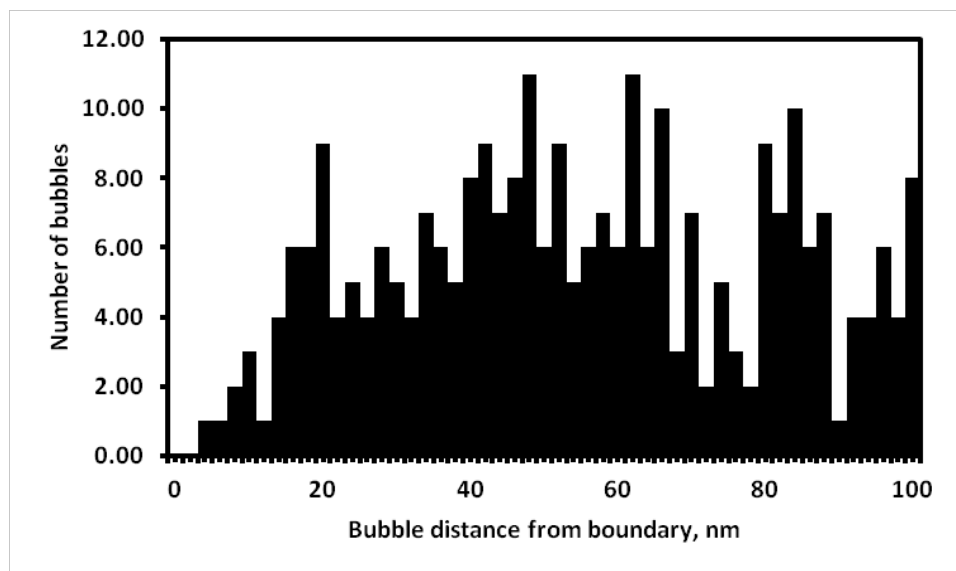
**Figure 60: Helium bubble characterization of 51.2-55.0 dpa and 17300-18600 appm helium material irradiated at 120-280°C (same area as edge-on analysis shown in Figure 58 but tilted 15° off edge) (A) imaged in overfocus (+500 nm) condition, and (B) grain boundary helium bubble analysis. Boundary area coverage measured at approximately 8% with an average bubble spacing measured at approximately 3.1 nm.**

Figure 61 shows an edge-on grain boundary from 51.2-55.0 dpa and 17300-18600 appm helium material irradiated at 300-330°C. Each matrix bubble and grain boundary were analyzed for bubble diameter and (x, y) coordinates to give an approximate grain boundary coverage and grain boundary bubble depletion zone estimation. By plotting the minimum distance of matrix bubbles to the grain boundary, as shown in Figure 62, it can be seen that there is an approximate depleted zone size of 15-20 nm. Grain boundary helium coverage was measured to be approximately 14%. Figure 63 and Figure 64 show

a similar analysis for the same irradiation condition material but slightly thicker to give more statistics and confidence to the current results. The results were consistent giving an approximate 14% grain boundary coverage and a depletion zone of approximately 20 nm.



**Figure 61: Edge-on grain boundary helium bubble analysis for 51.2-55.0 dpa and 17300-18600 appm helium material irradiated at 300-330°C. (A) TEM micrograph imaged in the overfocus (+500 nm) condition, (B) helium bubble analysis of matrix (red) and boundary (blue) with a grain boundary area coverage loss of approximately 14%.**



**Figure 62:** Matrix helium bubble distribution from the grain boundary shown in Figure 61.

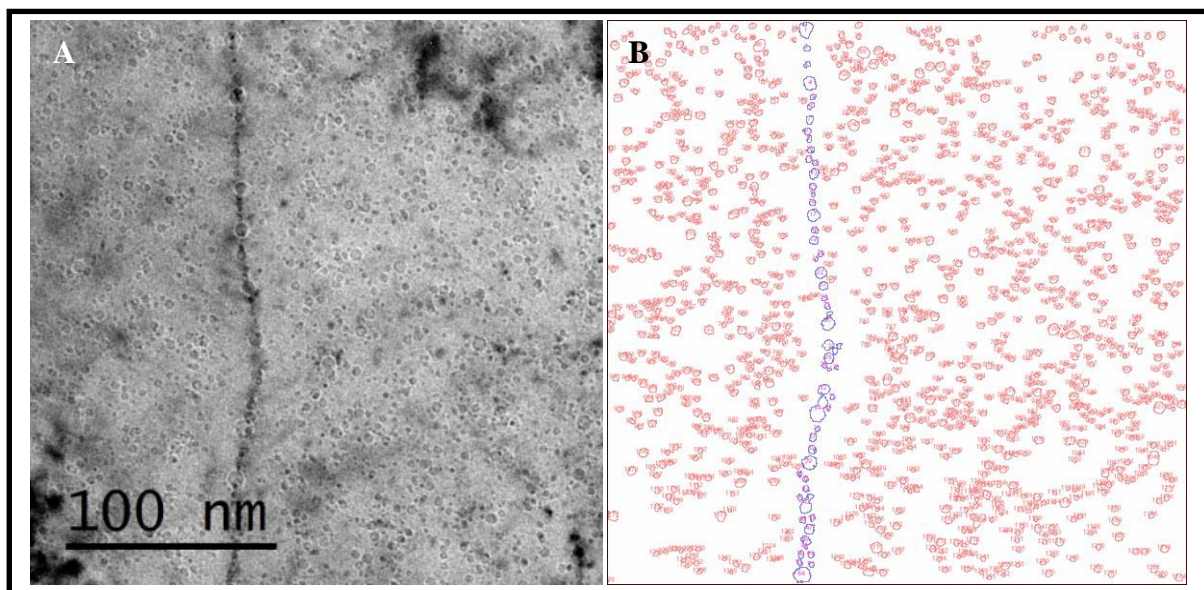


**Figure 63:** A second edge-on grain boundary helium bubble analysis for 51.2-55.0 dpa and 17300-18600 appm helium material irradiated at 300-330°C. (A) TEM micrograph imaged in the overfocus (+500 nm) condition, (B) helium bubble analysis of matrix (red) and boundary (blue) reporting a grain boundary area coverage loss of approximately 14%.

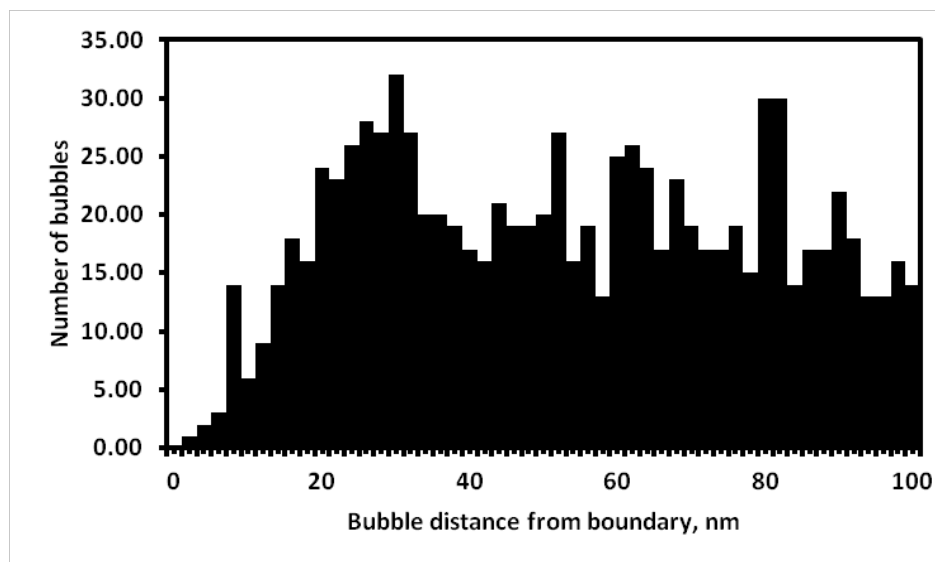


**Figure 64:** Matrix helium bubble distribution from the grain boundary shown in Figure 63.

Another approach to characterizing the grain boundaries is 3-D tomography<sup>7</sup>. Two regions were characterized with tomography (similar regions to that presented in Figure 61 and Figure 63) and are shown in Figure 65 and Figure 66. This technique allows for a 3-D representation of the bubble distributions. For the purposes of this dissertation, the tomography reconstruction is represented at five different tilt angles;  $-90^\circ$ ,  $-45^\circ$ ,  $0^\circ$ ,  $45^\circ$ , and  $90^\circ$ . Quantitatively, this dataset does not provide any data beyond that available from edge-on analysis, yielding the same 14% grain boundary coverage as documented above. The added value from the tomography approach is that the grain boundary bubbles can be analyzed in greater detail to visualize the potential overlap of smaller bubbles which may go unnoticed on the projected view of the edge-on analysis.

<sup>7</sup> Tomography is performed by imaging the same region at every  $1-2^\circ$  and reconstructing a microstructural feature of interest (i.e., bubbles) within a 3-D software.

These small bubbles however have a small impact on the area coverage measurements. Figure 67 shows an example of the spatial resolution capabilities that the 3-D tomography approach can provide. This example is the same 3-D tomography set as shown in Figure 65 (rotated 90° for presentation purposes) with the boundary bubbles highlighted. The HAADF image from the tilt series (0° tilt) is shown for comparative purposes. In the reconstruction software, tilting the boundary enables a clean view of the bubble distribution on the boundary, however, as the lamellae are so thin, the benefit of mapping in z-axis does not add significant value to the analysis. The lessons learned from this investigation are that for tomography to work on nano-sized helium bubbles, the material needs to be so thin that 3-D imaging is no longer relevant. Although it was determined that the technique did not yield any additional information in the present study, it is important to note that this investigation marks the first time irradiation induced, nano-sized helium bubbles have been analyzed using 3-D tomography. Continued improvements in this technique may allow for helium bubbles to be reconstructed from thicker regions enabling greater benefit from the 3-D tomography technique.

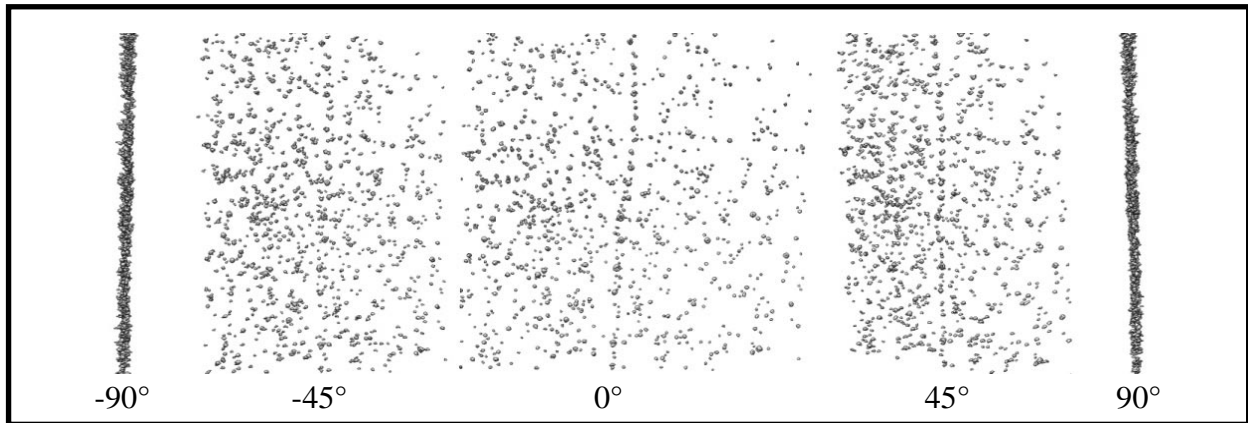


**Figure 65:** Frame images from 3-D tomography reconstruction of a grain boundary in 51.2-55.0 dpa and 17300-18600 appm helium material irradiated at 300-330°C.

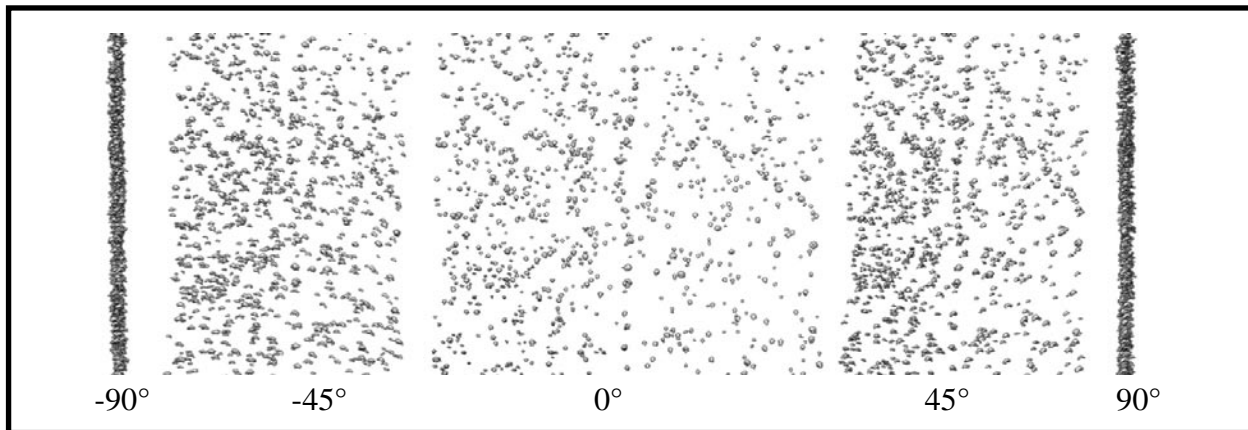


**Figure 66:** Frame images from 3-D tomography reconstruction of a second grain boundary for 51.2-55.0 dpa and 17300-18600 appm helium material irradiated at 300-330°C.

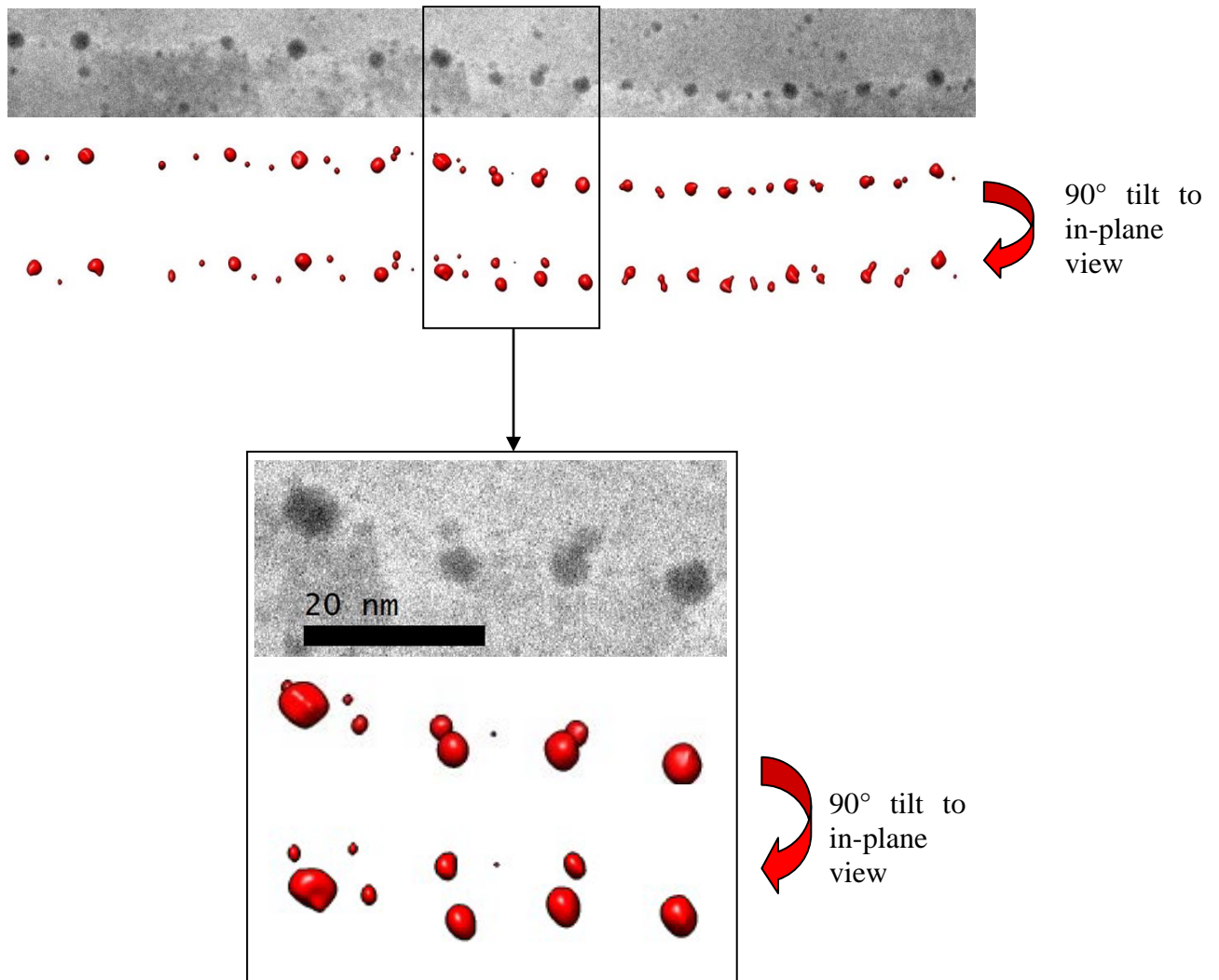


**Figure 67: Schematic representation of the 3-D tomography analysis of a grain boundary edge-on and tilted 90° to show the boundary plane giving a better representation of the bubble distribution and spacing on the boundary.**

The final approach at characterizing grain boundaries is imaging boundaries in-plane as opposed to on-edge. Imaging boundaries more in-plane is more difficult to rely on as a characterization approach, as it greatly depends on success of capturing a section of boundary relatively in-plane within the thin section of the TEM lamella. Figure 68(a) shows a boundary imaged in-plane from 51.2-55.0 dpa and 17300-18600 appm helium irradiated at 300-330°C. EELS analysis has confirmed that this region is pure matrix material (i.e., local crystal structure differences responsible for larger bubbles compared to the matrix). Quantitatively, it is difficult to isolate the boundary bubbles from matrix bubbles above or below the boundary within the foil and is more of an issue for smaller bubbles rather than the larger bubbles. Qualitatively, there is a clear bubble size difference between the matrix and the boundary. Bubbles identified as being on the boundary were measured, Figure 68(b), and give a size distribution as shown in Figure 68(c), providing an estimated bubble coverage of approximately 12%. This gives a slightly lower bubble coverage compared to the edge-on grain boundary analysis shown above. However, this is to be expected because the current analysis does not account for smaller bubbles which could not be isolated from the matrix above or below the grain boundary planes (typically bubbles < 4 nm were excluded from the analysis). As the boundary is characterized in-plane and the foil thickness is known, the spacing between each grain boundary bubble (> 4 nm) was measured, providing an average bubble spacing of approximately 3.5 nm<sup>8</sup>. The reported spacing is an average spacing of the distance from bubble edge to bubble edge of adjacent boundary bubbles. This spacing should be

---

<sup>8</sup> Spacing was measured and reported as the average spacing minimum between adjacent bubbles. The value is equivalent to the distance from bubble edge to bubble edge.

treated as an upper estimate, as the inclusion of smaller bubbles will have a *significant* impact on the analysis. It should also be noted that this approximation is from limited statistics, and that many bubbles on the boundary were classified as having 0 nm spacing between them, decreasing the average to a number which is inconsistent with the bubble size distribution and approximate coverage. Figure 69 shows a comparison of the matrix bubble size distribution (previously reported in Figure 42(c)) compared with the grain boundary bubble size distribution (Figure 69 (a)), and the grain boundary bubble spacing distribution (Figure 69 (b)).

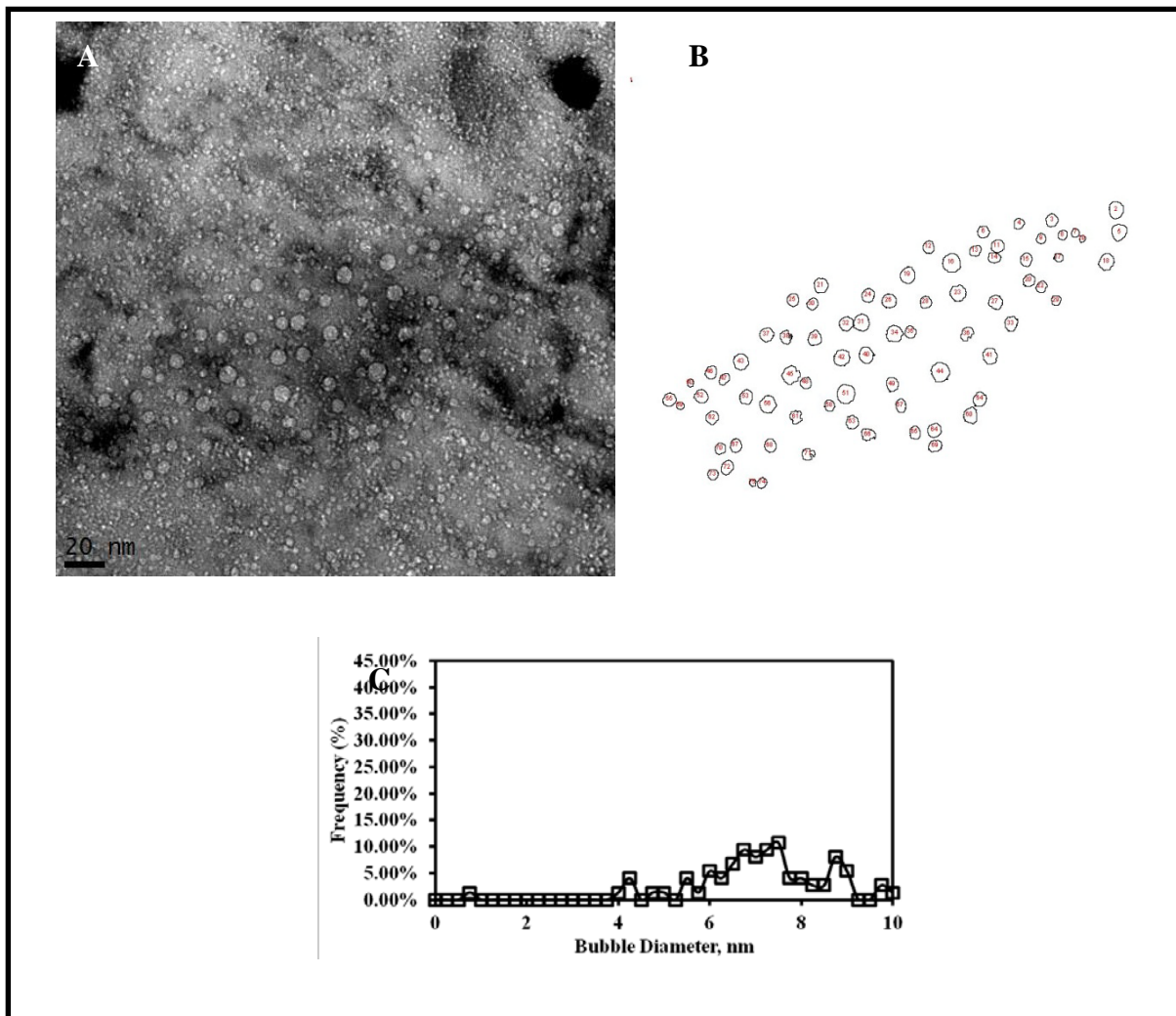


**Figure 68: In-plane grain boundary analysis boundary for 51.2-55.0 dpa and 17300-18600 appm helium material irradiated at 300-330°C. (A) TEM micrograph underfocus (-500 nm) condition (B) helium bubble analysis assuming only larger bubbles on boundary (i.e., neglecting smaller bubbles which may be in matrix either above or below boundary through thickness), and (C) helium bubble distribution on in-plane grain boundary. Grain boundary area coverage loss estimated at ~12% and average spacing of 3.5 nm.**

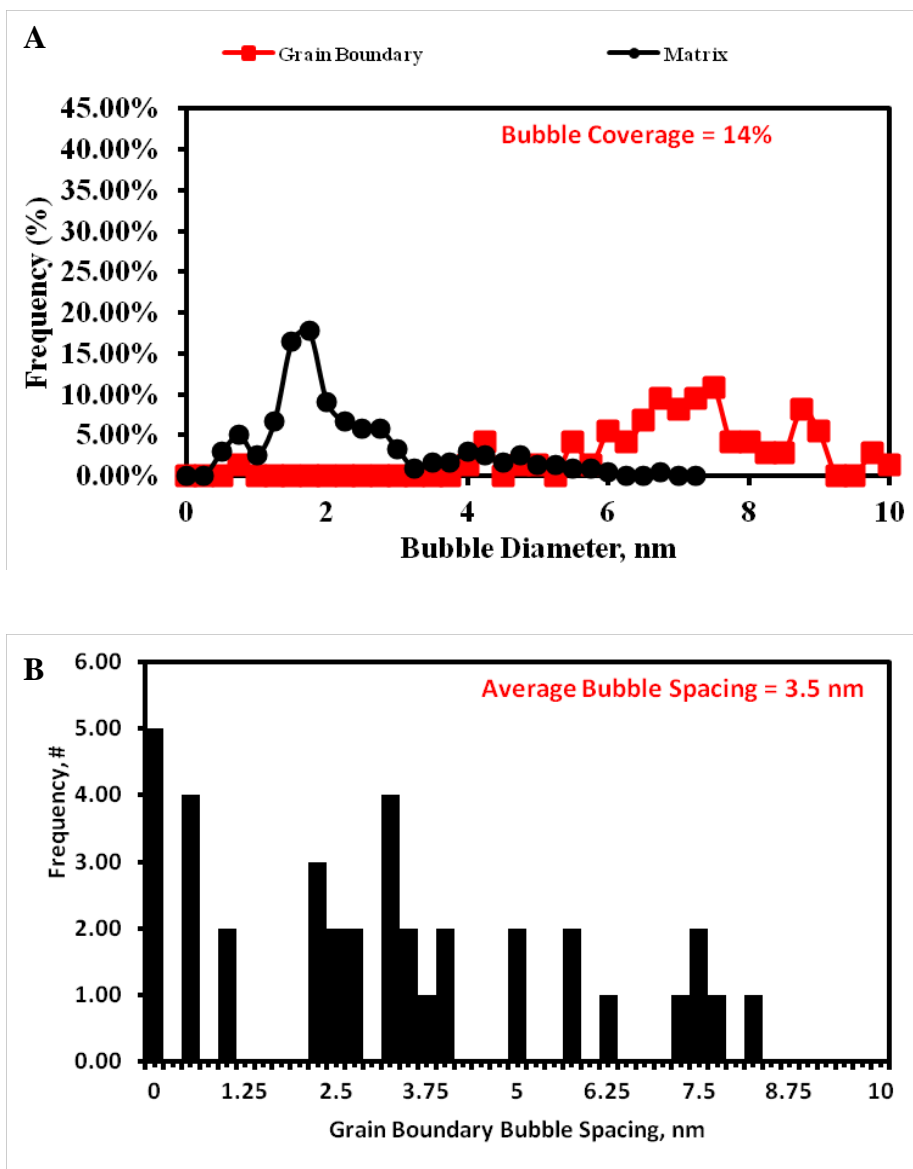


**Figure 69:** Analysis of grain boundary analysis from Figure 68. (A) Helium bubble size distribution comparison between in-plane boundary presented in Figure 68 and matrix presented in Figure 42(c), and (B) the bubble spacing distribution on the grain boundary presented in Figure 68.

#### 4.1.2.3 Characterization of Helium Bubbles in Grain Boundary Precipitates

Grain boundary degradation appears to be leading to reduced strength and ductility of ex-service Inconel X-750 spacers, it is important to understand the interplay of helium bubbles with grain boundary precipitates. The fractography shown in Section 4.1.1 shows micro-dimples of a consistent size with these grain boundary carbides. Inconel X-750 grain boundaries are very heavily decorated with grain boundary precipitates; primarily  $\text{Cr}_{23}\text{C}_6$  carbides, but also a few MC carbides (typically Ti or Nb carbides), and sparse eta phase  $\text{Ni}_3\text{Ti}$  precipitates [7, 111, 132].

$\text{Cr}_{23}\text{C}_6$  carbides are the most abundant grain boundary precipitates found within Inconel X-750 spacers. In material irradiated at 120-280°C, the bubble size and distribution found within the  $\text{Cr}_{23}\text{C}_6$  carbides is indistinguishable compared to the homogeneous helium bubbles found in the matrix. However, material irradiated at 300-330°C shows a helium bubble size and density difference within the precipitates as compared to the homogeneous helium bubbles. Figure 70(a) and Figure 71 (a) show two  $\text{Cr}_{23}\text{C}_6$  grain boundary precipitates imaged in the overfocus (+500 nm) condition from material with 51.2-55.0 dpa and 17300-18600 appm helium. Analysis gives a distribution with a maximum size as shown in Figure 70(b) and Figure 71(b). This distribution can be compared for reference to the matrix and nominal grain boundary distributions presented in Figure 69. EELS mapping is also provided for these precipitates, Figure 70(c) and Figure 71(c). This gives confidence that the bubbles included for analysis are only from within the precipitate and not from matrix material above or below the precipitate. This is evident from the lack of Ni at the precipitate location.

There are not many Ni<sub>3</sub>Ti eta phase precipitates found within the material. In this investigation, only one such precipitate was located for detailed analysis and it was found in material with approximately 51.2-55.0 dpa and 17300-18600 appm helium irradiated at 120-280°C, Figure 72(a). The unique aspect of this precipitate is that the bubble size is noticeably larger within the precipitate compared to the matrix material, Figure 72(b). The EELS mapping of the precipitate is shown in Figure 72(c). Similar to previous precipitates analyzed, this gives us some confidence that the bubbles included in the analysis are only from the precipitate and not from the matrix material above or below the precipitate. In this instance this is evident by the lack of Cr signal coming from the precipitate.

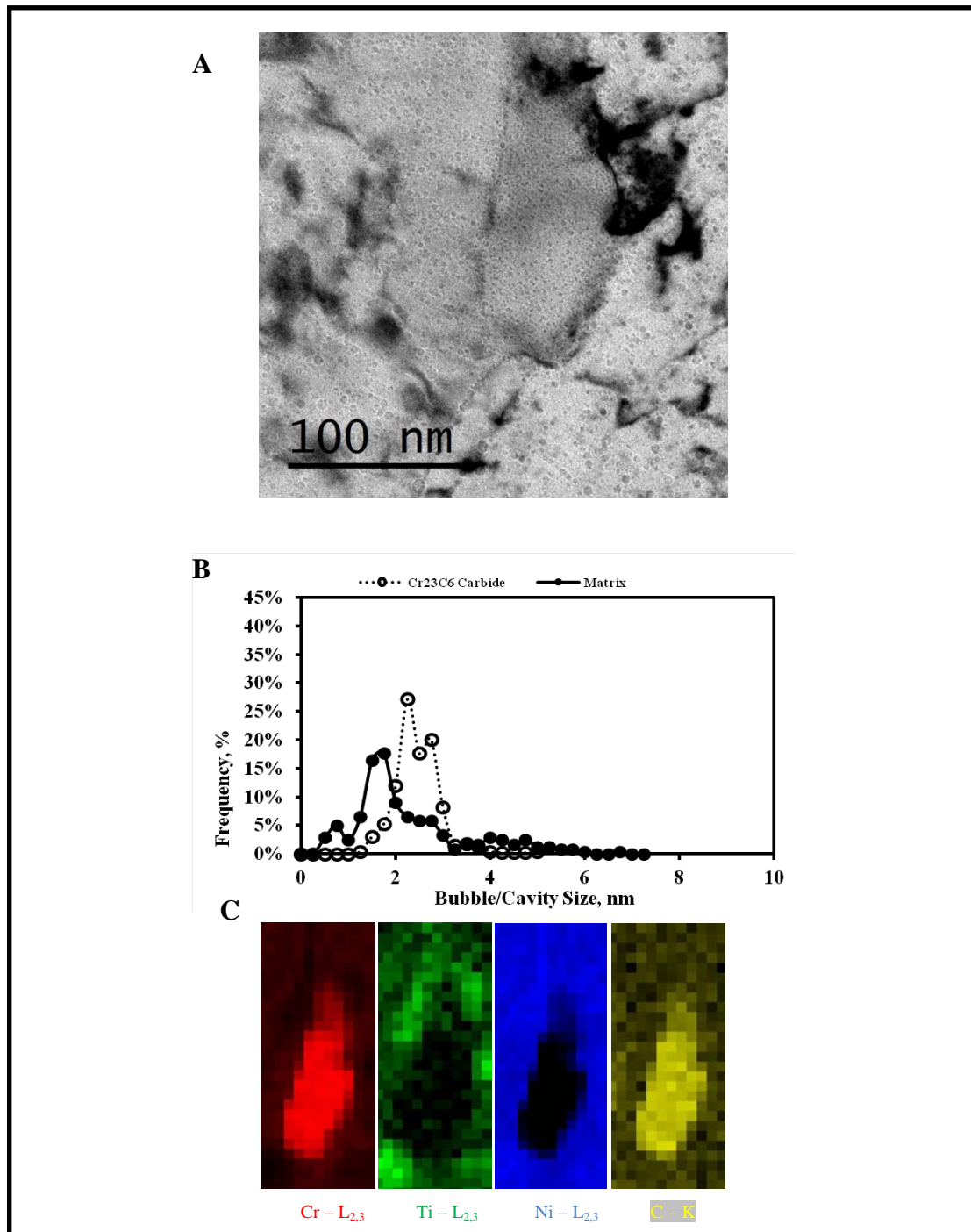


**Figure 70: Helium bubble size distribution within a grain boundary chromium carbide in material irradiated to approximately 51.2-55.0 dpa with 17300-18600 appm helium at 300-330°C. (A) TEM micrograph imaged in the overfocus condition (+ 500 nm), (B) bubble size distribution, and (C) EELS mapping.**

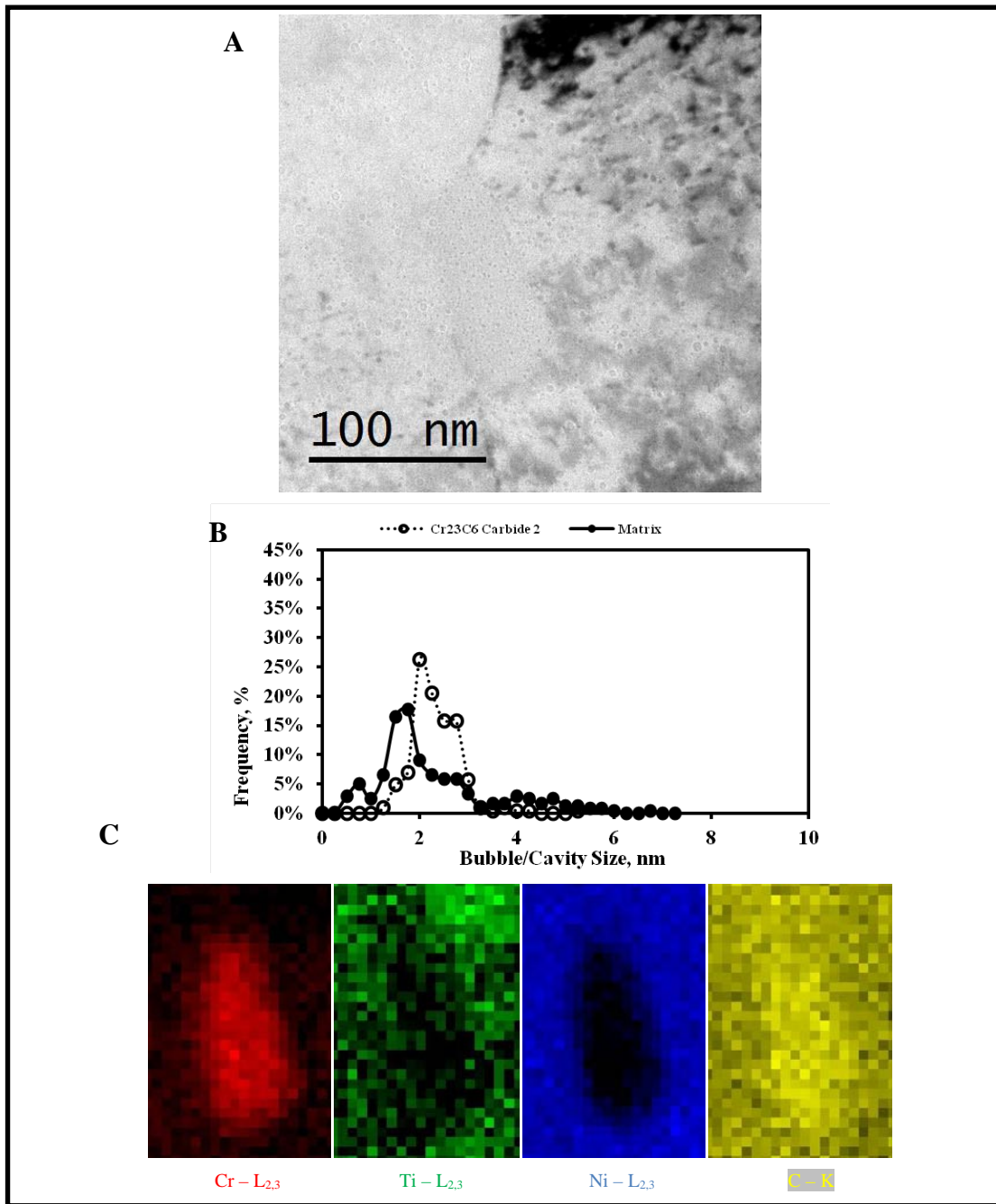


**Figure 71:** Helium bubble size distribution within a second grain boundary chromium carbide in material irradiated to approximately 51.2-55.0 dpa with 17300-18600 appm helium at 300-330°C. (A) TEM micrograph imaged in the overfocus condition (+ 500 nm), (B) bubble size distribution, and (C) EELS mapping.

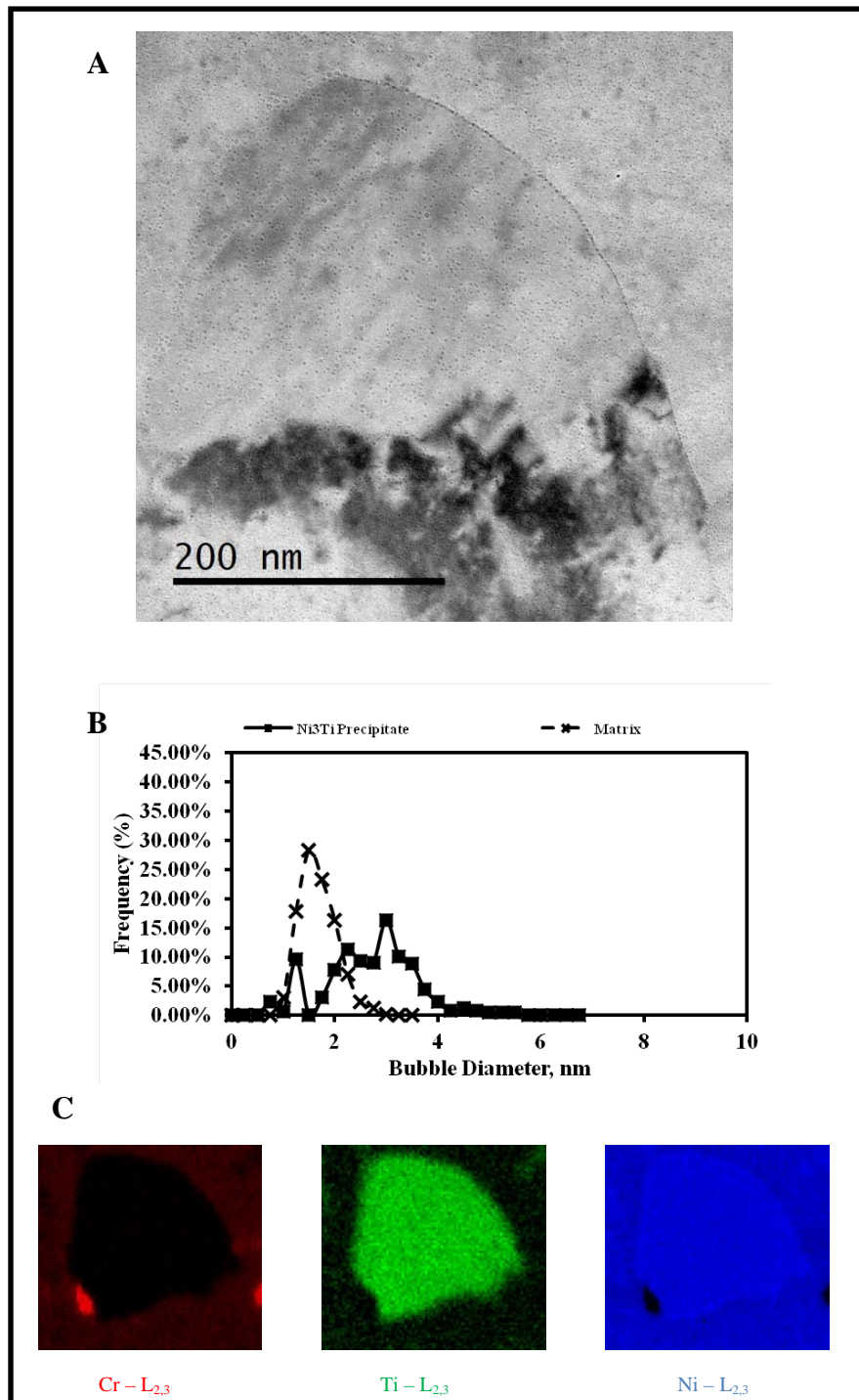


**Figure 72: Helium bubble size distribution within a grain boundary eta precipitate in material irradiated to approximately 51.2-55.0 dpa with 17300-18600 appm helium at 120-280°C. (A) TEM micrograph imaged in the overfocus condition (+ 500 nm), (B) bubble size distribution, and (C) EELS mapping.**

#### **4.1.2.4 Characterization of Helium Bubble Alignment on Dislocation and Subgrain Features**

It has been shown that helium bubbles form on grain boundaries, but helium bubbles will also form on sinks such as dislocations, and subgrain boundaries within the material, leading to local variation in bubble size and density distributions. The observation of such features is very dependent on TEM lamella quality/thickness. If the lamellas are too thick or too thin, these features may go unnoticed. Figure 73 and Figure 74 show two examples of helium bubble alignment on sub-grain features. There is a noticeable bubble alignment within the matrix, and an apparent size difference, similar to observations made for helium bubbles on grain boundaries presented in Section 4.1.2.2. The nature of these sub-grain boundaries remains unknown, but it is worth acknowledgement that determining size and density distributions from within the matrix material, as was done in Section 4.1.2.1, with the inclusion or exclusion of sub-grain features may greatly impact the results.

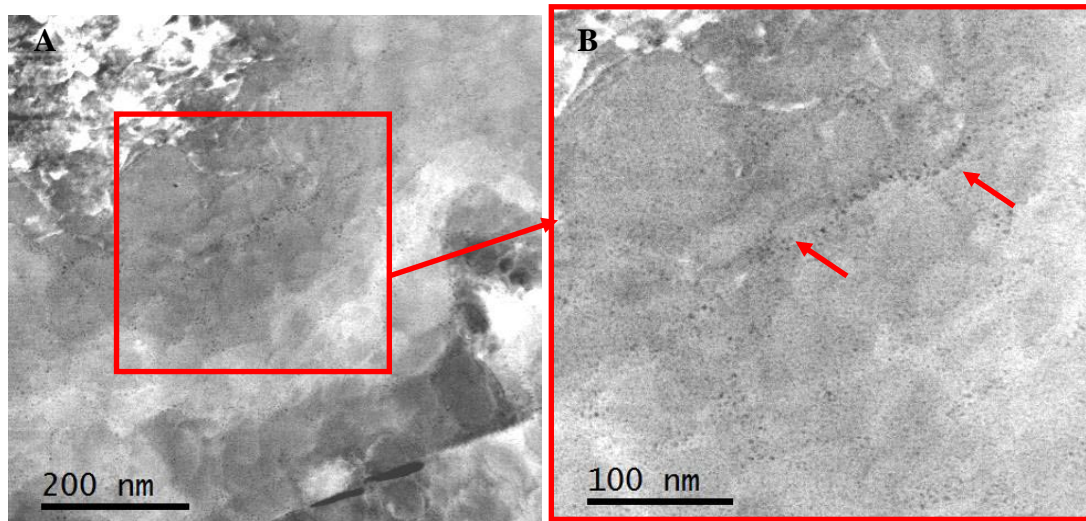


**Figure 73: HAADF image of sub-grain features with helium bubble alignment (a) low magnification, and (b) higher magnification.**

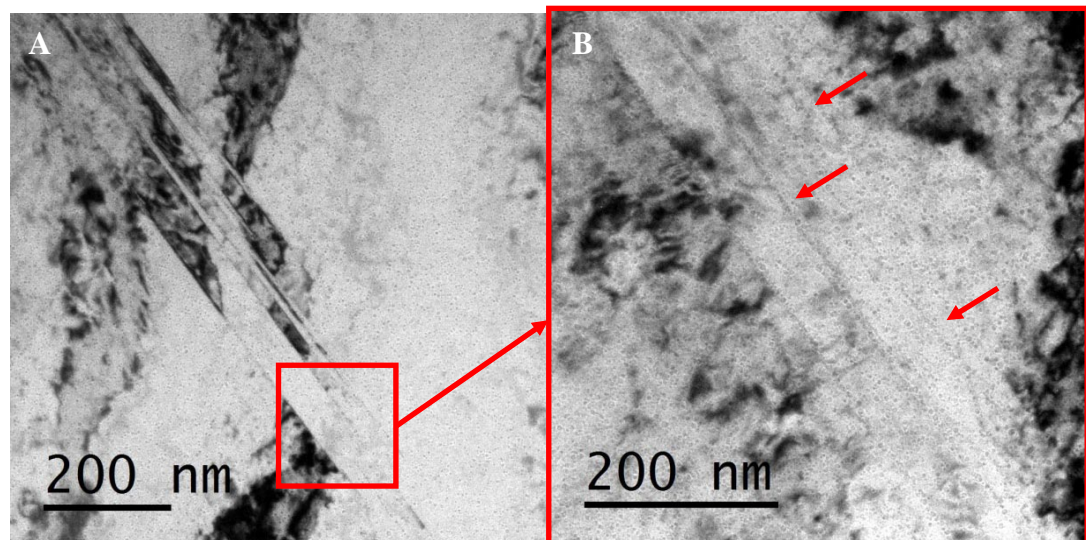


**Figure 74: Bright-field TEM image of sub-grain features with helium bubble alignment imaged in the overfocus condition (+500 nm) (a) low magnification, and (b) higher magnification.**

#### **4.1.2.5 Characterization of Gamma Prime Precipitate Stability**

The characterization of gamma prime in Inconel X-750 was performed using bright-field imaging, electron diffraction and EELS analysis to look for the chemical signatures of the gamma prime. Following irradiation, the material was heavily damaged, and viewing the gamma prime in bright-field imaging was problematic due to the high density of other defects in the material. Figure 75 shows a bright-field image, and electron diffraction pattern with gamma prime superlattice reflections in unirradiated material. Figure 76 and Figure 77 show unirradiated gamma prime characterized with EELS mapping and electron diffraction. In both examples, the diffraction patterns are sharp and clear, however, the EELS maps are not clear. This issue is believed to be associated with sample thickness. If the features of interest are smaller than the foil thickness and high in density they may sufficiently overlap to the point that in transmission, the chemical signatures of the precipitates are beyond the detection limits for EDS or EELS in a TEM. For our purposes, because we cannot locate the gamma prime from the strain field in bright-field, we use high quality TEM lamella (i.e. samples approximately 20-50 nm thick) and map the chemical signatures of the irradiated material with EELS, and then perform electron diffraction on that same region. This gives us the confidence that we know at least that gamma prime was present at these locations prior to irradiation (assuming limited elemental segregation/diffusion). Figure 78 and Figure 79 show the gamma prime characterization from material irradiated to 51.2-55.0 dpa and 17300-18600 appm helium at 120-280°C and 300-330°C respectively. No evidence of a superlattice

reflection could be obtained from the 120-280°C material, whereas a very weak reflection was collected from the 300-330°C material. It is possible, and thus important to note, that although no superlattice reflection is observed for 120-280°C material, the volume fraction of ordered structure is so low that the TEM cannot detect them (i.e. beyond the detection limits of the TEM). Although the difference in ordering is subtle, these observations support a temperature dependence on gamma prime disordering under these irradiation conditions, consistent with literature presented in Section 2.4.2. One notable difference between this data and previous investigations is that many studies have reported early disordering of gamma prime for these temperatures and irradiation conditions. These results confirm gamma prime is still somewhat ordered up to 51.2-55.0 dpa with 17300-18600 appm helium, and is contradictory to previous studies. Helium has been shown to suppress the disordering of gamma prime, as shown in Figure 13 to Figure 15 [48]. It appears as if this high concentration of helium may have limited the disordering of gamma prime enabling a new equilibrium state of the  $\gamma'$ .

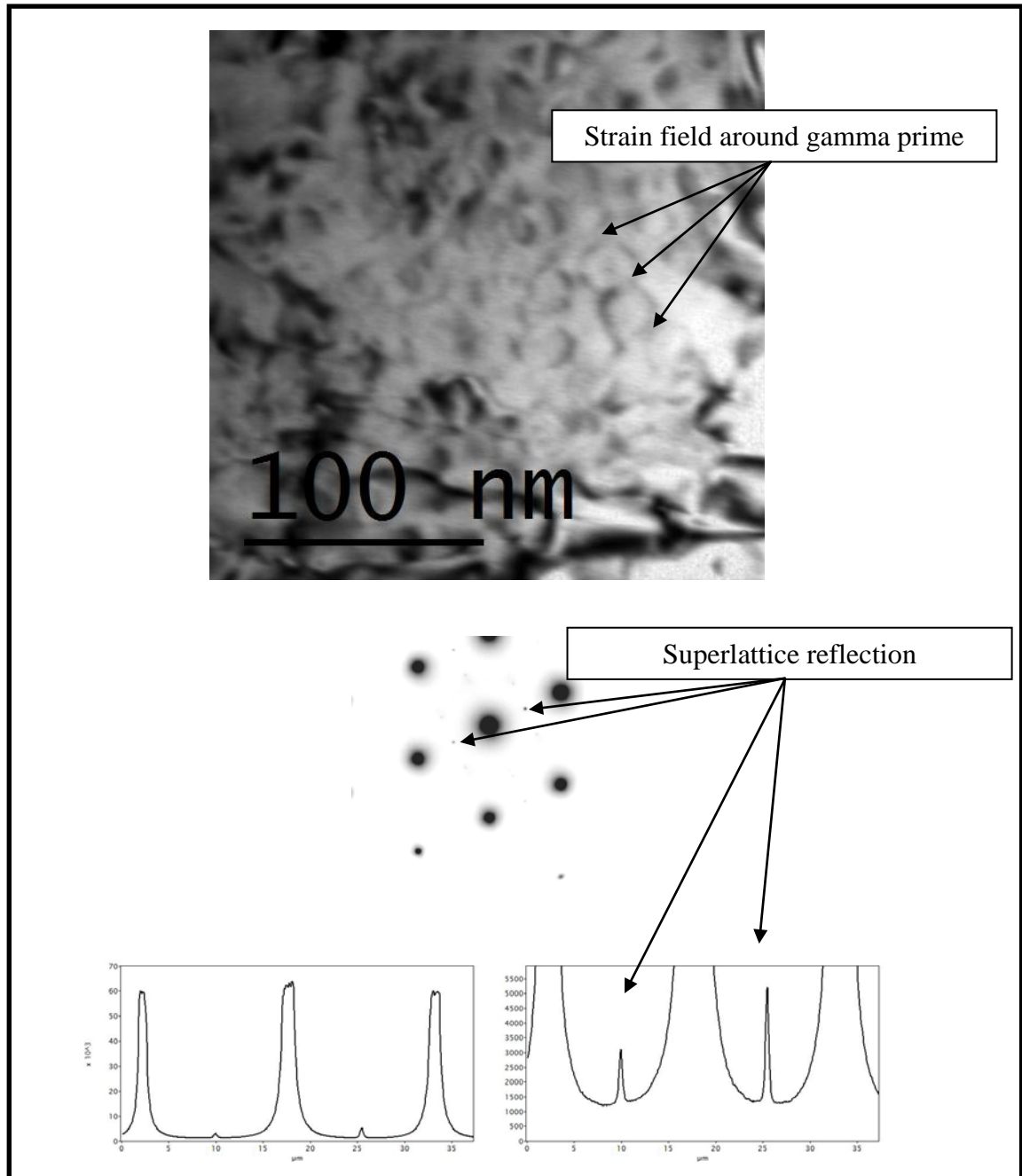


**Figure 75: Gamma prime characterization of non-optimized Inconel X-750 spacers (A) bright-field TEM image showing strain field around gamma prime, (B) TEM diffraction showing gamma prime superlattice points, (C)&(D) intensity profiles of electron diffraction pattern showing gamma prime superlattice reflection.**

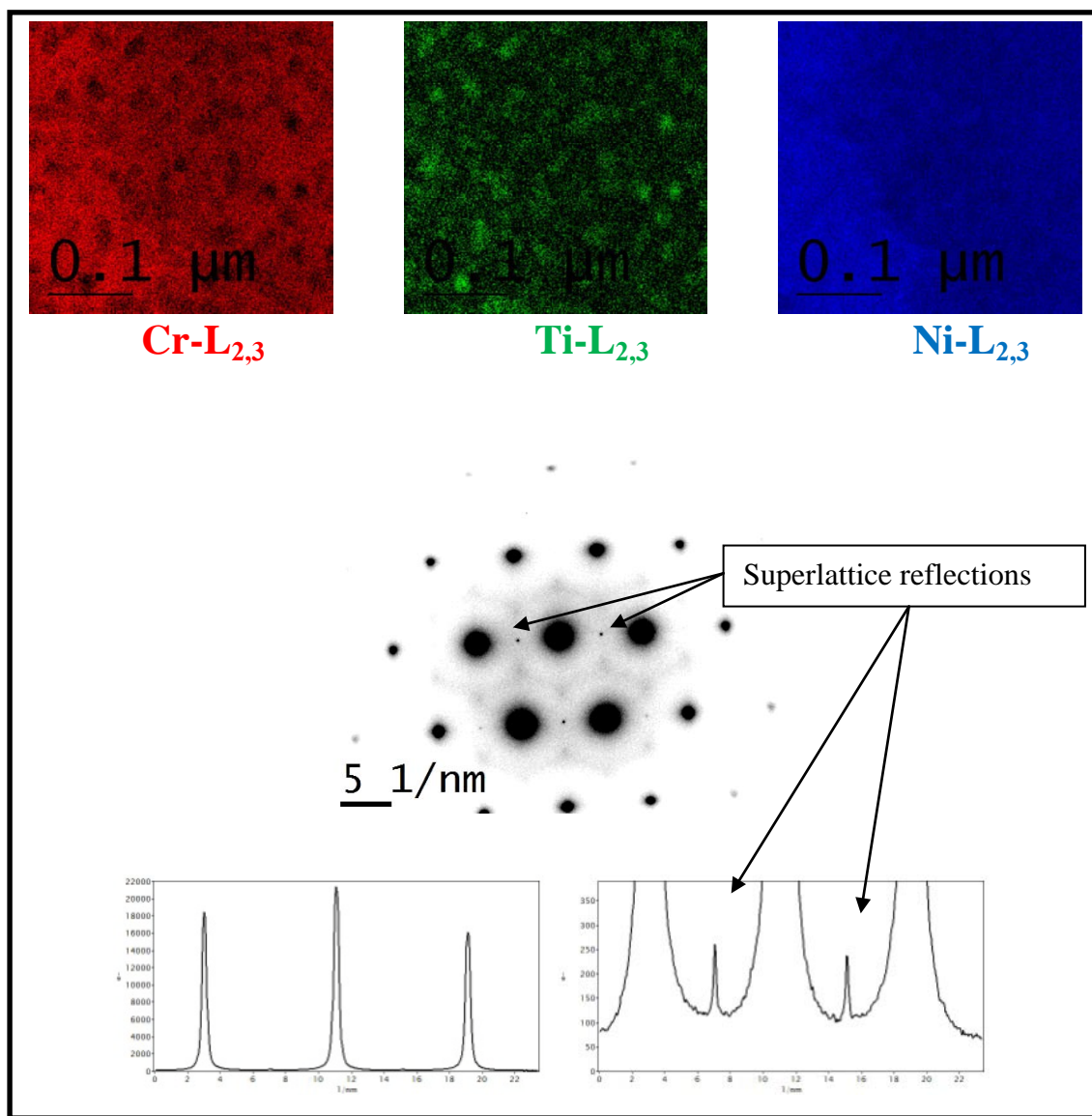


**Figure 76: Gamma prime characterization of TEM lamella #1 from unirradiated optimized Inconel X-750 spacer. (A) EELS maps of Cr, Ti and Ni, (B) electron diffraction pattern showing gamma prime superlattice reflections, and (C)&(D) intensity profiles of electron diffraction pattern showing gamma prime superlattice reflections.**

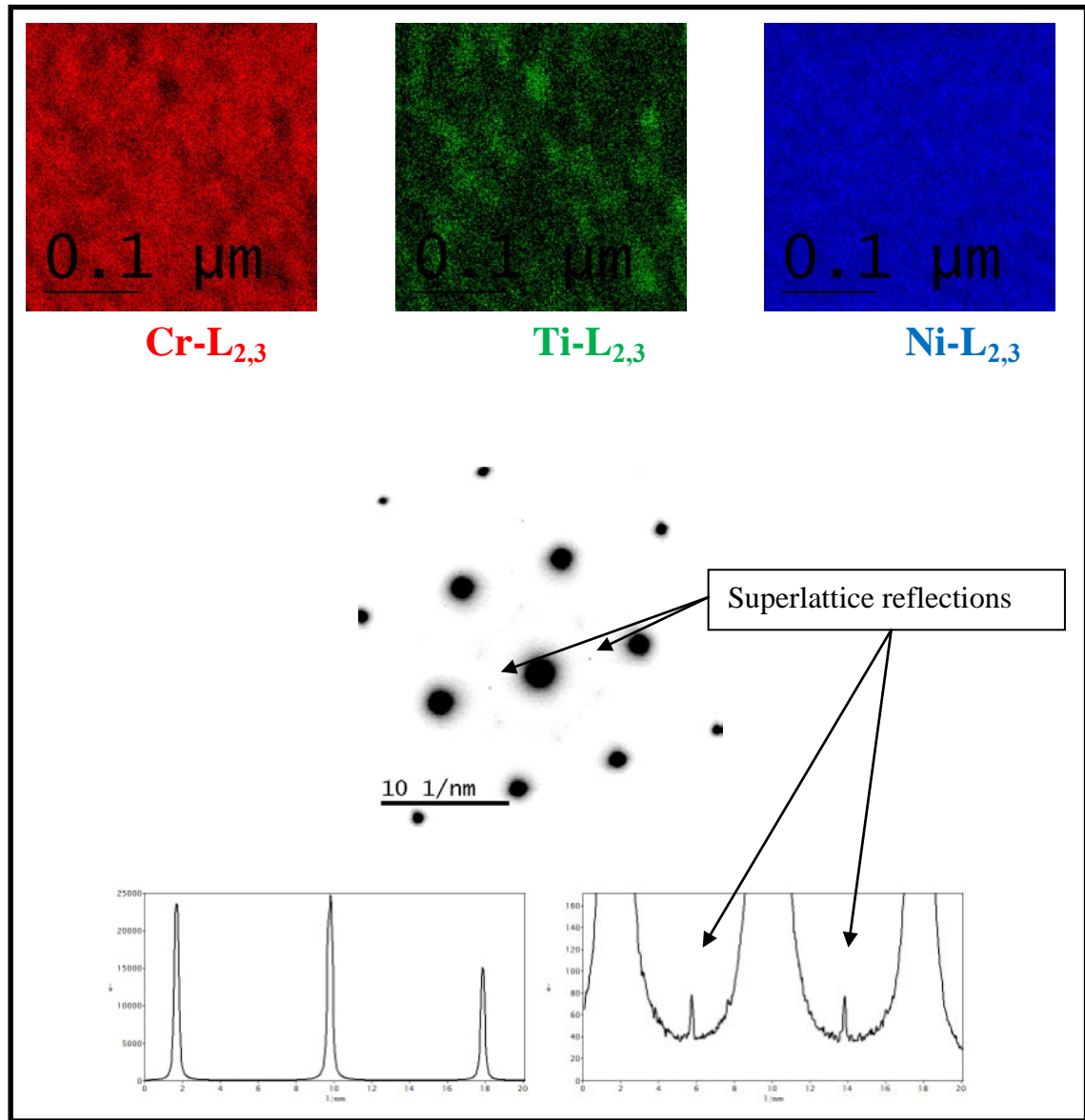


**Figure 77: Gamma prime characterization of TEM lamella #2 from unirradiated optimized Inconel X-750 spacer. (A) EELS maps of Cr, Ti and Ni, (B) electron diffraction pattern showing gamma prime superlattice reflections, and (C)&(D) intensity profiles of electron diffraction pattern showing gamma prime superlattice reflections.**

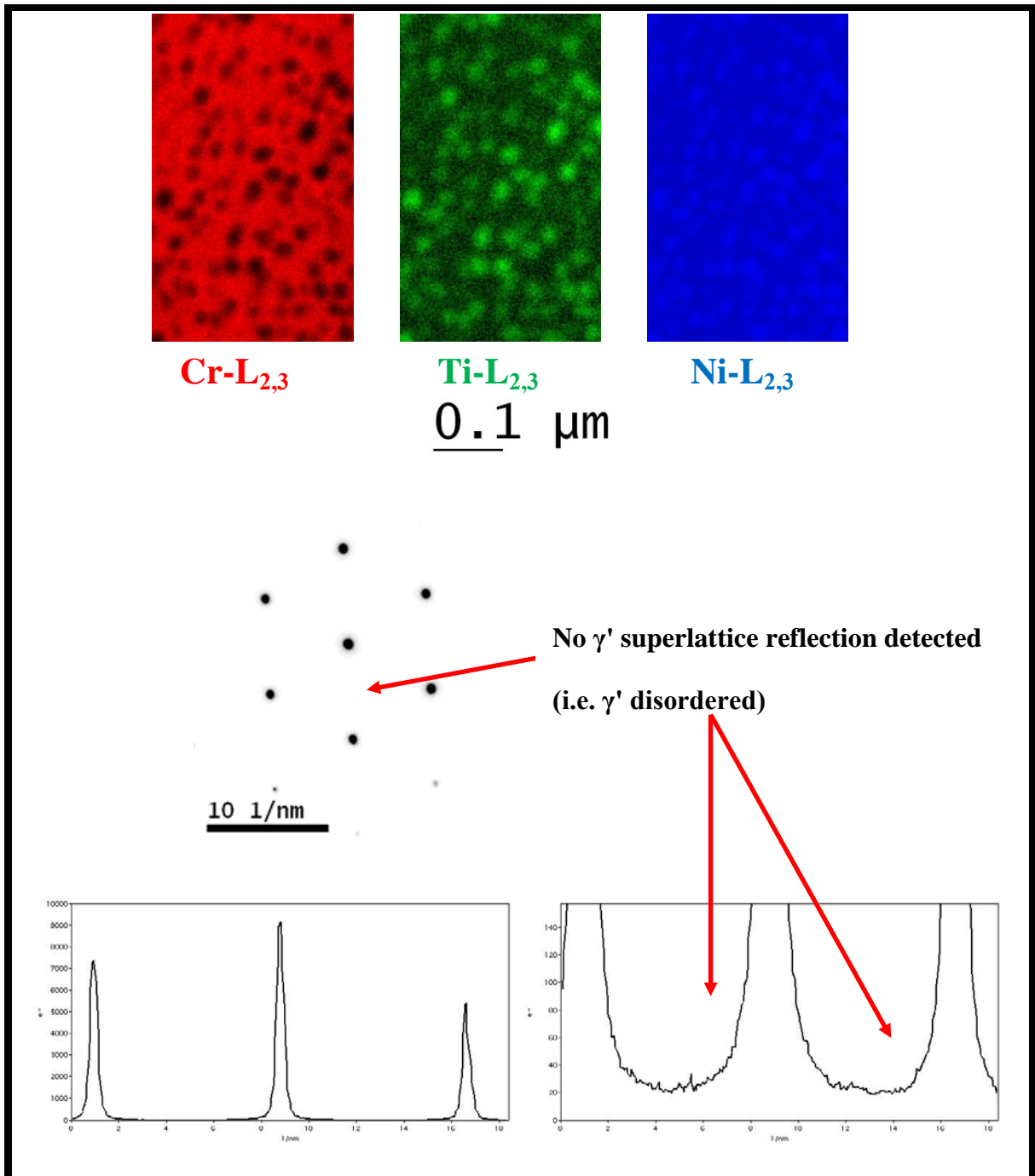


Figure 78: 51.2-55.0 dpa and 17300-18600 appm He, 120-280°C gamma prime characterization.

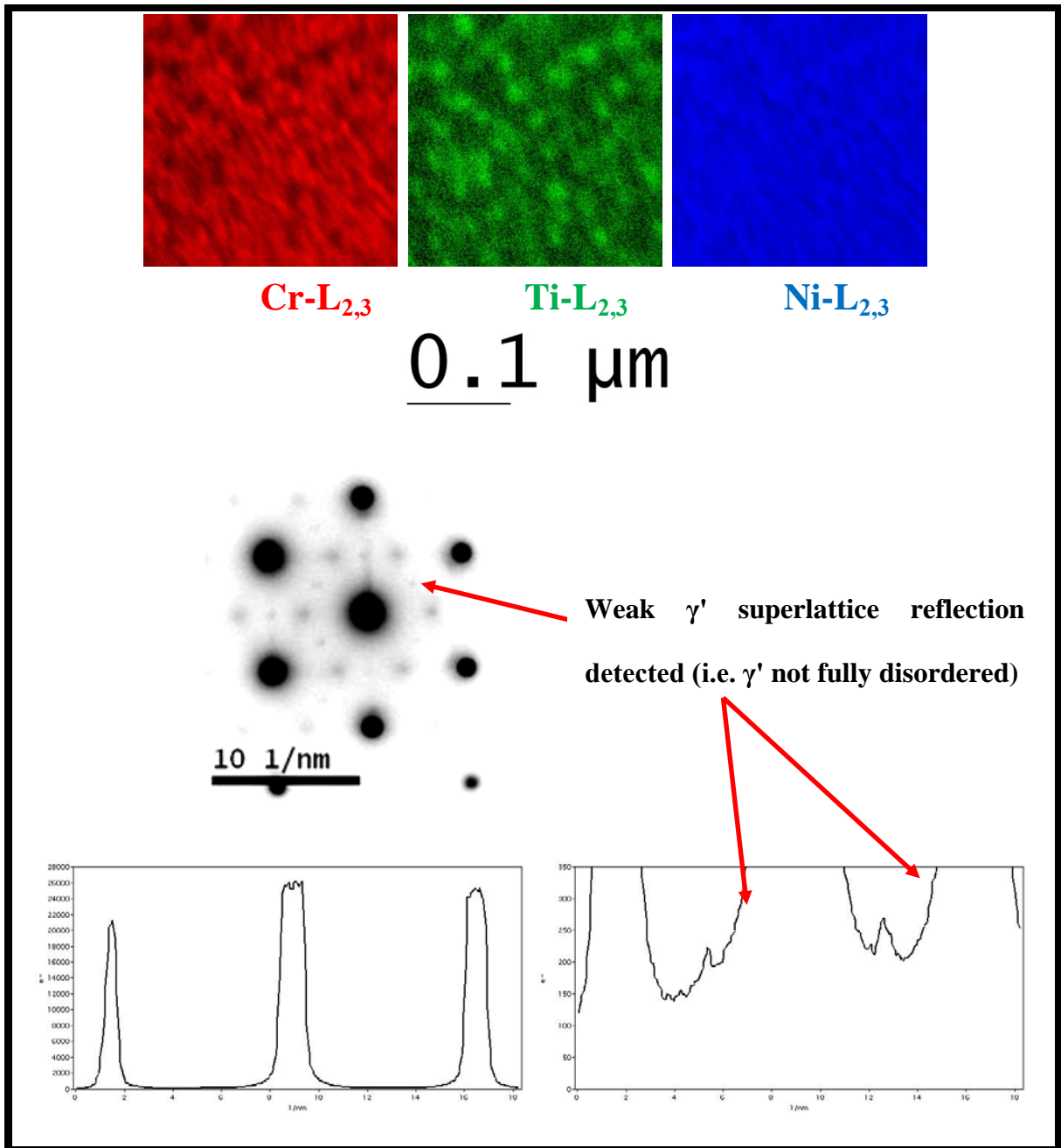


Figure 79: 51.2-55.0 dpa and 17300-18600 appm He, 300-330°C gamma prime characterization.

#### **4.1.2.6 FIB and TEM Characterization of Intergranular Fracture Surfaces**

In characterizing the effects of irradiation on the microstructural evolution, it is perfectly acceptable to prepare specimens from all together “random” locations to ascertain the influence of irradiation (Section 4.1.2), however, if the objective of the investigation is to determine the direct cause of lost strength, ductility and intergranular fracture, a slightly different approach may be warranted.

As we have shown in Section 4.1.1, the fracture surfaces of ex-service neutron irradiated Inconel X-750 is entirely intergranular. The current evidence suggests a direct link between lost strength, ductility and intergranular fracture with grain boundary helium bubbles. Although this remains the most plausible explanation for the material degradation, there remains no direct evidence to support this theory.

With the use of a focussed ion beam, a TEM lamella has been extracted directly from an intergranular fracture surface from material with 51.2-55.0 dpa and 17300-18600 appm helium (300-330°C). This enables us to investigate features on the fracture surfaces in a TEM (i.e. with higher resolution compared to an SEM), and in addition, characterize material directly ahead of an intergranular secondary crack. Figure 80 shows a series of images collected during the TEM lamella preparation. It was desired to produce a TEM lamella within an area that includes a secondary crack to enable characterization of not only the fracture surface, but of a crack tip as well. Figure 80-(b) shows the rough milling of the TEM lamella, and Figure 80-(c) shows the final TEM lamella.

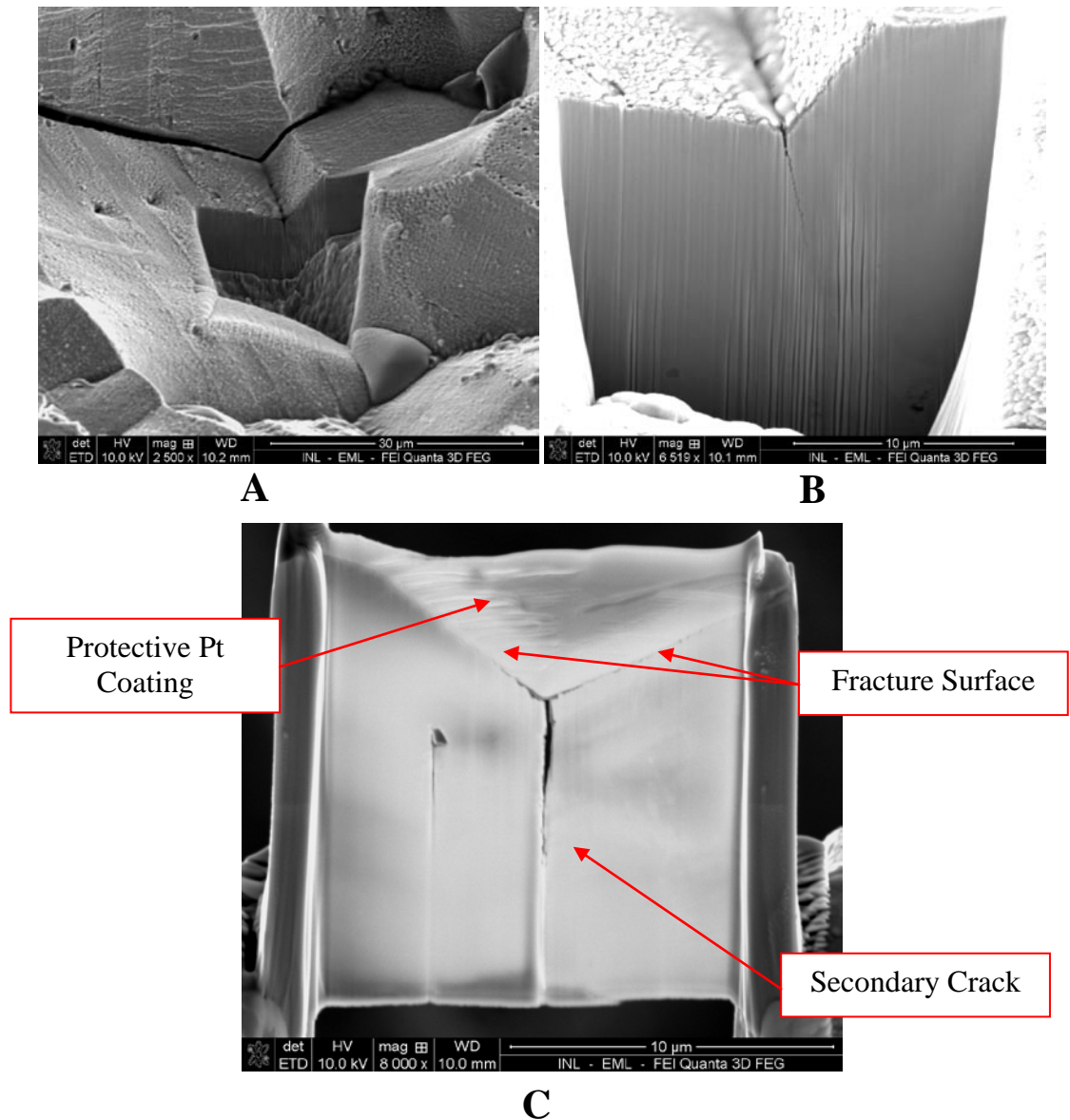


**Figure 80: FIB lamella preparation from the intergranular fracture surface of ex-service neutron irradiated Inconel X-750 irradiated to approximately 51.2-55.0 dpa and 17300-18600 appm helium at 300-330°C. Images showing a) rough milling, b) higher magnification of rough milling showing secondary intergranular crack, and c) final TEM specimen with secondary intergranular crack for detailed analytical TEM characterization.**

The fracture surface was characterized with scanning transmission electron microscopy (STEM) in HAADF imaging mode and EELS spectrum mapping, Figure 81. A bandpass image filter was applied to the HAADF image to reduce the contrast from thickness variations. Along the intergranular fracture there are a series of “pulled” out precipitates and some remaining precipitates along the grain boundary. This is consistent across the entire fracture surface of the lamella. The size scale of these features are consistent with micro-dimples observed on the intergranular fracture surfaces presented in Section 4.1.1. The EELS mapping shows regions enriched in Ti (or depleted in Cr) directly adjacent to the fracture surface. Because these features are directly adjacent to where Cr carbides have been “pulled” out or remain, it is unclear if this is local depletion of Cr surrounding the carbides (present in as-fabricated material), or if this may be supporting evidence of radiation induced segregation (i.e. Ti enrichment and Cr depletion at boundaries).

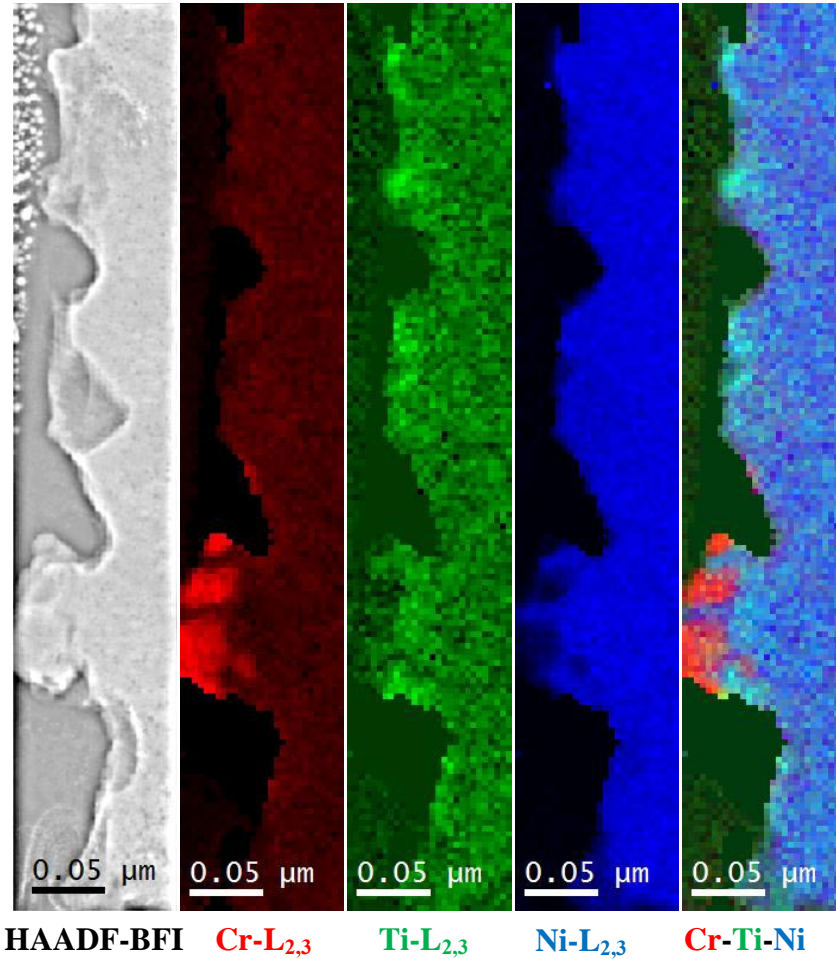


**Figure 81: EELS maps of intergranular fracture surface from ex-service neutron irradiated material with approximately 51.2-55.0 dpa and 17300-18600 appm helium at 300-330°C.**

An overview of the secondary crack in the TEM lamella was characterized with STEM – HAADF imaging (bandpass filtered to reduce thickness contrast variations), Figure 82. The fracture path follows the grain boundary, and propagates around grain boundary precipitates, not through them. This observation is significant in this study because it helps rule out a prominent failure mechanism of embrittlement associated with second phase grain boundary plating as described in Section 2.6.3. There are regions in the Ti map near the grain boundary that enriched in Ti, however no precipitates were found at these locations. Similar to previous notes, it is unclear if this enrichment is evidence of elemental segregation, or simply segregation associated with the formation of Cr carbides in the solution annealing process.

Figure 83 shows a higher magnification and resolution image of a region along the secondary crack confirming that the crack path propagates around the grain boundary precipitates and not through them. Figure 84 shows a higher magnification and higher resolution image of the crack tip. A note of extreme importance from this work is that the crack path follows grain boundary helium bubbles, providing the first direct evidence linking intergranular fracture with grain boundary helium bubbles, and providing strong supporting evidence suggesting helium embrittlement is the primary degradation mechanism for Inconel X-750 irradiated in CANDU reactors. Helium bubbles are imaged ahead of the crack along the same grain boundary as shown in Figure 85. There is a region (highlighted with arrows) where bubbles seemed to coalesce, or crack, providing further supporting evidence of helium bubble involvement as the likely failure mechanism.

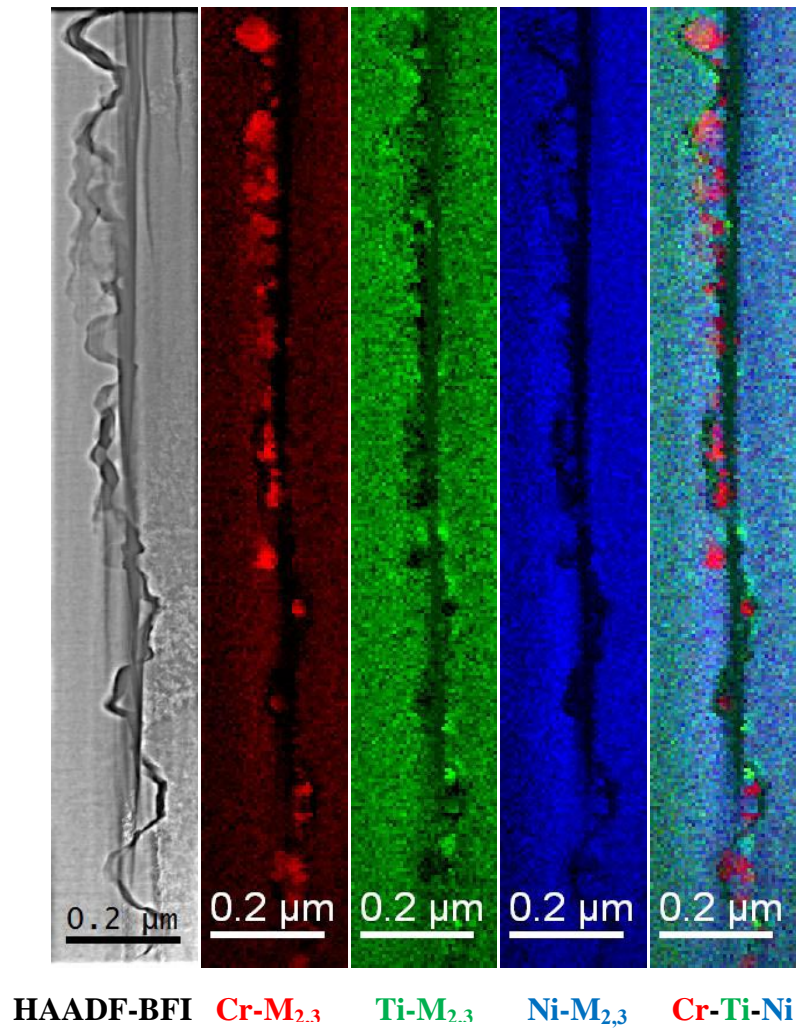


**Figure 82: EELS maps of a secondary crack tip from ex-service neutron irradiated material with approximately 51.2-55.0 dpa and 17300-18600 appm helium at 300-330°C.**

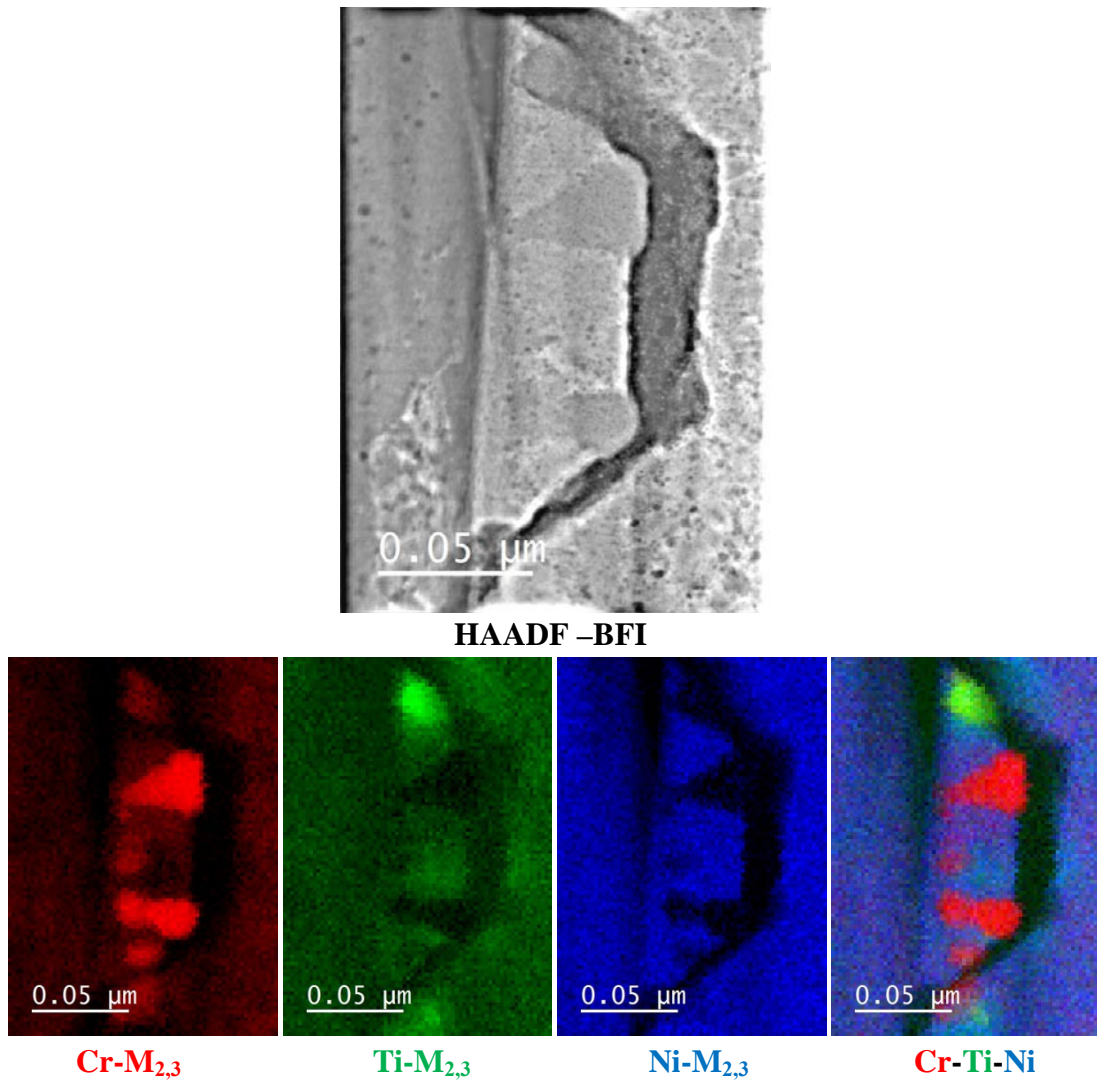


**Figure 83: Higher magnification and resolution EELS maps of secondary crack shown in Figure 82 (near bottom of crack).**

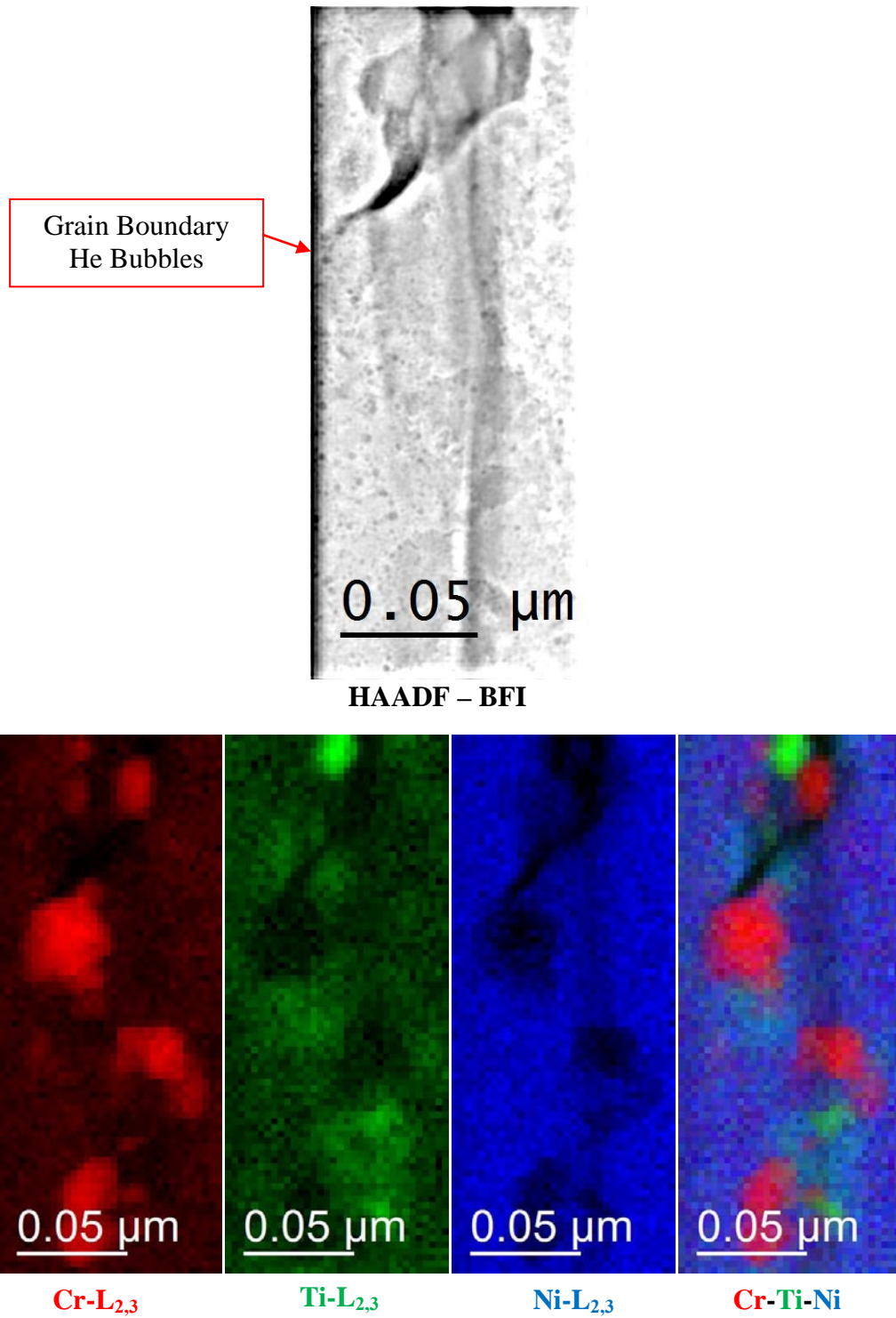


**Figure 84: Higher magnification EELS map of secondary crack tip shown in Figure 82 (near bottom of crack).**

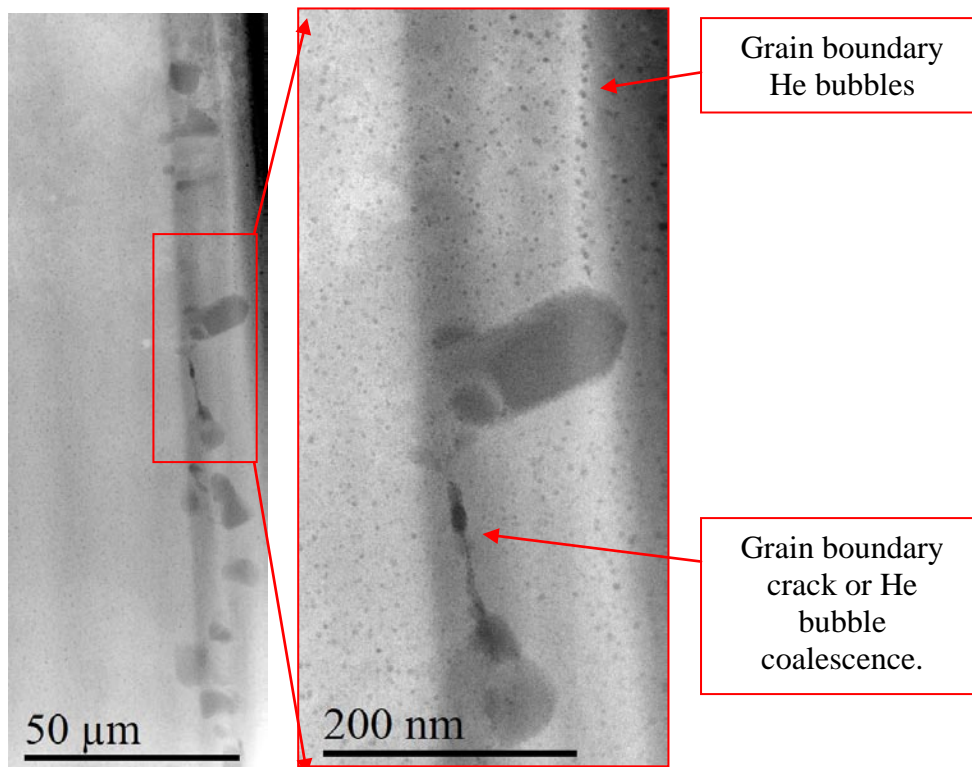


**Figure 85: HAADF image of grain boundary ahead of secondary crack shown in Figure 81 and Figure 82.**

#### **4.1.3 Micro-Hardness of Ex-Service Inconel X-750 CANDU Spacers**

Micro-hardness is performed on the same bulk material that was used for TEM characterization reported in Section 4.1.2 so that a direct comparison can be made between the microstructure and the material hardening. The starting unirradiated material hardness is measured at between 400-430 VHN, however, it should be noted that these results have been obtained from a limited number of unirradiated material and it has been reported that material variability in Inconel X-750 could lead to hardness ranging from 320-490 VHN. This variability is likely linked with the precipitation hardening (i.e. gamma prime) and/or strain hardening during spacer fabrication. Following irradiation, it is generally recognized that the degree of radiation damage drowns out the influence of cold work on irradiation hardening, and gamma prime has been shown to largely become disordered following irradiation. In other words, the variability influencing hardness from the unirradiated material may no longer be present in the material, and trends in hardening may be inferred.

Other influences with continued irradiation to note are the helium bubble evolution and continued disordering and dissolution of gamma prime. The degree of dissolution is not reported within this analysis based on limitations of the experimental approach, however, it is at least shown that gamma prime is not fully dissolved up to the most extreme irradiations conditions examined in this work (i.e. 51.2-55.0 dpa and 17300-18600 appm helium), and there does seem to be an effect of temperature on disordering.

Figure 86 reports the hardness as a function of dpa for the ex-service spacer material. It appears that the lower temperature material is softer comparatively to higher temperature material, however, no significant<sup>9</sup> change in hardness occurs with irradiation.

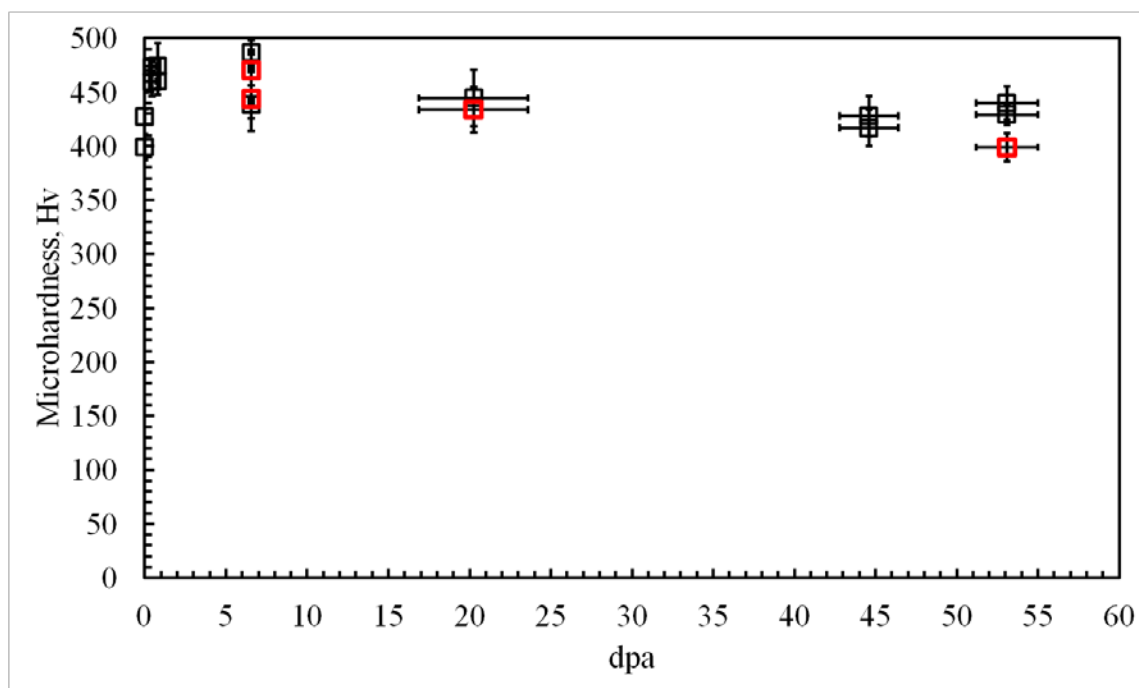


**Figure 86: Micro-hardness of ex-service material as a function of dpa. Measurements were performed on same material presented in Section 4.1.2. Red data points are representative of material irradiated at approximately 120-280°C and black data points are representative of material irradiated at approximately 300-330°C.**

<sup>9</sup> In this case, a “significant” change refers to a change beyond the starting material variability.

#### **4.1.4 Discussion: Ex-Service Inconel X-750 CANDU Spacers**

In this section, the results of the fractography, microstructural characterization, and microhardness measurements of ex-service Inconel X-750 CANDU spacers will be discussed. The primary objectives of this thesis are to investigate the influence of neutron irradiation and reactor operating conditions on the evolution of the microstructure and mechanical properties of Inconel X-750. These results will be discussed in terms of elucidating the potential degradation mechanisms responsible for reduced ductility and strength of these reactor components.

##### **4.1.4.1 Intergranular Fracture and Likely Fracture Mechanisms**

The fractography examination of ex-service, neutron irradiated, Inconel X-750 outlines the primary motivation for this research; spacers are losing strength, ductility and fracture along the grain boundaries. Following an initial incubation period, the fracture mechanism is entirely intergranular and has no temperature sensitivity, suggesting the primary mechanism of intergranular fracture for the two irradiation temperatures is the same. Although the evidence suggests the fracture mechanism is the same, other mechanical properties appear different. The test observations from post irradiation examination (i.e. crush tests) of different irradiation temperatures show some mechanical differences, suggesting a difference in mechanical properties [10, 13, 14]. Material irradiated at 300-330°C showed limited to no plasticity, and lower crush strength, whereas material irradiated at 120-280°C showed minor plasticity and higher crush strength (see Section 3.2 and Figure 34 for further details). Understanding the impact of irradiation temperature on the microstructural evolution is a crucial component in

understanding the primary degradation mechanism for these reactor components. Although the fractures were predominantly intergranular, evidence was found to support local plasticity at/near grain boundaries. The primary fracture mechanisms discussed in background section were hydrogen embrittlement, brittle precipitate plating on boundaries, and grain boundary cavities/bubbles.

Hydrogen was measured in this material at CNL (unpublished) with hot vacuum mass spectroscopy (HVEMS) using an approach outlined in [133], however, nothing was detected above normal background. For hydrogen to become trapped within irradiation induced defects such as bubbles, it must form molecular hydrogen ( $H_2$ ). Due to the extremely high defect density (on the order of  $10^{24}$  bubbles/ $m^3$ ), it is likely that no two hydrogen atoms would be present within an individual bubble in order to form  $H_2$ , enabling hydrogen to freely diffuse through the material without becoming trapped. It is however, possible that strong traps such as grain boundary carbides may locally retain trace hydrogen concentrations, and thus hydrogen embrittlement cannot be entirely ruled out. Even very low, but local concentrations of hydrogen may have deleterious effects on grain boundary embrittlement [1, 109]. The primary mechanism of hydrogen embrittlement is associated with decreases CRSS for dislocation motion enabling easier local plasticity near grain boundaries. Based on the high density of grain boundary helium bubbles in the material, if hydrogen were to influence the grain boundary strength, it would likely be a secondary mechanism.

The FIB and TEM analysis presented in Section 4.1.2.6 gives the first direct evidence linking intergranular fracture and crack propagation to grain boundary helium bubbles.

This analysis also shows that the crack path propagated around grain boundary precipitates (not through), ruling out the potential for grain boundary embrittlement through a second phase plating on the boundary, as presented in Section 2.6.3. Also in support of this claim is the lack of Ti enriched precipitates on the grain boundary. Although Ti rich regions are found near the grain boundary as reported in Figure 81- Figure 84, it is unclear if these enrichments are formed during manufacturing and precipitation of the Cr carbides on the boundaries, or if the analysis has captured irradiation induced segregation in process. Figure 72 shows an eta phase on the grain boundary, which has been linked with grain boundary embrittlement [110, 111]. The unirradiated microscopy of X-750 presented in [132] shows these precipitates in the unirradiated material (sparsely). As these precipitates are found in unirradiated material, it is unlikely that the observation of eta phase in this case is evidence of irradiation induced precipitation on grain boundaries. This observation was an isolated case.

In light of the microstructural results, it is likely that the primary degradation mechanism for Inconel X-750 in a high thermal power reactor is helium bubble embrittlement. Figure 87 shows a schematic of the potential mechanism [10]. This follows the principles outlined by Trinkhaus [25] where links between neighbouring helium bubbles will have a higher local stress compared to the bulk matrix, leading to a decreased grain boundary strength. Trainkaus' work was slightly different, whereby grain boundary helium bubbles were used to justify growth and coalescence of bubble through a diffusion process. In the present case, the bubble growth, coalescence and ultimate crack propagation would be

linked more with dislocation dynamics. Nevertheless, grain boundary strength as a result of either mechanism would be reduced based on a perforated boundary.

The evolution of mechanical properties within the matrix material and grain boundaries will impact the degree of embrittlement from this mechanism. The primary microstructural features influencing the change in strength of the matrix are precipitation strengthening via gamma prime, irradiation induced defects, and helium bubbles. The microstructural components which may influence the change in strength of the grain boundary are the bubble size and density (i.e., area coverage), bubble spacing, and bubble depletion zone. The microstructural characterization will be discussed in terms of impact to bulk mechanical hardening and grain boundary strength.

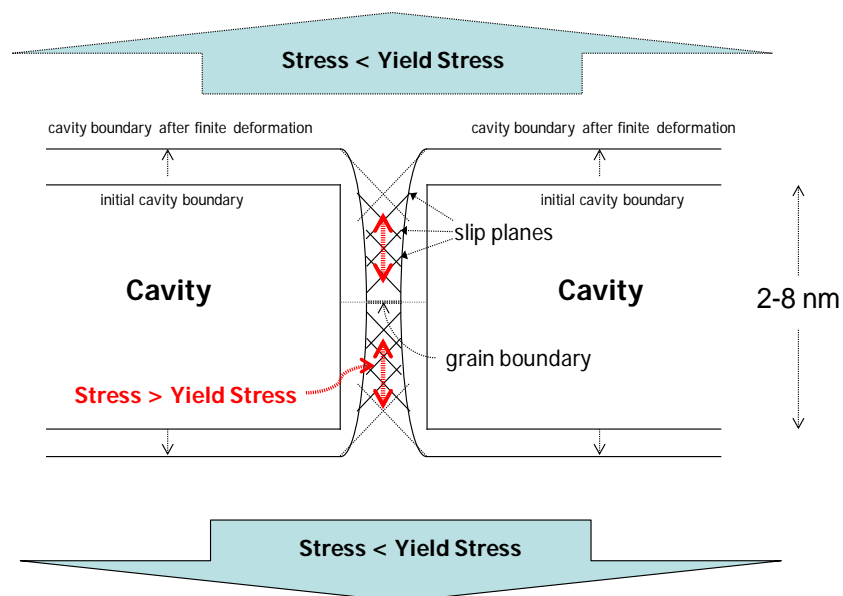


**Figure 87: Schematic of potential interaction of grain boundary helium bubbles on material degradation [10].**

#### **4.1.4.2 Microstructural and Mechanical Property Evolution of the Matrix**

The results performed on the microstructure as part of this thesis were primarily focused on the characterization of helium bubbles, and gamma prime stability. Complementary work performed by Zhang et al at Queen's University focused on the characterization of defect structures in the same neutron irradiated material [11, 49]. For the purposes of this discussion section, the results are limited to the highest dose condition (i.e. 51.2-55.0 dpa and 17300-18600 appm helium) to link the microstructural evolution with mechanical properties. The combined results from these studies can be used to investigate the overall impact of the microstructure on the hardening of the bulk material through the use of a dispersive barrier hardening model as presented in Section 2.4. Table 7 outlines the relative contributions to the unirradiated material strength, and the barrier strengths from the literature reported in Section 2.4.3. Because the nature of the irradiated microstructure is so complex, it is difficult to separate out individual hardening mechanisms from the overall material hardness, however, an attempt is made through a sensitivity study and the rule of superposition (root sum of the squares for short range defects and additive for long range defects) as outlined in Equation 14-Equation 16 [36]. Short range hardening mechanisms are associated with irradiation induced loops, bubbles, and  $\gamma'$ , and long range hardening mechanisms are assumed to be simply the network dislocations. For simplicity of the model, it is assumed that the long range mechanisms do not change with irradiation. This sensitivity study is aimed at identifying the impact of individual microstructural defects on hardening in Inconel X-750.

**Table 7: Summary of individual components to unirradiated material strength, and relative barrier strengths for main microstructural defects with irradiation.**

<b>Component</b>	<b>Barrier Strength, <math>\alpha</math></b>	<b>Unirradiated Strength, MPa</b>
<b>Solution Annealed Material</b>	N/A	600 [134]
<b>Cold Work (Network Dislocations)</b>	N/A	300 [134]
<b>Gamma Prime</b>	N/A	300 [134]
<b>Loops, SFTs</b>	0.1 [36]	N/A
<b>Bubbles</b>	0.2-1[36]	N/A

**Equation 14**             $\sigma_{LR} = \sigma_{Network\ Dislocations}$

**Equation 15**             $\sigma_{SR}^2 = \sigma_{loop}^2 + \sigma_{bubbles}^2 + \sigma_{\gamma'}^2$

**Equation 16**             $\sigma_T = \sigma_{SA} + \sigma_{LR} + \sigma_{SR}$

#### 4.1.4.2.1 Irradiation Induced Defects

The defect structures (SFTs and loops) were not characterized during this research, however, Queen's University studied these defects from the 51.2-55.0 dpa and 17300-18600 appm helium irradiated material in complementary investigation reported in [11], and the results will be utilized to determine the potential contribution of loops to hardness. The size distributions are shown in Figure 18 for the two irradiation temperatures, however, the defect densities were not reported. Because the lower temperature material seemed to be in a recombination dominated regime with limited freely migrating point defects, it is likely that this material will have a lower overall density of irradiation induced defects. Typical densities of loops and SFTs at irradiation conditions like this are approximately  $10^{22}/m^3$ . If we assume that the defect density for 120-280°C material is  $0.5 \times 10^{22}/m^3$  and 300-330°C material is  $1 \times 10^{22}/m^3$ , we can use the size distribution data shown in Figure 18 to calculate the impact of loops to hardness.

Using a dispersive strength of 0.1, the increase individual contribution from loops is calculated at approximately 25 MPa and 47 MPa respectively. This is a relatively small change with irradiation.

#### 4.1.4.2.2 Helium Bubbles

If we are to take the bubble size and density distributions presented in Figure 42, and calculate the contribution to hardening from the bubble distribution as a function of dispersive barrier strength,  $\alpha$ , we see that in all cases the hardening from the lower irradiation material is greater than the higher temperature irradiated material, as shown in Figure 88. The degree of hardening from bubbles using barrier strengths from the literature of 0.2-0.5 is substantial; on the order of 500-3000 MPa (~170-1000 VHN). This is significantly more than the observed changes in hardness reported in Figure 86.

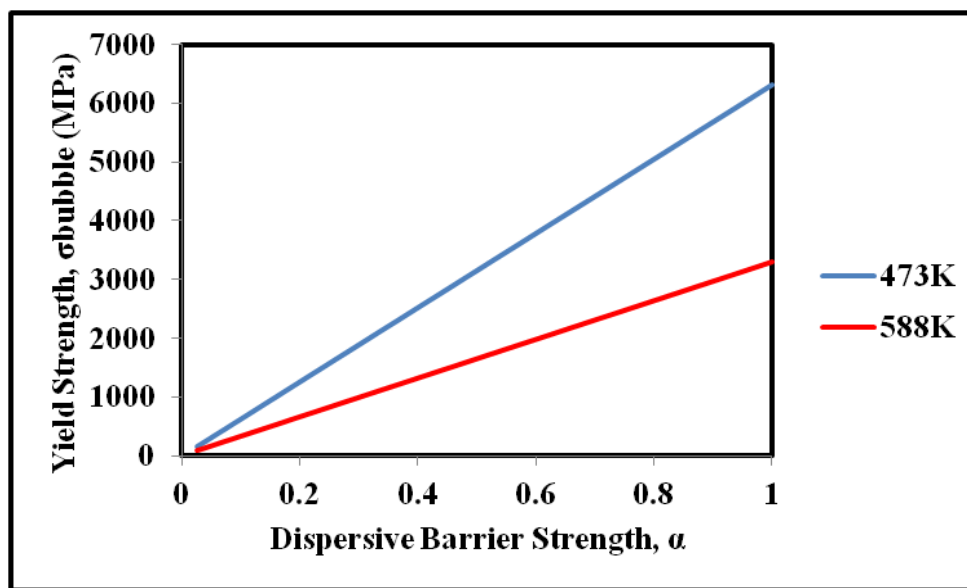


Figure 88: Yield strength increase for helium bubbles as a function of applied barrier strength.

The calculated pressure of the helium bubbles reported in Section 4.1.2.1.2 suggest that the bubbles are at or below equilibrium bubble pressure. Figure 51 show the pressures required to punch out dislocation loops around the bubbles are slightly higher than equilibrium pressures. Therefore, based on the experimental observations, and theoretical calculations, it can be concluded that no loop punching has occurred. Without loop punching, the likely hardening mechanism for bubbles is a dislocation bypass mechanism. No direct evidence for shearing of bubbles was found in the experimental results, however, the fact that no recognizable hardening has occurred in the bulk material (Figure 86) supports the claim that the bubbles are not acting as strong barriers to dislocation motion. Recall that some MD simulations support the claim that the barrier strength for cavities (bubbles in this specific case) has a transition size, whereby smaller bubbles are weaker compared to larger bubbles. The specific transition size greatly depends on the material; 2 nm for pure Ni. If we adopt a transition size in this study of approximately 2.25 nm (alloying leading to a slightly larger size), and assign a transition in barrier strengths to the bubble size and density distributions presented in Figure 42, we can calculate the contribution to material hardening from bubbles. Values for different barrier strengths are selected through trial and error. This analysis is for discussion purposes only. If we adopt a barrier strength of 0.03 for bubbles  $<2.25$  nm, and 0.1 for bubbles  $>2.25$  nm we see an approximate hardening of 244 MPa and 252 MPa for material irradiated at 120-280°C and 300-330°C respectively. Although the lower temperature material has approximately 4 times the bubble density, the majority of these bubbles are below 2.25 nm in size and their contribution to hardening is less significant.

This may help explain why the lower temperature irradiated material has a lower hardness in comparison to the higher temperature irradiated material. This analysis however is pure speculation with nominal barrier strengths appointed for discussion purposes. The point to be made is that working with a few assumptions, supported by literature, arguments could be given to justify the lower irradiation hardening associated with a higher defect density material. MD simulations using the experimental measurements of bubble size, density and pressures from this investigation may help gain further insights into the impact of helium bubbles on hardening.

#### **4.1.4.2.3            Gamma Prime Precipitates**

The EELS analysis of the gamma prime shows that no measurable dissolution has occurred at either irradiation temperature. The electron diffraction results show that the higher irradiation temperature material remained partially ordered. The degree of ordering is not verified. Supporting literature in other precipitation hardened superalloys [43, 44, 114] suggests that these precipitates would still have some strengthening contribution from both the ordered structure and the solution strengthening of Al and Ti. The lower temperature material however had no observable gamma prime superlattice reflection. This would indicate that precipitates are disordered. However, just because something is not observed does not mean it is not there. It is possible that the gamma prime volume fraction is below the detection limits of the technique. Nonetheless, these results show that the lower irradiation temperature is more disordered in comparison to the higher irradiation temperature material, and the impact on hardness would be less. The degree of hardening however remains unknown. For the purposes of this

investigation we can assign a contribution to hardening of 100 MPa and 150 MPa for 120-280°C and 300-330°C material respectively. This assigns a contribution to solution hardening for the gamma prime of 100 MPa (same for both temperatures), and 50 MPa for partial ordering of gamma prime in the higher irradiation material. It is understood that this train of thought is purely speculative, but will be informative from the standpoint of better understanding the overall hardness Inconel X-750 following irradiation in a high thermal flux. The main point to be made is lower temperature irradiated material would be softer with respect to precipitation hardening compared to higher temperature material.

#### **4.1.4.3 Hardening Mechanisms**

Recall that there was no significant change to hardness following irradiation, and that lower irradiation temperature results in softer material (Figure 86). The previous sections discussed how the microstructural evolution may impact the hardness of the material. The intent of this section is to bring each individual mechanism together through the rules of superposition outlined in Equation 14-Equation 16. Table 8 shows a summary of the hardness contributors and estimated total hardness for material irradiated at 120-280°C and 300-330°C. This exercise of linking the microstructural defects with the mechanical properties was not expected to be a perfect match, but provide insights into different mechanisms for hardening. The main take away point from this work is that helium bubbles do not appear to harden Inconel X-750 irradiated in a high thermal flux to the extent the open literature suggests [26, 29, 36, 68]. It is possible that helium bubbles in previous work were overpressurized, having higher respective barrier strengths. In many of these experimental studies, the material investigated was pre-implanted with helium to

high doses. In-reactor irradiation with helium and damage occurring simultaneously may give different equilibrium pressure states for the helium and justify the experimental differences. It is also possible that other irradiation induced defects were present in their material yet not captured in their microstructural analysis. Other possibilities could be that that bubbles may form on precipitate boundaries, and the hardness contribution was given solely to helium instead of from both precipitates and bubbles [36].

The lower irradiation results in fewer defect clusters, higher bubble density with smaller bubbles, and more disordering. It can be shown that each hardening mechanism (loops, bubbles and gamma prime) would be less significant for Inconel X-750 irradiated at lower temperatures, and together can help rationalize why material irradiated at lower temperature is softer in comparison.

**Table 8: Summary of contributors to strength following irradiation.**

	Barrier strength		Yield Strength	Yield Strength
	Literature	This Research	120-280°C (MPa)	300-330°C (MPa)
$\sigma_{\text{cold work}}^{10}$	N/A	N/A	300	300
$\sigma_{\text{solution anneal}}$	N/A	N/A	600	600
$\sigma_{\text{loop}}$	0.1	0.1	25	47
$\sigma_{\text{bubbles}}$	0.25-0.5	<b>0.03 &lt; 2.25 nm</b> <b>0.10 &gt; 2.25 nm</b>	244	252
$\sigma_{\gamma'}$	N/A	N/A	100	150
$\sigma_{\text{irradiated}}$			1164	1197
<b>hardness</b>			<b>388</b>	<b>399</b>

#### 4.1.4.4 Microstructural Features Which May Influence Grain Boundary Strength

The primary features in the irradiated microstructure that will influence the grain boundary strength are helium bubbles. In an attempt to understand how the helium bubbles influence the overall strength of the component, it may be important for us to understand differences on the grain boundary as a function of irradiation temperature. Recall that lower temperature material behaved better in crush test relative to higher temperature material (i.e. higher crush strength and higher relative plasticity). The question then arises as to why. The primary differences between the low and high

<sup>10</sup> The value of 300 MPa is selected as constant for the two irradiation temperatures. It is understood that the dislocations from cold work are not likely the same following irradiation, however, to simplify the discussion for the purposes of investigating the effects of irradiation, this assumption is made.

temperature material are associated with bubble size, bubble area coverage loss, bubble spacing and relative size of the helium bubble depletion zone.

Table 9 shows a summary of the grain boundary analysis for material irradiated to 51.2-55.0 dpa and 17300-18600 appm helium irradiated at 120-280°C and 300-330°C. Figure 57 shows a grain boundary comparison of the two relative irradiation temperatures for this dose and helium content. In both the low temperature and high temperature irradiation conditions, the bubble size is larger on the boundaries compared to the matrix material, suggesting that more helium may be migrating to the boundaries. Although the results suggest that the total bubble volume in the material is similar (0.9% compared to 1.1 %) for the two temperatures the area coverage on the grain boundary is noticeably different. Material irradiated at higher temperatures has a higher area fraction loss associated with grain boundary bubbles, in addition to a larger bubble depletion zone. The bubble spacing appears to be similar in comparison, however, it is important to note that the high temperature analysis for this was done on a small dataset from an in-plane image. Bubbles less than 4 nm were omitted from the analysis and a high population of nearing coalescence greatly deflates the spacing results. The larger grain boundary bubble depletion zone size for higher irradiation temperature is supporting evidence suggesting different vacancy and helium mobility in the two temperature regimes. It is likely that at least half of the helium from within this depletion zone has migrated to the grain boundary, leading to a higher overall helium density on the boundary. The lower temperature irradiated material has a smaller depletion zone, which may mean that more helium becomes trapped in the matrix and the boundaries have less helium in comparison

to the higher temperature condition. More helium on the boundary would lead to a larger area coverage loss (supported by the observations), and could lead to lower strength and ductility. The matrix material near the boundary being somewhat softer in the lower temperature material enables more plasticity to be accommodated in the surrounding matrix (i.e. spreading the load more uniformly, away from the boundary). This enables more plasticity prior to eventual fracture, but does not change the nature of the failure, or the failure mechanism.

**Table 9: Summary Table of grain boundary characterization for 51.2-55.0 dpa and 17300-18600 appm helium material irradiated at 120-280°C and 300-330°C.**

Feature	120-280°C	300-330°C
Bulk Bubble Density (bubbles/m <sup>3</sup> )	3.9x10 <sup>24</sup>	0.9x10 <sup>24</sup>
Bulk Volume (%)	0.9	1.1
Bulk Mean Bubble Diameter (nm)	1.5 ± 0.4	2.2 ± 1.2
Boundary Mean Bubble Diameter (nm)	1.9 ± 0.7	4.7 ± 2.3 <sup>11</sup>
Grain Boundary Area Coverage (%)	6-8	12-14
Grain Boundary Depletion Zone Size (nm)	4	20
Grain Boundary Bubble Spacing (approximate) (nm)	3.1	3.5 <sup>12</sup>

<sup>11</sup> This mean bubble diameter is taken from an edge-on analysis (not in-plane case as shown in Figure 68) because mean bubble size analysis is not meaningful when a subset of the bubble distribution was omitted from the analysis.

<sup>12</sup> Recognize that the mean spacing in this case was calculated without the inclusion of < 4 nm bubbles, and few statistics. Some bubbles close to coalescence greatly deflate the mean spacing value.

#### **4.1.4.5 Estimating the Helium-Vacancy Ratio**

Using EELS to probe individual bubbles to measure the helium density and experimentally verify individual He/V ratios as a function of bubble diameter has created a link between the nanometre scale (TEM-EELS) to the bulk (isotopic analysis), and provided insights into the distribution of helium within the microstructure. Using the EELS approach combined with quantitative bubble size and density distributions, approximately  $75 \pm 12\%$  of the total helium is shown to reside within homogenous helium bubbles in the matrix (away from grain boundaries). Using this direct measure of helium density enables a more accurate representation of He/V ratio, and bubble pressures compared to the mean approximation approach which assumes a uniform helium distribution and mean bubble size. The technique to measure the bubbles in STEM has also provided experimental verification of some helium residing in sub-microscopic defects which may be smaller than the detection limits of the technique. This result supports previous literature which postulated that helium must reside within smaller defects for the experimental results to be theoretically possible [76-87]. The other possibility for missing helium is that the helium distribution is not uniform and higher local concentrations may reside on strong sinks such as grain boundaries and other sub-grain defects. This is supported by TEM observations discussed in Sections 4.1.2.2 and 4.1.2.4, and helps support the conclusions derived in the previous section.

#### **4.1.4.6 Estimating the Bubble Pressure with a Hard Sphere Equation of State and Measured Helium Density**

The calculated pressures for helium bubbles appear to follow closely the equilibrium pressures as defined by Equation 6. The validity of this equation for nano-sized bubbles has yet been verified. There were three small, high pressured helium bubbles which strongly followed the equilibrium bubble pressure trend which were investigated in greater detail, Figure 52 and Table 5. Both experimental approaches used to measure the helium density (integrated intensity and helium cross section and Equation 10) show relatively good agreement for these three data points, and the variance plot in Figure 48 confirms the agreement. Therefore it appears as though the pressure of the homogeneous helium bubbles follow closely the bounds of equilibrium set by the balance of the surface tension of a cavity as outlined by Equation 6.

#### **4.1.4.7 Effect of Local Microstructural Inhomogeneities on Bubble Size and Density**

Section 4.1.2.3 outlines the observation that helium bubbles in grain boundary precipitates differ from within the matrix. This was observed for  $\text{Cr}_{23}\text{C}_6$  carbides and  $\text{Ni}_3\text{Ti}$  eta phase. The densities from within the precipitates were not quantified because of the relative thickness to density relationship (i.e., bubbles are smaller and density higher). Qualitatively the densities appear to differ between the carbides and the matrix. These observations are similar to that made by Mazumder et al [115] in irradiated martensitic steel where helium bubbles were found to preferentially form within grain boundary carbides compared to within the matrix or grain boundaries. Differences in microstructure and microchemistry of the precipitates will ultimately lead to differences

in vacancy and interstitial mobility. Therefore it is not altogether surprising that differences are observed with respect to bubble size and qualitative densities compared to the matrix material. The main point to take away from this observation is that Inconel X-750 grain boundaries are heavily decorated with precipitates. With respect to grain boundary embrittlement, differences in bubble structure in precipitates should be characterized to verify the evolution with dose and temperature. With continued irradiation, the bubble density is extremely high which will suppress helium mobility and likely shut down the mechanism Mazumder suggests. It is also important to note that although hydrogen embrittlement has largely been omitted from the discussion, it was noted that if hydrogen would be retained within the microstructure, it may reside within grain boundary carbides. The combined nature of local hydrogen and helium bubbles within carbides is largely unstudied in the open literature. Although outside of the scope of this thesis program, this interplay of helium and hydrogen in carbides is something which should be considered for future research.

## **4.2 Proton Irradiated Material**

The aim of the proton irradiation is to complement the experimental dataset from ex-service material and gain additional insights regarding the effects of irradiation and temperature on microstructural evolution and mechanical property evolution in Inconel X-750. Unlike working with ex-service material, the experimental conditions (temperature, dose, and helium concentration) have been carefully controlled throughout the proton irradiation. Specimens were pre-implanted with helium at room temperature followed by subsequent proton irradiations to target doses and helium concentrations of 20, 40 and 60 dpa<sup>13</sup> with 6000, 12000 and 18000 appm helium respectively. Specific insights gained from this investigation include direct relationships between microstructure and mechanical property evolution for irradiated materials with and without helium; the investigation of gamma prime disordering to very high damage levels with and without helium; and insights regarding the impact of helium in suppressing void growth during irradiation.

### **4.2.1 Effect of Proton Irradiation on the Microstructural Evolution of Inconel X-750**

To characterize the microstructure evolution, a FIB was used to prepare cross section lamella incorporating all irradiation conditions as a function of depth. This includes unirradiated material, enabling a direct comparison in each case to the unirradiated material without concern of material variability issues. The FIB samples are shown in Figure 89 for all irradiation conditions. Each TEM lamella has local helium

---

<sup>13</sup> Note that SRIM full-cascade was used to calculate doses. If the K-P approximation was performed, the doses would be approximately half.

concentrations and a local dpa. The microstructure is characterized for each lamella as a function of depth from the irradiated surface. Due to the helium concentration and dpa profiles shown in Figure 89, the specific results can be referred to by the local dose, helium, and irradiation temperature (i.e. xx dpa and yy appm helium irradiated at zz °C).

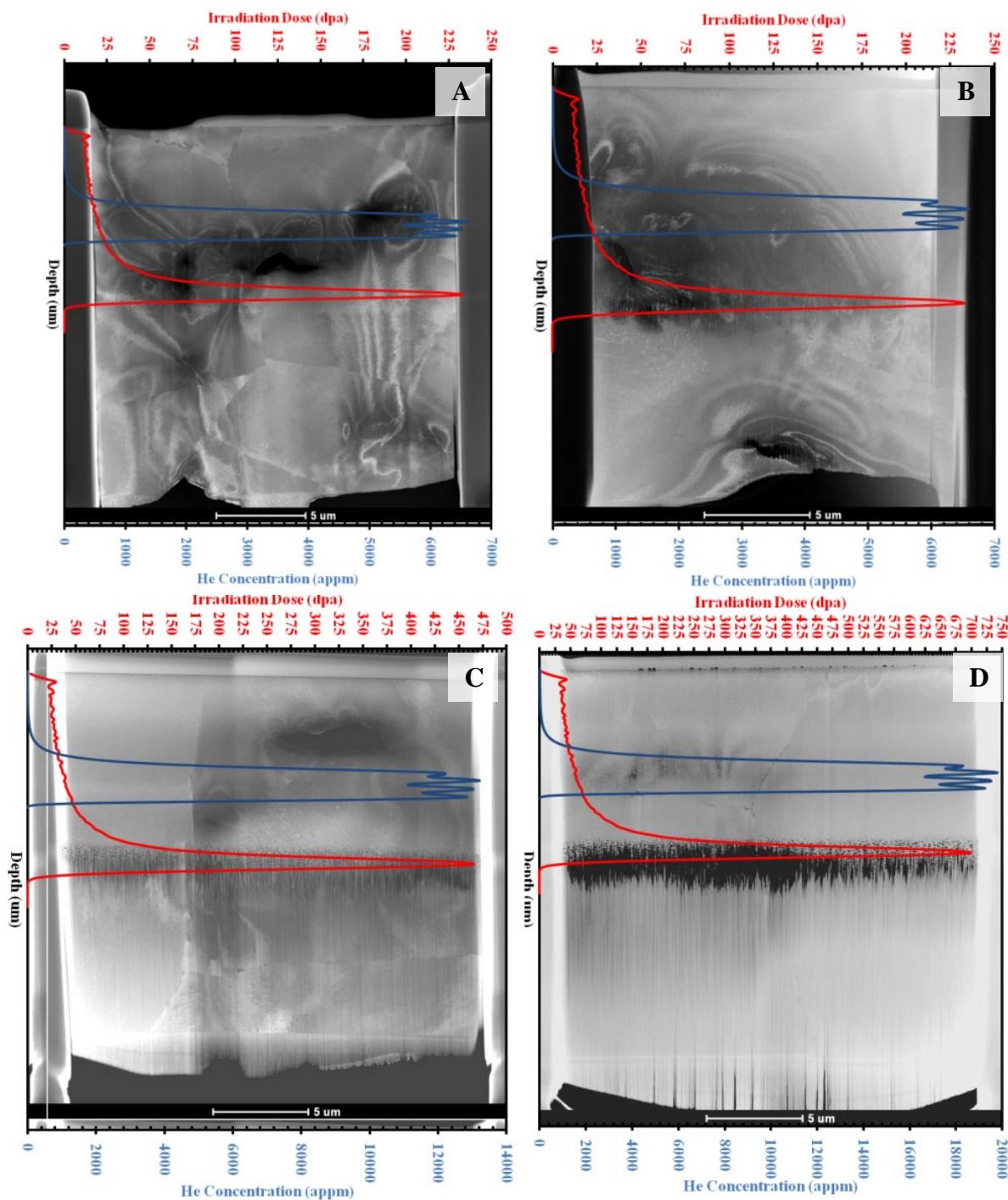


**Figure 89:** TEM cross section lamella from material irradiated to target damage and helium level at 5  $\mu\text{m}$  depths of (a) 20 dpa, 6000 appm helium irradiated at 250°C, (b) 20 dpa, 6000 appm helium irradiated at 380°C, (c) 40 dpa, 12000 appm helium irradiated at 380°C, and (d) 60 dpa, 18000 appm helium irradiated at 380°C. The profiles show the dpa depth profile (red) and helium density profile (blue) for all samples. Note that all irradiation conditions can be examined in detail within each TEM lamella, including unirradiated material for reference.

#### **4.2.1.1 Helium Bubbles**

Figure 90 shows helium bubbles imaged in the Fresnel underfocus condition ( $\sim 500$  nm) from 20 dpa-6000 appm helium irradiated at 250°C (Figure 90(a)) and 380°C (Figure 90(b)) and 40 dpa-12000 appm helium and 60 dpa-18000 appm helium irradiated at 380°C (Figure 90(c)&(d) respectively). The samples were prepared to less than 50 nm thickness, however due to the high density of bubbles, and the degree of bubble overlap, a quantitative density of the bubbles could not be obtained. There was no bubble size dependence observed as a function of irradiation temperature up to 20 dpa. The bubble size did qualitatively change from 1-2 nm in diameter to 3 nm (max) from 20 dpa-6000 appm helium to 60 dpa-18000 appm helium respectively. It is important to recognize that helium implantation was performed prior to irradiation, and at room temperature. The helium will force itself into the microstructure creating many tiny bubbles in the absence of irradiation, and subsequent implantations between irradiation phases would likely place the helium in pre-existing sinks (i.e. pre-formed bubbles). With irradiation, these bubbles grow with freely migrating point defects to an equilibrium state, but the general density of bubbles was pre-determined based on the implantation process (i.e. density of bubbles was not affected by irradiation process). The matrix bubbles were only observed within a small, 1  $\mu\text{m}$  band within the target dose and helium region as shown in Figure 32, and Figure 89 respectively.

As expected, the helium bubbles also align along grain boundaries, Figure 91. This was observed in all irradiation conditions and temperatures. No detectable grain boundary bubble denuded zones were observed in any of the irradiated samples.

#### 4.2.1.2 Voids

In addition to a small band of helium bubbles at a depth of 1  $\mu\text{m}$ , voids were observed in all specimens. Voids in this material are likely associated with irradiation induced swelling, and in the form of stable vacancy clusters within the microstructure. For the 20 dpa specimens irradiated at 250°C and 380°C, the voids were limited to the high dpa range at approximately 9-10  $\mu\text{m}$  from the irradiation surface; however the 40 dpa and 60 dpa irradiations at 380°C had voids present at depths of 0-4  $\mu\text{m}$  and 6-10  $\mu\text{m}$  from the irradiation surface coincident with locations in the material with no implanted helium. The size and density of the voids were dependent on the dose. Figure 92 shows voids in regions with 40 dpa and 60 dpa (no helium) and dose transition zones between 40-450 dpa and 60-675 dpa (no helium). Figure 93 shows voids in regions without helium pre-implantation from the 60 dpa-18000 appm helium (380°C) specimen. It is important to note that within the region of helium pre-implantation (i.e. 4.5  $\mu\text{m}$  – 5.5  $\mu\text{m}$  from the irradiation surface), only the 1-3 nm bubbles were observed. It shows that helium has suppressed void formation by creating a high density of defects to limit freely migrating point defects within the material. Very large voids were found at the stopping depth of the proton irradiation (i.e. a depth of approximately 9-10  $\mu\text{m}$  from the irradiation surface). This was observed in all irradiated specimens. The void size and the width of the void band increase with continued irradiation. The formation of the voids are evidence that Inconel X-750 irradiated at these conditions are in the sink dominated regime shown in Figure 10 and Figure 31. Vacancies and SIA are not recombined allowing for more vacancy mobility leading to stable cluster and void formation. Another possibility which

cannot be ruled out is the interplay of hydrogen atoms assisting in the nucleation of these voids. If molecular hydrogen forms, it will assist in stabilizing irradiation induced voids, and thus this cannot be ruled out. This is a major limitation of using protons for the investigation of void swelling in materials.

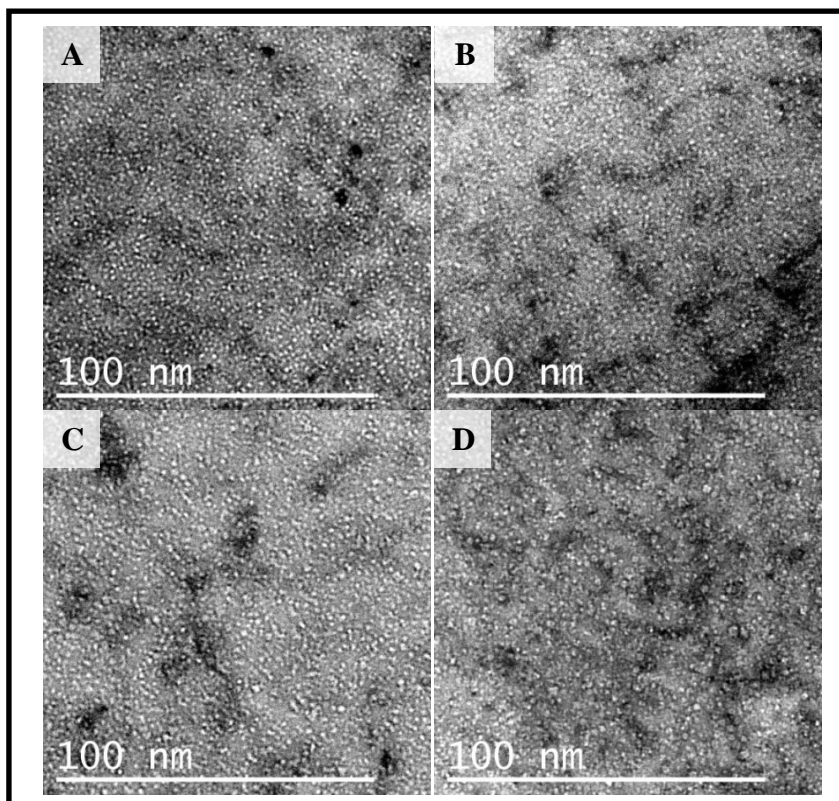


**Figure 90: He bubbles in the underfocussed condition (-500 nm) for (a) 20 dpa 6000 appm He 250°C, (b) 20 dpa 6000 appm He 380°C, (c) 40 dpa 12000 appm He 380°C, and (d) 60 dpa 18000 appm He 380°C.**

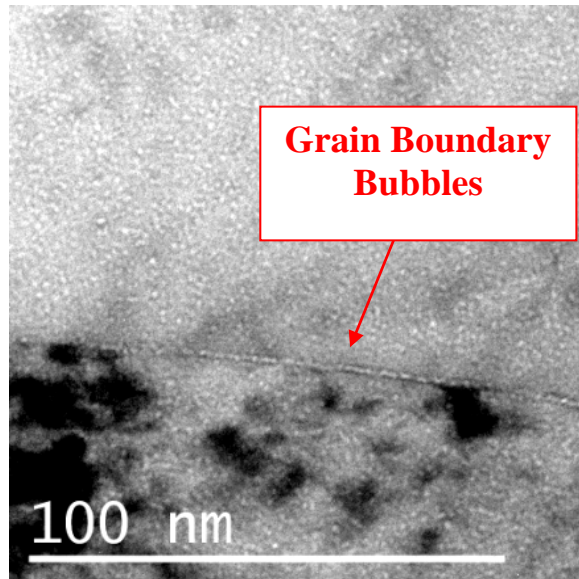


**Figure 91: Grain boundary helium bubbles for 20 dpa 6000 appm He 380°C conditions. All conditions show similar bubble alignment on grain boundaries.**

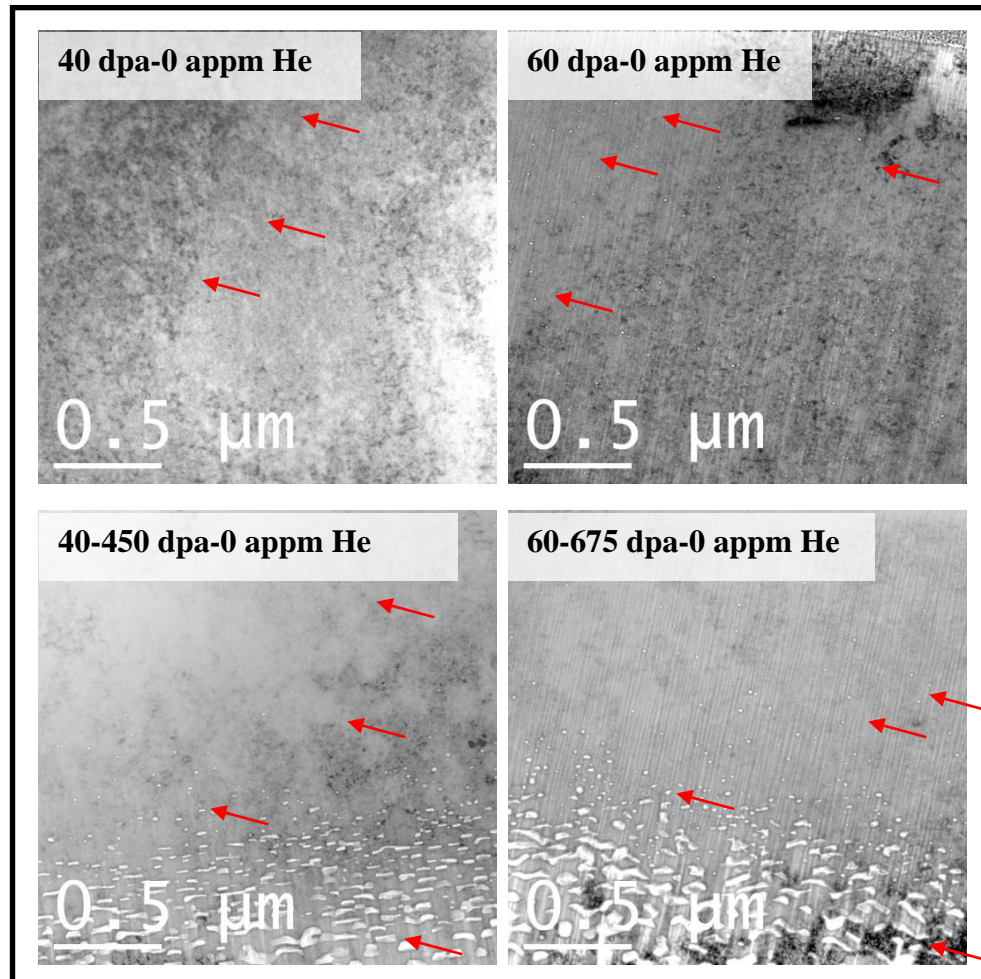


**Figure 92: Voids in irradiated material without He implantation for material irradiated at 380°C up to 40 dpa and 60 dpa and 40-450 dpa and 60-675 dpa respectively. Red arrows indicate locations of voids (but not limited to).**

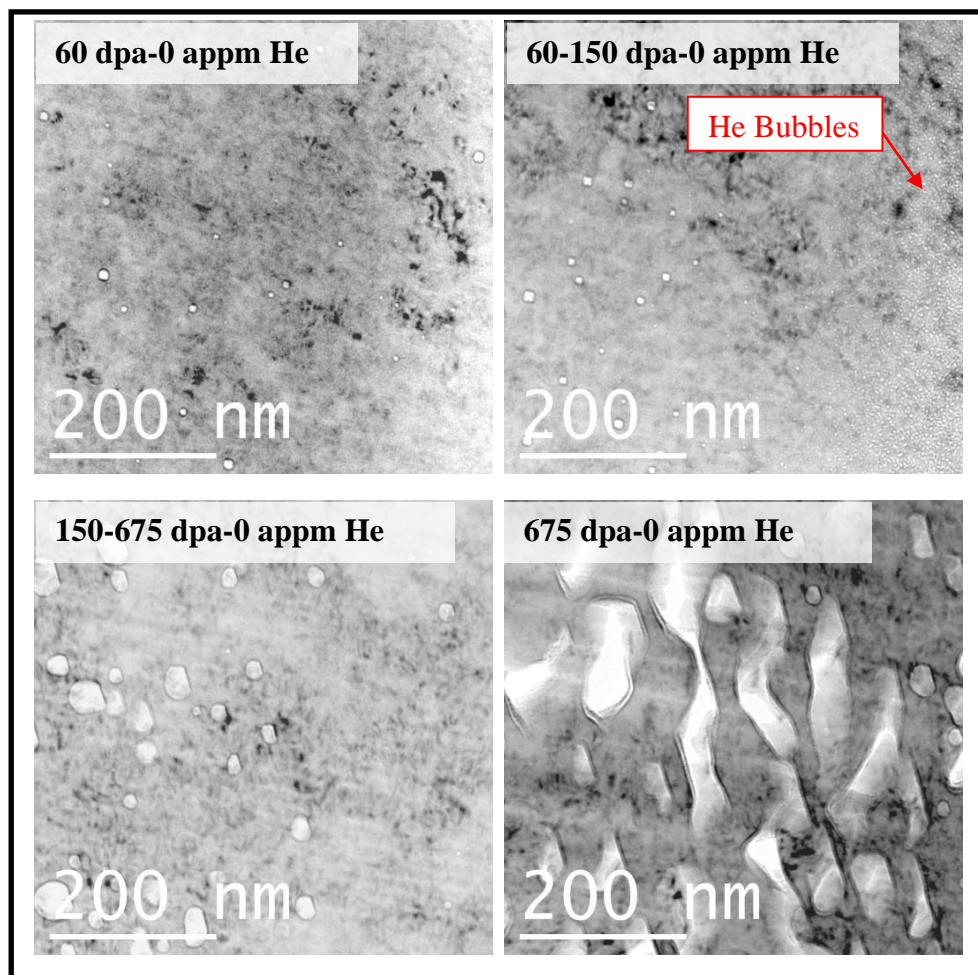


**Figure 93: Voids in regions with no helium implantation for 60 dpa, 60-150 dpa, 150-675 dpa and 675 dpa respectively. Red arrow indicating location of 1-3 nm He bubbles in region pre-implanted with 18000 appm He.**

Figure 94 shows a high angle annular dark-field (HAADF) image of voids for the 225 dpa region irradiated at 250°C. This specimen shows a void lattice structure within the matrix (voids are lower density compared to the matrix and are therefore showing up as dark dots in the microstructure). Note that the voids only formed within the matrix material, and not within secondary precipitates. The lack of voids in the secondary precipitates would indicate different vacancy mobility compared to the matrix.

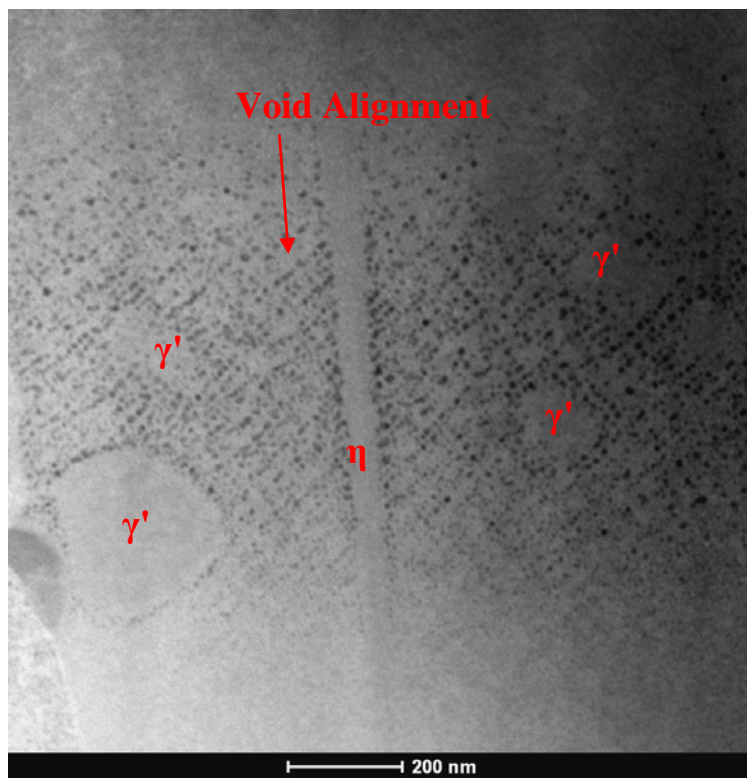


**Figure 94: STEM HAADF image of large voids at 225 dpa 0 He irradiated at 250°C. The voids align along precipitate boundaries (gamma prime and eta phases highlighted) indicating different vacancy mobility in secondary precipitates compared to the matrix.**

#### 4.2.1.3 Stability of Gamma Prime

Figure 95 shows the characterization of gamma prime in unirradiated material. In bright-field imaging, Figure 95(a), the strain field surrounding the  $\gamma'$  is very apparent. In diffraction, clear (011) or (001) superlattice reflections are strong compared to the (022) and (002) matrix reflections, Figure 95(b). When imaged in dark-field, there is very strong diffraction contrast, Figure 95(c). EELS spectrum imaging shows the elemental distribution of Ti, Ni and Cr associated with  $\gamma'$ . There is a bimodal size distribution associated with the  $\gamma'$  in this material. This differs slightly from the  $\gamma'$  present in the

CANDU spacers (no bimodal distribution). The size of the selected area diffraction (SAD) aperture does not enable individual assessment of order structure as a function of  $\gamma'$  size, and therefore differentiation of disordering between large and small  $\gamma'$  is not possible with this technique. This is addressed later with the aid of STEM nano-diffraction.

Figure 96 and Figure 97 show the  $\gamma'$  characterization for material irradiated to a target of 20 dpa and 6000 appm helium at 250°C and 380°C respectively. In both irradiation conditions, the strain field surrounding the  $\gamma'$  in bright-field was no longer observed. This may suggest dissolution of  $\gamma'$ , however the EELS analysis shows no evidence of dissolution, suggesting that the strain field surrounding the  $\gamma'$  is linked with the ordered structure of the precipitate and not the local lattice mismatch associated with local enrichment of Al and Ti. Alternatively, the lack of strain field may be present but difficult to differentiate in the microstructures as a result of high density of irradiation induced defects. In both conditions, the  $\gamma'$  superlattice reflection was weakly observed, and diffraction contrast in dark-field imaging of gamma prime giving evidence of partial disordering (Figure 96(c) and Figure 97(c)). The dark-field images show weak contrast, yet the EELS spectrum imaging, Figure 96(d) and Figure 97(d) shows no apparent local diffusion of Ti, Cr or Ni. Because the sample thickness varies from different samples and within samples, this data is not sufficient to add comment regarding elemental segregation or degree of dissolution of gamma prime. Figure 98 through Figure 101 show the complete  $\gamma'$  electron diffraction and EELS spectroscopy for all conditions in the irradiated specimens. Evidence of gamma prime superlattice reflections was found for all

irradiation conditions including the stopping depth for protons at approximately 9  $\mu\text{m}$  and doses of up to a maximum dose of 675 dpa (SRIM full-cascade).

This work differs from the literature for the dose rates and temperatures studied. Unlike assessments using high energy Kr ions [47-49], the current irradiation conditions and characterization shows that to very high doses with and without helium,  $\gamma'$  is not fully disordered. It is important to recognize that although some ordering is observed in all of the irradiation conditions; the relative intensity of the superlattice reflection with respect to the matrix reflections is very weak compared to the unirradiated material. Therefore, it can be concluded in the current study that  $\gamma'$  remains ordered. The degree of ordering, or the volume fraction of  $\gamma'$ , has not been quantified. The observation of gamma prime superlattice reflections was possible at the expense of oversaturating the TEM camera, and it should be noted that the detection of these patterns may be dependent on the camera system sensitivity. This may account for differences between the current results the observations in the open literature. The fact that a superlattice is observed in all irradiation conditions in this study is unambiguous compared to not detecting it, and therefore the present conclusions are significant compared to the observations in the open literature.

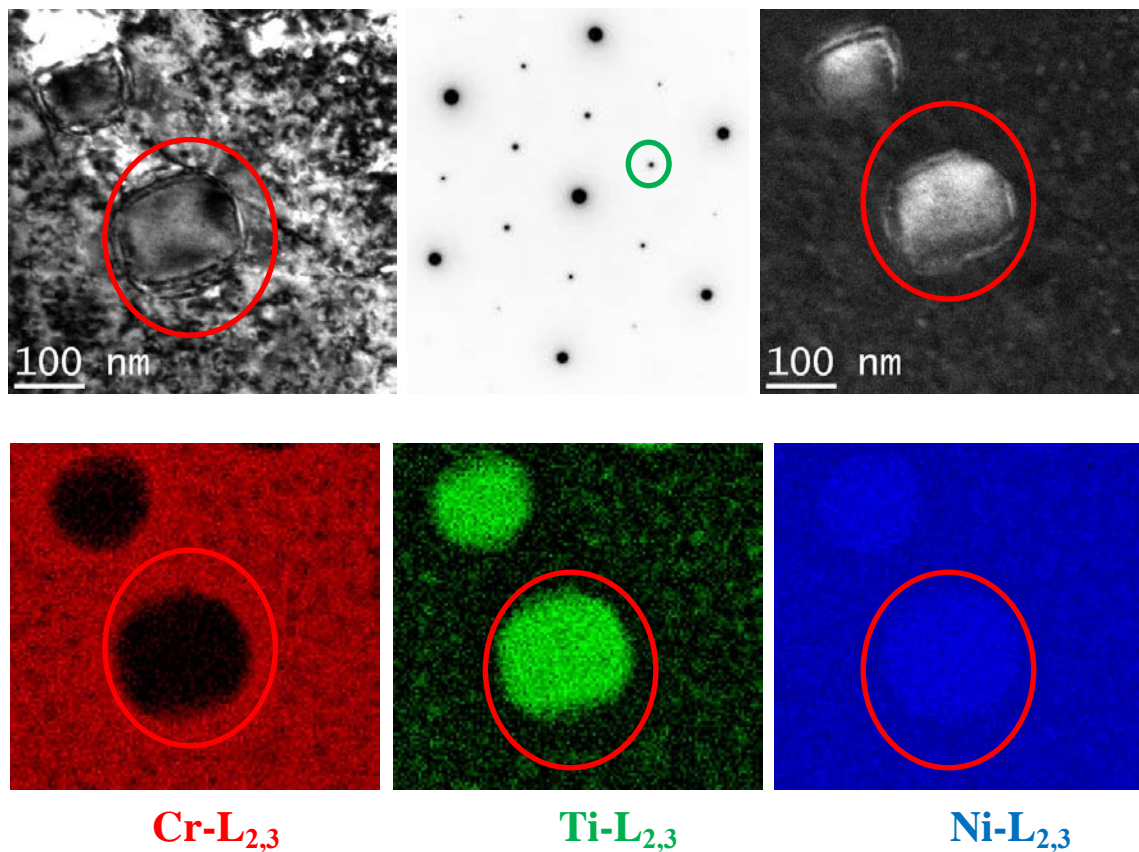
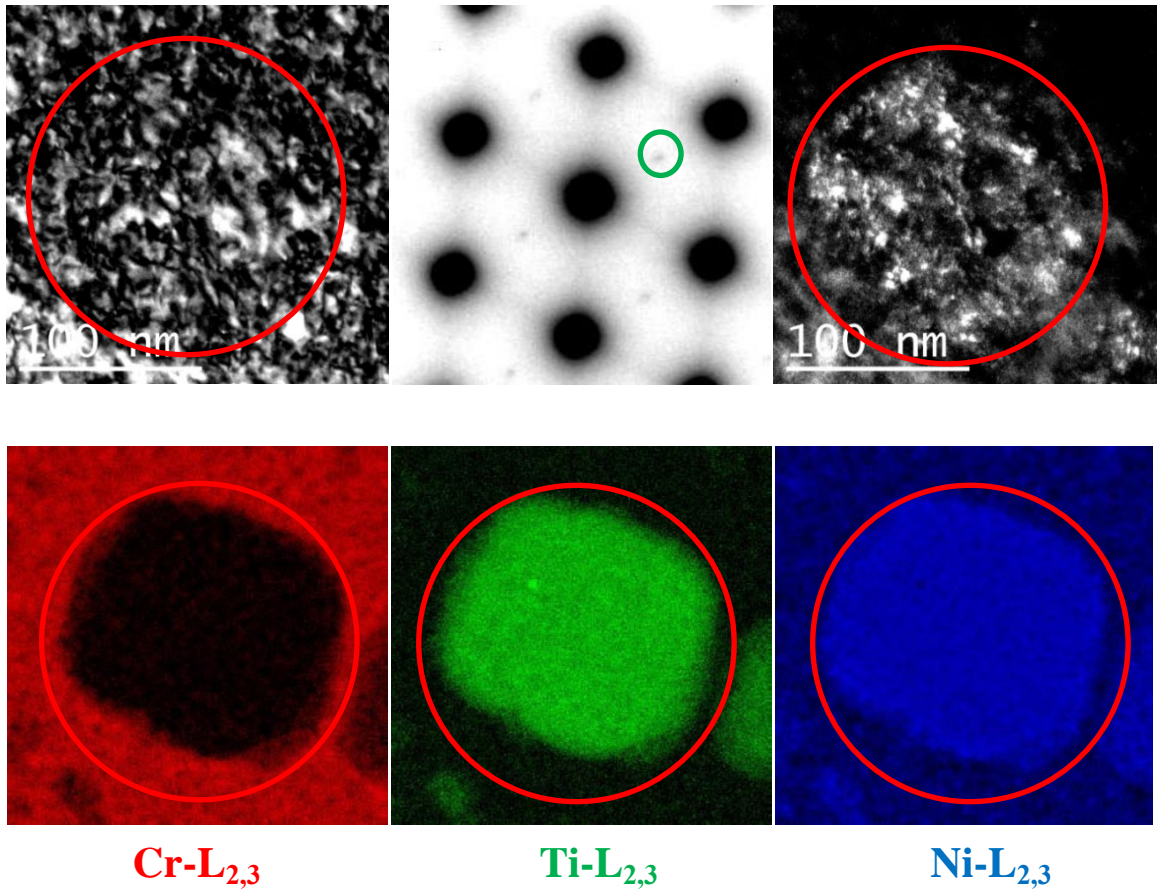


**Figure 95: Bright-field and dark-field images of  $\gamma'$  in unirradiated material imaged in (A) Bright-field, (B) electron diffraction showing gamma prime superlattice reflection (green circle), (C) dark-field, and (D) EELS spectrum imaging of  $L_{2,3}$  edges of Cr, Ti, and Ni. Red circles highlight location of  $\gamma'$ . Green circle highlights selection for dark-field on (110) superlattice reflection.**



**Cr-L<sub>2,3</sub>**                      **Ti-L<sub>2,3</sub>**                      **Ni-L<sub>2,3</sub>**

**Figure 96: Bright-field and dark-field images of  $\gamma'$  in irradiated material (20 dpa-6000 appm He) irradiated at 250°C. EELS spectrum imaging of the same region was performed to show the chemical signatures of the precipitate have not changed significantly. Red circles highlight location of  $\gamma'$ . Green circle highlights selection for dark-field on (110) superlattice reflection.**

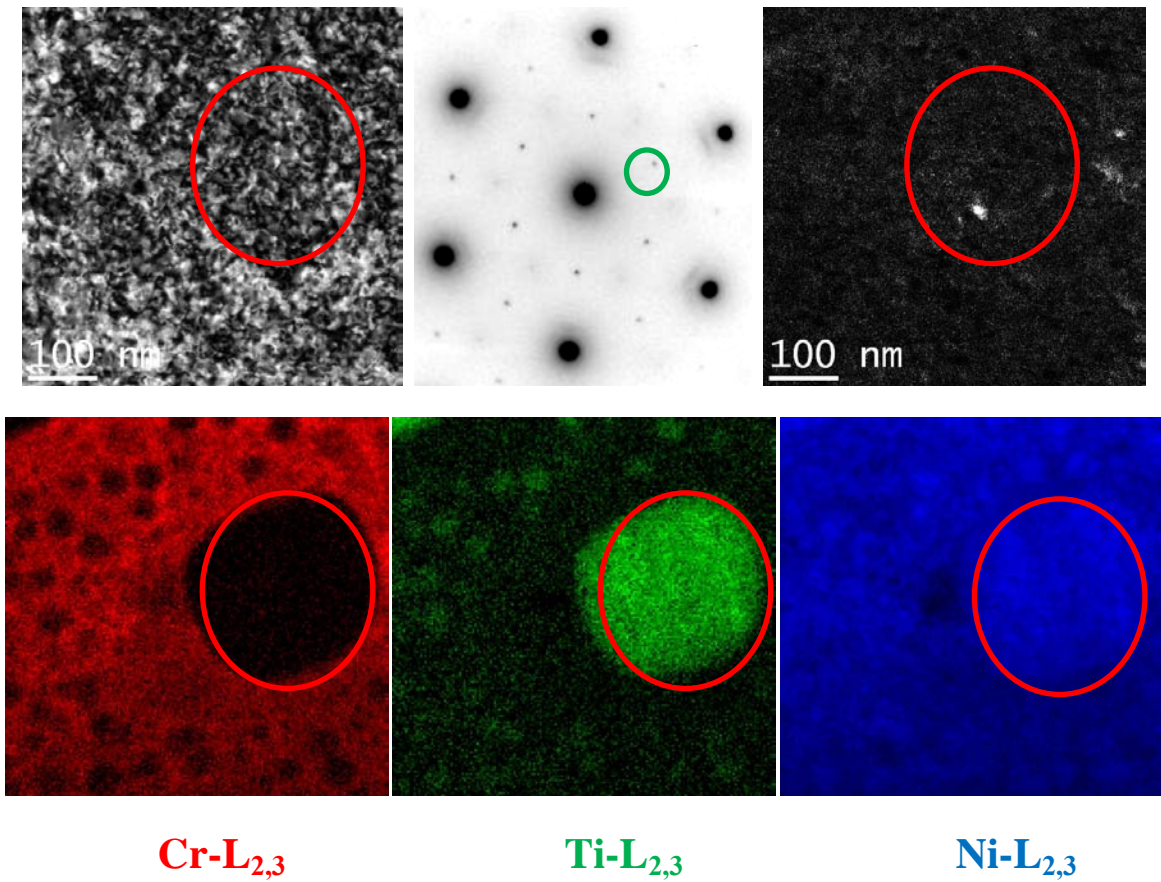


**Figure 97: Bright-field and dark-field images of  $\gamma'$  in irradiated material (20 dpa – 6000 appm He) irradiated at 380°C. EELS spectrum imaging of the same region was performed to show the chemical signatures of the precipitate have not changed significantly. Red circles highlight location of  $\gamma'$ . Green circle highlights selection for dark-field on (110) superlattice reflection.**

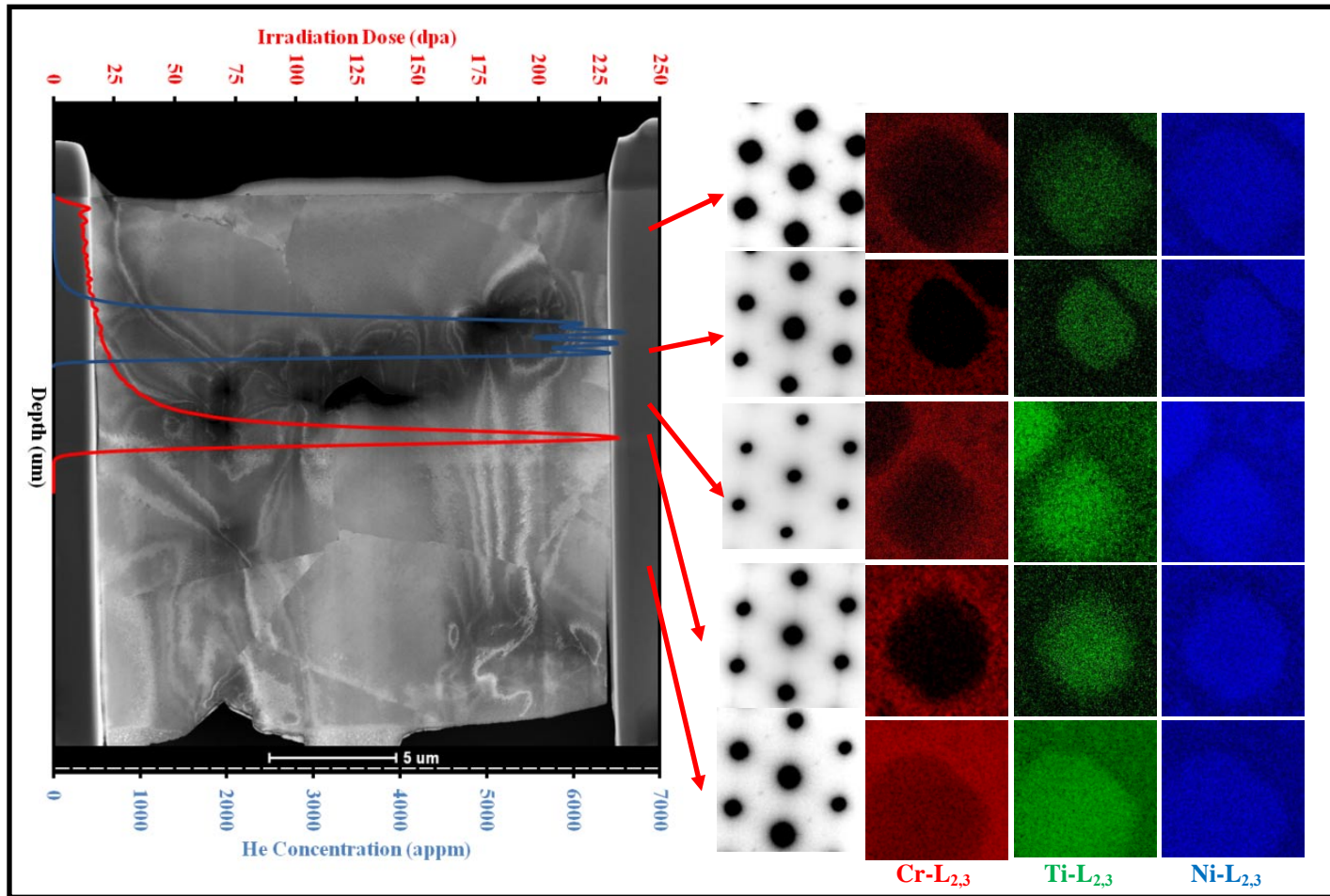


Figure 98: Gamma prime characterization in specimen irradiated to target 20 dpa, 6000 appm He irradiated at 250°C.

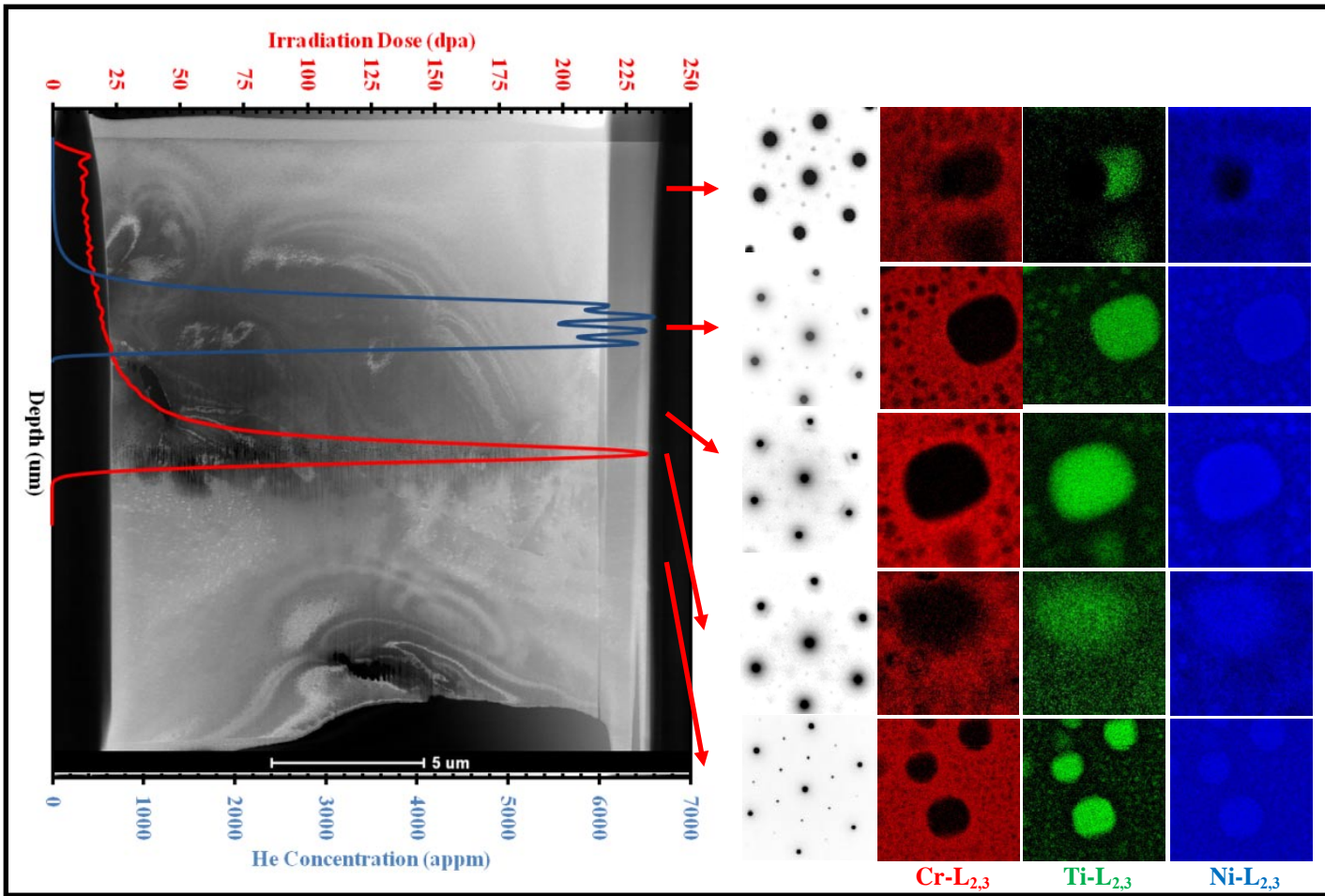


Figure 99: Gamma prime characterization in specimen irradiated to target 20 dpa, 6000 appm He irradiated at 380°C.

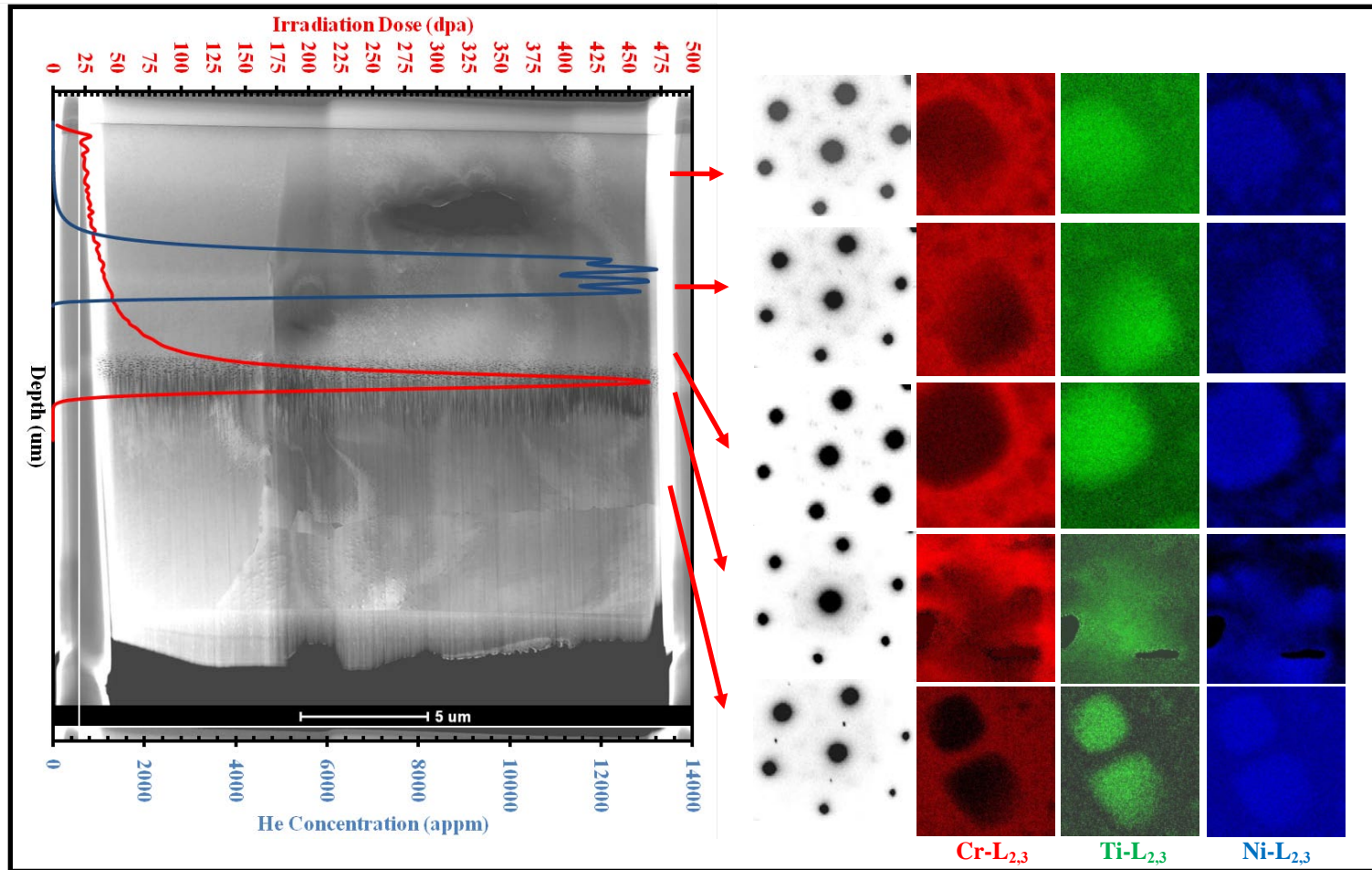


Figure 100: Gamma prime characterization in specimen irradiated to target 40 dpa, 12000 appm He irradiated at 380°C.

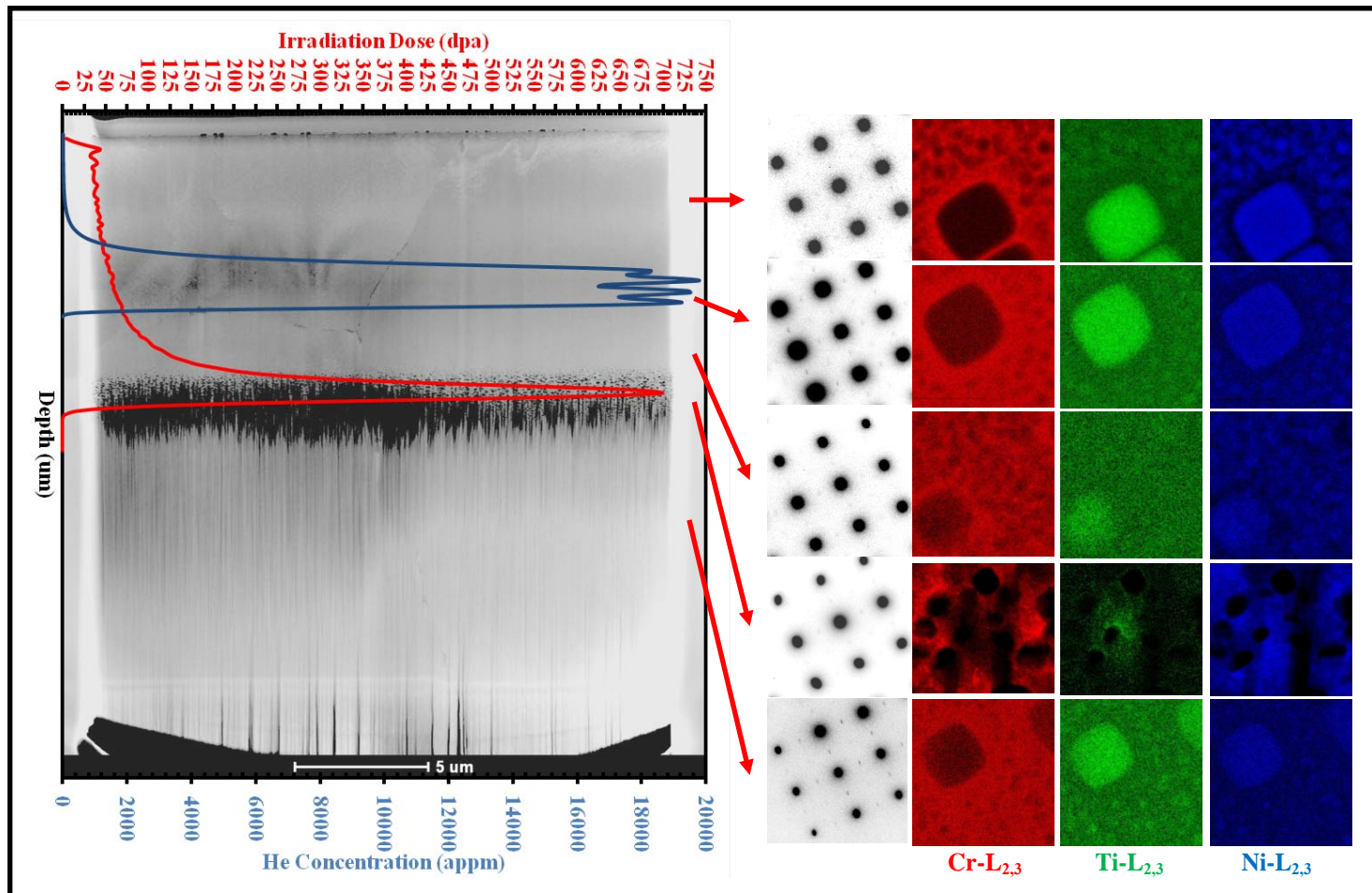


Figure 101: Gamma prime characterization in specimen irradiated to target 60 dpa, 18000 appm He irradiated at 380°C.

#### 4.2.1.3.1 STEM Diffraction of Gamma Prime

Because the SAD aperture used for the study was rather large, it was difficult to differentiate if disordering of the precipitates was influenced by the precipitate size. In other words, the gamma prime in the proton irradiated material was bimodal; having larger 80-150 nm  $\gamma'$  and smaller 10-20 nm  $\gamma'$  (similar to size scale of  $\gamma'$  in ex-service material). To link the observations of  $\gamma'$  in the proton study with the ex-service neutron irradiation, it should be determined if disordering of  $\gamma'$  is dependent on the relative size of the precipitate. STEM diffraction was therefore performed on unirradiated material and material irradiated to a target dose of 20 dpa and 6000 appm helium at 380°C.

Figure 102 shows the diffraction analysis for unirradiated material, showing a strong superlattice reflection from the larger  $\gamma'$ , a faint superlattice from the smaller  $\gamma'$ , and no detectable superlattice in a region in the gamma matrix. The relative intensity of the superlattice between the smaller and larger  $\gamma'$  is a result of the volume fraction of the precipitate in the excitation volume of the transmitted beam. Larger  $\gamma'$  being the entire thickness and smaller  $\gamma'$  being only a fraction. Figure 103 shows the STEM analysis for material irradiated at 380°C to a target of 20 dpa with 6000 appm helium. The larger  $\gamma'$  still has a faint superlattice (much fainter compared to Figure 102), but no detectable superlattice could be found in the surrounding matrix. Because the strain field surrounding the smaller  $\gamma'$  was not visible in the irradiated condition the diffraction pattern shown is labelled as from the surrounding matrix. It should be noted that this is believed to be representative of the smaller  $\gamma'$  as no visible differences in the diffraction patterns could be discerned. The advantage of STEM diffraction is that for every pixel, a

diffraction pattern is collected. It is important to note that there was no evidence of a superlattice reflection within this map other than the larger  $\gamma'$ .

These results support for the conclusion that the superlattice reflections observed in Figure 96 through Figure 101 are linked with the larger  $\gamma'$  precipitates, and the smaller  $\gamma'$  may be fully disordered. It is possible that the detection limits of STEM diffraction differ from diffraction limits with a SAD aperture, which may limit TEM sensitivity to study the smaller  $\gamma'$ .

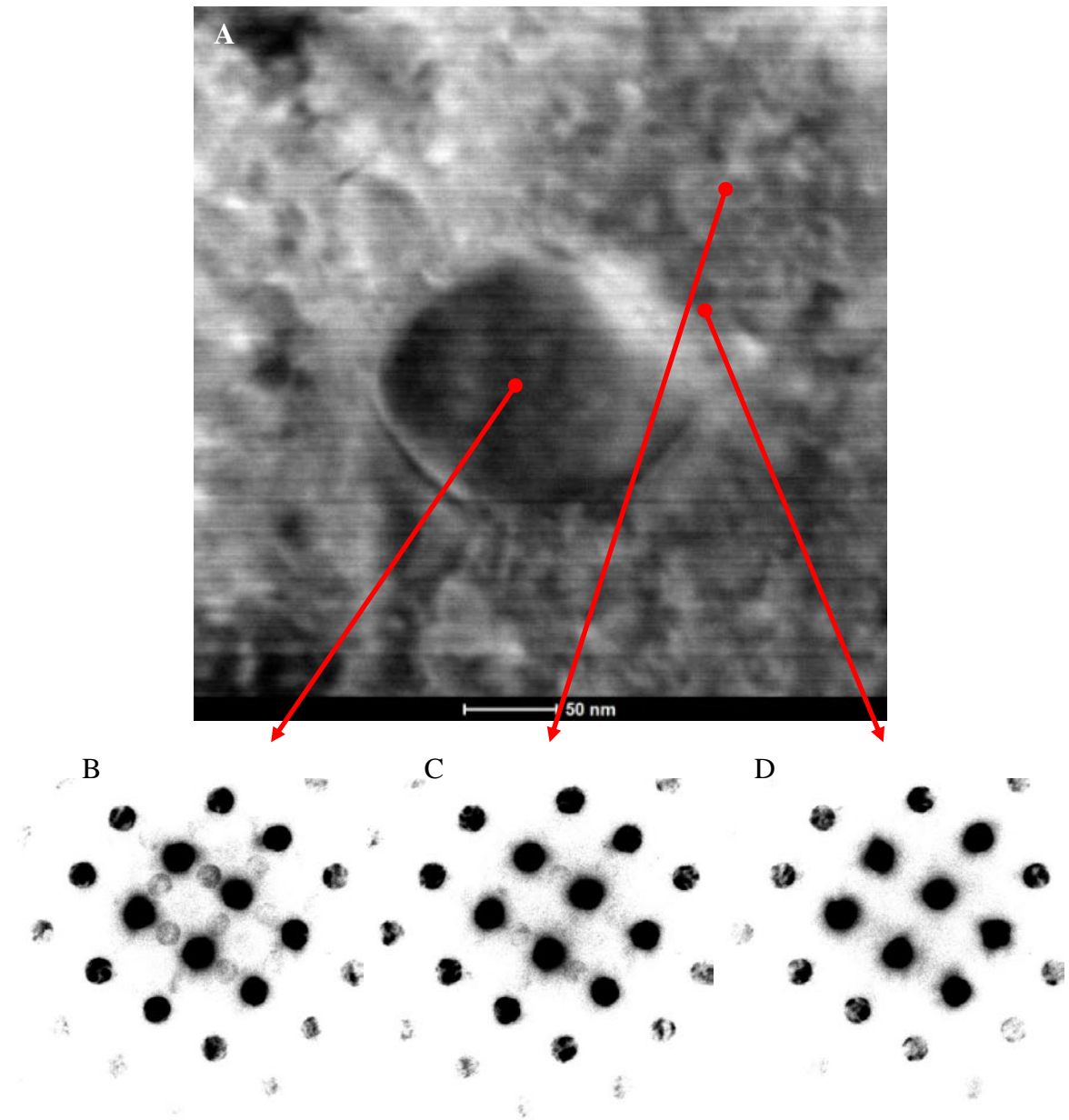


**Figure 102: STEM diffraction on the (001) zone axis for unirradiated material. (A) HAADF image of gamma prime, (B) diffraction pattern from large gamma prime precipitate showing a strong superlattice reflection, (C) diffraction pattern from small gamma prime precipitate showing a weak superlattice reflection, and (D) diffraction pattern from gamma matrix with no superlattice reflection.**

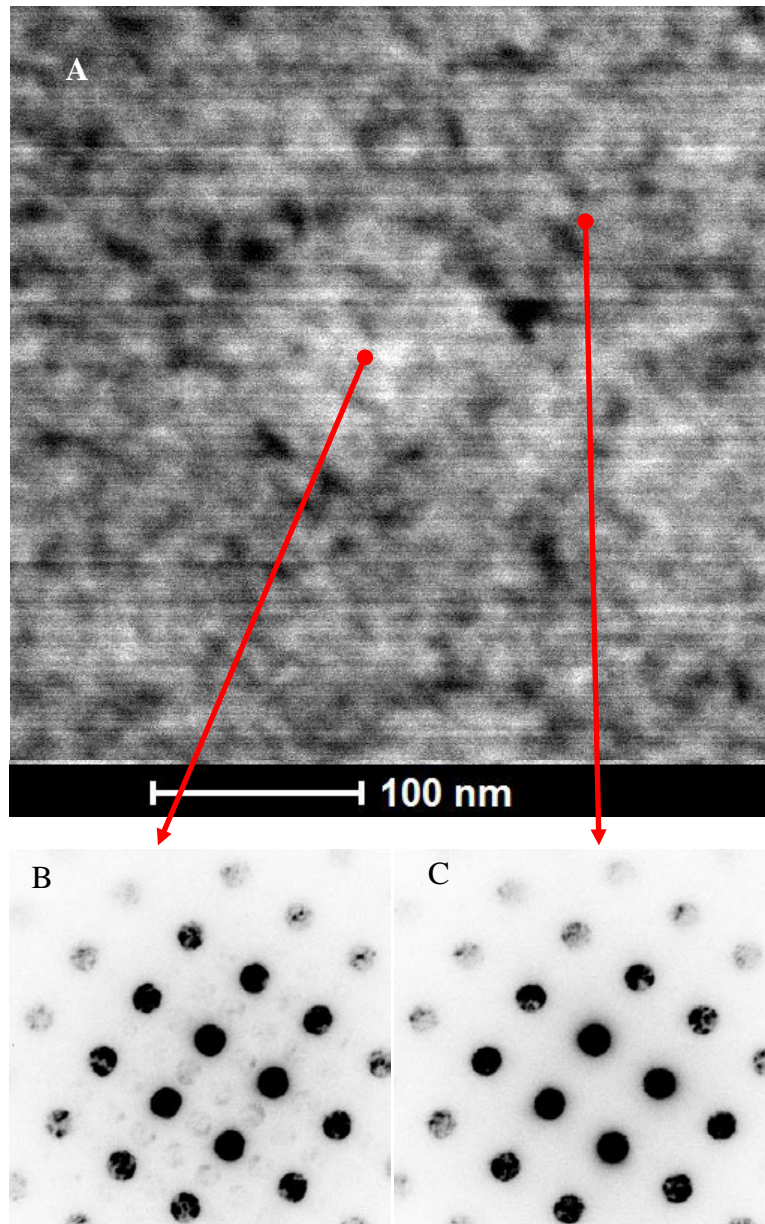


**Figure 103: STEM diffraction on the (001) zone axis for material irradiated to 20 dpa with 6000 appm helium. (A) HAADF image of gamma prime, (B) diffraction pattern from large gamma prime showing a faint superlattice reflection, and (C) diffraction pattern from gamma matrix (small gamma prime) with no superlattice reflection.**

#### **4.2.2 Effect of Proton Irradiation on the Mechanical Property Evolution of Inconel X-750**

The mechanical property evolution in irradiated Inconel X-750 has been measured with microhardness and nanohardness. The microhardness testing was performed on the irradiated surfaces, however, the scale of the measurement is not appropriate for comparing the hardness as a function of the depth profile in the material and directly link with the microstructural evolution presented in the previous chapter. Therefore, nanohardness profiles are performed on all specimens.

##### **4.2.2.1 Micro-Hardness**

The microhardness test results are shown in Figure 104 and presented as a percent change with respect to the starting unirradiated hardness. It should be noted that the Vickers microhardness was performed using a load of 25 g which would indent approximately 2  $\mu\text{m}$  into the material and the plastic zone would average much of the irradiation profile shown in Figure 33. The results indicate that the hardness increased 15% following helium pre-implantation. This increase may be a result of one of two factors: 1) helium bubble formation at the 5  $\mu\text{m}$  depth, or 2) irradiation damage produced as a result of implanting the helium into the material estimated at approximately 1 dpa. Following irradiation, a hardening of approximately 30-40% was observed with no difference observed as a function of dpa, helium or irradiation temperature.

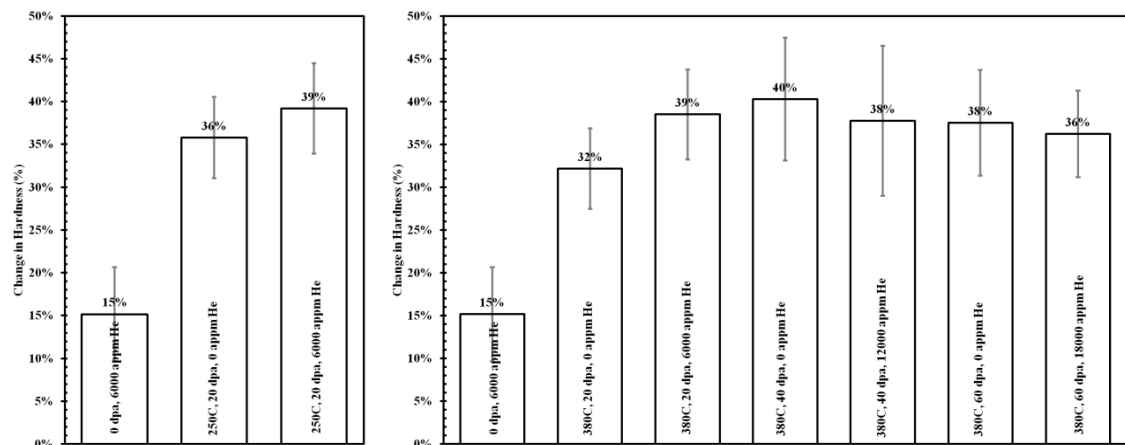


**Figure 104: Change in Micro-hardness for samples implanted with helium (0 dpa), and with and without helium irradiated to 20 dpa, 40 dpa and 60 dpa respectively (dpa values representative of full-cascade SRIM).**

#### 4.2.2.2 Nanohardness

It is important for us to differentiate regions within the irradiation depth profile. Nanohardness profiles were therefore performed on each sample implanted with helium and irradiated. Figure 105 shows the nanohardness profile for material irradiated to a target dose of 20 dpa with 6000 appm helium at 250°C. The depths beyond 12  $\mu\text{m}$  show the relative unirradiated hardness used for measuring the hardening as a fractional change. This allows for comparing changes within the material directly without the need for complex models to understand the size effect associated with testing at different scales. This enables a relative comparison with microhardness results, however, to obtain specific values for comparing, complex modelling is a requirement.

Within the uniform damage layer the hardness has increased by approximately 20-25%. There does appear to be a minor increase in hardening at the region implanted with

helium, however, this high hardness extends deeper into the material at regions with higher damage. Due to the number of defects introduced during this type of irradiation, it is unclear if this increase can be attributed to helium bubble formation, however this degree of hardening is less than would be expected should a dispersive barrier model be applied to the size and density of helium bubbles (similar to observations from hardening in ex-service material). Figure 106, Figure 107, and Figure 108 show the nanohardness profiles for material irradiated to 20, 40 and 60 dpa with 6000, 12000 and 18000 appm helium irradiated at 380°C respectively. The hardening appears to have saturated at low dose. 20, 40 and 60 dpa material all have hardened by approximately 20-25%. As with the low temperature irradiation, a minor increase in hardening occurs at the depth of helium implantation, however the change is minor.

An interesting feature to note is associated is the softening which occurs in the 40 and 60 dpa specimens. This softening coincides with the proton stopping depth at approximately 9  $\mu\text{m}$ . As shown in Figure 92 and Figure 93, this region in the material is filled with a high density of large voids. Although voids were also observed in 20 dpa samples, the voids were smaller in comparison. Another feature to note is that the width of the softened region increases with dose (i.e. from 40 to 60 dpa). This is likely attributed to the relative depth at which protons stop. SRIM calculations are performed assuming a uniform density material, however, with continued irradiation, this is no longer the case, and the protons will penetrate deeper within the material. The reasoning for the softened material remains unknown. This may be a result of the large voids, and/or a local temperature spike attributed with the proton stopping depth.

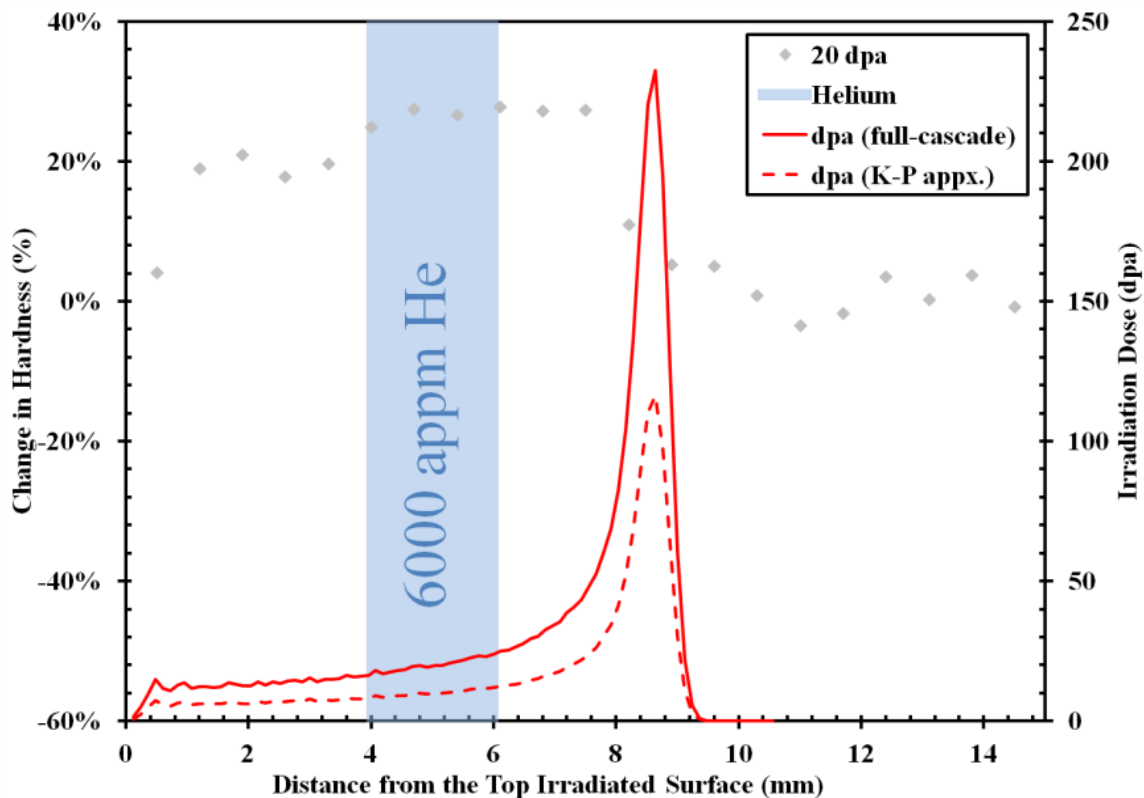


Figure 105: Nanohardness profile for material irradiated to a target dpa and helium concentration of 20 dpa and 6000 appm helium at 250°C.

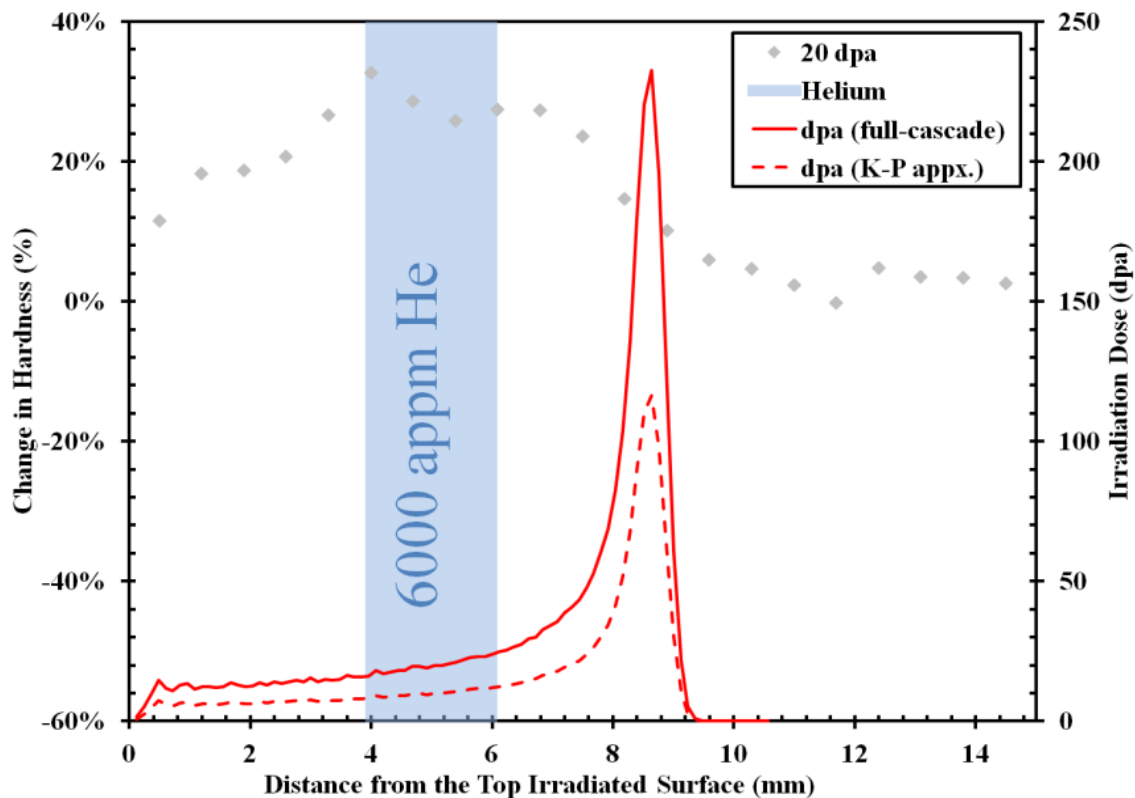
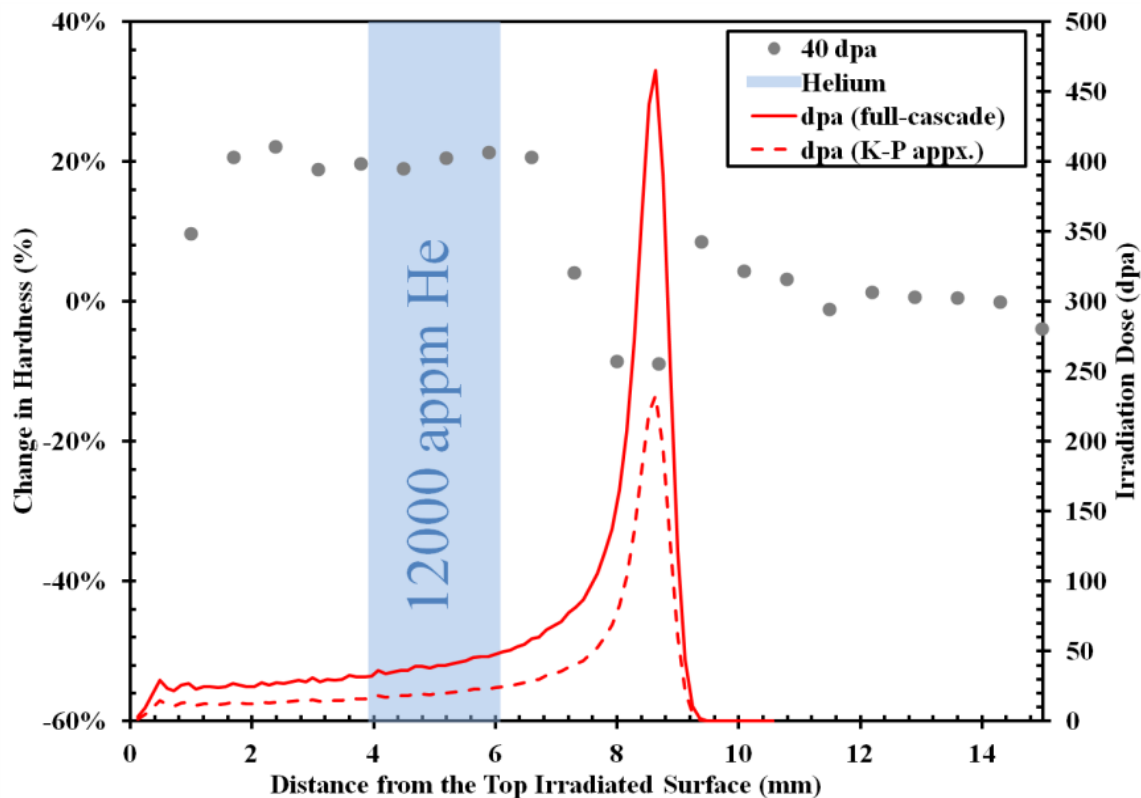


Figure 106: Nanohardness profile for material irradiated to a target dpa and helium concentration of 20 dpa and 6000 appm helium at 380°C.



**Figure 107:** Nanohardness profile for material irradiated to a target dpa and helium concentration of 40 dpa and 12000 appm helium at 380°C.

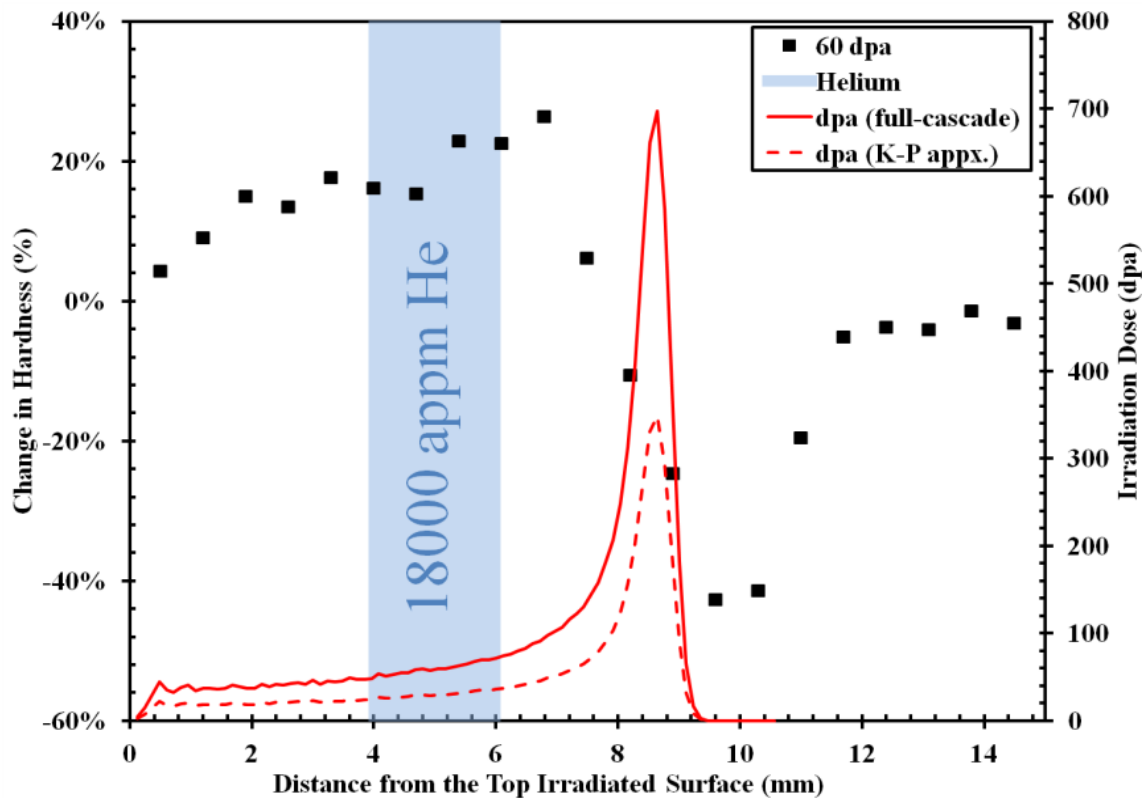


Figure 108: Nanohardness profile for material irradiated to a target dpa and helium concentration of 60 dpa and 18000 appm helium at 380°C.

### **4.2.3 Discussion: Proton Irradiated Materials**

In this section, the results of the proton irradiation microstructure characterization, microhardness, and nanohardness will be discussed. The objectives of this research is to investigate the influence of proton irradiation on the evolution of the microstructure and mechanical properties of Inconel X-750. These results will be discussed in terms of gaining additional insights into the fundamental mechanisms of irradiation damage in Inconel X-750.

#### **4.2.3.1 Suppression of Void Formation with Helium**

The main focus of this thesis has been on helium bubble evolution and distribution within the matrix. The aim of the proton program was to investigate the differences in microstructure as a function of dose, helium density and temperature in a controlled environment. Following the first phase of irradiation, there was no noticeable difference in helium bubbles between the low temperature and higher temperature irradiated material. This suggests that although the material is irradiated at 250°C and 380°C respectively, the formation of helium bubbles may have been pre-determined through the implantation process at room temperature. The aim of the program was to investigate the nature of vacancy mobility and recombination on bubble dynamics. If the bubble density was dictated during the helium implantation process then the only reasonable observation to make is a difference in bubble size which would indicate a differences in freely migrating point defects. No noticeable bubble size difference between 250°C and 380°C would indicate that the temperature shift for irradiation may not have been enough to put the higher temperature material into the sink dominated regime. Alternatively, it is possible that bubble growth occurs at higher doses, as supported by the neutron irradiated observations for low dose material (i.e. similar bubble size distributions for different temperatures). A minor increase in bubble diameter is shown in Figure 90 between 20 dpa, 40 dpa and 60 dpa, however, the change is very small.

A noteworthy observation in this investigation is that helium bubbles seemed to suppress void formation. In the 40 dpa and 60 dpa material, large voids were observed throughout the material, increasing in size with higher doses. No large voids were observed in the region of helium implantation (i.e.,  $5 \pm 0.5 \mu\text{m}$  from the irradiation surface) as shown in Figure 92 and Figure 93. This would suggest that although Inconel X-750 is prone to void swelling at these irradiation conditions helium has acted to suppress void growth. This is likely because of the high concentration of defect (i.e., bubbles) limiting vacancy mobility. It should be noted that with irradiation via protons (i.e. H atoms), it is possible that the hydrogen may play a role in the formation of voids in the microstructure. This has highlighted a limitation of the use of protons for irradiation experiments.

In all irradiation conditions, very large voids were observed at the stopping depth for protons (approximately  $9 \mu\text{m}$  from the irradiation surface). The void size increased as a function of total damage, and the width of the void band increased with increasing dose. The  $250^\circ\text{C}$  material showed larger void formation, and preferential void formation at  $\gamma'$  and eta phase boundaries. There was a lack of void formation within the secondary precipitates. This suggests differences in defect mobility and potential preferential void formation at coherent interfaces in the matrix. No observed preferential nucleation for helium bubbles at these interfaces has been made.

#### **4.2.3.2 Characterization of Gamma Prime**

Characterization of the  $\gamma'$  in the proton samples shows that gamma prime was partially ordered in all irradiation conditions (with and without helium). There was no observed difference in gamma prime disordering or dissolution as a function of dose or temperature. The gamma prime characterization performed on this material suggests a slightly different metric for gamma prime

disordering compared to the literature. Figure 95-Figure 97 shows bright-field, dark-field, electron diffraction and EELS mapping of the gamma prime. The dark-field imaging suggests that the  $\gamma'$  has disordered, dissolved and re-precipitated as smaller  $\gamma'$ . This is similar to observations made in past disordering studies [43-46]. The difference in the current investigation is that the  $\gamma'$  precipitates were also characterized with EELS, and shows that no dissolution of the precipitates has occurred. Therefore the current results suggest that dissolution may not be necessary to explain previous experimental results. It is possible that larger gamma prime may partially disorder, and smaller regions within the original precipitate either remain ordered or re-order with irradiation.

The question also arises regarding a  $\gamma'$  size effect on disordering. Unlike the ex-service Inconel X-750, the proton material had a bimodal  $\gamma'$  size distribution. The nature of using a SAD aperture for electron diffraction did not enable the results to differentiate between larger and smaller gamma prime, and therefore it is unclear if ordering resides only within the larger precipitates or from both large and small  $\gamma'$ . STEM diffraction was therefore performed, as reported in Figure 102 and Figure 103. The camera sensitivity in STEM does not appear as good comparatively, but these results seem to strongly support the argument that the larger gamma prime would give the larger contribution to the superlattice intensity in the SAD electron diffraction observations. No detectable signal could be obtained within the matrix where smaller  $\gamma'$  reside. These results could indicate a precipitate size effect on disordering, or the result is indicative of the detection limits of the diffraction technique.

#### **4.2.3.3 Irradiation Hardening**

The microhardness results suggest an increase in hardening of approximately 30-40% compared to the unirradiated material, however, with this approach it is not possible to differentiate the

impact of hardening from the irradiation damage, or the bubbles. The low and high irradiation temperature material had apparently similar changes in hardening.

To understand the impact of different irradiation induced defects on the microstructural evolution, the nanohardness profiles reported in Figure 105-Figure 108 were more useful. There was no major change in hardening at depths where helium bubbles are observed (i.e. approximately 5  $\mu\text{m}$ ) compared to depths with no helium (0-5  $\mu\text{m}$ ) and (6-9  $\mu\text{m}$ ). This is generally consistent with observations in ex-service material, whereby the influence of helium bubbles was minor compared to expectations. No size or density distributions could be obtained from these samples due to the relative density and size of the bubbles, and the thickness of the TEM lamella. Therefore, no attempt has been made to utilize a dispersive barrier model to help predict and understand how much the bubbles may impact the mechanical evolution. As there were no significant changes in hardening at depths of helium implantation, this suggests that the impact of helium bubbles is comparable to the loss due to other defects within this region (i.e. the high density of helium bubbles may decrease the generation of other point defects, or relative ordered gamma prime volume fraction). The defect densities were however, not measured in this investigation because the FIB may have induced damage during lamella fabrication and would be difficult to differentiate between damage induced during proton irradiation and damage produced during FIB. Also, the degree of ordering in gamma prime was not possible to measure because the diffraction patterns were consistently oversaturated in the electron diffraction investigation. Therefore, although this hypothesis is plausible, it is unverified, and would warrant future characterization to validate.

Unlike the ex-service neutron irradiation, the hardness results from the proton irradiated material has a direct comparison to the unirradiated material (sometimes in the same grain), and it is

possible to make conclusive statements regarding a change in hardness. The nanohardness results show a change of only approximately 25% compared to the microhardness showing a change of 30-40%. This difference may be affected by a testing size relationship. The added value from the nano scale hardness testing is associated with the ability to plot the results as a profile of dose.

The most significant change in the hardness was observed at the depth at which the protons stop in the material. This coincides with the presence of large voids observed in the TEM analysis at a depth of approximately 9-10  $\mu\text{m}$ . At these depths, there may be a significant temperature spike associated with the energy transfer from the protons to the material. The temperature monitoring during the analysis was limited to the irradiation surface, and no estimates of the temperatures at this depth are available. It is also possible that the formation of the high density of large voids may have lead to the material acting like a sponge during a standard indentation test such as nanohardness. The width of the softened zone increases with dose, and this can likely be attributed to the formation of voids, and the extended range of the protons in higher dose material because less material is present at these depths to stop the protons.

## **CHAPTER FIVE**

### **GENERAL DISCUSSION**

At points during the microstructural investigation (both ex-service and proton irradiation), there have been many lessons learned and advancements in approach which have changed the focus of the investigation. Many of these lessons learned have not yet been discussed because it would have interrupted the flow of the dissertation, however, a discussion is warranted so that others may benefit as a result.

#### **5.1 How Well did Protons Emulate Neutron Irradiation**

The proton irradiation was added to the program originally because the available material from ex-service was rather limited, and the concept of a controlled laboratory experiment was attractive in the sense of gaining further understanding on how irradiation influences the microstructural and mechanical property evolution. As with any accelerated irradiations, the success of the experimental conditions cannot be validated until the experiment is over. The biggest advantage associated from this experiment are the lessons learned which will help perform the experiment better the second time around. The questions to ask at this point are “what part of the neutron irradiation do we wish to emulate?”. The temperature shift used in the experimental conditions greatly influences this result. In this study, we were interested in the helium bubbles and the gamma prime. In the case of the helium bubbles, our interests were to further understand the influence of vacancy mobility on helium bubble growth. Unfortunately, the size and density of the helium bubbles was likely governed by the implantation process, and not the proton irradiation. If the implantation was performed at an elevated temperature as

opposed to room temperature, the helium bubbles may have produced fewer, larger bubbles and may have been more representative of ex-service material. Some success in doing this was achieved by Zhang et al at Queen's University [47, 48]. If obtaining representative helium bubble sizes and densities are the focus of future studies, it is recommended to implant the materials at elevated temperatures to obtain more representative irradiated microstructures. It is also possible that because we compromised on the temperature shift to be between the appropriate shift for swelling and radiation induced segregation, the test may have been compromised. If the temperature shift applicable to maintaining swelling rate was applied, the helium bubble evolution could be more representative of ex-service material, whereas the gamma prime disordering and dissolution may have been compromised as the defects lost to sinks per unit volume would not be maintained. If this lower irradiation temperature shift was applied, it is possible that the gamma prime disordering may be more representative but the helium bubble evolution and swelling would be securely in the recombination dominated regime. In the case of the current investigation, the proton irradiation was aimed at furthering our understanding of the effects of irradiation on the microstructural and mechanical property evolution of Inconel X-750, and although the study has not perfectly emulated ex-service material, the goal of the investigation has been completed.

## **5.2 Considerations in Characterizing Grain Boundary Helium Bubbles**

In characterizing helium bubbles within the material, and specifically grain boundary helium bubbles, the relative size, density, and sample thickness all play a role in obtaining reliable results. For example: with a bubble size of 1-2 nm, and a relative thickness of 40 nm TEM lamella, the highest possible helium bubble coverage which can be obtained from a grain boundary imaged edge-on is approximately 5%. This is because the boundary would appear as a

string of pearls, and one uniform layer approximately 2 nm by the length of the boundary. In retrospect, having an in-plane boundary gives the added advantage of the ability to quantify grain boundary coverages which are more reliable. In the case of the investigation performed in Section 4.1.2.2, grain boundaries were imaged on-edge and slightly off-edge to increase confidence in the data.

To assist in obtaining more reliable boundary coverage and bubble spacing, 3-dimensional tomography was attempted. This analysis marks the first time 3-D tomography was performed on nano-sized helium bubbles. Unfortunately, the technique is rather limited with respect to imaging resolution of bubbles and relative sample thickness. The only samples which worked for 3-D tomography were the same samples which were so thin that the benefits of 3-D tomography were not required. In other words; there were no bubble overlap issues in the analysis, and reliable quantitative analysis was possible without the need for more complicated 3-D tomography techniques.

For in-plane boundaries and on-edge boundaries, special attention could be given during analysis to obtain suitable stereographic image pairs to help identify grain boundary bubbles and isolate the bubbles which exist on the boundary plane only. Such characterization considerations could have improved upon the analysis shown in Figure 68 and Figure 69 (in-plane grain boundary analysis). In this example, only bubbles greater than 4 nm were included in the analysis, however, if stereographic image pairs were performed, the reliability of the results could be improved upon by enabling the analysis to differentiate between matrix bubbles and bubbles on the boundary. This would improve on the grain boundary area coverage approximations, mean bubble size, and spacing statistics. This analysis however, must be performed manually and

would be rather time extensive, which may limit its practical application. It is recommended that this be performed where possible in future investigations.

### **5.3 Considerations in Characterization of Gamma Prime**

In understanding the results of the gamma prime characterization it is important to first note the complication that can arise from comparing spectroscopy data from different samples. There is an influence on TEM lamella thickness with respect to the gamma prime size that needs to be considered. The gamma prime in the ex-service spacers is only 10-20 nm in size. If a TEM lamella is approximately 50-100 nm, as illustrated in the schematic shown in Figure 109 [135], the potential overlap of the gamma prime may be too great in transmission to allow for individual gamma prime to be isolated. In samples such as this, spectroscopic analysis via EELS or EDX would yield a blurring effect in the relative compositional maps. In the research presented in this dissertation, this realization has helped guide the procedure in characterizing gamma prime in ex-service spacers. No contrast from gamma prime could be identified in bright-field and dark-field imaging, making it difficult to locate the gamma prime during TEM imaging. Therefore, in characterizing the gamma prime, regions sufficiently thin (20-40 nm in thickness) were characterized with EELS followed by electron diffraction analysis. To obtain reliable results, the lamella should be on the same thickness scale as the gamma prime itself (i.e. 10-20 nm). Obtaining reliable TEM lamella from ex-service material at these thicknesses was rather limited. Samples begin to lose structural integrity and break prior to performing TEM analysis, and therefore although it is recognized the samples need to be as thin as possible for reliable results, this may be a significant experimental limitation. The results that were reported in Section 4.1.2.5 show the limited results obtained from high dose (51.2-55.0 dpa and 17300-18600 appm helium) material irradiated at both 120-280°C and 300-330°C. In both temperature

regimes, there is evidence that the gamma prime has not dissolved, however, a superlattice reflection could only be detected for the material irradiated at elevated temperatures (i.e. 300-330°C). This may be an indication that the gamma prime has disordered at the lower irradiation temperature. This conclusion should be made with caution however, because the detection of gamma prime may be instrument sensitive, and the signal from very weak gamma prime may simply be below the detection limits of the TEM. Queen's University has reported that the gamma prime is fully disordered at both irradiation temperatures [11, 49] for this same ex-service material which is contradictory to the results reported within this dissertation. It is recognized that the results were made from different samples, and this may suggest some level of material variability. Alternatively, it is also possible that the dynamic range of the camera system used in their study was not quite as sensitive as the one used in this study. The results from Queen's University also conclude a temperature sensitivity on gamma prime dissolution (lower temperature more dissolved compared to higher temperature). The results reported in this dissertation contradict this observation. It is possible that the effect of sample thickness as shown in Figure 109 may be of great experimental significance to help explain these discrepancies. It is argued that the samples characterized by Queen's University were thicker in comparison to those used in the present study which may lead to these observational differences. It could equally be argued that damage induced from FIB preparation may induce some damage to the samples which will influence the gamma prime characterization. This is unlikely, as the damage produced during FIB preparation would not only affect the gamma prime, but also the bubble structure, and as the bubbles were not affected, the damage from the FIB can be discounted as the source for the discrepancy. It is recommended that the sample thickness be

measured and reported at the region of analysis in the future so that this effect can be accounted for during data interpretation.

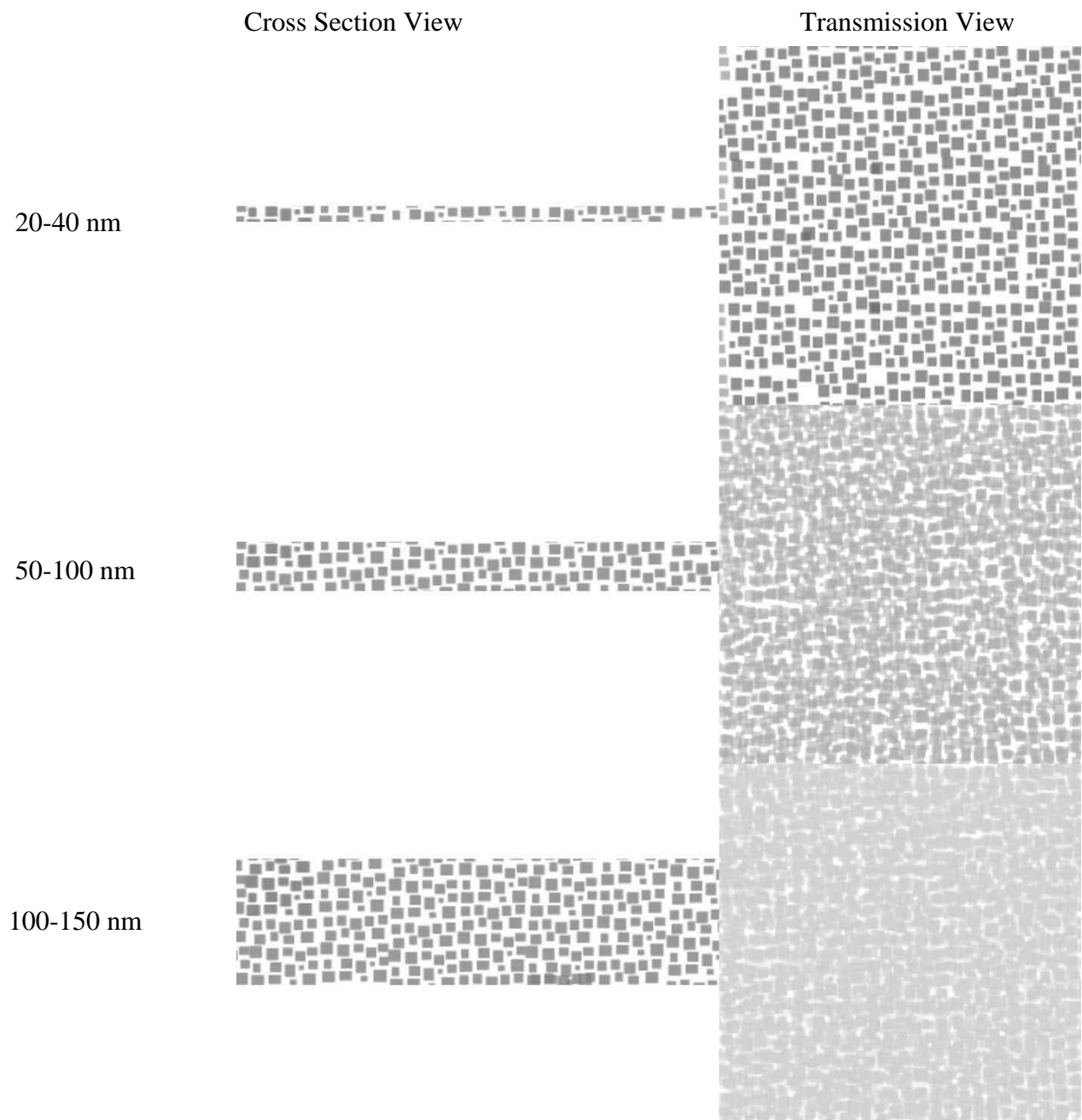


**Figure 109: Effect of thickness on characterizing  $\gamma'$  with TEM. As thickness increases, it becomes increasingly more difficult to differentiate individual  $\gamma'$  or comment on elemental distribution if characterized with spectroscopy techniques in STEM. Image created courtesy of Allan Lockley [135].**

## **CHAPTER SIX**

### **CONCLUSIONS**

#### **6.1 Thesis Overview and Conclusions**

The research presented in this dissertation aims to understand the effects of irradiation on Inconel X-750 microstructure and mechanical properties. This has been fulfilled for ex-service, neutron irradiated Inconel X-750 CANDU spacers and proton irradiated Inconel X-750 with the use of advanced microscopy and mechanical testing techniques. When power reactors were first designed and built, the adverse effect of neutron irradiation on the core materials was largely unknown. Accelerated irradiations in high flux reactors and particle irradiations were therefore conducted to rapidly reach end-of-life doses. This approach has given excellent correlations for many alloys, however, does not successfully capture the influence of a high thermal flux on Ni rich components. The high thermal flux in the CANDU reactor has lead to very high production of helium and an enhancement of the total atomic displacements to levels which have not been investigated prior to this research.

This dissertation was broken into two main results and discussion sections; ex-service Inconel X-750 CANDU spacers, and proton irradiated Inconel X-750. These two sections warrant themselves to having individual conclusions and contributions.

## 6.2 Ex-Service Inconel X-750 CANDU Spacers

The primary objective of this research was to use advanced microscopy techniques to elucidate the fundamental degradation mechanisms responsible for lost strength, ductility and intergranular fracture. The primary conclusions from this research are as follows:

- 1) Although the mechanical behaviour of lower temperature and higher temperature irradiated ex-service spacers show different mechanical responses with respect to ductility and total crush strength, the fracture behaviour remains constant: entirely intergranular. The fracture mechanism remains unchanged with higher dose and helium density, indicating that although the strength and ductility are reducing with continued irradiation, the degradation mechanism appears to be unchanged.
- 2) The very high helium density within the material results in the nucleation and growth of helium bubbles within the matrix and along grain boundaries. The size and density of the bubbles have been shown to be temperature dependent, with fewer ( $10^{24}$  bubbles/m<sup>3</sup>) larger bubbles (<10 nm) in material irradiated at higher temperatures compared to the higher density ( $4 \times 10^{24}$  bubbles/m<sup>3</sup>) of smaller bubbles (<3 nm) in material irradiated at lower temperatures. It was determined that the bubble size on grain boundaries were larger compared to bubbles within the matrix.
- 3) Direct evidence has been gathered (for the first time) to link helium bubble embrittlement with grain boundary helium bubbles. This was done with the use of a focused ion beam to extract a TEM lamella directly from an intergranular fracture surface. The crack path propagated around grain boundary precipitates (not through), and linked along grain boundary helium bubbles.

- 4) The hardness of the material appears to increase slightly with low dose, followed by a gradual reduction in yield strength. The lower temperature irradiated sections appear softer in comparison to the higher temperature irradiated material. Although minor changes in hardness are observed, the total change does not appear to be significant compared to the unirradiated material.
- 5) The microstructural analysis of the irradiated components has been linked with the microhardness measurements, providing valuable insights into the individual contributions to hardening. Helium bubbles have been viewed in the industry as relatively strong barriers to dislocation motion, however, the current work shows strong supporting evidence to the contrary. Although the hardness is influenced by many factors such as defect structures, and gamma prime disordering/dissolution, the lack of hardening in the matrix associated with such a high defect density indicates a lower than expected barrier strength for helium bubbles. This may be greatly influenced by the pressure state of the helium within the bubbles (i.e. underpressurized, overpressurized or at equilibrium). The experimental results supports some theoretical molecular dynamic models which show a transition in barrier strength with bubble size; i.e., smaller bubbles (<2 nm) are weaker in comparison to larger bubbles (>2 nm).
- 6) Electron energy loss spectroscopy has been used to probe individual helium bubbles to measure the helium density as a function of bubble size. This data has then been used to calculate the He/V ratios, and estimate the bubble pressures through the use of a hard sphere equation of state. It has been shown that the helium bubbles at approximately 55 dpa and 18000 appm helium (irradiated at 300-330°C) are at or below equilibrium bubble pressure with no observable loop punching. Linking the helium density

measurements with the bubble size and density distributions, a more accurate representation of the nominal He/V ratio for the material system can be obtained, and an estimate of the total helium concentration within the matrix material can be derived. The EELS measurements can account for approximately  $75 \pm 12$  % of the total helium in the material. This indicates that some helium may reside in sub-microscopic defects as other researchers suggest in their work and as confirmed in the present study. This also is indicative that the helium distribution within the material is not uniform, and tends to form on local sinks such as dislocations, sub-grain boundaries, and grain boundaries.

- 7) Characterization of the gamma prime precipitates show a temperature dependence on the disordering at doses of approximately 55 dpa; lower irradiation temperature resulting in no observable superlattice reflection, while higher irradiation temperature results in a very weak superlattice reflection. EELS analysis shows no evidence of gamma prime dissolution at either irradiation temperature (i.e., no observable transport or diffuse mixing of Ti, Cr, or Ni in the matrix material). This is another potential explanation for a lower material hardness associated with lower irradiation temperature.

### **6.3 Proton Irradiated Inconel X-750**

The objectives of the proton irradiation was to assist in understanding some of the fundamental effects of irradiation on Inconel X-750 in a controlled laboratory environment. There are fundamental differences in the nature of the irradiation which limits this experiment from perfectly emulating the in-reactor material, however, this work has contributed to the following conclusions:

- 1) Gamma prime remains partially ordered at all irradiation conditions and temperatures investigated in this study, nor was there any direct evidence of gamma prime dissolution.

This supports the observations from higher temperature ex-service neutron irradiated materials, where gamma prime remains partially ordered with no observable dissolution. The low temperature proton irradiation was not carried out to high doses, so a direct comparison could not be made with the ex-service material.

- 2) The disordering of gamma prime appears to be precipitate size dependent; larger gamma prime remaining partially ordered and smaller gamma prime disordered. This conclusion is strongly supported by STEM diffraction, however, the sensitivity of the technique may strongly influence the conclusion. It is recommended that smaller selected area diffraction apertures be used (not available in this study) to investigate this further.
- 3) In regions with helium implantation, large voids were not observed, whereas regions with no helium, voids ranging in size of 10-15 nm were observed, indicating that regions with a high density of helium tends to suppress void growth by limiting vacancy mobility in the matrix.
- 4) The microhardness and nano hardness measurements show an increase in hardness of approximately 25% with irradiation. Only a minor change in hardness was observed at regions with helium implantation. This observation supports the conclusions in ex-service, neutron irradiated material that the contribution of helium bubbles is smaller than claimed in open literature.

## **RECOMENDATIONS FOR FUTURE WORK**

This was the first time that the microstructure of Inconel X-750 irradiated to these conditions has been investigated in detail, and as a result, there are many outstanding, open ended questions, which warrant continued research to help explain. The work presented in this dissertation is only a small part of a large, ongoing, industrial research program. Some recommendations from this program have already been shared with our industrial partners, and have been or are currently being incorporated for future work.

- 1) The ex-service material examined to date has been from material removed after only approximately 15 effective full power years of service. Additional material with higher doses will continue to become available until reactor end-of-life. It is recommended that material continue to be examined to higher dose and helium concentrations for trending purposes. This work is being continued by CNL through the CANDU Owners Group Joint Projects 4452 and 4491.
- 2) It was noted that difficulties occurred in obtaining a “true” pinched section of spring for microstructural analysis as part of this research. As a result, this has increased the level of uncertainty concluding the effects of irradiation temperature on the microstructural evolution. It is recommended that further characterization be performed from regions of material with higher certainty.
- 3) Further thinning of available test specimens will give more quantitative analysis of the microstructural evolution as a function of dose and temperature. Specifically, more details can be obtained regarding; helium density, boundary coverage, gamma prime

disordering/dissolution, and helium bubble pressure. This can be performed at McMaster University in collaboration with the newly constructed Centre for Advanced Nuclear Systems – Post Irradiation Examination (CANS-PIE) facility currently under construction. This facility will be equipped with a FEI Versa 3D focused ion beam (FIB) capable of thinning active material.

- 4) The EELS analysis of helium bubbles in the current investigation was limited to one irradiation and temperature condition (i.e., ~55dpa, 18000 appm helium irradiated at 300-330°C). It is recommended that a similar investigation be performed as a function of temperature and dose to better understand the helium bubble evolution. It is also recommended to investigate the difference in bubble pressure for matrix and grain boundary helium bubbles. Differences may help explain helium transport within the material local to grain boundaries. This may require further thinning of samples available (potential involvement of the new facilities being installed at McMaster University, Centre for Advanced Nuclear Systems' Post-Irradiation Examination (CANS-PIE) facility which is installing a new active focused ion beam).
- 5) Thermal annealing of the irradiated specimens may validate the state of helium bubbles. This may be performed in bulk samples, or with the use of a heat stage in the TEM, can be performed in-situ. This work is ongoing as part of continued CNL research through the CANDU Owners Group.
- 6) Micro-mechanical testing can be performed in conjunction with TEM analysis to ascertain the grain boundary strength, and provide a direct link with quantitative bubble coverage and boundary strength. It is important to note that some on-going collaborative work has already begun with Prof. Peter Hosemann at University of California, Berkley,

specific to this recommendation. Some preliminary results have been discussed at the 2015 TMS conference, and Hotlab 2015 conference.

- 7) If the target of the proton irradiation is to better simulate the ex-service material, helium implantation at elevated temperatures may be warranted. The current study was intended to understand the influence of irradiation temperature on microstructural evolution, and it was thought that elevated implantation temperature would too greatly influence the diffusion of helium prior to commencement of the study (i.e. diffuse during implantation prior to irradiation). This may give opportunities for using proton irradiated samples for more systematic studies of micro-mechanical testing suggested above.
- 8) The sensitivity of the camera systems for investigating gamma prime disordering has been suggested in the discussion section. A more detailed investigation regarding this sensitivity should be investigated to understand the limitations of TEM for identification of low volume fraction ordered structures.
- 9) The impact of temperature variations during irradiation similar to that expected for the pinched material should be investigation with the use of ion or proton irradiations. Working with ex-service material, experimentalists typically assume an operating temperature of the time weighted mean, however, the impact of temperature fluctuations during irradiation is largely unknown in reactor materials. This unknown increases the experimental uncertainty.

## REFERENCES

- [1] Young, G.A., Lewis, N., Hanson, M., Matuszyk, W., Wiersma, B. and Gonzalez, S.C.; KAPL Report LM-01K034; *Microstructural and Microchemical Characterization of Dual Step Aged Alloy X-750 and Its Relationship to Environmentally Assisted Cracking*; May 2001.
- [2] Waheed, A.; 6400-37000-220-001; *Test Results of Inconel X-750 Bottom Guide Spring in Hanaro Bundle*.
- [3] Symons, D.M., *Journal of Nuclear Materials* 1998, 264, 225-231.
- [4] Jenssen, A., Efsing, P. and Sundberg, J., Influence of Heat Treatment, Aging and Neutron Irradiation on Fracture Toughness in X-750. In *Proceedings of the 12th International Conference on Environmental Degradation of Materials in Nuclear Power System-Water Reactors*, T.R. Allen, P. J. K., and L. Nelson, Ed. TMS: 2005; pp 73-85.
- [5] Grove, C.A. and Petzold, L.D. In *Mechanisms of Stress Corrosion Cracking of Alloy X-750 in High Purity Water*, International Conference on Corrosion of Nickel Base Alloys, Cincinnati, Ohio, October 23-25, 1984; ASM: Cincinnati, Ohio, 1985.
- [6] Judge, C.D., Griffiths, M., Walters, L., Wright, M., Bickel, G.A., Woo, O.T., Stewart, M., Douglas, S.R. and Garner, F., Embrittlement of Nickel Alloys in a Candu\* Reactor Environment. In *Effects of Radiation on Nuclear Materials*, Yamamoto, T., Ed. ASTM International: Anaheim, CA, 2012; Vol. 25, pp 161-175.
- [7] *Superalloys II*. John Wiley and Sons, Inc.: 1987.
- [8] Smith, G.D. and Petel, S.J., *TMS 2005, 2005*.
- [9] Judge, C.D., Gauquelin, N., Walters, L., Wright, M., Cole, J.I., Madden, J., Botton, G.A. and Griffiths, M., *Journal of Nuclear Materials* 2015, 457 (0), 165-172.
- [10] Griffiths, M., Bickel, G.A., Donohue, S.A., Feenstra, P., Judge, C.D., Walters, L. and Wright, M.D. In *Degradation of Ni-Alloy Components in Candu Reactor Cores*, 16th Int. Conference on Environmental Degradation of Materials in Nuclear Power Systems – Water Reactors, Asheville, North Carolina, USA, August 11-15, 2013; Asheville, North Carolina, USA, 2013.
- [11] Zhang, H.K., Yao, Z., Morin, G. and Griffiths, M., *Journal of Nuclear Materials* 2014, 451 (1-3), 88-96.
- [12] Walters, L., Bickel, G.A. and Griffiths, M., The Effects of Microstructure and Operating Conditions on Irradiation Creep of Zr-2.5Nb Pressure Tubing. In *Zirconium in the Nuclear Industry: 17th International Symposium*, ASTM International: 2014.
- [13] Griffiths, M., Poff, D., Yao, Z. and Zhang, H.K. In *Performance of Ni Alloy Components in Candu Reactors*, International Conference on Materials Science and Technology, Montreal, Quebec, Canada, October 27-31, 2013; Montreal, Quebec, Canada, 2013.
- [14] Griffiths, M., *AECL Nuclear Review* 2013, 2 (1).
- [15] Garner, F., Griffiths, M. and Greenwood, L.R., Enhancement of Irradiation Creep of Nickel-Bearing Alloys in Thermalized Neutron Spectra Characteristic of Lwr and Candu Reactors. In *Effects of Radiation on Nuclear Materials*, Yamamoto, T., Ed. ASTM International: Anaheim, CA, 2012; Vol. 25.
- [16] Bickel, G.A., Griffiths, M., Douchant, A., Douglas, S.R., Woo, O.T. and Buyers, A., *Journal of ASTM International* 2011, 8 (2).

- [17] Greenwood, L.R. and Garner, F.A., *Journal of Nuclear Materials* 1996, 233–237, Part 2 (0), 1530-1534.
- [18] Garner, F., Greenwood, L.R. and Oliver, B.M. In *A Re-Evaluation of Helium/Dpa and Hydrogen/Dpa Ratios for Fast Reactor and Thermal Reactor Data Used in Fission-Fusion Correlations*, Proceedings of a Technical Committee meeting held in Obnisk, Russian Federation, 16-19 June 1997; 1997.
- [19] Heald, P.T. and Speight, M.V., *Acta Metallurgica* 1975, 23 (11), 1389-1399.
- [20] Greenwood, L.R., Garner, F., Oliver, B.M., Grossbeck, M.L. and Wolfer, W.G., *Journal of ASTM International* 2004, 1 (4).
- [21] Zinkle, S.J., 1.03 - Radiation-Induced Effects on Microstructure\*. In *Comprehensive Nuclear Materials*, Konings, R. J. M., Ed. Elsevier: Oxford, 2012; pp 65-98.
- [22] Yamamoto, T., Odette, G.R., Kishimoto, H., Rensman, J.-W. and Miao, P., *Journal of Nuclear Materials* 2006, 356 (1–3), 27-49.
- [23] Yamamoto, N., Chuto, T., Murase, Y. and Nagakawa, J., *Journal of Nuclear Materials* 2004, 329–333, Part B (0), 993-997.
- [24] Trinkaus, H. and Ullmaier, H., *Journal of Nuclear Materials* 1988, 155–157, Part 1 (0), 148-155.
- [25] Trinkaus, H. and Ullmaier, H., *Journal of Nuclear Materials* 1994, 212–215, Part 1 (0), 303-309.
- [26] Mansur, L.K. and Grossbeck, M.L., *Journal of Nuclear Materials* 1988, 155–157, Part 1 (0), 130-147.
- [27] Imasaki, K., Hasegawa, A., Nogami, S. and Satou, M., *Journal of Nuclear Materials* 2011, 417 (1-3), 1030-1033.
- [28] Hunn, J.D., Lee, E.H., Byun, T.S. and Mansur, L.K., *Journal of Nuclear Materials* 2000, 282 (2-3), 131-136.
- [29] Grossbeck, M.L., 1.04 - Effect of Radiation on Strength and Ductility of Metals and Alloys. In *Comprehensive Nuclear Materials*, Konings, R. J. M., Ed. Elsevier: Oxford, 2012; pp 99-122.
- [30] Evans, J.H., *Journal of Nuclear Materials* 1977, 68, 129-140.
- [31] Dai, Y., Odette, G.R. and Yamamoto, T., 1.06 - the Effects of Helium in Irradiated Structural Alloys. In *Comprehensive Nuclear Materials*, Konings, R. J. M., Ed. Elsevier: Oxford, 2012; pp 141-193.
- [32] Edwards, D.J., Simonen, E.P., Garner, F.A., Greenwood, L.R., Oliver, B.M. and Bruemmer, S.M., *Journal of Nuclear Materials* 2003, 317 (1), 32-45.
- [33] Edwards, D.J., Garner, F.A., Bruemmer, S.M. and Efsing, P., *Journal of Nuclear Materials* 2009, 384 (3), 249-255.
- [34] Endf/B-Vi Nuclear Library, [Http://T2.Lanl.Gov](http://T2.Lanl.Gov).
- [35] Greenwood, L.R., *Journal of Nuclear Materials* 1983, 115 (2-3), 137-142.
- [36] Was, G.S., *Fundamentals of Radiation Materials Science*. Springer: 2007.
- [37] Orowan, E., *Internal Stresses in Metals and Alloys*. The Institute of Metals: London, 1948.
- [38] Stoller, R.E. and Zinkle, S.J., *Journal of Nuclear Materials* 2000, 283–287, Part 1 (0), 349-352.
- [39] Bement, A.L.J., *Strength of Metals and Alloys*. ASM International: Metals Park, OH, 1973.
- [40] Kelly, P.M., *International Metallurgical Reviews* 1973, 18 (31).

- [41] Kocks, U.F., *Materials Science and Engineering* 1977, 27, 291-298.
- [42] Stoller, R.E., Personal Communication. 2015.
- [43] Carsughi, F., Derz, H., Ferguson, P., Pott, G., Sommer, W. and Ullmaier, H., *Journal of Nuclear Materials* 1999, 264 (1-2), 78-88.
- [44] Thomas, L.E. and Bruemmer, S.M., Radiation-Induced Microstructural Evolution and Phase Stability in Nickel Base Alloy 718. In *Pro. 8th International Symposium of Environmental Degradation of Materials in Nuclear Power Systems - Water Reactors*, S Bruemmer, S. M.; McLirree, A. R., Eds. American Nuclear Society: 1997; p 772.
- [45] Camus, E., Abromeit, C., Bourdeau, F., Wanderka, N. and Wollenberger, H., *Physical Review B* 1996, 54 (5).
- [46] Nelson, R.S., Hudson, J.A. and Mazey, D.J., *Journal of Nuclear Materials* 1972, 44 (3), 318-330.
- [47] Zhang, H.K., Yao, Z., Judge, C. and Griffiths, M., *Journal of Nuclear Materials* 2013, 443 (1-3), 49-58.
- [48] Zhang, H.K., Yao, Z., Daymond, M.R. and Kirk, M.A., *Journal of Nuclear Materials* 2014, 445 (1-3), 227-234.
- [49] Zhang, H.K. Irradiation Induced Damage in Candu Spacer Material Inconel X-750. Queen's University, 2013.
- [50] Yao, Z. The Relationship between the Irradiation Induced Damage and the Mechanical Properties of Single Crystal Ni. 2005.
- [51] Yao, Z., Schäublin, R. and Victoria, M., *Journal of Nuclear Materials* 2002, 307-311 (1 SUPPL.), 374-379.
- [52] victoria, M., Baluc, N., Bailat, C., Dai, Y., Luppò, M., Schaublin, R. and Singh, B., *Journal of Nuclear Materials* 2000, 276, 114-122.
- [53] Schäublin, R., Yao, Z., Spatig, P. and Victoria, M., *Materials Science and Engineering* 2005, A (400-401), 251-255.
- [54] Schäublin, R., Yao, Z., Baluc, N. and Victoria, M., *Philosophical Magazine* 2005, 85, 769-777.
- [55] Zinkle, S.J. and Snead, L.L., *Journal of Nuclear Materials* 1995, 225, 123-131.
- [56] Zinkle, S.J., Maziasz, P.J. and Stoller, R.E., *Journal of Nuclear Materials* 1993, 206 (2-3), 266-286.
- [57] Zinkle, S.J., Farrell, K. and Kanazawa, H., *Journal of Nuclear Materials* 1991, 179-181, 994-997.
- [58] Yao, Z., Schaublin, R. and Victoria, M., *Journal of Nuclear Materials* 2002, 311, 374-379.
- [59] Yang, J., Ao, B., Hu, W. and Wang, X., *Journal of Physics: Conference Series* 2006, 29, 190-193.
- [60] Stoller, R.E. and Odette, G.R., *Journal of Nuclear Materials* 1985, 131, 118-125.
- [61] Peixuan, W., Yupu, L., Jiarui, L., Guoguang, Z., Ruzhang, M., Peiruan, Z., Changqing, Q. and Tianbing, X., *Journal of Nuclear Materials* 1989, 169 (C), 167-176.
- [62] Mansur, L.K., Lee, E.H., Maziasz, P.J. and Rowcliffe, A.P., *Journal of Nuclear Materials* 1986, 141-143, Part 2 (0), 633-646.
- [63] Jäger, W., Lässer, R., Schober, T. and Thomas, G.J., *Radiation Effects* 1983, 78 (1-4), 165-176.
- [64] Golubov, S.I., Stoller, R.E., Zinkle, S.J. and Ovcharenko, A.M., *Journal of Nuclear Materials* 2007, 361 (2-3), 149-159.

- [65] Ullmaier, H., *Nuclear Fusion* 1984, 24 (8), 1039-1083.
- [66] Mansur, L.K. and Coghlan, W.A., *Journal of Nuclear Materials* 1983, 119 (1), 1-25.
- [67] Mansur, L.K. and Lee, E.H., *Journal of Nuclear Materials* 1991, 179-181, 105-110.
- [68] Knapp, J.A., Follstaedt, D.M. and Myers, S.M., *Journal of Applied Physics* 2008, 103 (013518-1).
- [69] Young, J.A., Wirth, B.D., Robach, J. and Robertson, I.M. In *Dislocation Interactions with Voids and He Bubbles in Fcc Materials*, 11th International Conference on Fusion Reactor Materials, Kyoto, Japan, December 7-12, 2003; Kyoto, Japan, 2003.
- [70] Simar, A., Voigt, H.-J.L. and Wirth, B.D., *Computational Materials Science* 2011, 50 (5), 1811-1817.
- [71] Evans, J.H., Escobar Galindo, R. and van Veen, A., *Nuclear Instruments and Methods in Physics Research Section B: Beam Interactions with Materials and Atoms* 2004, 217 (2), 276-280.
- [72] Donnelly, S.E., *Radiation Effects* 1985, 90, 1-47.
- [73] Trinkaus, H., *Radiation Effects* 1983, 78 (1-4), 189.
- [74] Carnahan, N.F. and Starling, K.E., *The Journal of Chemical Physics* 1979, 51 (2).
- [75] Stoller, R.E. and Osetsky, Y.N., *Journal of Nuclear Materials* 2014, 455 (1-3), 258-262.
- [76] Fenske, G., Das, S.K., Kaminsky, M., Miley, G., Terrault, B., Abel, G. and Labrie, J.P., *Journal of Applied Physics* 1981, 52 (5), 3618.
- [77] Fenske, G., Das, S.K., Kaminsky, M. and Miley, G., *Journal of Nuclear Materials* 1978, 76/77, 247.
- [78] Fenske, G., Das, S.K., Kaminsky, M. and Miley, G., *Journal of Nuclear Materials* 1979, 85/86, 707.
- [79] Fenske, G., Das, S.K., Kaminsky, M. and Miley, G., *Nuclear Instruments and Methods* 1980, 170 (1-3), 465.
- [80] Fenske, G., Das, S.K., Kaminsky, M. and Miley, G., *Transactions of the American Nuclear Society* 1978, 28, 196.
- [81] Fenske, G., Das, S.K. and Kaminsky, M., *Journal of Nuclear Materials* 1982, 104 (1-3), 1231.
- [82] Fenske, G., Das, S.K. and Kaminsky, M., *Journal of Nuclear Materials* 1979, 80 (2), 373.
- [83] Fenske, G. University of Illinois, 1979.
- [84] Van Swygenhoven, H., Stals, L.M. and Knuyt, G., *Radiation Effects Letters* 1983, 76 (1-2), 29.
- [85] Van Swygenhoven, H. and Stals, L.M., *Radiation Effects* 1982, 78 (1-4), 157.
- [86] Van Swygenhoven, H., Knuyt, G., Vanoppen, J. and Stals, L.M., *Journal of Nuclear Materials* 1983, 114 (2-3), 157.
- [87] Van Swygenhoven, H. Limburgs Universitair Centrum, 1982.
- [88] Lucas, A.A., Vigneron, J.P., Donnelly, S.E. and Rife, J.C., *Physical Review B* 1983, 28 (5), 2485-2496.
- [89] Taverna, D., Kociak, M., Stéphan, O., Fabre, A., Finot, E., Décamps, B. and Colliex, C., *Physical Review Letters* 2008, PRL 100 (035301), 1-4.
- [90] Jäger, W., Manzke, R., Trinkaus, H., Zeller, R., Fink, J. and Crecelius, G., *Radiation Effects* 1983, 78, 315-325.
- [91] Jäger, W., Manzke, R., Trinkaus, H., Crecelius, G. and Zeller, R., *Journal of Nuclear Materials* 1982, 111&112, 674-680.

- [92] Walsh, C.A., Yuan, J. and Brown, L.M., *Philosophical Magazine* 2000, 80 (7), 1507-1543.
- [93] Fréchar, S., Walls, M., Kociak, M., Chevalier, J.P., Henry, J. and Gorse, D., *Journal of Nuclear Materials* 2009, 393 (1), 102-107.
- [94] Wu, Y., Odette, R.G., Yamamoto, T., Ciston, J. and Hosemann, P., An Electron Energy Loss Spectroscopy Study of Helium Bubbles in Nanostructured Ferritic Alloys. In *DOE/ER-0213/54*, Program, F. R. M., Ed. 2013; Vol. 54.
- [95] Mazey, D.J., *Journal of Nuclear Materials* 1990, 174 (2–3), 196-209.
- [96] Was, G.S., Busby, J.T., Allen, T., Kenik, E.A., Jensson, A., Bruemmer, S.M., Gan, J., Edwards, A.D., Scott, P.M. and Andreson, P.L., *Journal of Nuclear Materials* 2002, 300 (2–3), 198-216.
- [97] Was, G.S. and Averback, R.S., 1.07 - Radiation Damage Using Ion Beams. In *Comprehensive Nuclear Materials*, Konings, R. J. M., Ed. Elsevier: Oxford, 2012; pp 195-221.
- [98] Was, G.S. and Allen, T., *Materials Characterization* 1994, 32 (4), 239-255.
- [99] Griffiths, M., Styles, R.C., Woo, C.H., Phillipp, F. and Frank, W., *Journal of Nuclear Materials* 1994, 208 (3), 324-334.
- [100] Griffiths, M., Loretto, M.H. and Smallman, R.E., *Journal of Nuclear Materials* 1983, 115 (2–3), 323-330.
- [101] Griffiths, M., *Journal of Nuclear Materials* 1993, 205 (0), 225-241.
- [102] Hinks, J.A., *Nuclear Instruments and Methods in Physics Research Section B: Beam Interactions with Materials and Atoms* 2009, 267, 3652-3662.
- [103] Kirk, M.A., Baldo, P.M., Liu, A., Ryan, E.A., Bircher, R.C., Yao, Z., Xu, S., Jenkins, M.L.H.-M., M., KLaoumi, D. and Motta, A.T., *Microscopy Research and Technique* 2009, 72, 182-188.
- [104] Was, G.S. and Kruger, R.M., *Acta Metallurgica* 1985, 33 (5), 841-854.
- [105] Was, G.S., Allen, T.R., Busby, J.T., Gan, J., Damcott, D., Carter, D., Atzmon, M. and Kenik, E.A., *Journal of Nuclear Materials* 1999, 270 (1–2), 96-114.
- [106] Busby, J.T., Hash, M.C. and Was, G.S., *Journal of Nuclear Materials* 2005, 336 (2-3), 267-278.
- [107] Bruemmer, S.M., Simonen, E.P., Scott, P.M., Andresen, P.L., Was, G.S. and Nelson, J.L., *Journal of Nuclear Materials* 1999, 274 (3), 299-314.
- [108] Boothby, R.M. and Harries, D.R., Irradiation-Induced Embrittlement and Precipitation in Nimonic Pe16. UKAEA Atomic Energy Research Establishment: 1981.
- [109] Hasegawa, M., Osawa, M. and Natori, A., in *Japanese buth with English titles for Figures, Tetsu To Hagane; Japan* 1979, 65:8.
- [110] Yang, W.J.S., Gelles, D.S., Straalsund, J.L. and Bajaj, R., *Journal of Nuclear Materials* 1985, 132 (3), 249-265.
- [111] Rowcliffe, A.F., Mansur, L.K., Hoelzer, D.T. and Nanstad, R.K., *Journal of Nuclear Materials* 2009, 392 (2), 341-352.
- [112] Zhang, H.K., Long, F., Yao, Z. and Daymond, M.R., *Journal of Microscopy* 2013, 252 (3).
- [113] Yamakawa, K. and Shimomura, Y., *Journal of Nuclear Materials* 1999, 264, 319-326.
- [114] Sencer, B.H., Bond, G.M., Garner, F.A., Hamilton, M.L., Oliver, B.M., Thomas, L.E., Maloy, S.A., Sommer, W.F., James, M.R. and Ferguson, P.D., *Journal of Nuclear Materials* 2000, 283-287 (PART I), 324-328.

- [115] Mazumder, B., Bannister, M.E., Meyer, F.W., Miller, M.K., Parish, C.M. and Edmondson, P.D., *Nuclear Materials and Energy* 2015, 1 (0), 8-12.
- [116] Aitkaliyeva, A., Madden, J.W., Miller, B.D., Cole, J.I. and Gan, J., *Journal of Nuclear Materials* 2015, 459 (0), 241-246.
- [117] Williams, D.B. and Carter, C.B., *Transmission Electron Microscopy*. New York, 1996; Vol. 3.
- [118] Jenkins, M.L. and Kirk, M.A., *Characterization of Radiation Damage by Transmission Electron Microscopy*. Institute of Physics Publishing: Bristol and Philadelphia, 2001.
- [119] Kato, T., Nakata, K., Masaoka, I., Takahashi, H., Takeyama, T., Ohnuki, S. and Osanai, H., *Journal of Nuclear Materials* 1984, 122 (1–3), 721-726.
- [120] Kai, J.-J. and Lee, R.D., *Journal of Nuclear Materials* 1993, 207 (0), 286-294.
- [121] Egerton, R.F., *Electron Energy-Loss Spectroscopy*. 3rd ed.; Springer: 2011.
- [122] Tabor, D., *British Journal of Applied Physics* 1956, 7 (5), 159.
- [123] Was, G.S., Temperature Shift Discussion. 2014.
- [124] Was, G.S., Dpa on Helium Implantation Discussion. Judge, C. D., Ed. 2015.
- [125] Stoller, R.E., Toloczko, M.B., Was, G.S., Certain, A.G., Dwaraknath, S. and Garner, F.A., *Nuclear Instruments and Methods in Physics Research Section B: Beam Interactions with Materials and Atoms* 2013, 310, 75-80.
- [126] Imagej. 2014.
- [127] Messaoudii, C., Boudier, T., Sanchez Sorzano, C.O. and Marco, S., *BMC bioinformatics* 2007, 8, 288.
- [128] Chimera, U., <http://www.cgl.ucsf.edu/chimera/>.
- [129] Fink, J., Recent Developments in Energy-Loss Spectroscopy. In *Advances in Electronics and Electron Physics*, Hawkes, P. W., Ed. Academic Press, Inc: 1989; Vol. 75.
- [130] Oliver, B.M., Bradley, J.G. and Farrar, H., *Geochimica et Cosmochim. Acta* 1984, 48, 1759.
- [131] Jäger, W. and Trinkaus, H., *Journal of Nuclear Materials* 1993, 205, 394-410.
- [132] Woo, O.T., Judge, C.D., Nordin, H., Finlayson, D. and Andrei, C., The Microstructure of Unirradiated and Neutron Irradiated Inconel X-750. In *Microscopy and Microanalysis*, Nashville, Tennessee, 2011.
- [133] Bickel, G.A., Green, L.W., James, M.W.D., Lamarche, T.G., Leeson, P.K. and Michel, H., *Journal of Nuclear Materials* 2002, 306 (1), 21-29.
- [134] Buyers, A., Seguin, M. and Lockley, A., Unpublished Microhardness Measurements as a Function of Fabrication for Inconel X-750 Candu Spacers. Canadian Nuclear Laboratory: 2015.
- [135] Lockley, A., Personal Communication. 2015.